An investigation of the processes involved in tracer transport and exchanges within and between the different layers in the atmosphere

by

Réal D'Amours

A thesis submitted in partial fulfillment of the requirements for the degree of

Doctor of Philosophy

Department of Earth and Atmospheric Sciences
University of Alberta

©Réal D'Amours, 2015

Abstract

This thesis investigates the transport and dispersion of substances injected in the different layers of the atmosphere, and the mechanisms by which these substances may be transferred from one layer to another. These investigations are based on results of simulations using Lagrangian dispersion models that were "driven" by large scale wind fields provided by the numerical weather analysis and prediction sytems in operation at the Canadian Meteorological Centre. The main substance of the thesis consists in three papers published during the course of my doctoral studies. Although each one of the papers constitutes a distinct scientific study, as a group, they are unified by their collective focus on transport within and exchange between the atmospheric layers.

After a brief overview of the three main layers that account for most of the atmosphere's mass, and of their interfaces, the fundamental aspects of Lagrangian modelling, specially those concerning stochastic processes, are reviewed and discussed. Special attention is given to the relationship between the particles' trajectories in phase-space produced using a stochastic differential equation and the Fokker-Planck equation describing the time evolution of the probability density distribution of those particles in phase-space.

The Lagrangian transport models developed and used operationally at the Canadian Meteorological Centre (CMC) of Environment Canada are presented, and the various simulated physical processes are also discussed. The models are applied to real cases of atmospheric transport and dispersion in the boundary layer, and are compared to available observations.

Transport and dispersion of aerosols injected deeply into the stratosphere during the eruptions of the Alaskan volcanoes Okmok and Kasatochi in the summer of 2008 is investigated. The sulfate aerosol plumes resulting from these eruptions can be followed for many days after their injection into the stratosphere, illustrating clearly that the air circulates in rather well maintained streams with little vertical mixing in these layers.

Investigations for the possible source regions of the ^{7}Be observed near the surface at Harlech in the Alberta foothills, show that transfers between the lower stratosphere and the upper troposphere do occur regularly, but are generally confined to regions close to the tropopause. It is also seen that tropopause folds associated with well developed cyclonic systems induce strong and deep subsidence frequently enough to feed well maintained streams of stratospheric air into the mid and low troposphere, which later can be entrained into the boundary layer.

The mechanisms governing exchange between the free troposphere and the planetary boundary layer are examined in detail with the aid of a simple diagnostic model developed to estimate the turbulent kinetic energy and the turbulent velocity variances. This model produces plausible profiles of the vertical velocity variance σ_w^2, and of the vertical distribution of buoyancy production/destruction of this variance. The diagnosed entrainment zone (EZ) proves just as credible as that resulting from more complex models. It is found that the diagnosed σ_w^2 profiles are smoothly attenuating in the entrainment zone, which is a few hundreds of meters deep, justifying a simplification in the calculation of Lagrangian trajectories across this zone.

Preface

Chapters 4, 5 and 6 of this thesis have been published in peer reviewed scientific journals. I was responsible for the manuscripts' composition, and for most of the calculations and diagrams. My co-authors contributed to the manuscripts' edits, and/or participated in the development of the models used, and to some of the calculations. Publication details are given at the beginning of each of these chapters.

Dedication

À Ginette ma bien aimée

Acknowledgements

I want to express my gratitude to my supervisor Professor John Wilson for his continuing support and patience. I would also like to thank those who served on my supervisory and examining committees, in particular Professor John Lin (University of Utah) as external examiner, along with Professors Gerhard Reuter, Bruce Sutherland, Carlos Lange, Peter Steffler and Paul Myers (University of Alberta).

Finally I also wish to acknowledge Environment Canada for giving me access to the meteorological data and for allowing the use of the informatic facilities in order to conduct the major part of my research. Specially, I want to recognise Mr Pierre Bourgouin and Mr Richard Hogue for having made this possible several by supporting several projects closely related to my research.

Contents

List of Tables

List of Figures

Acronyms

ABL	Atmospheric Boundary Layer
ATMES	Atmospheric Transport Model Evaluation Study
AURA/OMI	Ozone Monitoring Instrument on board the Aura spacecraft
AVO	Alaska Volcanic Observatory
AVHRR	Advanced Very High Resolution Radiometer
BL	Boundary Layer
CBL	Convective Boundary Layer
CMC	Candian Meteorological Centre
CTBT	Comprehensive Test Ban Treaty
EC	Environment Canada
ETEX	European Tracer Experiment
ECMWF	European Center for Medium Range Weather Forecasting
EZ	Entrainment Zone
EST	Eastern Standard Time
FB	Fractional Bias
FNEP	Federal Nuclear Emergency Plan
FOR	Field of Regard (proportional to time interated SRS)
FPE	Fokker-Planck Equation
FMS	Figure of Merit in Space
FT	Free Troposphere
GDPS	Global Deterministic Prediction System (at CMC)
GEM	Global Environmental Multiscale (name of the NWP model in operation at CMC)
HRDPS	High Resolution Deterministic Prediction System at CMC
IAEA	International Atomic Energy Agency
ICAO	International Civil Aviation Organisation
LSE	Lagrangian Stochastic Equation
LSM	Lagrangian Stochastic Model
MFDOAS	Multi-Function Differential Optical Absorption Spectrometer
MLCD	Modèle Lagrangien Courte Distance (short range Lagrangian dispersion model)

MLDPmm	Modèle Lagrangien de Dispersion de Particules mode mixte (Mixed mode Lagrangian Dispersion Model)
MLDP0	Modèle Lagrangien de Dispersion de Particules ordre 0 (Zeroth Order Lagrangian Dispersion Model)
MLDP1	Modèle Lagrangien de Dispersion de Particules ordre 1 (First order Lagrangian Dispersion Model)
MOE	Measure of Effectiveness
NOAA	National Oceanographic and Atmospheric Administraion (US)
NWP	Numerical Weather Prediction
OSF	Objective Scoring Function
PBL	Planetary Boundary Layer
$PM_{2.5}$	Particulate Matter of size greather than 2.5 μm
PCMH	Perfluorocrabon inert tracer
PNNL	Pacific Northwest Nuclear Laboratories
PVU	Potential Vorticity Unit
RDE	Random Displacement Equation
RDPS	Regional Deterministic Prediction System (at CMC)
RH	Relative Humidity
RSMC	Regional Specialised Meteorological Centre
SSA	Singular Spectrum Analysis
SDE	Stochastic Differential Equation
SL	Surface Layer
SRS	Source-Receptor Sensitivity coefficient
ST	Stratosphere
STT	Stratosphere – Troposphere Transfer
TKE	Turbulent Kinetic Energy
UTC	Universal Time Coordinated
VAAC	Volcanic Ash Advisory Center
WMC	Well Mixed Constraint
WSU	Washington State University

Roman Variables

$\mathbb{A}$	Random acceleration vector
a_i	i component of the acceleration/damping term in the LSE
B	Turbulence production (destruction) due to buoyancy
b_{ij}	Tensor coefficient in the LSE
c_i	Concentration at location i
$c(\boldsymbol{r}, t)$	Concentration field
C_0	A universal dimensionless constant $\sim$4.0
$d\xi_i$	Random component increment in the LSE
E	Turbulent kinetic energy(TKE)
E_p	Ertel's potential vorticity
$\overline{F_t^l}$	Average residence time above level l for time t
f	the Coriolis parameter
$\boldsymbol{F_x}(\boldsymbol{x}, \boldsymbol{u}, t)$	Flux of probability density in the position space
$\boldsymbol{F_u}(\boldsymbol{x}, \boldsymbol{u}, t)$	Flux of probability density in the velocity space
g	Acceleration due to earth's attraction
$g()$	Distribution of fluid elements in phase space
$g_a()$	Dstribution of atmospheric fluid elements in phase space
H, h	Boundary layer thickness
H_{sl}, h_{sl}	Surface layer thickness
k_v	von Karman constant (~ 0.4)
K, K_z	Eddy diffusivity (vertical)
L	Monin-Obukhov lengthscale
m_p	Mass of particle p
m_{uv}	fraction of the TKE attributed horizontal turbulent velocity variance
m_w	fraction of the TKE attributed vertical turbulent velocity variance
N	Brunt-Vaisala buoyancy frequency
$p(A\|B)$	Probability density of A given B
Q_0	Sensible heat flux at the ground surface
R_i	Richardson number

$S(\mathbf{r}, t)$	Source function
S_u	Turbulence production due to shear in the u component of the horizontal wind
S_v	Turbulence production due to shear in the v component of the horizontal wind
T_4	Brightness temperature from channel 4 (10.3 – 11.3 μm)
T_5	Brightness temperature from channel 5 (11.5 – 12.5 μm)
T_L	Lagrangian time scale
$T_\star$	Potential temperature scale for the surface layer
U	Mean horizontal wind component in the x direction Also relative humidity
U_0	Relative humidity threshlod for cloud fraction estimation
u	Turbulent wind component in the x direction
u_i	Component i of the turbulent wind in the x direction
u_m	Meandering component of the horizontal wind
u_*	Friction velocity
V	Mean horizontal wind component in the y direction
v	Turbulent wind component in the y direction
v_d	Deposition velocity
v_m	Meandering component of the horizontal wind
$\boldsymbol{V}(\boldsymbol{r}, t)$	3D wind velocity vector
W	Mean vertical velocity
w	Turbulent vertical velocity
$\overline{W_t^l}$	Average weighted residence time above level l for time t
W_{in}, W_{out}	Particles' random transition rate in and out of an elemental volume

Greek Variables

β	Constant (0.85)
$\tilde{\nabla}_{ij}$	Symbolic divergence operator
ϵ	Turbulent kinetic energy dissipation rate
γ	Dry adiabatic lapse rate
λ	Lengthscale
$\mathbf{\Phi}$	Acceleration vector
ϕ_i	i component of the acceleration vector $\mathbf{\Phi}$
ϕ_h	Dimensionless potential temperature gradient in the surface layer
ϕ_m	Dimensionless wind shear in the surface layer
ρ	Air density
ρ_0	Air density of the reference state
θ	Potential temperature
θ_0	Potential temperature for the reference state
τ	Time scale (also short time interval)
τ_η	Kolmogorov time scale
τ_m	Time scale for the meandering wind component
$\tau_p(> z_l)$	Residence time of particle p above level z_l
$\tau_p^w(> z_l)$	Weighted residence time of particle p above level z_l
τ_w	Time scale for vertical eddies

CHAPTER 1

Introduction

When substances are injected in the middle of the atmosphere, they can travel over long distances before being mixed downward towards the surface. For example, the April 1986 accident at the Chernobyl Nuclear Power Plant produced a radioactive plume that spread over the Northern Hemisphere and reached North America within a matter of days [*Pudykiewicz*, 1989]. While most of the radioactive aerosols were released in the atmospheric boundary layer (ABL), the large fires also projected material into the lower parts of the free troposphere (FT). Long range dispersion model simulations indicate that transport in the mid and upper troposphere had an important effect on observed surface concentrations over North America [*Pudykiewicz*, 1988]. This is also seen with radioactive tracers produced in the stratosphere, like ^{7}Be, which get transported downward into the mid-troposphere where they can travel over large distances before being mixed into the boundary layer [*D'Amours et al.*, 2013], and being detected at surface monitoring stations.

On the other hand, substances injected in the boundary layer will often remain confined to the ABL, even when transported over large distances. This was the case for radioactive substances released during the the Fukushima Dai-ichi Nuclear Power Plant accident in March 2011, which were injected in the lower part of the boundary layer [*Terada et al.*, 2012]. The resulting plume travelled over the Northern Pacific for several days staying

close to surface before reaching North America [*Leon et al.*, 2011; *D'Amours et al.*, 2015]. Nevertheless, the importance of exchange between the boundary layer and the troposphere, in large scale transport of pollutants, is well documented. A good example is found in *Colette et al.* [2008] showing the connection between Saharan dust outbreaks and aerosols observed in the Paris area.

This thesis investigates the transport and dispersion of substances injected in the different layers of the atmosphere, and the mechanisms by which these substances may be tranferred from one to the other. The investigations are based on results of simulations using Lagrangian dispersion models. The main substance of the thesis consists in three papers published during the course of my doctoral studies. Although each one of the papers constitutes a distinct scientific study, as a group, they are unified by their collective focus on transport within and exchange between the atmospheric layers.

It will be shown that eddy diffusion is not the principal mechanism by which mixing occurs throughout the atmosphere. In the stratosphere, air circulates in well maintained streams with little vertical mixing. Frequent exchanges between the stratosphere and the troposphere do occur, but are mostly confined to the immediate layers near the tropopause. Injections from the stratosphere to the troposphere, associated with low pressure systems, happen frequently enough to feed streams of stratospheric air circulating at different levels of the troposphere. These tropospheric streams are also maintained over large distances and for relatively long periods of time with little horizontal or vertical mixing. Exchanges between the boundary layer and the free troposphere occur in a limited zone near the top of the boundary layer, the entrainment zone. However the main mechanism by which tropospheric air is entrained in, or "detrained" from, the boundary layer is associated with the growth and decay of the boundary layer associated with the diurnal cycle.

Chapter 2 gives a brief overview of the three main layers accounting for most of the atmospheric mass, and of their interfaces, with an emphasis on the atmospheric boundary layer, where interactions with the surface of the earth occur. This is intended as a preamble to the investigations presented.

In Chapter 3, the fundamental aspects of Lagrangian modelling, specially those concerning stochastic processes, are reviewed and discussed. Special attention is given to the relationship between the particles' trajectories in phase-space produced using a stochastic differential equation, and the Fokker-Planck equation describing the time evolution of the probablity density distribution of those particles, in phase-space.

The papers are not presented in the chronological order of their publication. Chapter 4 presents the most recent, *D'Amours et al.* [2015], and describes the Lagrangian transport models used operationally at the Canadian Meteorological Centre (CMC) of Environment Canada, for which I was the lead developer. Many details about the various simulated physical processes are also discussed. The models are applied to real cases of atmospheric transport and dispersion in the boundary layer, and are compared to available observations.

Chapter 5 presents a study [*D'Amours et al.*, 2010] on the transport and dispersion of aerosols injected deeply into the stratosphere during the eruptions of the Alaskan volcanoes Okmok and Kasatochi in the summer of 2008. The importance of the eruptions and the information which became available, both on the eruptions' characteristics and on the plumes generated, provided a unique opportunity to test the transport model and improve our understanding of transport in those regions of the atmosphere. We will see that sulfate aerosol plumes resulting from these eruptions can be followed for many days after their injection into the stratosphere illustrating clearly that the air circulates in well maintained streams with little vertical mixing in these layers

Chapter 6 presents a study [*D'Amours et al.*, 2013] on the transport of Beryllium-7, a substance known to be produced in the upper portions of the atmosphere. This study investigates the exchange processes between the stratosphere and the troposphere, and downward to the surface. The study illustrates vividly how frequent are exchanges between the lower stratosphere and the upper troposphere and shows that episodes of high ozone concentrations which occurred in the foothills of the Canadian Rockies, during the study period, were the result of very long range transport, and most likely of stratospheric origin. The perspective of the study is unique in the sense that it is the influence of large potential

source areas on a single surface station which is investigated. Special metrics were developed for this purpose: the layer residence time fraction, the weighted layer residence time fraction, the layer exit rate and the layer exit time.

Chapter 7 focuses on exchange between the free troposphere (FT) and the planetary boundary layer (PBL or BL). A simple diagnostic model for the variances of the turbulent components of the wind was developed and used to explore the concept of the entrainment zone associated with the convective boundary layer, and how this should be accounted for in a dispersion model. The model is applied to micrometeorological observations from the Wangara field experiment [*Clarke*, 1970] and data taken at the release site of the European Tracer Experiment [*Gryning et al.*, 1998]. The modelling of these exchanges discussed in section **f** of *D'Amours et al.* [2015] is addressed again.

It will be shown that in general, the vertical profiles of turbulence generated give a good representation of turbulence in the transition zone at the top of the boundary layer, and that no special treatment for the particle trajectory calculations appears to be necessary in Lagrangian dispersion models.

CHAPTER 2

The atmosphere: a layered fluid

2.1 Introduction

This purpose of this chapter is to present a brief description of the three main layers of the atmosphere, since the specific characteristics of each of those layers have an important effect on transport and dispersion. In the following chapters, Lagrangian models are used to investigate the behaviour of aerosol plumes projected by volcanic eruptions reaching heights near 15 km. As well, transport across these layers of radioactive substances generated by cosmic radiation at high altitudes, and which are detected near the surface, will be examined.

2.2 The troposphere

Figure 2.1 shows schematic average vertical profiles of air temperature and density according to the U.S. Standard Atmosphere, 1976 (document: NOAA-S/T 76-1562). These average vertical profiles are essentially the result of the dominant physical processes occurring at various altitudes in the atmosphere. Most of the solar energy is absorbed by the surface of the Earth and is transferred to the lower portions of atmosphere mainly through vertical transport of sensible heat and of latent heat associated with the evaporation and condensation of water (p. 403 *Holton* [1992]). This transport is either the product

of convective clouds (e.g. thunderstorms) or of large scale vertical motion associated with synoptic weather systems, which are induced by the latitudinal variation of the solar input, and are responsible for the large scale transport of energy to the polar regions. This large scale vertical transport results in a rapid decrease of temperature with height, at a rate of about 6 K km^{-1}, up to an altitude of 10 to 12 km, delineating the troposphere.

2.3 The stratosphere

Above the troposphere, in the stratosphere, the solar ultraviolet radiation interacts with molecular oxygen to form the ozone layer. The absorption of the UV radiation warms the layer, producing a steady increase of the mean temperature with increasing height, up to to a maximum near 50 km, the stratopause (p. 404 *Holton* [1992]). This results in a stratified thermally stable layer where very little vertical mixing is occurring. The tropopause defines the boundary between the stratosphere and the troposphere. The tropopause height is usually estimated from Ertel's potential vorticity (E_p) expressed in isentropic coordinates. From *Holton* [1992], the vertical component of vorticity on the isentropic surface is defined as:

$$\zeta_\theta = \left.\frac{\partial v}{\partial x}\right|_\theta - \left.\frac{\partial u}{\partial y}\right|_\theta \tag{2.1}$$

where the partial derivatives are evaluated on surfaces of constant potential temperature θ. Then the potential vorticity is defined as:

$$E_p = (\zeta_\theta + f)\Big(-g\frac{\partial \theta}{\partial p}\Big)\,. \tag{2.2}$$

where f is the Coriolis parameter and g the accelaration due to Earth's gravity. E_p is conserved for frictionless adiabatic flow. It can be seen on Figure 6.12 that there is a fairly strong vertical gradient of E_p which separates the troposphere and the stratosphere. In the literature, potential vorticity thresholds used to estimate tropopause height range between 1 – 3.5 potential vorticity units (PVU, 1 PVU $= 1\times10^{-6}\,\mathrm{m^2\,K\,kg^{-1}\,s^{-1}}$) [*Bachmeier et al.*, 1994; *Holton et al.*, 1995; *Stohl et al.*, 2000; *Colette et al.*, 2005]).

When injected high above the tropopause, substances which are not subject to gravitational

settling can travel long distances without much mixing. Such transport is investigated in a study on volcanic aerosols presented in chapter 5.

Exchanges between the stratosphere and the troposphere are continually taking place and are associated with tropopause folding processes, occurring in synoptic weather systems. Beryllium–7 (^{7}Be) is a relatively short-lived radioactive isotope, with a half-life of 53.3 days, and is naturally produced in the upper parts of the atmosphere, mostly in the high stratosphere. ^{7}Be can therefore be used as an indicator of the presence of air masses of stratospheric origin near the surface. In a study by *D'Amours et al.* [2013], inverse Lagrangian transport modelling is used together with concurrent measurements of surface air concentrations of ozone (O_3) and of ^{7}Be at Harlech, in the Alberta Foothills, to investigate the origin of the air with elevated O_3 concentrations. This study is presented in chapter 6

2.4 The boundary layer

In the lowest part of the troposphere, exchanges of heat and momentum with the ground produce turbulent motion which is confined in a relatively thin layer (roughly 1000 m deep) described as the atmospheric boundary layer (ABL), or alternatively, the planetary boundary layer (PBL). In the layer above the ABL, turbulent motions are less frequent, intermittent and localized in space. This layer is usually referred to as the free troposphere (FT). Climatologically speaking, most of the solar energy is absorbed by the Earth's surface. It is then transferred to the lowest portions of the ABL, in contact with the ground – the surface layer (SL) – in the form of sensible heat and of latent heat by evaporation of surface water into the air. The surface air is then transported in the rest of the ABL by turbulent mixing and, on a longer time scale, mixes with the FT. There is a strong latitudinal dependence in this process. This in turn generates horizontal pressure gradients driving the various wind regimes observed at all levels of the atmosphere. The preponderance of the momentum associated with those wind circulations is in the FT. However this momentum must be transferred back to the Earth surface through turbulent momentum fluxes within the ABL, otherwise the atmosphere would be accelerated continuously, even taking into account angular momentum conservation.

Figure 2.2 shows an example of the daytime evolution of the water vapour mass mixing ratio observed [*Clarke*, 1970] in the lower portion of the atmosphere. The portion near the ground dries up as the water vapour gets vertically mixed, more or less uniformly, in a well defined layer, the ABL. This layer thickens with time. Above the ABL (above 1500 m in Figure 2.2) there is very little change in the mixing ratio, indicating that in this case, not much water vapour is transferred into the free troposphere above. There is a transition zone where the mixing ratio changes almost linearly. This zone is almost 500 m thick at time 12H00 EST, and about 300 m at time18H00 EST, between a third and a fifth of the depth of ABL.

The turbulent interactions between the ABL and the FT occur in this layer, known as the entrainment zone (EZ). Stull describes the EZ in the context of a convective boundary layer, where rising thermals penetrate and/or deflect the capping inversion layer. A similar EZ also exists for a shear driven boundary layer; in that case the BL is almost thermally neutral and some of the vigorous eddies and vortices interact with the capping layer [*Moeng and Sullivan*, 1994], [*Colonna et al.*, 2009]. *Wyngaard* [2010] describes the EZ as an interfacial layer:

> "The top of the CBL is locally and instantaneously quite thin: averaging over time, space, or an ensemble produces a much thicker *interfacial layer*"

Figure 2.3 from *Crum and Stull* [1987] shows another example of humidity profiles from the Oklahoma Boundary Layer Experiment - 1983 [*Stull and Eloranta*, 1984]. The profile is quite jagged in the layer between the two purple arrows, $\sim$ 860-820 millibars, and one can assume that it corresponds to the local entrainment zone. Presumably an average performed in that layer (perhaps in time or along the flight legs), would result in a profile similar to those shown in Figure 2.2. In those two experiments it seems that the vertical the extent of the EZ is about the same, approximately 400 m.

The entrainment zone has been the subject of investigation and modelling for some time. Nevertheless, in Chapter 7, a simple diagnostic model of the convective boundary layer (CBL) is presented which seems to yield a plausible statistical description of the BL, including the EZ. This model is used to investigate the modelling of exchanges between the

BL and the FT.

2.5 Figures

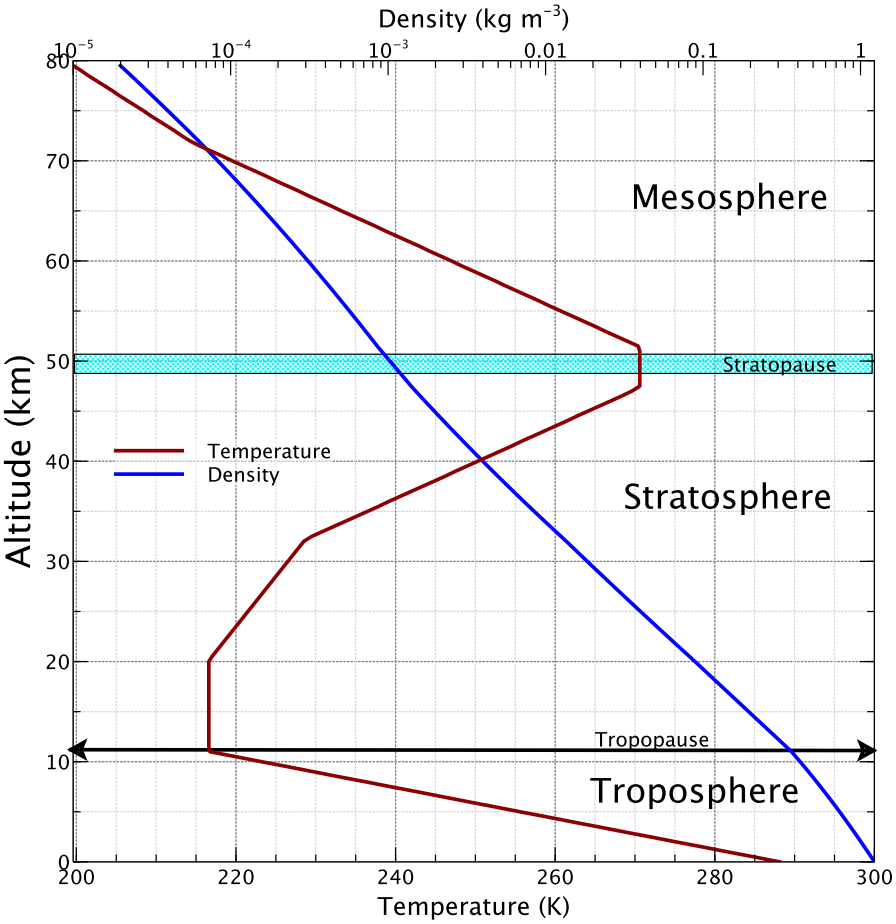

Figure 2.1: Vertical profiles of temperature and density for the US Standard atmosphere.

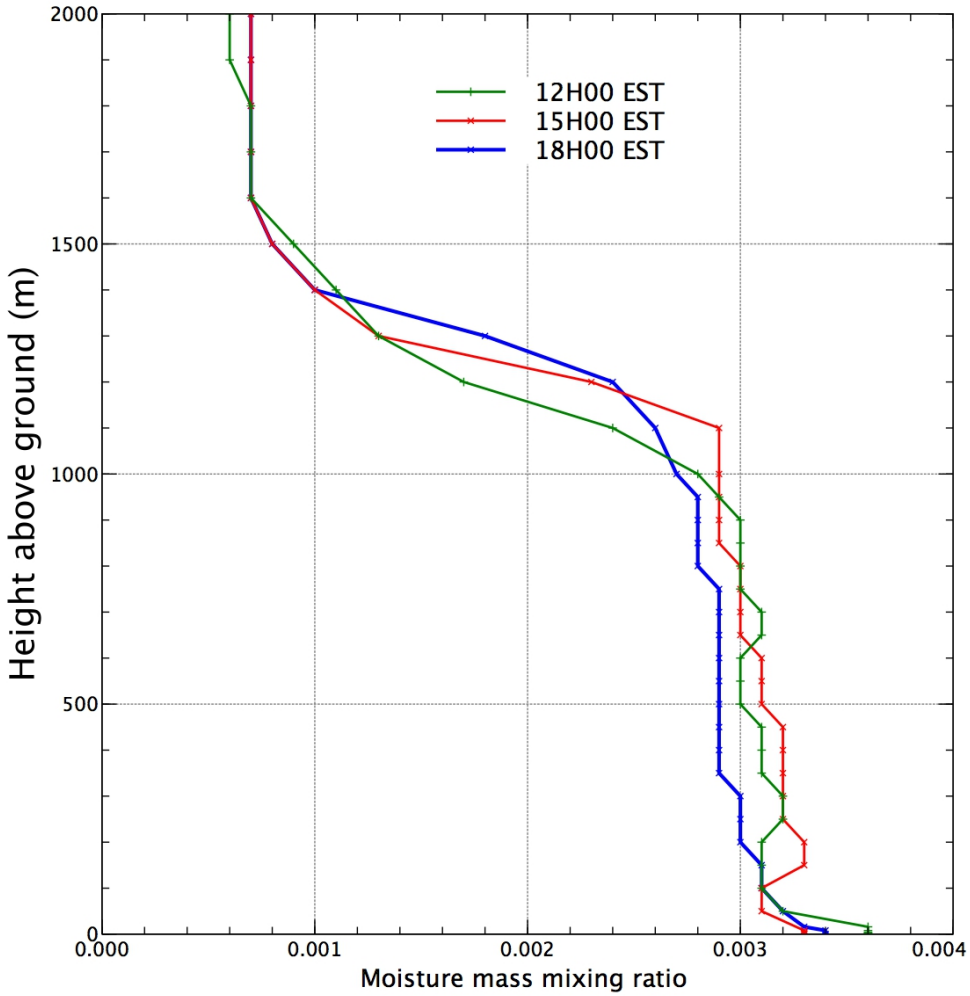

Figure 2.2: Observed mean specific humidity profiles for day 33 of the Wangara experiment, at three different times, 12H00 EST, 15H00 EST and 18H00 EST.
It is difficult to estimate the averaging time of the data, from the information provided in *Clarke et al.* [1971] one understands that mixing ratio shown represent spatial averages of the order of the height intervals at which they are given, every 50 m up to 1000 m, and every 100 m afterwards. Here it would seem that the EZ is resolved within three to five 100 m layers.

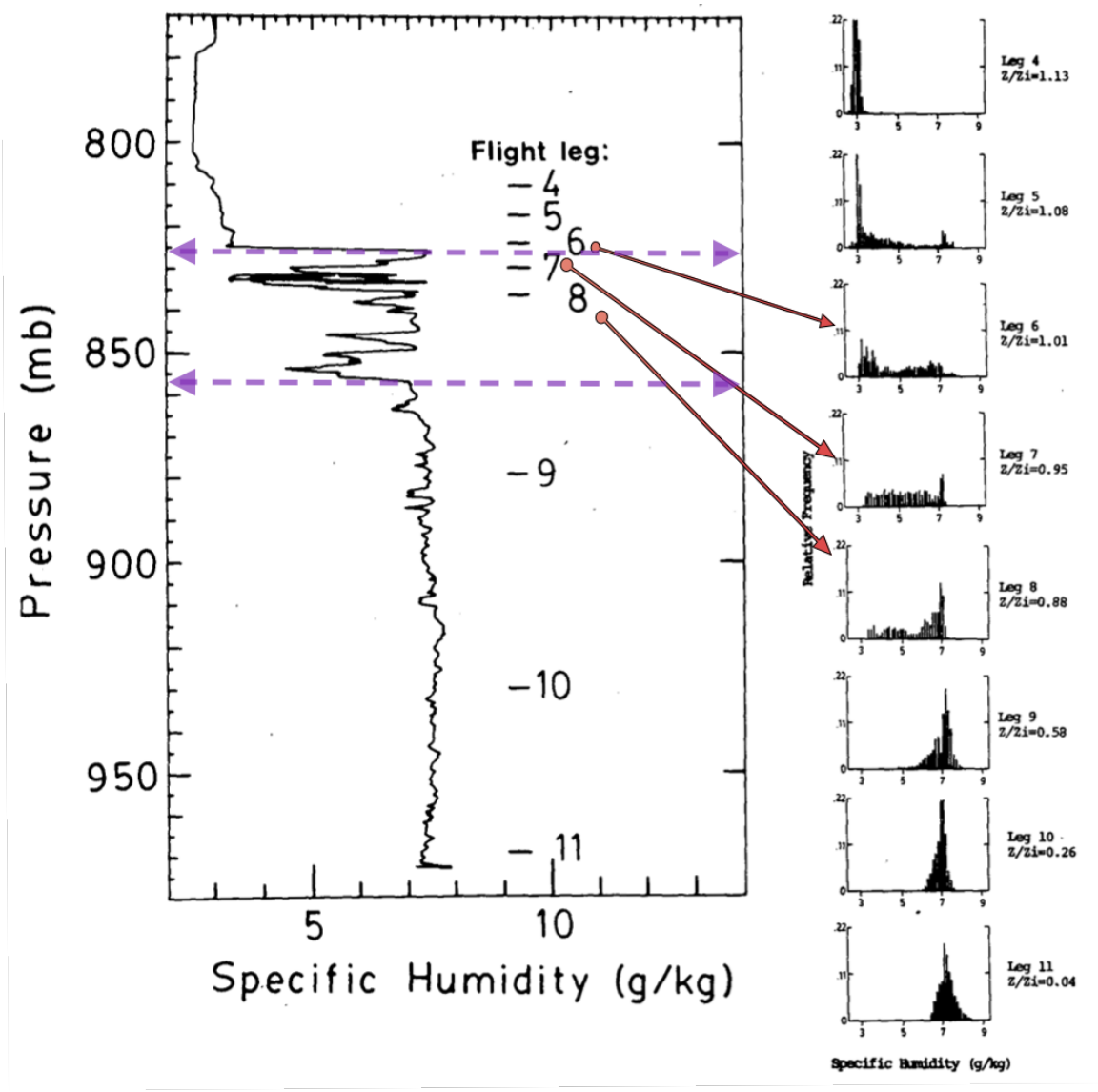

Figure 2.3: Observed specific humidity profile during the Oklahoma Boundary Layer Experiment - 1983.
The profile is quite jagged in the layer between the two purple arrows, $\sim$ 860-820 millibars, and one can assume that it corresponds to the local entrainment zone. The boundary layer height (labelled Z_i) is defined as the height where a 50 - 50% mixture of mixed layer air from below and free atmosphere air from above exists. Histograms of relative frequency of occurrence specific humidity at different heights above the ground, are shown on the right hand side of the figure, and labelled according to the flight leg number. The histogram for the observations taken above the entrainment zone shows (Leg 4) that measurements are nearly constant, with a low specific humidity, approximately 3 g/kg. There is a bit more spread for measurements below the entrainment zone (Legs 9-10-11), but the distribution is fairly constant, through most of the BL depth, with a much higher mean than in the FT, around 7 g/kg. However within the entrainment zone, the distribution of the measurements is almost uniformly spread between the BL and the FT means (Legs 6 and 7). This indicates that the concentration of water vapor is quite variable, therefore there is a fair amount of horizontal variability in the EZ.

CHAPTER 3

Fundamentals of Lagrangian modelling of atmospheric dispersion

3.1 Introduction

The investigations on the transport and exchanges of substances in the different layers of the atmosphere presented in this thesis are based on simulations using Lagrangian dispersion models. In this chapter, some fundamental aspects of Lagrangian modelling, specially those concerning the stochastic processes, are reviewed and discussed. Special attention is given to the relationship between the phase-space trajectories produced using a stochastic differential equation and the Fokker-Planck equation.

3.2 The Langevin equation

Langevin [1908] proposed an equation (his equation number 3) to describe the motion of a particle suspended in a fluid, in reaction to collisions with the fluid's thermally agitated molecules – Brownian motion. For direction x, the equation is:

$$m\frac{d^2x}{dt^2} = a\frac{dx}{dt} + X\,, \tag{3.1}$$

where m is the particle mass, and a, a coefficient controlling the strength of viscous damping of the motion[1]. Langevin also described the term X as a complementary force

[1] In Langevin's words "une résistance visqueuse"

having zero mean, maintaining the particle's agitation. This Langevin equation can be applied to model the trajectories of air particles in the atmosphere, where turbulence becomes the source of the particles "agitation". The Langevin equation is transformed into the following set of stochastic differential equations (SDE):

$$du_i = a_i(\boldsymbol{x}, \boldsymbol{u}, t)dt + b_{ij}(\boldsymbol{x}, \boldsymbol{u}, t)d\xi_j \,, \tag{3.2}$$

$$dx_i = u_i dt \,, \tag{3.3}$$

where:

$$b_{ij}d\xi_j = b_{i1}d\xi_1 + b_{i2}d\xi_2 + b_{i3}d\xi_3 \,, \tag{3.4}$$

$$d\xi_j \in N(0, dt) \,. \tag{3.5}$$

The $d\xi_j$ are independent, therefore the term $b_{ij}(\boldsymbol{x}, \boldsymbol{u}, t)d\xi_j$ represent a multinormal random variate, with zero means and $b_{ik}b_{jk}dt$ variances. There are three components to the random term, to allow for the possibility of random stresses in any of the three axes to "shock" the particle in the u_i direction (e.g. *Wilson et al.* [1993]). These equations form the basis of the first order Lagrangian stochastic model (LSM).

In practical applications, dispersion is estimated by calculating the trajectories of a number of air particles (or fluid elements) large enough to adequately sample the dispersing plume. In general, these particles only differ from the other fluid elements because they are "marked". It is assumed that the marked particles conserve their identity during their flight. However they can transport some amount of material that may be subject to various physical processes like dry deposition, wet scavenging and radioactive decay. A fluid element can also be viewed as representing an ensemble of real particles or aerosols. Upon release, the fluid element is assigned a mass that depends on the total quantity of the substance emitted and the total number of particles released. This mass is only marking the fluid element and has no effect on its trajectory. Other processes, like radioactive decay, deposition and scavenging, gravitational settling can also be included in the model. These are discussed in Chapter 4.

3.3 Relationship between the LSM and the Fokker-Planck equation

There is an implied Fokker-Planck equation (FPE) associated with the LSM set of equations (3.2) and (3.3). This FPE describes the time evolution of the probability density function for a fluid parcel to occupy a given elemental volume in the phase-space of positions and velocities. The FPE is useful in the determination of the SDE coefficients.

Here we illustrate that equations (3.2) and (3.3), when applied to a large number of particles, describe the evolution of a cloud of particles in phase-space, which can also be seen as describing the evolution of the probability density cloud, in phase-space. Then at any point in phase-space, the passing of the probability cloud corresponds to a flux of probability density and the local rate of change of the probability density results from the convergence/divergence of this flux.

Let the number of fluid elements in an elemental phase-space volume be $N(\boldsymbol{x}, \boldsymbol{u}, t)d\boldsymbol{u}d\boldsymbol{x}$. Then this quantity is proportional to $g(\boldsymbol{x}, \boldsymbol{u}, t)d\boldsymbol{u}d\boldsymbol{x}$, where g is the distribution of the fluid elements in phase-space or, equivalently[2], the probability density distribution of those fluid elements. Equation (3.2) shows the displacement of a given fluid element in the velocity dimensions of this elemental volume, and equation (3.3), its displacement in the spatial dimensions. The flux through the phase-space volume which can make N and g fluctuate locally can be expressed as:

$$\boldsymbol{F}_{\boldsymbol{x}}(\boldsymbol{x}, \boldsymbol{u}, t) = g(\boldsymbol{x}, \boldsymbol{u}, t)\boldsymbol{u} \tag{3.6}$$

$$\boldsymbol{F}_{\boldsymbol{u}}(\boldsymbol{x}, \boldsymbol{u}, t) = g(\boldsymbol{x}, \boldsymbol{u}, t)\boldsymbol{\Phi}\,, \tag{3.7}$$

where $\boldsymbol{F}_{\boldsymbol{x}}(\boldsymbol{x}, \boldsymbol{u}, t)$ is the flux of probability density in the position subspace, and $\boldsymbol{F}_{\boldsymbol{u}}(\boldsymbol{x}, \boldsymbol{u}, t)$, the flux of probability density in the velocity subspace. $\boldsymbol{\Phi} = (\boldsymbol{a} + \mathbb{A})$ is the acceleration vector and includes the stochastic component $\mathbb{A}$. Then, the rate of change of $g(\boldsymbol{x}, \boldsymbol{u}, t)$ can be understood, conceptually at least, as the divergence of the two fluxes in their respective

[2]Within a normalization factor. This is discussed in *Thomson* [1987]

portions (i.e. subspaces) of the position-velocity phase space:

$$\frac{\partial g(\boldsymbol{x},\boldsymbol{u},t)}{\partial t} = -\left[\boldsymbol{\nabla}\cdot\boldsymbol{F}_{\boldsymbol{x}}(\boldsymbol{x},\boldsymbol{u},t) + \tilde{\boldsymbol{\nabla}}\cdot\boldsymbol{F}_{\boldsymbol{u}}(\boldsymbol{x},\boldsymbol{u},t)\right] \tag{3.8}$$

$$= -\frac{\partial}{\partial x_i}(gu_i) - \frac{\partial}{\partial u_i}(ga_i) - \tilde{\nabla}_{ij}(\mathbb{A}_{ij}g) \tag{3.9}$$

The term $\tilde{\nabla}_{ij}$ is used symbolically because the stochastic term $\mathbb{A}$ is not differentiable, being discontinuous everywhere, and cannot be handled with the rules of ordinary calculus.

The purpose of the random term in equation (3.2) is to model the unpredictable portion of the fluid element trajectory, which may "jump" inside or outside a given elemental volume. Here, this effect occurs only in the velocity dimensions of the phase space. Defining $W_{in}(\boldsymbol{x},\boldsymbol{u},t)$ as the *transition probability per unit time* (*Van Kampen* [2008], chapter V, section 1) for a fluid element to move into the elemental volume $d\boldsymbol{u}d\boldsymbol{x}$, and $W_{out}(\boldsymbol{x},\boldsymbol{u},t)$ as the transition probability per unit time for a fluid element to exit the elemental volume, then $(W_{in}-W_{out})g$ gives the net inward flux of particles across the faces of the elemental volume. Therefore by analogy with the divergence theorem (e.g. *Sokolnikoff and Redheffer* [1966], equation 7.4):

$$-\tilde{\nabla}_{ij}(\mathbb{A}_{ij}g) = [W_{in} - W_{out}]g \tag{3.10}$$

The term $[W_{in} - W_{out}]g$ is evaluated using the Kramers-Moyal expansion of the so called "Master Equation" [*Van Kampen*, 2008; *Rodean*, 1996]. For this particular case, i.e. a multivariate Gaussian process with zero mean and variance $\mathbb{B}_{ij}$:

$$[W_{in} - W_{out}]g = \frac{1}{2}\frac{\partial^2(\mathbb{B}_{ij}g)}{\partial u_i \partial u_j} \tag{3.11}$$

Denoting $\frac{1}{2}\mathbb{B}_{ij}$ as B_{ij}, and substituting into equation (3.9), we get:

$$\frac{\partial g}{\partial t} = -\frac{\partial}{\partial x_i}(g\,u_i) - \frac{\partial}{\partial u_i}(g\,a_i) + \frac{\partial^2(B_{ij}g)}{\partial u_i \partial u_j} \tag{3.12}$$

which is the Fokker-Plank equation applied to the distribution g as expressed by *Thomson* [1987], equation (5). This equation is also known as the Kolmogorov forward equation. It can be seen that calculating a large number of particle trajectories using equations (3.2) and (3.3), as is usually done in Lagrangian models, is equivalent to solving the FPE.

3.3.1 The well mixed constraint (WMC) and the FPE

Thomson [1987] formalized an intuitively logical constraint for an LSM, which he called the well mixed condition (WMC) in position-velocity space: "*If the particles of tracer are initially well-mixed (i.e. g proportional to g_a) will they remain so ?* " He recognized that for an LSM to satisfy the WMC, it is necessary and sufficient that the FPE associated with the LSM, equation (3.12), should also apply to $g_a(\boldsymbol{x}, \boldsymbol{u})$, the distribution of all of the fluid elements.

This FPE is re-written below, slightly differently:

$$\frac{\partial g_a}{\partial t} = -\frac{\partial}{\partial x_i}(g_a\, u_i) - \frac{\partial}{\partial u_i}\left[(g_a\, a_i) - \frac{\partial (B_{ij} g)}{\partial u_j}\right]. \tag{3.13}$$

Since the form of $\boldsymbol{a}$ is not determined at this stage, Thomson rewrites the FPE in terms of a vector $\vec{\boldsymbol{\phi}}$ as:

$$\frac{\partial \phi_i}{\partial u_i} = -\frac{\partial g_a}{\partial t} - \frac{\partial u_i g_a}{\partial x_i}\,, \tag{3.14}$$

or more conventionally:

$$\frac{\partial g_a}{\partial t} = -\frac{\partial u_i g_a}{\partial x_i} - \frac{\partial \phi_i}{\partial u_i}\,. \tag{3.15}$$

However, satisfying the WMC does not provide a unique solution for $\boldsymbol{a}$ and $\boldsymbol{\phi}$.

3.4 Determining the SDE coefficients a_i and b_{ij}

Here we illustrate the derivation of the SDE coefficients a_i and b_{ij} shown in equations (3) to (6) of the paper in section 4. In the interests of computational feasibility and rapidity, it is here assumed that the small scale velocity fluctuations can be treated as stationary, horizontally homogeneous and uncorrelated (one with another). These assumptions are made in the context of CMC models, which are required to be able to simulate processes out to the global scale, and given that the detailed information (e.g. velocity covariances) that would be required if the model were fully general simply is not routinely available.

3.4.1 The a_i coefficients, using Thomson's "simplest" solution

For fully general Gaussian turbulence admitting non-stationarity and inhomogeneity on any or all of the axes, Thomson proposes the following "simplest" solution, in his notation:

$$
\begin{aligned}
a_i &= B_{ij}(\boldsymbol{V}^{-1})_{jk}(u_k - U_k) + \frac{\phi_i(\boldsymbol{x}, \boldsymbol{u}, t)}{g_a}\,, && (3.16)\\
V_{ij} &= \overline{(u_i - U_i)(u_j - U_j)}\,, && (3.17)\\
\frac{\phi_i}{g_a} &= \frac{1}{2}\frac{\partial V_{il}}{\partial x_l} + \frac{\partial U_i}{\partial t} + U_l\frac{\partial U_i}{\partial x_l} && (3.18)\\
&+ \left[\frac{1}{2}(\boldsymbol{V}^{-1})_{lj}\left(\frac{\partial V_{il}}{\partial t} + U_m\frac{\partial V_{il}}{\partial x_m}\right) + \frac{\partial U_i}{\partial x_j}\right](u_j - U_j)\\
&+ \frac{1}{2}(\boldsymbol{V}^{-1})_{lj}\frac{\partial V_{il}}{\partial x_k}(u_j - U_j)(u_k - U_k)\,,
\end{aligned}
$$

where u_i is the instantaneous velocity, U_i the ensemble average, and $B_{ij} \equiv \frac{1}{2}b_{ik}b_{jk}$.

Now, using the notation that (U, V, W) describe the mean background flow, (u, v, w) the velocity fluctuations, and $(\sigma_u^2, \sigma_v^2, \sigma_w^2)$ their variances, introducing the approximation that the velocity fluctuations are uncorrelated, and also assuming quasi-steadiness and horizontal quasi-homogeneity, Thomson's solution becomes (see Appendix A):

$$
\begin{aligned}
\frac{\phi_x}{g_a} &= \frac{1}{2\sigma_u^2}\frac{\partial \sigma_u^2}{\partial z}wu\,, && (3.19)\\
\frac{\phi_y}{g_a} &= \frac{1}{2\sigma_u^2}\frac{\partial \sigma_v^2}{\partial z}wv\,, && (3.20)\\
\frac{\phi_z}{g_a} &= \frac{1}{2}\frac{\partial \sigma_w^2}{\partial z}\left(1 + \frac{w^2}{\sigma_w^2}\right). && (3.21)
\end{aligned}
$$

3.4.2 The coefficients b_{ij} for the stochastic component

Following the discussion in *Thomson* [1987] on the Lagrangian structure function, the velocity auto-covariance of a given fluid element after a short time interval τ is written as:

$$
\overline{(u_i(t+\tau) - u_i(t))(u_j(t+\tau) - u_j(t))} = \delta_{ij}C_0\epsilon\,\tau\,, \qquad \tau > \tau_\eta\,, \tag{3.22}
$$

where τ_η is the Kolmogorov time scale, the turnover time of the small, energy dissipating, eddies. Using equation (3.2) to estimate the differences, we get:

$$\overline{du_i du_j} = \overline{b_{ik} d\xi_k b_{jl} d\xi_l} + a_i a_j \tau^2 \tag{3.23}$$

However since $\overline{d\xi_k d\xi_l} = 0$ for $k \neq l$, and $\overline{d\xi_k^2} = \tau$, for all values taken by k or l,

$$\overline{du_i du_j} = b_{ik} b_{jk} \tau + a_i a_j \tau^2 \,. \tag{3.24}$$

For small enough τ, but still exceeding τ_η, $a_i a_j \tau^2$ is negligible, so that

$$b_{ik} b_{jk} = \delta_{ij} C_0 \epsilon \,, \tag{3.25}$$

which means that for all $i \neq j$, $b_{ik} b_{jk} = 0$. This is possible only if all "off-diagonal" terms of $b_{ik} b_{jk}$ are zero. Hence the coefficient b_{ij} has to be:

$$b_{ij} = \delta_{ij} (C_0 \epsilon)^{1/2} \,. \tag{3.26}$$

Therefore, consistency with Kolmogorov similarity theory for locally isotropic turbulence forbids the component-to-component correlation in the random forcing.

Finally, recalling that $B_{ij} \equiv \frac{1}{2} b_{ik} b_{jk}$, the complete set of equations for the particle velocities is written as:

$$du = \left[-\frac{1}{2} \frac{C_0 \epsilon}{\sigma_u^2} \, u + \frac{1}{2\sigma_u^2} \frac{\partial \sigma_u^2}{\partial z} wu \right] dt + \sqrt{C_0 \epsilon} \, d\xi \,, \tag{3.27}$$

$$dv = \left[-\frac{1}{2} \frac{C_0 \epsilon}{\sigma_v^2} \, v + \frac{1}{2\sigma_v^2} \frac{\partial \sigma_v^2}{\partial z} vu \right] dt + \sqrt{C_0 \epsilon} \, d\xi \,, \tag{3.28}$$

$$dw = \left[-\frac{1}{2} \frac{C_0 \epsilon}{\sigma_w^2} \, w + \frac{1}{2} \frac{\partial \sigma_w^2}{\partial z} \left(1 + \frac{w^2}{\sigma_w^2} \right) \right] dt + \sqrt{C_0 \epsilon} \, d\xi \,. \tag{3.29}$$

3.5 Inverse dispersion modelling

In many practical situations, one is concerned about the possible origin of a substance transported in the atmosphere and observed at one or more locations, and perhaps would like to assess the amounts released. Dispersion modelling, in inverse mode, can be used in those cases. Several examples of such applications are discussed in the next chapters. Here the theoretical bases for inverse dispersion modelling are reviewed.

3.5.1 Conditional probability and mass mixing ratio conservation

Let $p(\boldsymbol{x},\boldsymbol{u},t|\boldsymbol{y},\boldsymbol{v},s)$ be the probability density that a particle initially at phase-space position $(\boldsymbol{y},\boldsymbol{v})$, at time s will be later found at position $(\boldsymbol{x},\boldsymbol{u})$, at time $t > s$. It is of interest to estimate the probability that a particle *came* from phase-space point $(\boldsymbol{y},\boldsymbol{v})$, at time s, given that it is found at $(\boldsymbol{x},\boldsymbol{u})$, at time t. According to the conditional probability definition:

$$p(\boldsymbol{x},\boldsymbol{u},t|\boldsymbol{y},\boldsymbol{v},s) = \frac{p(\boldsymbol{x},\boldsymbol{u},t\cap\boldsymbol{y},\boldsymbol{v},s)}{p(\boldsymbol{y},\boldsymbol{v},s)}\,, \tag{3.30}$$

$$p(\boldsymbol{y},\boldsymbol{v},s|\boldsymbol{x},\boldsymbol{u},t) = \frac{p(\boldsymbol{x},\boldsymbol{u},t\cap\boldsymbol{y},\boldsymbol{v},s)}{p(\boldsymbol{x},\boldsymbol{u},t)}\,, \tag{3.31}$$

$$p(\boldsymbol{x},\boldsymbol{u},t|\boldsymbol{y},\boldsymbol{v},s)p(\boldsymbol{y},\boldsymbol{v},s) = p(\boldsymbol{y},\boldsymbol{v},s|\boldsymbol{x},\boldsymbol{u},t)p(\boldsymbol{x},\boldsymbol{u},t)\,. \tag{3.32}$$

Applying equation (3.32) to the atmosphere, the probability density distribution $p(\boldsymbol{x},\boldsymbol{u},t)$ for any atmospheric fluid element to be found at time t, in the vicinity of point $\boldsymbol{x},\boldsymbol{u}$ of the phase space, is proportional to $g_a(\boldsymbol{x},\boldsymbol{u},t)$, therefore,

$$\frac{p(\boldsymbol{x},\boldsymbol{u},t|\boldsymbol{y},\boldsymbol{v},s)}{g_a(\boldsymbol{x},\boldsymbol{u},t)} = \frac{p(\boldsymbol{y},\boldsymbol{v},s|\boldsymbol{x},\boldsymbol{u},t)}{g_a(\boldsymbol{y},\boldsymbol{v},s)}\,. \tag{3.33}$$

This is a probabilistic expression of the mass mixing ratio conservation along the trajectory of an air parcel. Equation (3.33) gives a basis for inverse Lagrangian modelling.

3.5.2 Reverse/backward diffusion

Equations (3.2) and (3.3) give a means to sample the probability density $p(\boldsymbol{x},\boldsymbol{u},t|\boldsymbol{y},\boldsymbol{v},s)$. Using the notation where $\boldsymbol{u}' = -\boldsymbol{u}$, $t' = -t$ and $dt' = -dt$, so that t' increases when going backward in time, *Thomson* [1987] proposes the following LSM:

$$du_i' = a_i'dt' + b_{ij}'d\xi_{ij}'\,, \tag{3.34}$$

$$d\boldsymbol{x} = \boldsymbol{u}'dt'\,. \tag{3.35}$$

These equations allow the sampling of the forward[3] transition probability associated with this model, denoted $p_f'(\boldsymbol{x},\boldsymbol{u}',t'|\boldsymbol{y},\boldsymbol{v}',s')$, where $t' > s'$; p_f' is the probability that a fluid element originating at $(\boldsymbol{y},\boldsymbol{v}')$ at time s', will be found at $(\boldsymbol{x},\boldsymbol{u}')$ at time t'.

[3] in the t' framework

$p'_f(\boldsymbol{x}, \boldsymbol{u}', t'|\boldsymbol{y}, \boldsymbol{v}', s')$, for $t' > s'$ should satisfy the FPE:

$$\frac{\partial p'_f}{\partial t'} = -\frac{\partial}{\partial x_i}(p'_f u'_i) - \frac{\partial}{\partial u'_i}(p'_f a'_i) + \frac{\partial^2 (B'_{ij} p'_f)}{\partial u'_i \partial u'_j}\,, \tag{3.36}$$

where the terms are to be evaluated at $(\boldsymbol{x}, -\boldsymbol{u}', -t')$. Transforming equation (3.36) $\partial t' \to -\partial t$, $u'_i \to -u_i$, $\partial u'_i \to -\partial u_i$:

$$-\frac{\partial p'_f}{\partial t} = +\frac{\partial}{\partial x_i}(p'_f u_i) + \frac{\partial}{\partial u_i}(p'_f a'_i) + \frac{\partial^2 (B'_{ij} p'_f)}{\partial u_i \partial u_j}\,, \tag{3.37}$$

$$\frac{\partial p'_f}{\partial t} = -\frac{\partial}{\partial x_i}(p'_f u_i) - \frac{\partial}{\partial u_i}(p'_f a'_i) - \frac{\partial^2 (B'_{ij} p'_f)}{\partial u_i \partial u_j}\,. \tag{3.38}$$

It is also required that this model satisfy the WMC, hence:

$$\frac{\partial g_a}{\partial t} = -\frac{\partial}{\partial x_i}(g_a u_i) - \frac{\partial}{\partial u_i}\left[(g_a a'_i) + \frac{\partial (B'_{ij} g_a)}{\partial u_j}\right], \tag{3.39}$$

$$\frac{\partial g_a}{\partial t} = -\frac{\partial}{\partial x_i}(g_a u_i) - \frac{\partial \phi'_i}{\partial u_i}\,. \tag{3.40}$$

In forward mode we have,

$$\frac{\partial g_a}{\partial t} = -\frac{\partial}{\partial x_i}(g_a u_i) - \frac{\partial}{\partial u_i}\left[(g_a a_i) - \frac{\partial (B_{ij} g)}{\partial u_j}\right], \tag{3.41}$$

$$\frac{\partial g_a}{\partial t} = -\frac{\partial}{\partial x_i}(g_a u_i) - \frac{\partial \phi_i}{\partial u_i}\,, \tag{3.42}$$

therefore:

$$a_i = \frac{\phi_i}{g_a} + \frac{1}{g_a}\frac{\partial (B_{ij} g_a)}{\partial u_j}\,, \tag{3.43}$$

$$a'_i = \frac{\phi'_i}{g_a} - \frac{1}{g_a}\frac{\partial (B'_{ij} g_a)}{\partial u_j}\,. \tag{3.44}$$

Following the discussion of [*Flesch et al.*, 1995] we note that b'_{ij} solely determine the intensity of the random component of the velocity fluctuations, therefore we can choose $b'_{ij} = b_{ij}$,which makes $B'_{ij} \to B_{ij}$. Since equations (3.40) et (3.42) imply that

$$\frac{\phi_i}{g_a} = \frac{\phi'_i}{g_a}\,, \tag{3.45}$$

we must have

$$a'_i = \frac{\phi_i}{g_a} - \frac{1}{g_a}\frac{\partial (B_{ij} g_a)}{\partial u_j}\,. \tag{3.46}$$

Therefore a_i and a'_i differ from each other only by the sign of the last term on the right hand side of the equation.

3.5.3 Inverse equations for quasi-steady, horizontally homogeneous Gaussian turbulence

The general forward and inverse LSM equations are given by the equations (3.2) and (3.3) for the forward mode, and equations (3.34) and (3.35) for the inverse mode. Equations (3.43) and (3.46), reproduced below, give the relationship between a_i and a_i':

$$a_i = -\frac{1}{g_a}\frac{\partial(B_{ij}g_a)}{\partial u_j} + \frac{\phi_i}{g_a}\,,$$
$$a_i' = +\frac{1}{g_a}\frac{\partial(B_{ij}g_a)}{\partial u_j} + \frac{\phi_i}{g_a}\,.$$

Therefore the inverse equations for 3-D quasi-steady, horizontally homogeneous Gaussian turbulence can be written as:

$$a_u' = \frac{C_0\epsilon}{2\sigma_u^2}u + \frac{1}{2\sigma_u^2}\frac{\partial\sigma_u^2}{\partial z}wu\,, \tag{3.47}$$

$$a_v' = \frac{C_0\epsilon}{2\sigma_v^2}v + \frac{1}{2\sigma_u^2}\frac{\partial\sigma_v^2}{\partial z}wv\,, \tag{3.48}$$

$$a_w' = \frac{C_0\epsilon}{2\sigma_w^2}w + \frac{1}{2}\frac{\partial\sigma_w^2}{\partial z}\left(1+\frac{w^2}{\sigma_w^2}\right). \tag{3.49}$$

3.5.4 The source-receptor relationship

Equations (3.34) and (3.35), together with equations (3.47) to (3.49) can be used to sample the "*backward*" probability density $p(\boldsymbol{y},\boldsymbol{v},s|\boldsymbol{x},\boldsymbol{u},t)$, and equation (3.33) gives the quantitative relationship with the "*forward*" counterpart $p(\boldsymbol{x},\boldsymbol{u},t|\boldsymbol{y},\boldsymbol{v},s)$. These equations provide powerful tools to estimate the amount of air exchanged between two locations. This quantity is often described as the source-receptor sensitivity (SRS) coefficient (see for example *Wotawa et al.* [2003]). The use of this relationship is illustrated in chapters 5 and 6.

CHAPTER 4

"The Canadian Meteorological Centre's Atmospheric Transport and Dispersion Modelling Suite" (published in Amosphere-Ocean)

4.1 Preamble

The paper presented in this chapter was written to provide a comprehensive scientific reference for the Lagrangian transport models used operationally at the Canadian Meteorological Centre (CMC) of Environment Canada, for which I was the lead developer. In the paper, the theoretical basis of Lagrangian modelling is sketched out and many details on the various physical processes simulated are discussed. A major re-coding combined with the addition of several minor improvements gave the occasion for the application of the models to real cases of atmospheric transport and dispersion in the boundary layer, and verification against available observations. The validation of the models is extensive and covers all scales, from the very local (hundreds of metres) to the global scale.

The models presented here constitute the main research tool underlying the findings of my thesis.

4.2 Publication details

4.2.1 Journal

Atmosphere - Ocean 53 (2) 2015, 176-199,
http://dx.doi.org/10.1080/07055900.2014.10002609

4.2.2 Authors

Réal D'Amours, Alain Malo, Thomas Flesch, John Wilson, Jean-Philippe Gauthier

4.3 Introduction

The Canadian Meteorological Centre (CMC) is part of the Meteorological Service of Canada and is responsible for providing guidance on the transport and dispersion of dangerous substances suddenly released in the atmosphere. The various national and international environmental emergency response mandates assumed by the CMC cover scales ranging from the very local, a few kilometres, to continental and global scales. For example, the CMC provides guidance on the atmospheric dispersion of radioactive material in the framework of the Federal Nuclear Emergency Plan (FNEP), [*Health Canada*, 2014]. The CMC also holds the following international designations: (1) Volcanic Ash Advisory Centre (VAAC) Montreal through the International Civil Aviation Organization [*ICAO*, 2004] and (2) Regional Specialized Meteorological Centre (RSMC) Montreal through the World Meteorological Organization (WMO) and International Atomic Energy Agency (IAEA) [*WMO*, 2010, updated 2012].

To fulfill these mandates, an integrated suite of Lagrangian transport and dispersion models has been developed and implemented. These dispersion models have been used for several years, on a regular basis in VAAC Montreal and RSMC Montreal, to predict and track volcanic ash/gas (e.g. *D'Amours et al.* [2010]; *Simpson et al.* [2002]; *Witham et al.* [2007]) , as well as radioactive material released by nuclear accidents or tests, (e.g. *Draxler et al.* [2015]; *Becker et al.* [2007]). The models are important tools for the contribution of the CMC to the Canadian response to nuclear emergencies, and are regularly used for other environmental emergencies such as smoke from forest fires, dust storms, toxic spills in the

atmosphere and chemical fires (e.g. *Joly et al.* [2010]). The models can also be applied to the dispersion of viruses transported on aerosols (e.g. *Gloster et al.* [2010]).

This paper presents the transport and dispersion models in operation at the CMC. The theoretical bases of the models as well as the practical aspects of their operational implementation are described in some detail in sections 4.4 to 4.6. In section 4.7, results from real case simulations using these models are compared and validated with available observation data.

4.4 Lagrangian modelling

In the context of Lagrangian modelling, dispersion in the atmosphere is estimated by calculating the trajectories of a very large number of air particles (or fluid elements), in order to adequately sample the dispersing plume. In general, these particles only differ from the other fluid elements because they are "marked". It is assumed that the marked particles conserve their identity during their flight. However they can transport some amount of material that may be subject to various physical processes like dry deposition, wet scavenging and radioactive decay. A particle can also be viewed as representing an ensemble of real particles. Upon release, it is assigned a mass that depends on the total quantity of the substance emitted and the total number of particles released, and which has little to do with the real mass or size distribution of the aerosols represented.

In most applications, especially when considering transport on a regional or larger scale, the 3-D structure of the atmosphere, and its evolution in time, must be taken into account. For that reason dispersion models are usually executed with meteorological fields provided by a Numerical Weather Analysis and Prediction (NWP) system, in an ''off-line" fashion. Those fields are available only at specific time intervals, and only at a limited number of discrete points in space (3D grids). Therefore, many scales of motion are not resolved. This is especially true of the turbulent components of the wind which are mostly responsible for the mixing of air parcels. The information provided by the NWP systems can be used to estimate at least some of the statistical features of the unresolved scales

and of atmospheric turbulence. Lagrangian Stochastic Models (LSM) use a stochastic differential equation (SDE) to calculate a probable trajectory for a given particle, based on those statistics.

The application of Monte Carlo methods to simulate dispersion in simple cases, by calculating the trajectory of several particles, started in the early 1970s [*Thompson*, 1971; *Thomson and Wilson*, 2012]. However, the idea of considering diffusion in the Lagrangian framework goes back to the beginning of the last century [*Langevin*, 1908], and in the context of atmospheric diffusion, to the 1920's [*Taylor*, 1922; *Krasnoff and Peskin*, 1971]. *Wilson et al.* [1981b] and *Wilson et al.* [1983] successfully applied Monte Carlo methods to dispersion, using a formulation of turbulent motion statistics based on realistic models of the atmospheric surface layer for different stability regimes. They compared the results with data from the Prairie Grass Experiment [*Barad*, 1958]. Their model was later formalized by *Thomson* [1984, 1987].

4.5 Accounting for turbulent mixing

4.5.1 A first order model for the particle velocities

Representing the real wind experienced by a particle as $U_i + u_i'$, where U_i is the resolved or large scale component usually provided by the NWP models, and u_i', is the unresolved fluctuating part, then the following SDE provides the basis for the evolution of the unresolved u_i' component [*Wilson and Sawford*, 1996]:

$$du_i' \;=\; a_i dt + b_{ij} d\xi_j \,, \tag{4.1}$$

where the terms a_i and b_{ij} (Einstein summation convention is used) are functions of time and space, and $d\xi_j$ is a Gaussian white noise, with zero mean and $(dt)^{1/2}$ standard deviation. The change in the particle's position is then evaluated:

$$dx_i = (U_i + u_i')dt \,. \tag{4.2}$$

Thomson [1987] discussed possible criteria for the determination of the a_i and b_{ij} terms. He recognized that they could essentially be subsumed under one criterion which he called "the well-mixed condition (wmc)": an initially well-mixed set of particles in a fluid,

(i.e. they are distributed in phase-space –position and velocity– like all the other fluid particles) will remain well-mixed. He also indicated that this criterion did not lead to a unique determination of the a_i and b_{ij} coefficients in equation (4.1)[1].

Consistency with Kolmogorov similarity theory for locally isotropic turbulence allows the determination of the b_{ij} coefficients [*Thomson*, 1987]:

$$b_{ij} = \sqrt{\epsilon C_0}\delta_{ij}\,, \tag{4.3}$$

where ϵ is the local turbulent kinetic energy (TKE) dissipation rate, C_0 a putatively universal constant and δ_{ij} the Kronecker delta function.

Neglecting the turbulent velocity covariances, and assuming quasi-stationary Gaussian turbulence, locally homogeneous in the horizontal, an expression for the coefficients a_i can be derived:

$$a_u = -\frac{C_0\epsilon}{2\sigma_u^2}u' + \frac{1}{2\sigma_u^2}\frac{\partial\sigma_u^2}{\partial z}u'(w'+W)\,, \tag{4.4}$$

$$a_v = -\frac{C_0\epsilon}{2\sigma_v^2}v' + \frac{1}{2\sigma_v^2}\frac{\partial\sigma_v^2}{\partial z}v'(w'+W)\,, \tag{4.5}$$

$$a_w = -\frac{C_0\epsilon}{2\sigma_w^2}w' + \frac{1}{2\sigma_w^2}\frac{\partial\sigma_w^2}{\partial z}w'(w'+W) + \frac{1}{2}\frac{\partial\sigma_w^2}{\partial z}\,, \tag{4.6}$$

where the usual 3-D definition (x, y, z, u, v, w) is used. σ_u^2, σ_v^2 and σ_w^2 are the turbulent velocity variances, and W represents the large scale vertical motion. The discretized form of this set of equations constitutes the basis of the first order dispersion models implemented at the CMC.

4.5.2 The random displacement model

Dispersion models based on the equations in Section 4.5.1 are called first order models because they relate to particle velocities. One of the constraints of a discretized first order model is that the time steps must be much smaller than the Lagrangian time scale

[1] Unless it so happens that the model is 1-dimensional, or the different velocity fluctuation components are independent.

for turbulence T_L, i.e. the particle velocity de-correlation time, which can be expressed as $2\sigma_w^2/C_0\epsilon$. For turbulent eddies generally associated with atmospheric diffusion, this time scale can be of the order of a minute in the middle of a fully developed boundary layer [*Hanna*, 1981] and much smaller close to the ground where the TKE dissipation rates can be very large.

While a first order LSM is required to properly calculate the particles' velocities as they move through the turbulent eddies, in large-scale dispersion applications one may not be interested in the precise details of the concentration field very close to the source. *Rodean* [1996] derived a Random Displacement Equation (RDE) by integrating the Lagrangian stochastic equation (LSE) over a time interval larger than T_L. This can be regarded as taking the diffusion limit of the first-order Lagrangian stochastic model [*Durbin*, 1980]. *Boughton et al.* [1987] also had emphasized the equivalence of the Eulerian advection-diffusion equation with the RDE. However, the connection between the diffusion equation and a random walk had long been known in physics. Considering the vertical component, the RDE is written as:

$$dz = \left[\frac{\partial K_z}{\partial z} + W\right] dt + \sqrt{2K_z} d\xi \tag{4.7}$$

$$K_z = \sigma_w^2 T_L \tag{4.8}$$

where K_z represents a vertical diffusion coefficient, W is the large scale (synoptic) vertical motion, and $d\xi$ again is a Gaussian random number with mean zero and variance dt. Since the RDE is applied to displacements, it is called a zero-th (0-th) order equation or model, in contrast to first order models. The main advantage of the RDE is that it allows for longer time steps than the discretized Langevin equation for particle velocities [*Wilson and Yee*, 2007].

4.6 CMC's dispersion modelling suite: MLCD, MLDP1, MLDP0 and MLDPmm, and the trajectory model

A suite of dispersion model codes has been implemented for environmental emergency response at the CMC. A short range model, MLCD (Modèle Lagrangien Courte Distance) is used for dispersion events having impacts at distances of one to ten kilometers. MLDP1 (Modèle Lagrangian de Dispersion de Particules d'ordre 1) is mainly used for regional scale problems (domains of the order of 100 km or less) and MLDP0 (Modèle Lagrangian

de Dispersion de Particules d'ordre zéro) is used for dispersion events having continental or global impacts. It is possible to switch from the MLDP1 kernel to the MLDP0 kernel within one simulation based on a criterion such as the age of a particle. It is also possible to produce simulations in ***m***ixed ***m***ode, within the MLDP1 kernel, switching from one mode to another according to specific criteria, and this is referred as MLDPmm. However the diffusion coefficient in MLDPmm differs from that of MLDP0.

To minimize the pre-processing of this meteorological input, the structure of the CMC dispersion models is closely matched to that of the driving meteorological numerical analysis and forecast models. For example they operate in the same vertical coordinate, and use the same formulation for the vertical motion, and MLDP1 normally uses the NWP turbulent kinetic energy (TKE). The meteorological data required to drive the models is provided by CMC's NWP system. For the global scale, the data comes from the CMC Global Deterministic Prediction System (GDPS) [*Canadian Meteorological Centre (CMC)*, 2013a] which is based on global 4D-Var data assimilation coupled to the Global Environmental Multiscale (GEM) forecast model having a horizontal resolution of approximately 25 km, and 79 vertical levels. For the continental scale, the data is provided by the Regional Deterministic Prediction System (RDPS) [*Canadian Meteorological Centre (CMC)*, 2013b], also based on regional 4D-var assimilation coupled to a limited area forecast model with a horizontal resolution of 10 km on a 996x1028 grid, and a vertical configuration similar to that of the GDPS. The GDPS executes twice a day, while the RDPS executes four times each day. The CMC also operates a High Resolution Deterministic Prediction System (HRDPS) [*Canadian Meteorological Centre (CMC)*, 2011] at a horizontal resolution of 2.5 km, on 5 windows covering specific sectors of Canada.

4.6.1 MLCD

The function of MLCD is to provide a quick estimate of the dispersion of a plume at local scales that would allow the input of local meteorological information and observations when available. MLCD is also a first order Lagrangian stochastic model based on the same equations as MLDP1. As well, the same parameterization is used to estimate the three components of the turbulent velocity variance. The meteorological conditions are

assumed to be uniform in the horizontal over all of MLCD domain. Even though stationarity is an assumption underlying the Lagrangian stochastic equations used in MLCD, the meteorology is allowed to change with time presuming, as with MLDP1, that the time scale of these changes is large compared to the turbulence time scale.

MLCD is supplemented with an average wind model needed to generate a vertical wind profile and other parameters describing the boundary layer [*Wilson and Flesch*, 2004]. This profile is obtained by matching the Monin-Obukhov surface layer profile to a baroclinic Ekman profile in the upper portion of the boundary layer. The resulting profile is adjusted – best fitted – to any meteorological information provided by the user (at least one wind data). An often-used procedure is to provide the wind model with a surface wind observation together with estimations of the horizontal wind in the upper portion of the boundary layer provided by NWP models. In that case estimates of the Monin-Obukhov length L (defined below) and of boundary layer height H have to be provided.

4.6.2 Estimation of the velocity variances for MLDP1

4.6.2.1 Using boundary layer parameters provided by NWP models

The TKE (denoted by E) provided by the CMC NWP models represents the sum of all the velocity variances [*Mailhot and Benoit*, 1982; *Bélair et al.*, 1999]:

$$E = \frac{1}{2}(\sigma_u^2 + \sigma_v^2 + \sigma_w^2)\,. \tag{4.9}$$

Therefore the E has to be partitioned into its three components in order to solve equations (4.4) to (4.6). Assuming that the horizontal variances $\sigma_u^2 = \sigma_v^2$, denoted by σ_{uv}^2, the partitioning is done by calculating ratios (m_{uv}, m_w) which are applied as factors to the E provided by the NWP models as follows:

$$\sigma_{uv}^2 = 2m_{uv}E \tag{4.10}$$

$$\sigma_w^2 = 2m_wE \tag{4.11}$$

with the constraints $2m_{uv} + m_w = 1$ and $2\sigma_{uv}^2 + \sigma_w^2 = 2E$ giving:

$$m_{uv} = \frac{\sigma_{uv}^2}{2\sigma_{uv}^2 + \sigma_w^2} \tag{4.12}$$

$$m_w = \frac{\sigma_w^2}{2\sigma_{uv}^2 + \sigma_w^2} \tag{4.13}$$

Boundary layer parameterizations suggested by *Nieuwstadt* [1984], *Weil* [1990] and *Rodean* [1996] are used to estimate the portion each component contributes to the total variance. A ratio is calculated and applied as a factor to the TKE provided by the NWP models.

For the unstable case, when the Monin-Obukhov lengthscale L is negative:

$$\sigma_{uv}^2 = u_*^2\left[4.5\Big(1 - \frac{z}{h}\Big)^{3/2} + 0.6\Big(-\frac{h}{L}\Big)^{2/3}\right] \tag{4.14}$$

$$\sigma_w^2 = u_*^2\left[\Big(1.6 - \frac{z}{h}\Big)^{3/2} - \frac{3z}{L}\Big(1 - 0.98\frac{z}{h}\Big)^{3/2}\right]^{2/3}, \tag{4.15}$$

where u_* is the friction velocity, z the height above ground, and h the depth of the boundary layer. For the stable case where $L \geqslant 0$:

$$\sigma_{uv}^2 = 4.5u_*^2\Big(1 - \frac{z}{h}\Big)^{3/2} \tag{4.16}$$

$$\sigma_w^2 = 1.96u_*^2\Big(1 - \frac{z}{h}\Big)^{3/2} \tag{4.17}$$

These variances are only used to estimate how the NWP TKE (denoted here as $\tilde{E}$) should be partitioned between the various components. Using the ratios from equations (4.12) and (4.13):

$$\tilde{\sigma}_{uv}^2 = 2m_{uv}\tilde{E} \tag{4.18}$$

$$\tilde{\sigma}_w^2 = 2m_w\tilde{E} \tag{4.19}$$

This is done because it should not be expected that the E estimates resulting from the sum of the variances given by the parameterizations will be equal to $\tilde{E}$; however it is assumed that $\tilde{E}$ provide a better representation of the real TKE, and consequently, $\tilde{\sigma}_{uv}^2$ and $\tilde{\sigma}_w^2$ a better representation of the real turbulent wind variances.

4.6.2.2 Diagnosis of L and u_*

When $\tilde{E}$, the NWP TKE, is not available, for example in diagnostic mode where one uses meteorological fields from objective analyses, the parameterizations of equations (4.14) to (4.17) are used directly. In that case L and u_* are also needed. Estimates are obtained from the low level horizontal wind profile, assuming that the two lowest levels at which the winds are available, $\sim$ 10 m and $\sim$ 40 m are within the surface layer. Following Monin-Obukhov similarity theory, the wind and potential temperature vertical gradients are expressed in terms of universal functions ϕ_m and ϕ_h of the non-dimensional height $\zeta = z/L$:

$$\frac{\partial U}{\partial z} = \frac{u_*}{kz}\phi_m\Big(\frac{z}{L}\Big)\,, \tag{4.20}$$

$$\frac{\partial \theta}{\partial z} = \frac{T_*}{kz}\phi_h\Big(\frac{z}{L}\Big)\,, \tag{4.21}$$

$L = -u_*^3\theta_0/kgQ_0$ is the Monin-Obukhov lengthscale, where k is the von Karman constant, θ_0 and Q_0 are the potential temperature and kinematic heat flux density very close to the ground, u_* is the friction velocity, and $T_* = -Q_0/u_*$. L can also be written as $u_*^2\theta_0/kgT_*$. There are no physical theories to help in the formulation of the functions ϕ_m and ϕ_h; they have to be determined experimentally. Based on the Kansas field experiment [*Haugen et al.*, 1971], *Businger et al.* [1971] obtained the following expressions:

$$\phi_m = \begin{cases} (1-15\zeta)^{-1/4} & \zeta < 0\,, \\ 1+4.7\zeta & \zeta \geq 0\,, \end{cases} \tag{4.22}$$

and:

$$\phi_h = \begin{cases} 0.74(1-9\zeta)^{-1/2} & \zeta < 0\,, \\ .74+4.7\zeta & \zeta \geq 0\,. \end{cases} \tag{4.23}$$

The formulation for the unstable case, $\zeta < 0$, was later revised by *Dyer and Bradley* [1982] to :

$$\phi_m = (1-28\zeta)^{-1/4} \tag{4.24}$$

$$\phi_h = (1-9\zeta)^{-1/2} \tag{4.25}$$

Expressing the vertical gradients of U and θ in equations (4.20) and (4.21) in terms of finite differences between the two lowest model levels, and using the formulations of *Dyer and Bradley* [1982] for $\zeta \leq 0$, and of *Businger et al.* [1971] for $\zeta > 0$, an estimate of u_* and T_* is obtained by iteration, using the gradient Richardson number Ri

$$Ri = \frac{g}{\theta_v} \frac{\partial \theta_v / \partial z}{(\partial U/\partial z)^2 + (\partial V/\partial z)^2} \,, \tag{4.26}$$

as a first guess for ζ.

4.6.3 Estimation of the diffusion coefficient K_z

The importance of vertical wind shear in horizontal diffusion is well known [*Smith*, 1965; *Wilson et al.*, 1993], and experience has shown that most of the lateral spread of a plume in the boundary layer results from the combined effects of vertical mixing and vertical wind shear (Ekman spiral). For that reason, only vertical diffusion is considered when executing the MLDP0 kernel. According to equation (4.8), $K_z = \sigma_w^2 T_L$. In NWP models, K_z is more often written in terms of a length scale (a mixing length). In the CMC NWP models, K_z is modelled as $a\lambda E^{1/2}$ where a is a constant, λ a mixing length, and E the TKE [*Bélair et al.*, 1999].

When available, this vertical diffusion coefficient can be used. However, this is not usually the case in diagnostic mode. In MLDP0, K_z is simply calculated with the *O'Brien* [1970] function:

$$K = K(h) + \left[\frac{(h-z)}{(h-h_{sl})}\right]^2 \left\{K(h_{sl}) - K(h) + (z-h_{sl})\left[\frac{\partial K}{\partial z}\Big|_{h_{sl}} + 2\frac{K(h_{sl}) - K(h)}{h - h_{sl}}\right]\right\} \tag{4.27}$$

where $h_{sl} \leqslant z \leqslant h$, h_{sl} being the height of the surface layer and h, the height of the boundary layer. Following *Delage* [1988], the height of the first level above ground of the driving NWP model is taken as the top of the surface layer h_{sl}. K_z at this level is calculated in terms of a mixing length, stability function, and vertical shear of the horizontal wind vector $\mathbf{U}$, according to *Delage* [1997].

$$K(h_{sl}) = \frac{(k\, h_{sl})^2}{\phi_m \phi_h} \left|\frac{\partial \mathbf{U}}{\partial z}\right| \tag{4.28}$$

$$\phi_m \phi_h = \begin{cases} \beta(1 + 12Ri)^2 & Ri > 0 \\ \beta(1 - 40Ri)^{1/2} & Ri \leqslant 0 \end{cases} \tag{4.29}$$

where Ri is the gradient Richardson number and k, the von Karman constant. The stability functions $\phi_m \phi_h$ are identical to those used in CMC's Global Environmental Multiscale (GEM) model [*Mailhot et al.*, 1998]. The boundary layer height h is provided by the NWP model, or is diagnosed from the wind and temperature fields as the height at which the bulk Richardson number reaches a critical value (0.25). In MLDPmm K_z is expressed as $\sigma_w^2 T_L$.

4.6.4 Effect of the vertical density gradient in the atmosphere

Thomson's well-mixed condition, mentioned in section 4.4, requires that dispersion models do not change with time, the distribution in phase space of tracer particles initially distributed like all the other fluid particles in which they are immersed. The set of stochastic equations shown in Section 4.5.1, equations (4.4) to (4.6), will tend to distribute particles uniformly in the vertical, while the real atmosphere air density ρ decreases with height. The net effect would be more tracer particles relatively to the other fluid particles at upper levels, and the reverse at lower levels. The difference may not be that important within a shallow boundary layer, but can become non-negligible when the BL top is well over a kilometre. *Stohl and Thomson* [1999] proposed the addition of the following term to equation (4.6):

$$\frac{\sigma_w^2}{\rho} \frac{\partial \rho}{\partial z} \,. \tag{4.30}$$

Such a term has been added to MLDP1. A similar correction has been derived for the RDE:

$$\frac{K_z}{\rho} \frac{\partial \rho}{\partial z} \,, \tag{4.31}$$

and has been implemented in MLDP0. In the first order model, the term (4.30) is an acceleration which is proportional to the vertical velocity variance and tends to accelerate the particle down the density gradient – i.e. downward in the hydrostatic atmosphere. Term (4.31) acts as a drift velocity, proportional to the diffusion coefficient, and also tends to move the particle downward.

4.6.5 Horizontal Diffusion

The presence of fluctuations or intermittency at time scales larger than those of atmospheric turbulence has been under investigation for some time [*Hanna*, 1986; *Gupta et al.*, 1997], and has been attributed to horizontal wind fluctuations of periods of a few hours also known as meandering. In order to simulate the average effect of this process, a first order Langevin equation has been included, similarly to *Maryon* [1998]:

$$du_m = -\frac{u_m}{\tau_m}dt + \sqrt{\frac{2\sigma^2_{u_m}}{\tau_m}}d\xi \tag{4.32}$$

where u_m is the u component of the meandering velocity, τ_m the time-scale and $\sigma^2_{u_m}$ the variance of these fluctuations. Here again, $d\xi$ is a Gaussian random number with mean zero and variance dt. The v component of the meandering velocity is modelled with an identical equation. The determination of τ_m and $\sigma^2_{u_m}$ is empirical, and these parameters are input by the user.

4.6.6 Dispersion at the top and above the boundary layer

Vertical mixing is greatly reduced at the top of the boundary layer because of the presence of a thermally stable layer which dampens the turbulence. While the ground surface constitutes an absolute boundary, there is no material lid at the top of the BL to prevent particles from moving back and forth. The transition zone at the top of the BL can be very thin but fluctuates quite a bit in space and in time [*Wyngaard*, 2010]. Temporal and/or spatial averaging will depict a layer where exchanges between the BL and the free troposphere (FT) above are occurring. This layer is often called the entrainment zone (EZ) [*Crum and Stull*, 1987]. Near the top of the BL, the variance of the vertical velocities σ^2_w decreases as the TKE decreases. The TKE dissipation rate ϵ also decreases, but faster than the TKE itself[2], so that the T_L increases. Therefore the constraint on the time step is less stringent and particles could cross the BL top simply because of numerical effects. Even though there is transport/entrainment across the EZ, transport strictly due to diffusion is often considered negligible. Particles that would move above the top are reflected downward (e.g. *Stohl et al.* [2005]). Such a reflection is implemented in the MLDP0 kernel

[2] In CMC NWP models $\epsilon \propto E^{3/2}$

and in MLCD. Transfer between the BL and the FT can occur through other mechanisms. For example, particles that were in the FT may become "entrained" in the BL if it rises above their vertical position during the simulation; conversely particles may be left out in the FT if the BL lowers below their position. Also in MLDP0, the synoptic vertical motion can move particles across the BL top. In the MLDP1 kernel, there is no imposed reflection at the top of the BL and particles follow the trajectories dictated by the 3-D winds and the ambient TKE.

There is no dominant mechanism producing mixing in the free troposphere (FT). Turbulence is rather localized in time and space and can be generated locally by gravity waves or deep convection. Very often substances injected above the BL travel in fairly well maintained streams for several days [*D'Amours et al.*, 2013; *Colette et al.*, 2008; *Gerasopoulos et al.*, 2006]. In MLDP0, the vertical diffusion coefficient falls to a very low threshold value in the FT and the RDE is essentially turned off. Nevertheless, there still can be a fair amount of dispersion induced by stretching and deformation in the horizontal wind and by vertical transport associated with large scale dynamics. Furthermore there is also the option of activating the lateral diffusion discussed in section 4.6.5.

4.6.7 Near the ground surface

4.6.7.1 Surface reflection

The average wind vanishes at height z_0, the roughness length. Near this level, the length scale of the turbulent eddies decreases, the TKE dissipation rate ϵ increases and the Lagrangian time scale T_L decreases. The problems arising from the treatment of this boundary condition in the context of a discretized Langevin equation like equation (4.1) were discussed in detail by *Wilson and Flesch* [1993]. Their concept of an unresolved basal layer (UBL) is used in MLDP1 and MLCD. A perfect reflection is applied to a particle that would enter the UBL. Depending on the depth of the UBL, the particle is required to wait a certain amount of time during which it will drift horizontally in the direction of the surface layer wind, following the UBL model described by *Wilson et al.* [2001]. The height of the UBL is chosen by the user based on practical considerations, the main one being the length of the time step which is constrained by the Lagrangian time scale.

4.6.7.2 Dry Deposition

Dry deposition is assumed to occur when a particle representing a tracer that could be absorbed or captured by surface elements enters the UBL. An absorption probability P is calculated according to *Wilson et al.* [1989]:

$$\begin{aligned} P &= 1 - R \\ R &= \frac{1-a}{1+a}; \qquad a = \left(\frac{\pi}{2}\right)^{\frac{1}{2}} \frac{v_d}{\sigma_w} \end{aligned} \tag{4.33}$$

where R is the reflection probability, v_d is the dry deposition velocity and σ_w, the standard deviation of the vertical turbulent wind component. In MLDP0, σ_w is approximated in terms of the variance of the discrete random vertical displacements, which following the RDE, equation (4.7), is given by:

$$\begin{aligned} \overline{\Delta z^2} &= 2K_z \Delta t \\ \sigma_w &\approx \frac{\sqrt{\overline{\Delta z^2}}}{\Delta t} = \sqrt{\frac{2K_z}{\Delta t}} \ . \end{aligned} \tag{4.34}$$

Because a model particle represents an ensemble of particles in the atmosphere, the modelled effect of dry deposition is to reduce the particle mass by a fraction given by P. This process is different from deposition due to gravitational settling.

4.6.8 Gravitational settling

Generally in Lagrangian modelling, the "marked" particles are not really different from the other fluid elements and they follow similar trajectories. However when modelling heavy particulates subject to gravitational acceleration, the LSE or RDE above are no longer valid. The simplest approach is to add a gravitational settling velocity W_g to the vertical component of equation (4.2), or to the synoptic vertical motion W in equation (4.7), and to consider that a model particle is an ensemble of those particulates. This approach is implemented in the CMC dispersion models.

Wilson et al. [1981a] have proposed a similar modification to their LSE. They compared their model results with data from an experiment they performed themselves using monodispersed glass beads, and showed that it worked satisfactorily. *Wilson* [2000] reviewed various stochastic models for heavy particle dispersion, including one based on the modified RDE, comparing model results with experimental data. The conclusion was that no significant increase in accuracy is obtained by using models more complex than equation (4.2) plus W_g. The model based on the RDE did not perform very well at distances very close to the release point but was adequate at distances beyond 200 m.

At CMC, the modelling of gravitational settling is mostly used for tracking volcanic ash plumes. In that case the settling velocity of ash particles is simply modelled in terms of Stokes law for spherical particles following *Sparks et al.* [1997] p. 384:

$$W_g = \frac{g\rho_{ash}d^2}{18\nu\rho_{air}}\,, \tag{4.35}$$

where g is the acceleration due to gravity, ρ_{ash} and ρ_{air}, respectively the ash and air densities, d the diameter of the spherical ash particle and ν the air kinematic viscosity. Since the size distribution of the ash particles is highly dependent on the magma characteristics and the eruption type, a few empirical distributions like those proposed by *Durant and Rose* [2009] are available to the user.

4.6.9 Wet scavenging radioactive decay

In CMC's dispersion models the removal of aerosols by clouds and precipitation is modelled in a rather crude fashion. This is because a good specification of the 3-D precipitation rate fields is seldom available in diagnostic mode, especially over the oceans. Simply, wet scavenging occurs when a particle is presumed to be in clouds. The fractional cloud cover f_c is estimated with a simple function of the local relative humidity U, and a threshold value U_0.

$$f_c = \begin{cases} 0 & U < U_0 \\ \dfrac{U - U_0}{1 - U_0} & U \geqslant U_0 \end{cases} \tag{4.36}$$

The tracer loss rate experienced by a fluid element is proportional to the cloud fraction, and the particle tracer mass m_p:

$$\left.\frac{\partial m_p}{\partial t}\right|_{w_s} = -(f_c w_s) m_p(t)\,, \tag{4.37}$$

where w_s is an empirical wet scavenging factor.

A more realistic physical parameterization *Feng* [2007] can be activated when precipitation rate fields are available.

Tracer loss rate due to radioactive decay is calculated using the standard formulation:

$$\left.\frac{\partial m_p}{\partial t}\right|_r = -ln(2)\ \frac{m_p(t)}{t_{1/2}}\,, \tag{4.38}$$

where $t_{1/2}$ is the half-life of the tracer species characterizing the particle, and m_p its mass. The fate of the elements resulting from the decay is not modelled. The possible in-growth from the decay of other radioactive tracers is also not taken into account.

4.6.10 Concentration estimation

LSMs yield particle trajectories. However, it is concentration fields and concentrations at specific locations that are needed most of the time. Assuming that the particle "mass" is given by m_p, an estimation of the concentration field is obtained by counting the number of particles in each of the cells of a 3-D array covering the domain of interest. The concentration at point $\mathbf{r}$ is simply:

$$c(\mathbf{r},t) = \frac{1}{\delta V_s} \sum_{p \in \delta V_s} m_p(\mathbf{r},t) \tag{4.39}$$

where δV_s is the volume of the cell centered at $\mathbf{r}$. A justification of this approach is given in Paper appendix 4.11.1.

4.6.11 Inverse modelling

Flesch et al. [1995] discussed the implementation of a backward first order LSE for the estimation of source of emission characteristics from concentrations. *Pudykiewicz* [1998] developed the adjoint operator of an Eulerian advection-diffusion model for similar applications. It turns out that the "adjoint" of the Eulerian advection-diffusion equation, and of the equivalent Lagrangian random displacement model, RDE equation (4.7), is simply the forward equation with the average or synoptic wind reversed. Diffusion and removal processes are treated the same way as in forward mode.

An inverse version of MLDP0 has been developed and is used to support the operations of the Comprehensive Nuclear-Test-Ban Treaty (CTBT) Organization [*WMO*, 2010, updated 2012]. The results of adjoint or inverse models are often referred as Source Receptor Sensitivity (SRS) coefficients [*Wotawa et al.*, 2003]. Simply put, the SRS coefficients are a measure of the amount of air transported from a given region of the atmosphere (a possible source location) into the sampler where the concentrations are measured.

4.6.12 The trajectory model

In some cases however, one is just interested in visualizing the tracks of a few large air parcels. A simple and fast trajectory calculation module has been implemented for that specific purpose. Again, it is assumed that the identity of the air parcels is preserved as they move with the wind, and that they are not affected by any other processes. The change in the position of a given air parcel is obtained by integrating it's velocity in time:

$$\Delta \mathbf{r} = \int_{t_0}^{t_0+\Delta t} \mathbf{V}(\mathbf{r}, t) dt \tag{4.40}$$

where $\mathbf{V}(\mathbf{r}, t)$ represents the 3D wind velocity. The time discretization is carried out using a Runge-Kutta algorithm. Because of 4^{th} order accuracy of this scheme, it is possible to use a large time step. Usually it is chosen as the time interval at which the 3-D wind fields are provided - one to six hours. Since the resulting horizontal finite displacements can be relatively large and that they are calculated on the sphere, some care must be used in their estimation. Because of its very basic approach, it is difficult to objectively evaluate a trajectory model. Nevertheless, the CMC trajectory model has been used extensively over the years in various contexts (e.g. *Mercier et al.* [2009]) and its usefulness amply demonstrated.

4.7 Validation

4.7.1 Validation of MLCD for local dispersion with the Gentilly SF_6 tracer experiment

Most short range dispersion tracer experiments are performed under ideal conditions (e.g. Project Prairie Grass, *Barad* [1958]), and often in controlled wind tunnel experiment [*Legg*

et al., 1986]. The algorithms used in the short range dispersion module MLCD have been well tested against data from such experiments e.g. *Wilson et al.* [1981a, 1993].

A short range tracer experiment was performed in September and October 1997 on the grounds of the Gentilly Nuclear Power Plant, on the east shore of the St-Lawrence river, with controlled releases of sulphur hexafluoride SF_6. Details about the experiment are given in *Davis et al.* [2005] (Atomic Energy of Canada Limited unpublished internal report). The site is fairly representative of the complex geometry usually found in large industrial compounds. The tracer gas was released from a stack on top of the service building of the power plant, at a height of 37 m above ground. Average tracer concentrations at each sampler for the first four releases were made available for the validation of MLCD. Table 4.1 shows the duration and the rates of the releases. For each release, the layout of the samplers was rearranged according to the mean wind direction. The samplers were placed on two arcs about 500 m and 1000 m from the release, near the ground . 15-minute averages of wind speed and direction and of air temperature, measured routinely at 10, 37 and 48 m levels, were used as meteorological input for MLCD. The height of the boundary layer had been estimated by *Davis et al.* [2005], and the Monin-Obukhov lengthscale L was evaluated from the tower measurements (see Paper appendix 4.11.2).

Figure 4.1 shows a scatter diagram of the modelled versus measured average concentrations. In total there are 81 measurements available, out of a possible 86; 5 are not available for technical reasons. The Pearson linear correlation coefficient for the total set is 0.88. 65% of the modelled concentrations are within a factor of two of the observations, and 87% within a factor of 5.

Figure 4.2 allows a more direct comparison of the average modelled and observed concentrations at each sampler, along the different arcs. The model is quite successful at positioning the axis of maximum concentrations and at depicting the lateral extent of the plume. The concentrations resulting from the modelling are somewhat overestimated for release #1. According to table 4.1 the thermal stability was fairly high, so a possible explanation could be that there was a bit much downward mixing in the modelled plume. Release #4 seems to show a somewhat different behaviour of the plume especially at 1000

m. For this case, the samplers were positioned on an axis more aligned with the shore of the St-Lawrence River. Even though the winds observed at the tower appear quite consistent with those reported at a meteorological station situated on the other side of the river (not shown here), it is suspected that local wind convergence induced by the roughness change between the land and water might have induced a pull of the plume towards the river, causing more lateral spread in the plume than the model could simulate.

4.7.2 Short to medium range dispersion: an accidental release of sulphur trioxide near Montréal, Canada

Around 22:00 EDT August 9 2004 (02:00 UTC August 10), about 6 tonnes of sulphur trioxide (SO_3) were accidentally released from a chemical factory in Salaberry-de-Valleyfield, about 50 km southwest of downtown Montréal. The incident triggered a real time emergency response from the CMC. The SO_3 escaped through a chimney stack about 80 m high during roughly 30 minutes. After entering the atmosphere, the SO_3 gases rapidly reacted with the ambient water vapor to form sulfate aerosols, resulting in a plume which reached the city of Montréal a few hours later. A fine mist was observed in downtown Montréal during the passage of the plume around midnight, and a significant increase in particulate matter concentrations ($PM_{2.5}$) was observed at some stations of the city's air quality monitoring network [*Paquin and D'Amours*, 2005]. Since most of the sulfate aerosols produced in the atmosphere have a diameter smaller than 1.0 μm [*Hazi et al.*, 2003], it can be safely assumed that the sudden increase in particulate matter was the result of the SO_3 plume. The availability of these observation data provides an opportunity to evaluate the performance of the dispersion models.

The intermediate scale of the problem was somewhat problematic for the operational response. Using the local model MLCD, at first appeared to be inappropriate, mainly because of the uniform horizontal wind field assumption. On the other hand, it seemed that the spatial scale of the release was at the resolution limit of the available regional meteorological fields provided by NWP (15 km grid-spacing). In the end, since meteorological conditions were estimated to be fairly uniform in the horizontal over the domain of concern, it was decided to use MLCD for the initial response. Figure 4.3 (a) shows the position of the MLCD estimated plume two hours and 30 minutes after the start of the release, based

on a prudent original estimation of 10 t for the release provided by the Emergency responders. The plume cuts off abruptly at the north-east end at the edge of the model domain. Figure 4.3 (b) shows an after the fact MLDPmm simulation for the same time, using 6–12 hour forecast meteorology from the CMC 15 km regional model in operation at the time, and would have been available for a real time response, also using a revised release of 6 t provided later by the plant authorities. In the MLDPmm configuration, particle trajectories were calculated with the first order algorithm, during the first hour after their release, and with the zero-th order algorithm afterwards.

Over the island of Montreal, the size and shape of the two modelled plumes are rather similar, but the slight shift in their trajectories is significant in terms of potential impacts. The MLDPmm plume sweeps right over the city downtown area, while the MLCD plume generally travels over the northern half of the island. Figure 4.4 shows time series of modelled SO_3 concentrations in comparison with observed $PM_{2.5}$ concentrations at two downtown air quality monitoring stations. The timing of the MLDPmm plume passage is very good. The MLCD plume arrives at the stations about 30 to 45 minutes early. Concentrations are lower than those of MLDPmm, reflecting the fact that the brunt of the MLCD plume just skimmed by the two stations.

Also, according to the MLCD simulation stations AUT and RDP should have seen increased concentrations, and that was not observed. There were no attempts to model the transformation of SO_3 into H_2SO_4 aerosols and to estimate the quantity of $PM_{2.5}$ that could result from the process, so a direct comparison is not possible. However it is not unreasonable to assume that the $PM_{2.5}$ concentrations would be larger than the un-transformed SO_3 concentrations. Therefore concentrations produced by the MLDPmm simulation appear quite reasonable. It also indicates that there is a real benefit in using the full time-varying 3-D meteorology, despite the fact that conditions seemed fairly uniform in space and time during the few hours following the incident.

4.7.3 Continental dispersion: the first release of the European Tracer Experiment ETEX-1

Details on ETEX can be found in *Girardi et al.* [1998]. The first release ETEX-1, took place on October 23 1994. An inert perfluorocarbon tracer (PMCH) was released from a

small chimney (~ 4 m high) at a constant rate, during 12 hours, starting at 16:00 UTC, in Monterfil in Western France. A total of 340 kg of tracer was released and 3-hour average concentrations were measured at 168 sampling stations for up to 96 hours after the start of release. Details on the observation data are given in *Nodop et al.* [1998].

ETEX-1 had two phases: a real time phase where participants had to respond with forecast wind fields, as if in a real accident, and a model evaluation study (ATMES II) where participants ran their model with analysed (diagnostic) meteorology, while having access to the measured concentration data. Results for the real time response can be found in *Graziani et al.* [1998], and a report on the model evaluation study in *Mosca et al.* [1998a]. *Warner et al.* [2004] later applied user-oriented measures of effectiveness (MOE) to the model results of the atmospheric transport model evaluation study ATMES II. According to Tables 2 and 3 of that study, the CMC simulations (models 105 and 202) using the Eulerian dispersion Canadian emergency response model (CANERM) in operation at the time, [*Pudykiewicz*, 1989; *D'Amours*, 1998] performed fairly well.

MLDP0, MLDP1 and MLDPmm simulations of the release were done using meteorological fields based on a sequence of short term forecasts (3 and 6 hours) from the CMC NWP model, which was executed at 15 km grid-spacing over a European domain specially for ETEX. These meteorological fields were produced for a study by *D'Amours* [1998]. The dispersion simulations were executed up to October 27 12:00 UTC, a duration of 92 hours from the start of the release.

Table 4.2 shows three verification scores for a concentration threshold of 0.01 ng m^{-3}[3] based on *Warner et al.* [2004] user oriented objective measures of effectiveness. Calculation details are given in Paper appendix 4.11.3 . The objective scoring functions (OSF), the figure of merit in space (FMS), and the fractional bias (FB), are calculated. The OSF is a measure of the distance between the perfect overlap, and the actual results. The FMS gives the ratio of the overlapping stations having concentrations above a threshold of interest, over the union of the stations where either the modelling or the observations show concentrations above that threshold. OSF $= 0$ and FMS $= 1$ are the target scores.

[3]The lowest non-zero concentration available in the observation data set

A FB $= 0$ means that the modelled and observed plume have about the same "size", and a negative FB indicates a tendency of the modelling to overestimate the extent of the plume.

In Table 4.2, MLDP0 refers to the zeroth order configuration of the transport model described in the first part of the paper. MLDP1 corresponds to the first order configuration. MLDPmm corresponds to a mixed mode configuration where the particles trajectories were calculated according to the first order Langevin equation mode for the first hour after their release, and afterwards, in zeroth order mode, using a diffusion coefficient calculated as $\sigma_w^2 T_L$. For MLDP1 and MLDPmm, the variance of the turbulent wind components, σ_u^2, σ_v^2 and σ_w^2 were estimated by splitting the turbulent kinetic energy TKE provided by the NWP model simulations, as described in 4.6.2.1.

According to the MOE scores in Table 4.2, the Eulerian model based on CMC meteorological analyses showed better results than when executed with ECMWF meteorological data. The score of the zeroth order Lagrangian MLDP0 is intermediate between models 202 and 105. The first order Lagrangian MLDP1, shows better results than the CANERM and MLDP0. However it is intriguing to note that the mixed mode Lagrangian MLDPmm shows the best results. The reasons for this have not been identified.

Figure 4.5 shows a scatter diagram of MLDPmm concentrations versus observed concentrations. A tendency to overestimate *in plume* concentrations, also noted in CANERM in ATMES II, is still present. Figure 4.6 shows the evolution of the surface plume produced by the MLDPmm simulations with a plot of the corresponding observed station concentrations. Since the minimum detected concentrations was 0.01 ng m^{-3}, only values above 0.05 ng m^{-3} are shown. The general evolution of the plume is well depicted, including the deformation and stretching taking place starting October 25 00:00 UTC. The model appears to underestimate the extreme tail end of the plume as it travels along the North Sea coastline, over the Netherlands and over Denmark, while somewhat overestimating the portion traveling over Central Europe. This can be seen also in some of the time series of the observed and modelled surface concentrations shown in Figure 4.7 (a) and Figure 4.7 (b). The timing of the passage of the plume is very well depicted, even at the extreme edges over Norway and Romania.

4.7.4 Global scale dispersion: arrival of the Fukusihma plume on the North American coast of the Northwestern Pacific.

The accidental release of radioactive substances from the Fukushima Daiichi Nuclear Power Plant, following the tsunami of March 11 2011, provides unique opportunities to test and validate dispersion models against observation data [*Draxler et al.*, 2015; *Draxler and Rolph*, 2012; *CHINO et al.*, 2011; *Terada et al.*, 2012]. A low level radioactive xenon (^{133}Xe) plume was detected with a high temporal resolution in Sidney, British Columbia (BC), in Canada. Radioactive caesium (^{137}Cs) was also observed but with much lower activity concentrations. Figure 4.8 shows a time series of the ^{133}Xe and ^{137}Cs activity concentrations observed in Sidney. ^{133}Xe was also measured with an airborne detector, at a high spatial resolution, along the west coast of Vancouver Island [*Sinclair et al.*, 2011]. The plume was also observed in Richland, at the Pacific Northwest National Lab (PNNL), in Washington State (Ian Hoffman, Health Canada, personal comm. 2011).

The amounts and timeline of the radioactive releases from Fukushima during the first days after the tsunami hit are still under investigation, however several studies on the subject are available (e.g. *Stohl et al.* [2012]; *CHINO et al.* [2011]; *Katata et al.* [2012]). To investigate the effects of the uncertainties in the radioactive emissions, a series of ^{133}Xe dispersion simulations, based on releases of one unit per hour over 6 hours, were conducted for a few days starting March 12 00:00 UTC. The resulting air concentrations from such unit releases can be seen as a measure of the relative amount of air originating from the source location, taking into account the effect of radioactive decay. This is often known as the source-receptor sensitivity factor (SRS) [*Wotawa et al.*, 2003], or source-receptor matrix (SRM) [*Seibert and Frank*, 2004], and also as the transfer coefficient matrix (TCM) [*Draxler and Rolph*, 2012].

According to news reports, the tsunami struck the power plant at 06:30 UTC on March 11 [*Stohl et al.*, 2012; *TEPCO*, 2012], and radioactive releases could have started some 15 hours later. Figure 4.9 shows the Sidney SRS time series resulting from a sequence of 6-hour unit emissions, starting March 12 00:00 UTC. Interestingly all SRS time series show rather similar patterns, although with different intensities. The Sidney location shows much reduced sensitivity to possible emission from Fukushima occurring after March 13, bottom panel of Figure 4.9 . These SRSs were combined and scaled into ^{133}Xe activity

concentration as follows. Let $\mathbb{S}_i$ represent a given combination of SRSs for observation i, and $\overline{\mathbb{S}}$ the average of all $\mathbb{S}_i$, then:

$$\tilde{c}_i = \mathbb{S}_i \frac{\overline{c_{obs}}}{\overline{\mathbb{S}}}\,, \tag{4.41}$$

where $\tilde{c}_i$ is the modelled or scaled concentration for observation i and $\overline{c_{obs}}$ the average observed concentrations. There is an implicit source term resulting from the scaling and it will be discussed further below.

In the top panel of Figure 4.10, one can see $\tilde{c}$ resulting from the simple summation of all scaled SRS time series (Scaled SRS sum), the green line. In general the model results give more sharp features than were observed. The time of the plume arrival, on March 19, some 7 days after the beginning of the release, is very well captured. There is double peak in the first period of elevated activity, which was not observed, but the timing of the sharp decline at the end of the high activity period is also well captured. The modelling shows a second relatively intense peak, where a plateau of clearly above background activity is seen. The observed timing of the return to background levels coincides quite well with the end of the second peak in the modelling. The application of *Stohl et al.* [2012] source term, mapped into 6-hour average emission rates (dark red line Figure 4.11), yields lower concentrations than were observed by about an order of magnitude. The bottom panel of Figure 4.10 shows in more detail the model response to *Stohl et al.* [2012] source term; the response pattern is very similar to that of a uniform release. This indicates that at long range the modelling results are more sensitive to the transport process than to the details of the release. Since *Stohl et al.* [2012] emission estimations are very credible, this suggests that MLDPmm underestimates concentrations in Sidney. Possible reasons for this are discussed further down.

SRS time series for Richland, WA, (PNNL), scaled into ^{133}Xe activity concentration $\tilde{c}$, in the same manner as for Sidney, are shown in Figure 4.12, along with observations. The patterns of model results for PNNL are very similar to those for Sidney. The *Stohl et al.* [2012] source term was also applied to the modelled SRS (dark red line). The resulting concentrations are much closer to the observations than for the case of Sidney, and, interestingly, the observed concentrations are lower than those seen in Sidney.

In Figure 4.13, the ^{133}Xe activity concentration measured by *Sinclair et al.* [2011] along the west coast of Vancouver Island, on March 20, between 18:00 UTC and 19: 00 UTC (black line with error bars), can be compared with the scaled model SRS's (red line) for the same observation points at the same time. The SRS's from the 6-hour emission runs were combined in the same manner as for Sidney, and were also scaled into activity concentrations. At a first glance, there does not appear to be much correlation between the modelling and the observations; indeed the linear correlation coefficient is 0.13. However, an inspection of the lagged cross-correlation (not shown) shows a maximum of about 0.8 at a lag of about 50 km. The dashed green line in Figure 4.13 displays the model results shifted southeastward by about 50 km. The correspondence with the observations is now very good, indicating that the model is depicting a real feature, but with a slight displacement error.

Figure 4.14 illustrates a possible explanation: after being released from Fukushima, the ^{133}Xe plume becomes stretched into relatively thin filaments around a developing low pressure system moving across the Pacific Ocean. These filaments seem to keep their identity, because of reduced mixing when traveling over the cold Pacific waters, and apparently it is their passage that results in the sharp features observed on Vancouver Island and in Richland.

Table 4.3 shows the different *implied* ^{133}Xe source terms in the scaling used for Figures 4.10, 4.12 and 4.13, as well as the *Stohl et al.* [2012] source term, for the period of March 12 00:00 UTC to March 15 12:00 UTC. The agreement between the estimate for PNNL and *Stohl et al.* [2012] is quite good, but there is an order of magnitude difference with those for Vancouver Island.

Figure 4.14 shows that the particle plume has become fairly mixed over Richland, after moving inland. There is not so much mixing near Vancouver Island, so a possible explanation would be that, while the model is able to simulate the sharp features associated with the filamenting, the model filaments are still not dense enough near the BC coast resulting in an underestimation of the in plume concentration. In other words, the model tends to dilute the dense filaments a bit too soon before they hit the coastal regions.

Figure 4.15 shows results of a simulation from MLDP0 for ^{137}Cs using the *Terada et al.* [2012] source term shown in Figure 4.11. There is a fair amount of similarity between the modelled ^{137}Cs time series and that of ^{133}Xe. There is a double peak associated with the first activity period, between March 19 and March 22. There is also a second peak, between March 23 and March 27, which correlates well with the observed second period of elevated activity. Interestingly, aside from a small spike around March 12 12:00 UTC, the strongest emissions occur between March 14 12:00 UTC and March 15 12:00 UTC. Even though the SRS shown in Figure 4.9 are for ^{133}Xe, they are an indication that the second ^{137}Cs plume seen in Sidney on March 24-25, was the result of the elevated emissions on March 14-15, whereas the first plume observed on March 19-20, would have resulted from the much smaller emissions on March 12. One could wonder why MLDP0 results are in fairly good agreement with ^{137}Cs observations in Sidney when MLDPmm underestimates ^{133}Xe at the same location. Results of ^{133}Xe simulations with MLDP0 (not shown) do not underestimate the concentrations in Sidney as much as MLDPmm does, however those in PNLL are overestimated. The reasons for this were not investigated in depth, but appear to be related to the "lid" condition at the top of the boundary layer imposed to MLDP0 (subsection 4.6.6).

4.7.5 Inverse modelling with ETEX

Results from inverse modelling can be validated only indirectly. A good measure would be the usefulness of the simulations in estimating the characteristics of a possible source of emission of tracer, given a set of concentration measurements. *Yee et al.* [2008] have used results of MLDP0, executed in inverse mode for the ETEX-1 case, in an illustration of the Bayesian method for source reconstruction, which demonstrated the model capabilities. The observation data set of ETEX-1 is extensive as was seen earlier in section 4.7.3, but *Yee et al.* [2008] used a much smaller subset for their study, 35 measurements taken at 10 sampling sites.

Figure 4.16 (a) shows what has been described as fields of regard (FOR) for two ETEX observing sites which have measured well above background tracer concentrations. Figure 4.16 (b) shows FORs from two stations which were measuring zero concentrations. Here

a FOR is the time average surface SRS field generated by a unit release from the observation site, at the time when the measurement was made. A FOR delineates the region which is "sensed" by the sampler, regardless of the time at which that sensing would have occurred at any given point in the region. Assuming that the measurements are due to a release from the same source, then the source should be in the region which is sensed by both samplers, i.e. where the FORs overlap, as illustrated by Figure 4.16 (a). When observations are scarce, a zero concentration observation can be very useful as well. In that case, the possible source should not be in any part of the areas covered by the FORs resulting from those observations (Figure 4.16 (b)). Consideration of both types of FORs helps to narrow the bounds on the possible location domain of the source. In Figure 4.16 (c), the overlap of CR03 and DK05 FORs is obtained by taking the geometrical mean of the two fields. This area is then reduced by excluding regions where FORs from A04 or N02 are above the 10^{-18} threshold, and this is where the ETEX source is found. It should be noted that the intensity of the average SRS field within the limited area is by no means a measure of the source location probability. If no other information was available, it could only be concluded that the source is most likely to be found anywhere within that area.

The case of Austrian station A04 is quite interesting since it never observed any of the released tracer. Nevertheless, according to Figure 4.6, the tracer plume appears to have moved around the station (indicated by the $\times$ symbol in dark red) for several hours during its complex stretching motion. The capacity of the models to reproduce zero concentrations can be quite important but was not assessed in the ATMES phase of ETEX [*Mosca et al.*, 1998b].

4.8 Conclusion

The Lagrangian transport and dispersion models in operation at the Canadian Meteorological Centre have been presented. These models are used for several types of Environmental Emergency responses, covering spatial scales from the very local, a few kilometers, to the Global scales. The theoretical bases of the models were discussed, and the main algorithms used in their implementation described. The performance of the models was evaluated with data from real cases of atmospheric spills of pollutants, confirming their usefulness. The dispersion models are being continuously validated and improved. Among

other things, there are plans to improve the particle release modules for a better simulation explosive releases and heavy gas emissions. Work towards the implementation of a 3D Lagrangian scheme, coupled with complex urban flow fields is also taking place. Investigations for operational implementation of a source reconstruction algorithm are proceeding. The construction of a validation database using the low level Xenon emissions from the medical isotope production facility in Chalk River and measurements from Health Canada monitoring network is expected to start soon.

4.9 Acknowledgments

The authors would like to thank Sohan Chouchan and Atomic Energy of Canada Limited for making available the Gentilly Tracer Experiment Data. Laurel Sinclair, of Geological Survey of Canada is gratefully acknowledged for providing the BC west coast aerial radioxenon concentration measurements. Ian Hofman and Kurt Ungar of the Radiation Protection Bureau, Health Canada, kindly provided the Sidney and PNNL ^{133}Xe and ^{137}Cs concentration data. Graphs were produced using the free software "Veuz" (http://home.gna.org/veusz/). Charts were produce using the CMC software SPI. Finally the authors would like to thank the anonymous reviewers for their useful and pertinent comments.

4.10 Tables

Table 4.1: *Some conditions during the SF_6 releases.*

Rel. #	Duration (s)	Rel. rate (m^3 s^{-1})	Mean M-O Length (m)	Inversion height (m)
1	3600	1.67 10^{-4}	203	700
2	3180	5.34 10^{-4}	448	700
3	3600	2.94 10^{-4}	-943	700
4	3600	2.95 10^{-4}	-460	900

Table 4.2: *User-oriented measures of effectiveness for three configurations of MLDP applied for the ETEX first release.*

Model	Objective score function OSF	Figure of merit in space FMS	Fractional bias FB
MLDP0	0.436	0.530	-0.17
MLDP1	0.407	0.554	-0.13
MLDPmm	0.388	0.570	-0.06
202[1]	0.419	0.545	–
105[2]	0.451	0.514	–

Results obtained by CANERM for ATMES II are also shown.

[1] CANERM executed with CMC global meteorological analyses. Results from taken from *Warner et al.* [2004], Table 2.

[2] CANERM executed with ECMWF meteorological analyses. Also taken from *Warner et al.* [2004], Table 2.

Table 4.3: *^{133}Xe activity mean release rate for the period March 12 00:00 UTC to March 15 12:00 UTC.*

Type	Release rate (Bq h^{-1})
Sidney Scaled SRS sum	2.4 10^{18}
VR Island tracks	2.0 10^{18}
PNLL Scaled SRS	4.0 10^{17}
Stohl et al. [2012]	1.7 10^{17}

4.11 Paper appendices

4.11.1 Paper appendix: Concentration calculations

LSMs yield particle trajectories. A 3-D concentration field, $c(\mathbf{r},t)$, is obtained by estimating the conditional probability distribution of the particles in time and space:

$$c(\mathbf{r},t) = \int_{-\infty}^{t} \int_{V} S(\mathbf{r}_0,t_0) p(\mathbf{r},t|\mathbf{r}_0,t_0) \mathrm{d}\mathbf{r}_0 \mathrm{d}t_0 \tag{4.42}$$

where $S(\mathbf{r}_0,t_0)$ is the source function, V is the 3-D domain where the source is defined, and $p(\mathbf{r},t|\mathbf{r}_0,t_0)$ the conditional probability that a particle is found at point $(\mathbf{r},t)$, given that it was at point $(\mathbf{r}_0,t_0)$ [*Sawford*, 1985]. In practice, particles are emitted at specific points in time and space, within the source volume, in a discrete fashion. For a single particle, the source function can be seen as a Dirac delta function, centered on the point where the particle is released. The particle concentration then becomes the conditional probability density function itself:

$$S(\mathbf{r}_0,t_0) = \delta(\mathbf{r}_0 - \mathbf{r}_p, t_0 - t_p) \tag{4.43}$$

$$\begin{aligned} c(\mathbf{r},t) &= \int_{-\infty}^{t} \int_{V} \delta(\mathbf{r}_0 - \mathbf{r}_p, t_0 - t_p) p(\mathbf{r},t|\mathbf{r}_0,t_0) \mathrm{d}\mathbf{r}_0 \mathrm{d}t_0 \\ &= p(\mathbf{r},t|\mathbf{r}_p,t_p)\,. \end{aligned} \tag{4.44}$$

If N particles are emitted with a "mass" m_p, from a set of points $(\mathbf{r}_p,t_p)$, then the resulting particle mass concentration is :

$$c(\mathbf{r},t) = \sum_{p=1}^{N} m_p(\mathbf{r},t) p(\mathbf{r},t|\mathbf{r}_p,t_p) \tag{4.45}$$

Here the tracer "mass" m_p is a qualifier, a tag, characterizing the fluid element to which it is associated. If one assumes that the number of particles used in a simulation is large enough so that their distribution in space at a given time is an adequate representation of the conditional probability distribution, then an estimation of this distribution can be obtained by counting the number of particles in each of the cells of a 3-D array covering the domain of interest. The concentration at point $\mathbf{r}$ is simply:

$$c(\mathbf{r},t) = \frac{1}{\delta V_s} \sum_{p \in \delta V_s} m_p(\mathbf{r},t) \tag{4.46}$$

where δV_s is the volume of the cell centered at $\mathbf{r}$.

Other methods have been proposed essentially based on equation (4.42). Indeed the validity of this equation is not restricted to source-receptor relationships, but can also form the basis to estimate the probability of a particle being at position $(\mathbf{r}, t)$ given that one is found at position $(\mathbf{r}_p, t_p)$. The problem is in the estimation of the functional form $p(\mathbf{r}, t|\mathbf{r}_p, t_p)$. Those functions are generally referred to as density kernels. Various formulations have been proposed [*de Haan*, 1999] and those all have a certain degree of arbitrariness.

4.11.2 Paper appendix: Evaluation of the Monin-Obukhov length-scale L

Following equation 13 of *Delage* [1997]:

$$\frac{z}{L} = \frac{\phi_m^2}{\phi_H} Ri, \tag{4.47}$$

where ϕ_m and ϕ_H are the well known universal functions for momentum and heat fluxes. These are normally written in terms of z/L, where z is the height above ground and L, the Monin-Obukhov length-scale, an important scaling parameter for the surface layer. *Delage* [1997] reformulates the functions in terms of the Richardson number, a formulation used in CMC's GEM model [*Mailhot et al.*, 1998].

For the unstable case, $Ri_{sl} < 0$:

$$\phi_m^2 = \frac{\phi_H}{\beta} = (1 + 40 Ri_{sl})^{-1/3}, \tag{4.48}$$

and for $Ri_{sl} > 0$:

$$\phi_m = \frac{\phi_H}{\beta} = (1 + 12 Ri_{sl}), \tag{4.49}$$

where $\beta = 0.85$, and Ri_{sl} is the gradient Richardson evaluated at height z_{sl} within the surface layer.

The surface layer is usually assumed to be about 10% of the boundary layer. The vertical profiles of wind and temperature above the G2 meteorological tower were not available for our own evaluation of the BL depth; however, it was estimated around 700 m for trials 1 to 3, and around 900 m for trial 4 by AECL scientists. We assumed that the tower data

would be representative of the surface layer.

The Monin-Obukhov stability parameter $1/L$ can be evaluated as follows:

$$\frac{1}{L} = \frac{Ri_{sl}}{z_{sl}\beta} \qquad Ri_{sl} < 0 \tag{4.50}$$

$$\frac{1}{L} = \frac{Ri_{sl}}{z_{sl}}\frac{\phi_H}{\beta^2} = \frac{Ri_{sl}}{z_{sl}\beta}(1 + 12Ri_{sl}) \qquad Ri_{sl} > 0\,. \tag{4.51}$$

For our purpose Ri_{sl} was approximated by calculating differences between the 10 m and 47 m levels assuming they were representative of the gradient at the 37m level.

$$Ri_{sl} \approx \frac{g}{\theta}\frac{\Delta\theta\Delta z}{|\Delta\mathbf{U}|^2}\,. \tag{4.52}$$

The potential temperature θ was approximated by $T + \gamma z$, γ being the dry adiabatic lapse rate, and T is expressed in Kelvin. Since in principle there is no wind direction change, in the vertical in the surface layer, and in fact there was not much observed, $|\Delta\mathbf{U}|^2$ was simply approximated by the square of the wind velocity differences between z_{10m} and z_{47m}

4.11.3 Paper appendix: MOE scores

Adopting *Warner et al.* [2004] convention,

$$x = \frac{N_{ov}}{N_{obs}} \qquad \text{and} \qquad y = \frac{N_{ov}}{N_{mod}}\,, \tag{4.53}$$

where N_{ov} is the overlap, i.e. the number of stations where both the modelling and observations show concentrations above a given threshold, N_{obs} is the total number of stations where concentrations above the threshold are observed and N_{mod} is the total number of stations where the modelling yields concentrations above the threshold. The objective scoring function (OSF) is calculated as:

$$\text{OSF} = \sqrt{(1-x)^2 + (1-y)^2}\,. \tag{4.54}$$

The figure of merit in space (FMS) is calculated as follows:

$$\text{FMS} = \frac{xy}{x + y - xy}. \tag{4.55}$$

In this framework, the fractional bias (FB) is given by:

$$\text{FB} = \frac{2(x-y)}{x+y}\,. \tag{4.56}$$

4.12 Figures

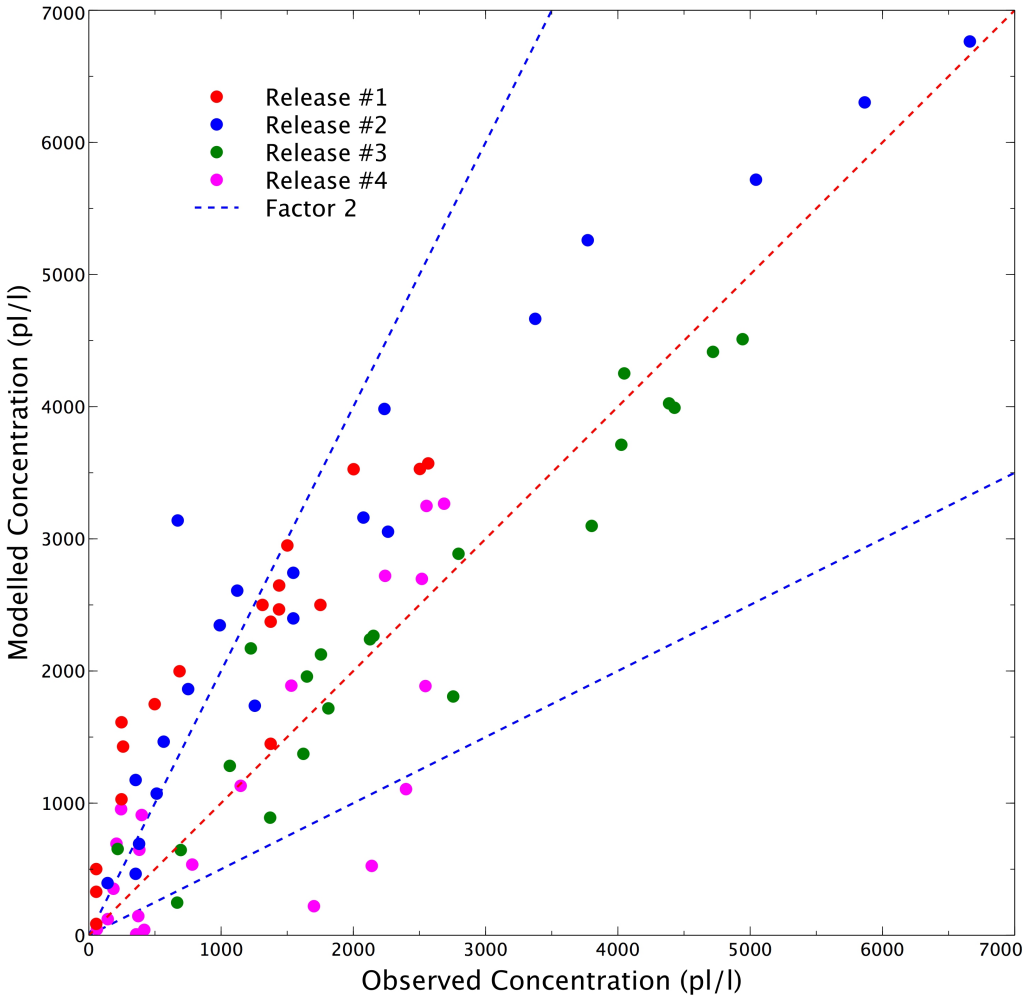

Figure 4.1: Global scatter diagram: MLCD modelled vs observed volume mixing ratios (picolitre/litre).
There is a total of 81 data points. The Pearson linear correlation coefficient is 0.88.

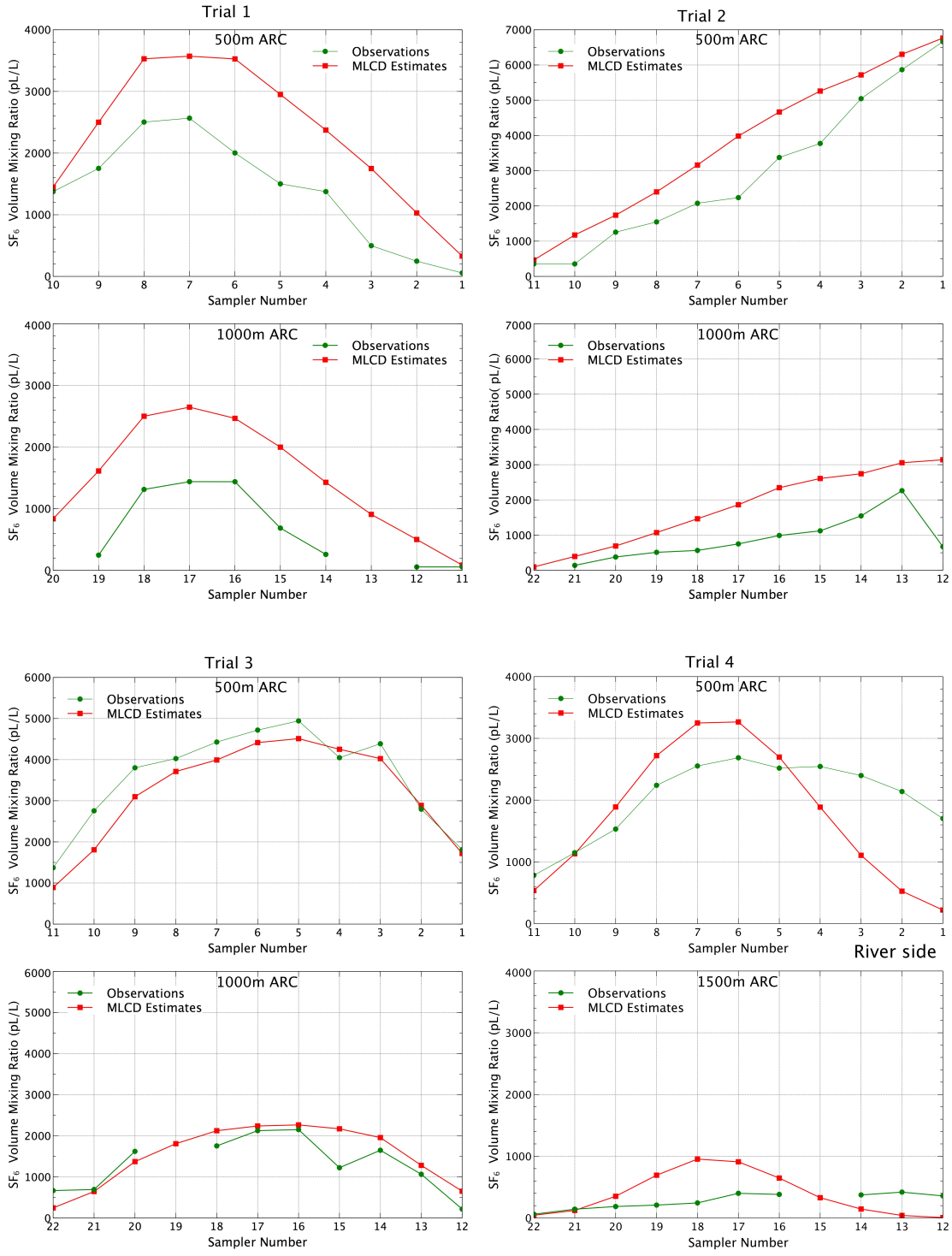

Figure 4.2: Average observed and MLCD modelled concentrations for each release and arc.

The sampler numbers increase from right to left in order to reflect their approximate East to West disposition, the plumes going generally from North to South. In trial #4 the wind was more or less along the St-Lawrence River.

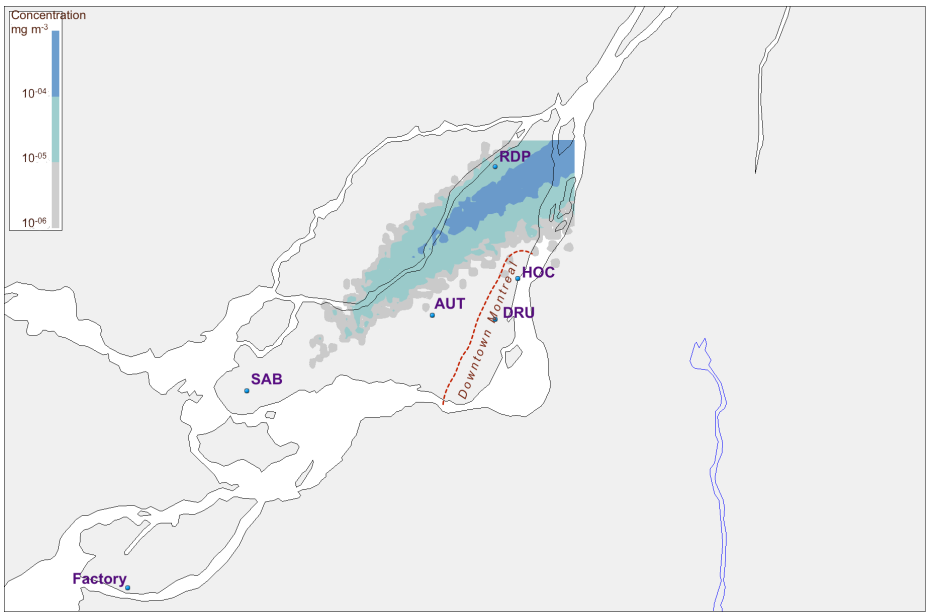

(a) MLCD simulation

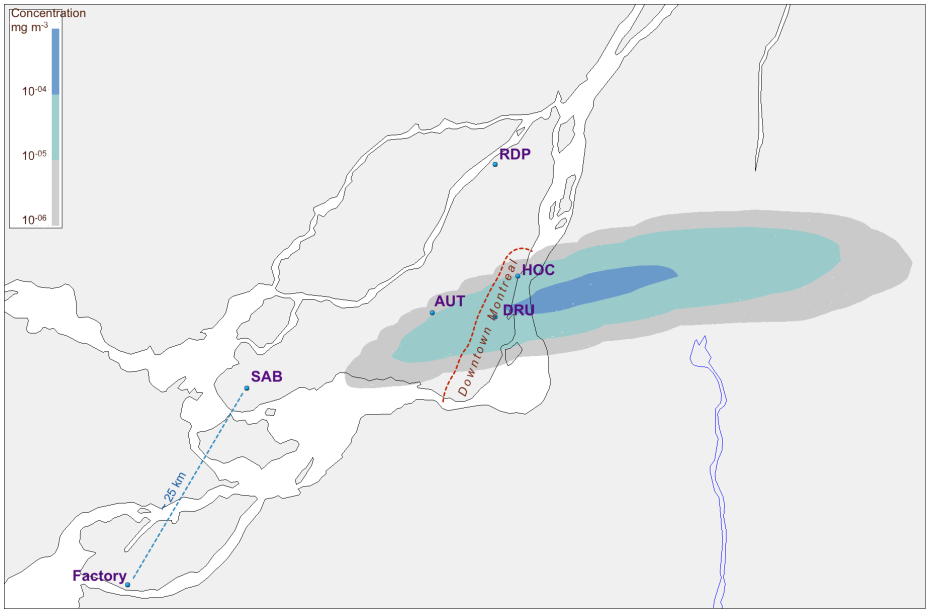

(b) MLDPmm simulation

Figure 4.3: Modelled surface concentrations at 00:30 EDT (04:30 UTC) August 10 2004, 2.5 hours after the start of the release.
Concentrations are in mg m^{-3}. The point labelled Factory shows the location of the SO_3 release. The other points show the location of the City of Montréal air quality monitoring stations. Only the downtown stations DRU and HOC reported significantly above background $PM_{2.5}$ concentrations. The distance between Factory and SAB is ~25 km, and between DRU and HOC just about 5 km. The MLCD modelling domain is smaller than the map shown.

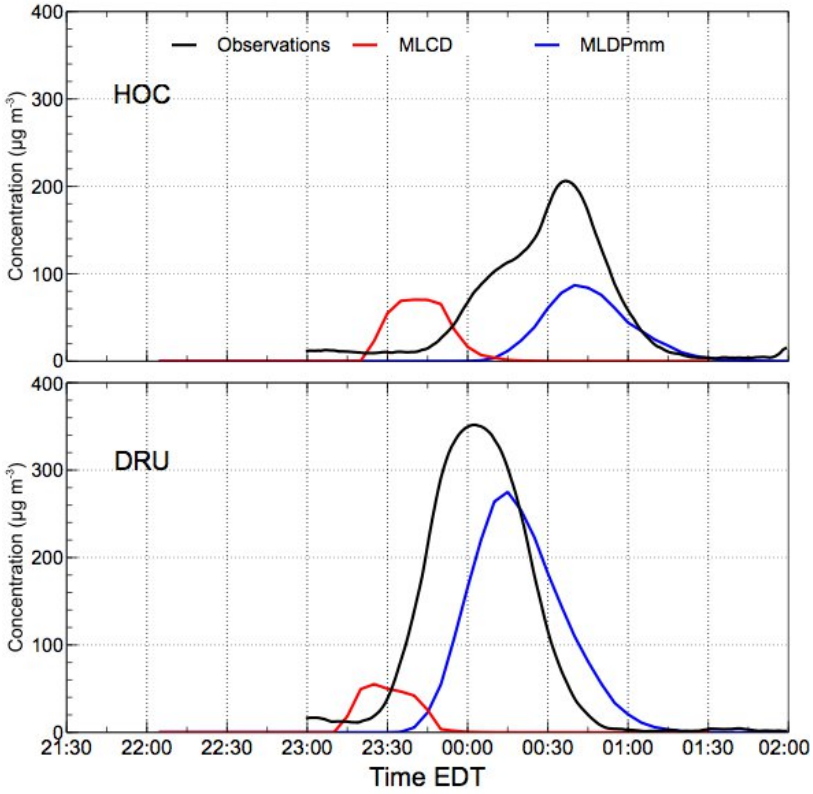

Figure 4.4: Time series (01:30-06:00 UTC, August 10) of modelled SO_3 and observed $PM_{2.5}$ concentrations at the two stations reporting above background levels.

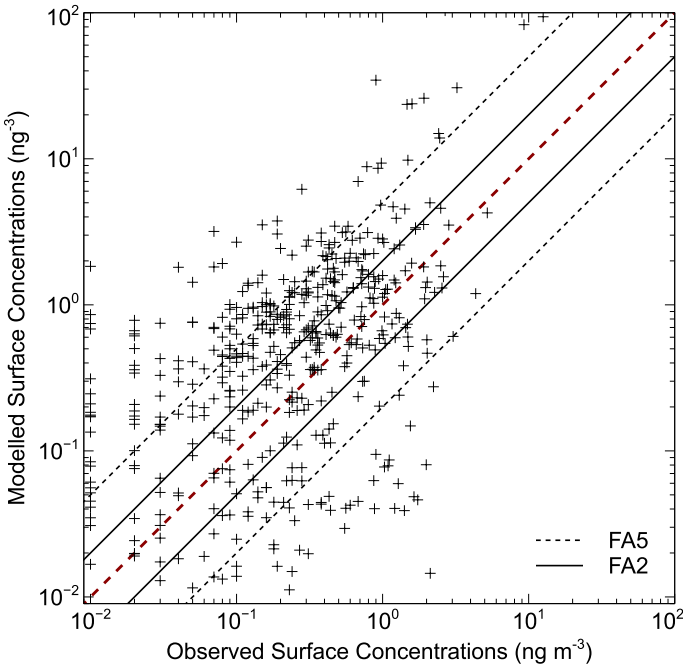

Figure 4.5: ETEX Global scatter diagram: MLDPmm vs Observed concentrations. FA2 and FA5 lines give the limits of the regions where concentrations are within a factor of 2 and a factor of 5 of each other.

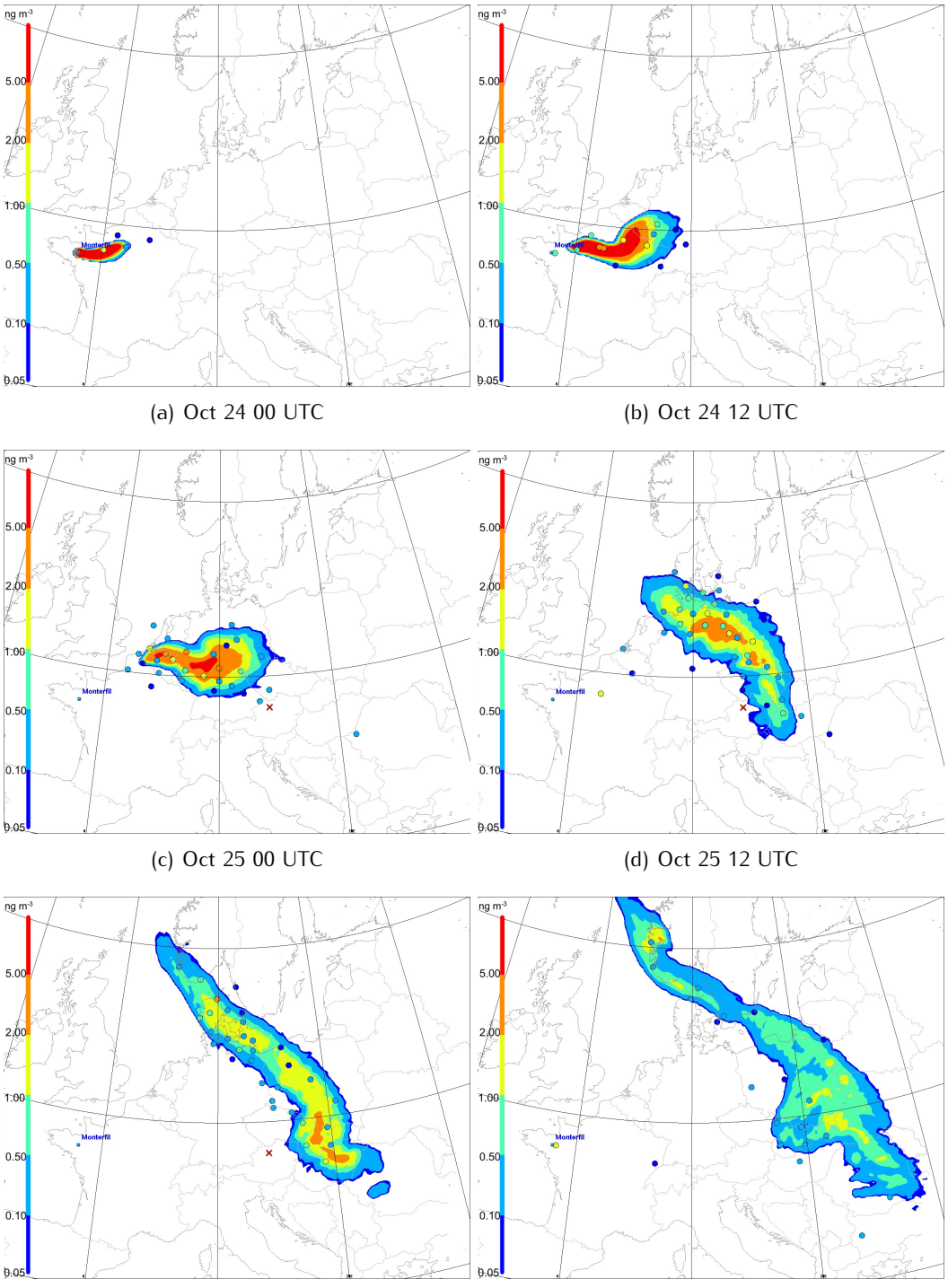

(a) Oct 24 00 UTC

(b) Oct 24 12 UTC

(c) Oct 25 00 UTC

(d) Oct 25 12 UTC

(e) Oct 26 00 UTC

(f) Oct 26 12 UTC

Figure 4.6: MLDPmm 3-hour average surface concentrations for 6 different times. Corresponding 3-hour average observed concentrations are also plotted as colored dots, using the same color pattern. The × symbol, in dark red, on panels (c), (d) and (e) shows the approximate position of Austrian station A04 where only zero tracer concentrations were observed during the experiment.

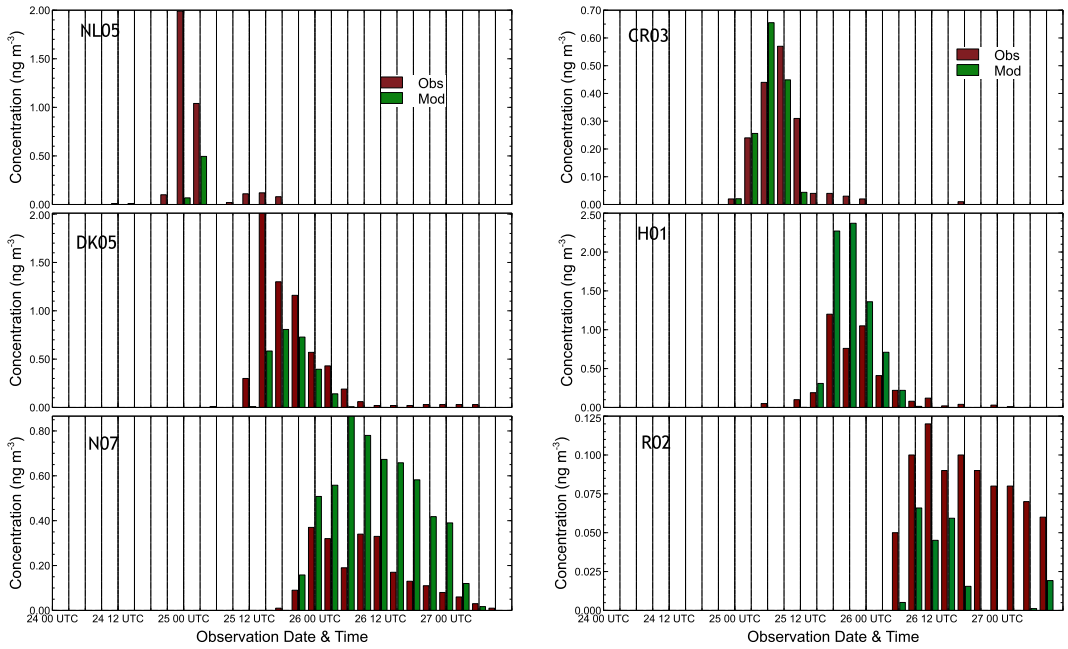

(a) North Sea coast

(b) Central and Eastern Europe

Figure 4.7: Time series of measured and modelled surface concentration at three stations near the North Sea coast line
which experienced the passage of the ETEX plume tail end: NL05, (Vlissingen, The Netherlands), DK05 (Hvide Sande, Denmark) and N07 (Stavanger, Norway); and at three stations over Central and Eastern Europe: CR03 (Praha, Czech Republic), H01 (Budapest, Hungary) and R02 (Bucuresti, Romania). *Note the different scales on the vertical axes.*

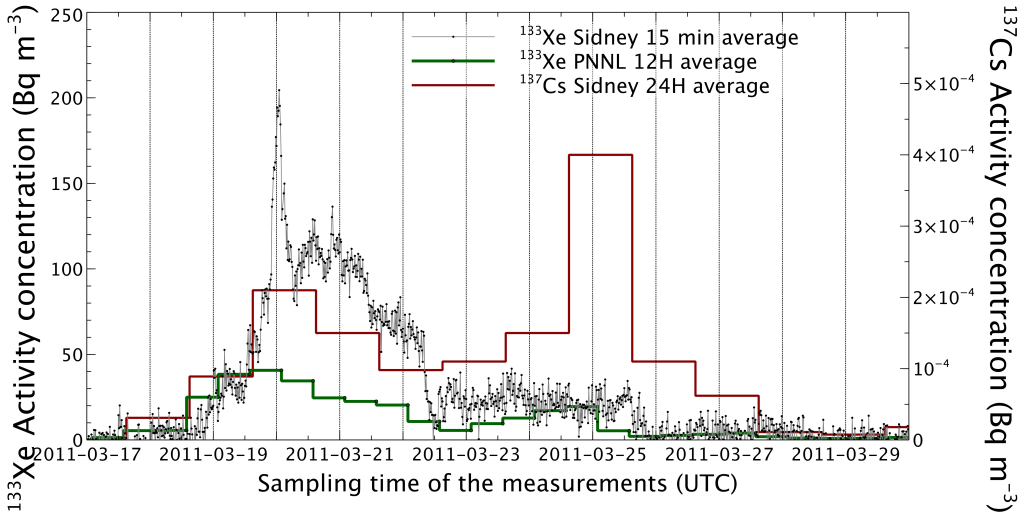

Figure 4.8: Time series of ^{133}Xe and ^{137}Cs activity concentrations observed in Sidney, on Vancouver Island, and ^{133}Xe observed at PNNL, Washington State.

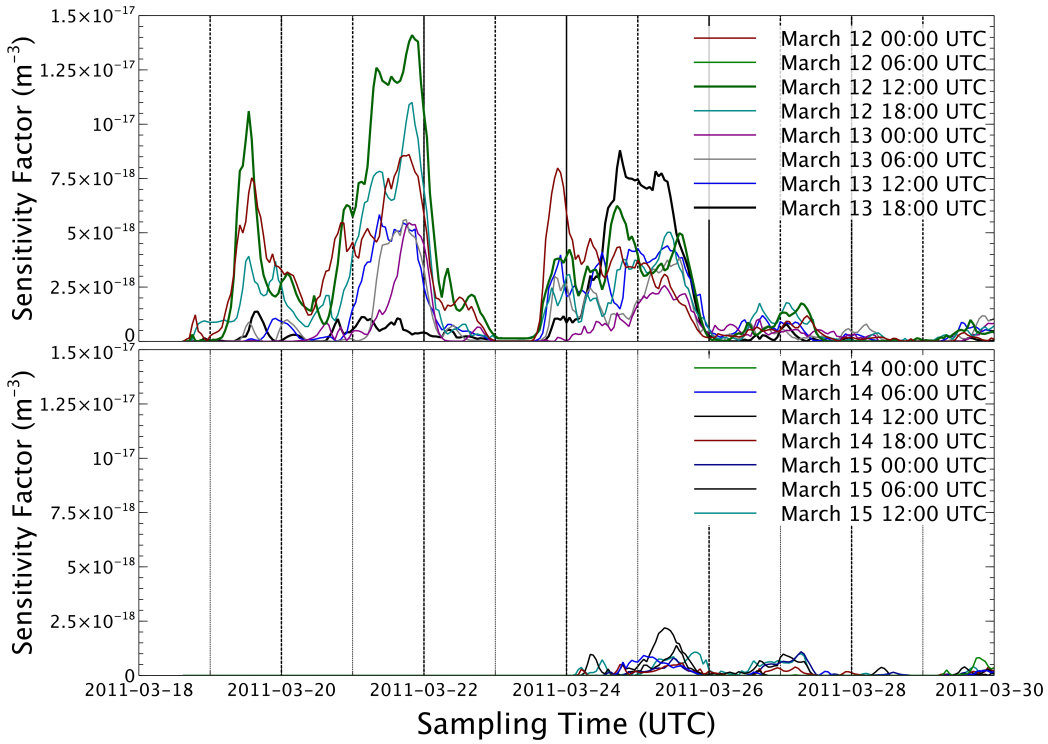

Figure 4.9: SRS time series for Sidney on Vancouver Island to 6-hour ^{133}Xe emissions (one unit) from Fukushima.
Top panel: March 12 00:00 UTC to March 13 18:00 UTC, bottom panel: March 14 00:00 UTC to March 15 12:00 UTC. The location of Sidney can be seen in Figure 4.14.

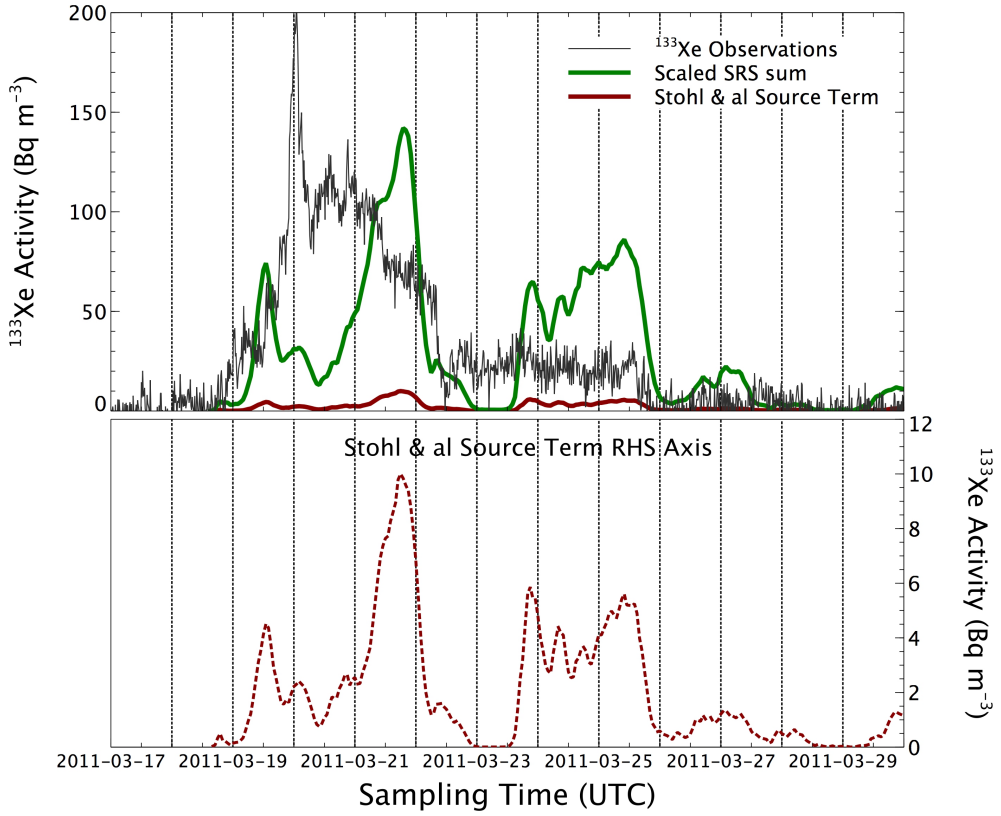

Figure 4.10: Time series of modelled and observed ^{133}Xe for Sidney on Vancouver island. The scaled SRS sum implies a constant emission rate from March 12 00UTC to March 14 00UTC (see Table 4.3). The lower panel reproduces the concentrations obtained using Stohl & al. source term, with a different axis, on the right hand side, in order to show the details of the time series more clearly.

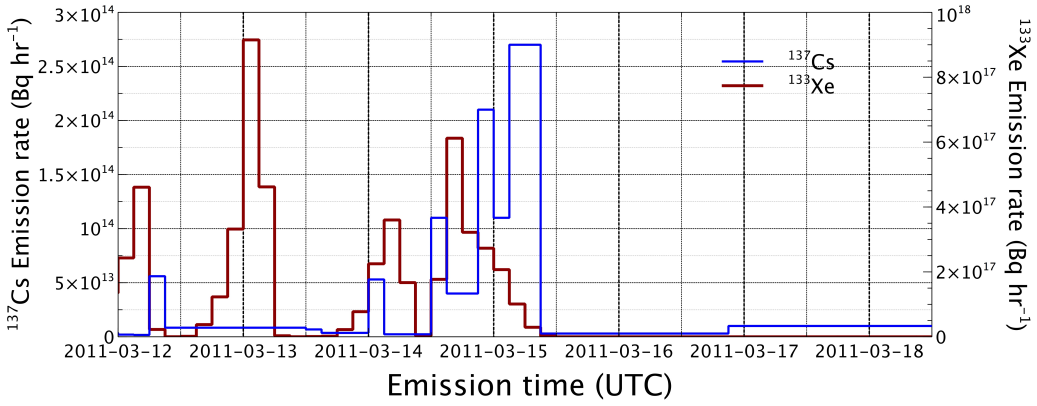

Figure 4.11: ^{137}Caesium and ^{133}Xenon emission rates used for the MLDP simulations. These rates are based on *Terada et al.* [2012] and *Stohl et al.* [2012].

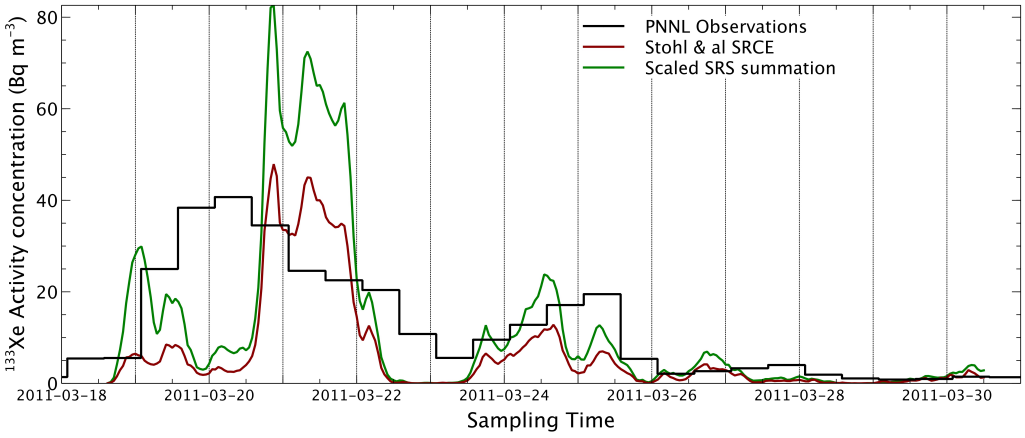

Figure 4.12: Time series modelled vs observed ^{133}Xe activity concentration, Richland, WA, shown as PNNL in Figure 4.14.

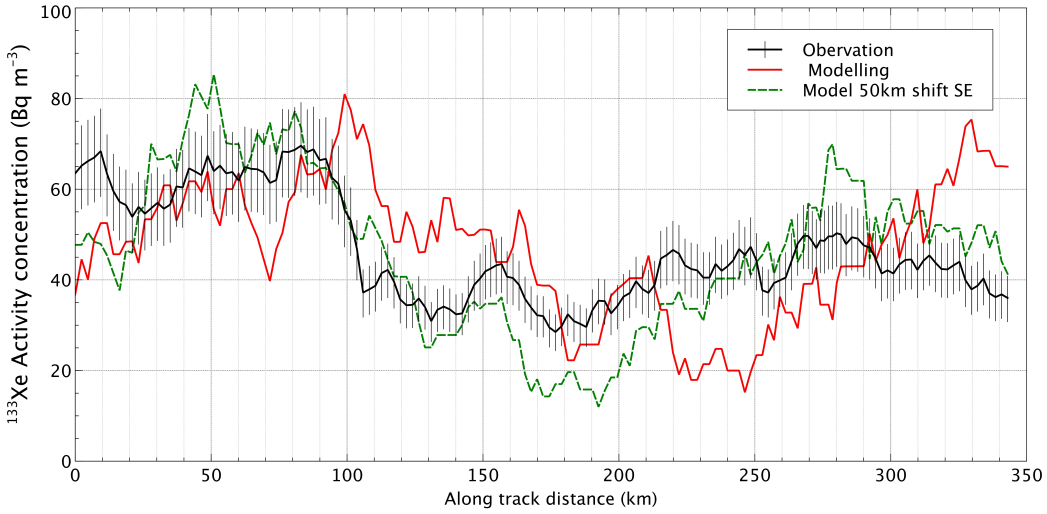

Figure 4.13: Modelled (see text) and observed ^{133}Xe activity concentration along a track on the west coast of Vancouver Island.
The track location can seen on the map in Figure 4.14.

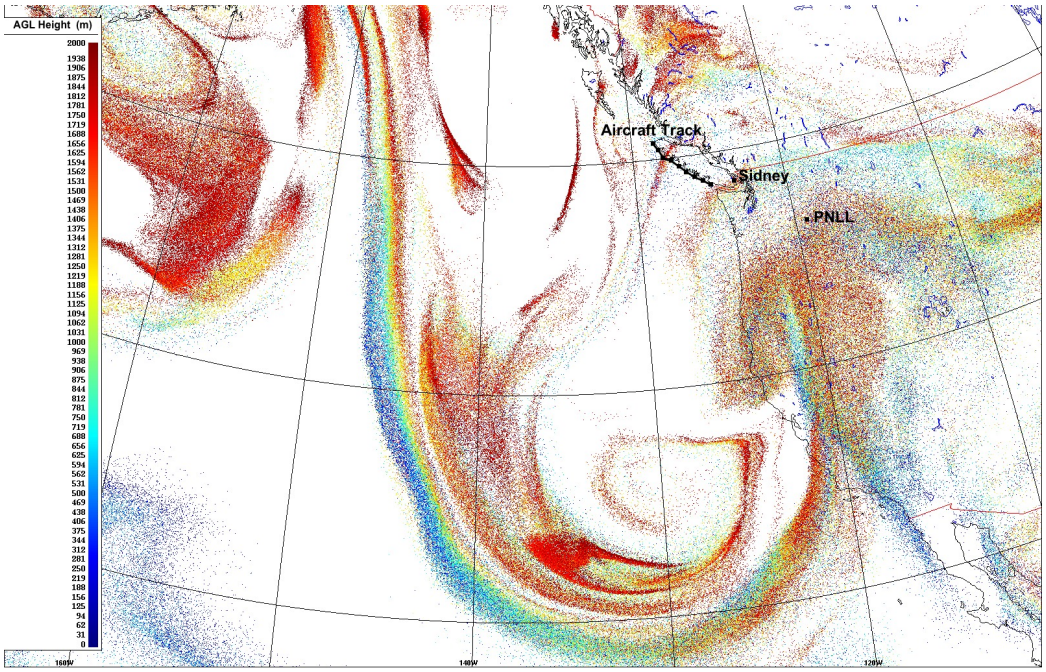

Figure 4.14: Position of model particles March 20 18:00 UTC resulting from a continuous emission from Fukushima, from March 12 00:00 UTC to March 13 00:00 UTC.
Only particles in the lower 2000 m layer are shown. The aircraft tracked from SE to NW over a distance of about 350 km.

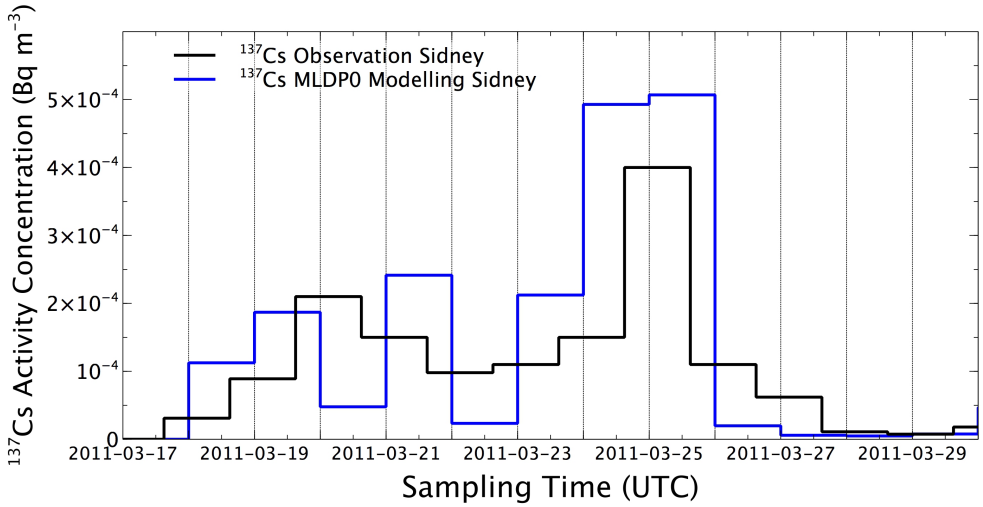

Figure 4.15: Time series of modelled and observed ^{137}Cs for Sidney on Vancouver island. The emission rates used are those of *Terada et al.* [2012] shown in Figure 4.11

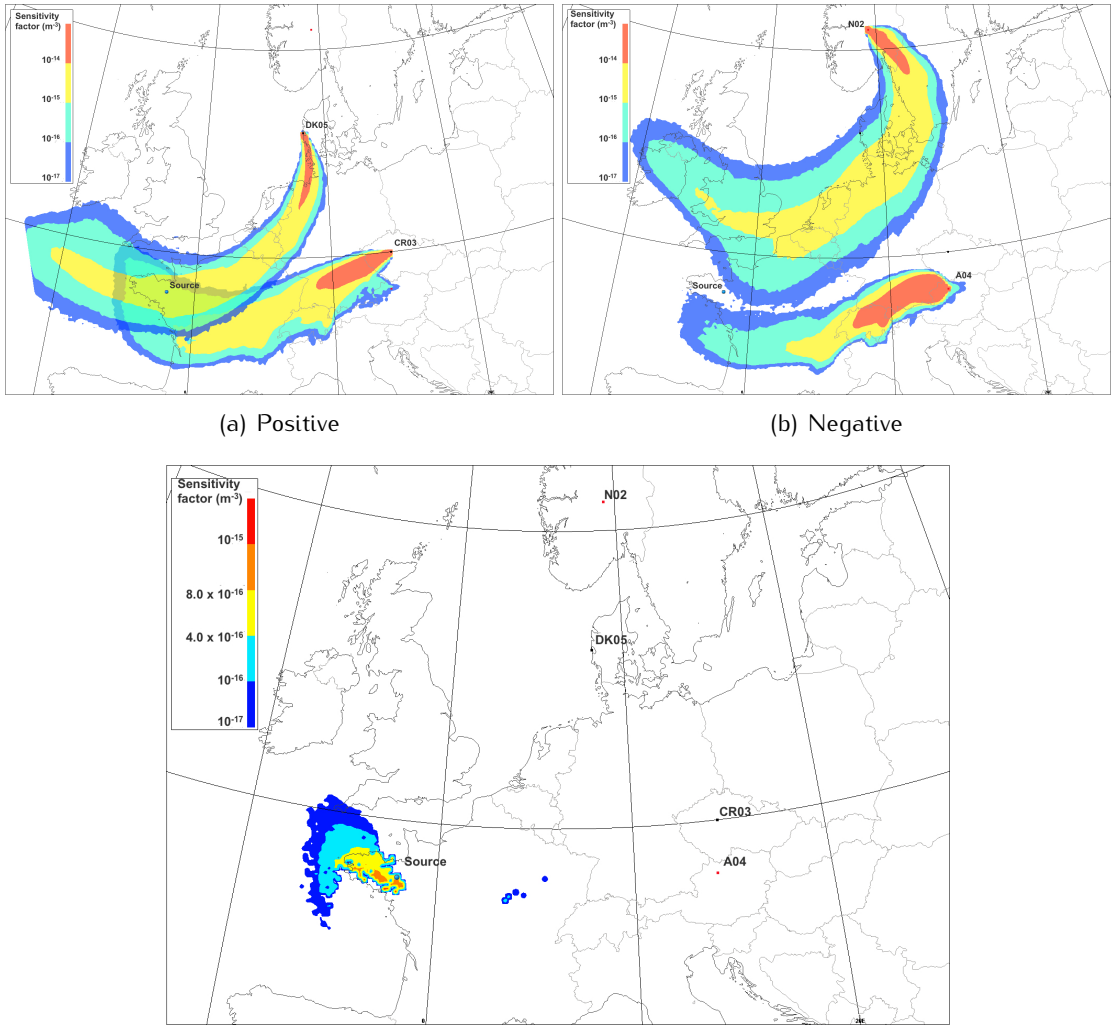

(a) Positive

(b) Negative

(c) Intersection

Figure 4.16: Fields of Regard (FOR) for two stations (a) which have seen clearly above above background tracer concentrations and (b) which were not measuring any tracer at a given time. (c) shows the average FOR in the region where the two plumes shown in Figure (a) overlap, excluding any area where the plumes of Figure (b) are seen. The observation time for CR03 is October 25 06H UTC and for DK05, October 25 18:00 UTC. For A04 the observation time is October 25 06:00 UTC, and for N02, October 26 18:00 UTC. All inverse simulations end October 23 15:00 UTC.

CHAPTER 5

"Application of the atmospheric Lagrangian particle dispersion model MLDP0 to the 2008 eruptions of Okmok and Kasatochi volcanoes" (published in J. Geophysical Research)

5.1 Preamble

In this chapter, transport taking place in the lower stratosphere (5 – 10 km above the tropopause) is investigated. The study consists in a paper written and published in the first years of my doctoral studies. The paper presents results of Lagrangian dispersion simulations in "zeroth" order mode. The stochastic equation used for those simulations is also called the random displacement equation (RDE). For the vertical component:

$$dz = \left[\frac{\partial K_z}{\partial z} + W\right] dt + \sqrt{2K_z}\, d\xi\,, \tag{5.1}$$

where K_z is a diffusion coefficient, W the synoptic scale vertical velocity, and $d\xi$ a random number of zero mean and $\sqrt{dt}$ variance. The details of the implementation of the RDE, its advantages and limitations, are discussed in sections 4.5.2 and 4.6.3 of the paper in Chapter 4.

The study mostly considers the transport of sulfate aerosols injected into the atmosphere by the Alaskan volcanoes Okmok and Kasatochi during the eruptions of the summer 2008. Diffusive processes are believed to be relatively small in the stratosphere so the vertical

eddy diffusion coefficient is kept constant at a minimum value (.01 m^2 s^{-1}). Since vertical motion is generally negligible, dispersion is mostly the result of horizontal shearing, stretching and deformation in the wind field, and of the initial spread of the eruptive column.

Quantitative measurements of SO_2 air concentrations, both from satellite and surface based instruments, together with forward and inverse modelling are used to estimate the amounts injected at various levels of the atmosphere. The results illustrate the usefulness of the model in assessing horizontal transport and dispersion in the lower 5 – 10 kilometres of the stratosphere. However no mechanisms by which vertical mixing would occur were evidenced by the modelling or appeared to be at work.

5.2 Publication details

5.2.1 Journal

JOURNAL OF GEOPHYSICAL RESEARCH, VOL. 115, D00L11
doi:10.1029/2009JD013602, 2010

5.2.2 Authors

Réal D'Amours, Alain Malo, René Servranckx, Dov Bensimon, Serge Trudel, and Jean-Philippe Gauthier-Bilodeau

5.3 Introduction

The atmospheric transport and dispersion model MLDP0 (Modèle Lagrangien de Dispersion de Particules d'ordre zéro) has been in use at the Canadian Meteorological Centre (CMC) for several years for Environmental Emergency Response. The model is also employed to simulate the release of volcanic ash to support the operations of the Montreal Volcanic Ash Advisory Centre (VAAC). During the eruptions of the Okmok and Kasatochi volcanoes in the summer of 2008, MLDP0 was used extensively and provided useful information to both scientific and aviation communities.

This paper briefly describes MLDP0, and simulations of plumes generated by the eruptions of Okmok in July 2008 and Kasatochi in August 2008 are presented and discussed. We

show examples from the real-time simulations, executed when limited information about the eruption was available. We then examine results from a quantitative analysis of SO_2 transport based on forward and inverse modeling, together with data available from AURA/OMI satellite remote sensing, as well as some ground-based observations (Washington State University, Pullman, WA, USA and Environment Canada, Toronto, CA).

5.4 A Brief Description of MLDP0

5.4.1 MLDP0 is a Lagrangian Model

In the context of Lagrangian modeling, dispersion in the atmosphere is estimated by calculating the trajectories of a very large number of individual air particles (or fluid elements), in order to adequately represent the dispersing plume. These particles are assumed to conserve their identity during their travel, and can transport some amount of material which, depending on its nature, may be subject to various physical processes like dry deposition, wet scavenging and radioactive decay.

For efficiency reasons, specially when considering transport on a regional or larger scale, a dispersion model is usually an off-line model which uses meteorological fields provided by a NWP system. MLDP0 is driven by the CMC's Global Environmental Multi-scale (GEM) NWP system (http://www.msc-smc.ec.gc.ca/cmc/op_systems/index_e.html). The meteorological fields (3-D winds, air temperature, relative humidity, to name a few) are available only at certain time intervals, and only at a limited number of discrete points in space (3D grids). Furthermore, dispersion models will very often be used "after the fact", to estimate the behavior the plumes in diagnostic mode. In these cases, dispersion simulations will be based on analyzed meteorological fields, which are generally available at six-hour time intervals. Therefore, many scales of motion are not resolved. This is especially true of the turbulent components of the wind which are mostly responsible for the "mixing" of air parcels. The information provided by the NWP systems can be used to estimate at least some of the statistical properties of atmospheric turbulence. Vigorous turbulent mixing occurs mostly in the atmospheric boundary layer (ABL) near the ground surface, and dispersion models focus on that part of the atmosphere. Details can be found in R. D'Amours and A. Malo (A Zeroth Order Lagrangian Dispersion Model MLDP0, Internal Report, Canadian Meteorological Centre, 2004).

There is no general parameterization for turbulence in the free troposphere (FT), which locally can be generated by gravity waves or deep convection. Very often substances injected above the ABL travel in fairly well maintained streams for several days [*Colette et al.*, 2008], [*Gerasopoulos et al.*, 2006]. In MLDP0, the vertical diffusion coefficient falls to a very low threshold value above the boundary layer, and essentially dispersion results from stretching and deformation induced by the horizontal winds, as well as vertical transport associated with fronts and large scale pressure systems.

An inverse version of MLDP0 has been developed and is used to support the operations of the Comprehensive Nuclear-Test-Ban Treaty (CTBT) Organization [*WMO*, 2007] (Appendix I-6, Regional and global arrangements for atmospheric backtracking and Appendix II-9, Products provided by RSMCs with activity specialization in atmospheric transport modeling – backtracking for CTBT verification support). The results of inverse simulations are often referred as Source Receptor Sensitivity (SRS) coefficients [*Wotawa et al.*, 2003]. Simply put, the SRS coefficients (usually in units of m^{-3}) are a measure of the amount of air transported from a given region of the atmosphere (a possible source location) into the sampler where the concentrations are measured.

5.4.2 Operational Applications of MLDP0

MLDP0 is designed for medium and long-range dispersion and has been in use for several years at CMC to support various types of activities associated to national and international mandates. CMC holds the following international designations: (1) VAAC Montreal through the International Civil Aviation Organization (ICAO) and (2) Regional Specialized Meteorological Centre (RSMC) Montreal through the World Meteorological Organization (WMO) and International Atomic Energy Agency (IAEA) [*WMO*, 2007]. The model is used by VAAC Montreal and RSMC Montreal operational staff to predict and track volcanic ash/gas as well as radioactive material released by nuclear accidents. The model is an important element in CMC's contribution to Canada's Federal Nuclear Emergency Plan (FNEP). MLDP0 is also regularly used in various environmental emergencies such as smoke from forest fires, dust storms, toxic spills in the atmosphere and chemical fires.

As reported by R. D'Amours and A. Malo (A Zeroth Order Lagrangian Dispersion Model MLDP0, Internal Report, Canadian Meteorological Centre, 2004) the model was validated with data from ETEX [*van Dop. H. et al.*, 1998] and data from the accidental radioactive

release in Algeciras, Spain, in May of 1998. The model is used regularly to track plumes of radio-xenon observed in the Ottawa Valley; some results are discussed in *Stocki et al.* [2008]. In support of Nuclear-Test-Ban Treaty verification, MLDP0 was used in the context of a global backward ensemble dispersion modeling study [*Becker et al.*, 2007]. More recently, two independent studies were conducted using MLDP0 to test source parameters for volcanic ash [*Webley et al.*, 2009] and to investigate meteorological influences on particle fallout sedimentation [*Durant and Rose*, 2009] for the August and September 1992 eruptions of Mount Spurr, Alaska.

5.4.3 Volcanic Ash Modeling

Volcanic eruptions can behave in many ways [*Sparks et al.*, 1997]. Often, the height of an eruption column is a good indicator of the intensity of the ash emission. For a maintained eruption, *Sparks et al.* [1997] have determined an empirical power law for the plume height in terms of the rate of discharge of erupted material. *Mastin et al.* [2009] obtained a result which is not significantly different from the best-fit equation of *Sparks et al.* [1997]. Because the initial plume height, the time of the eruption, and perhaps a duration estimate, are the few parameters that could be reported in real time, *Sparks et al.* [1997] formula is very useful for an initial evaluation of the ash emission. However, most of the mass ejected in the atmosphere is deposited very close to the volcano. Less than 10% of the total released mass is transported at distances greater than 10 km [*Sparks et al.*, 1997], and only this fraction is of interest to long-range transport.

Gravitational settling can be an important factor, especially in the early stages of the plume dispersion. In MLDP0 the settling velocity is simply modeled in terms of a terminal velocity according to Stokes' relationship for a spherical particle. Ash particle size distribution varies greatly depending on the eruption. Empirical distributions based on eruptions of the Redoubt volcano, as reported in *USGS* [1990], and in *Durant and Rose* [2009] for eruptions of Crater Peak (Mount Spurr), as well as improved eruption parameters based *Mastin et al.* [2009] study can be used in MLDP0. In most cases however, dispersion modeling is used to assess the transport of very fine ash at long distances from the volcano (for aviation interests as an example); in those cases only particles with small diameters are considered. Considering the large uncertainties in the emission parameters, in a real time response, 10% of the emission rate provided by *Sparks et al.* [1997] is normally used as

source term for fine ash, for which gravitational settling is not considered.

5.5 Modeling the Eruptions of the Summer 2008

The Okmok and Kasatochi volcanoes in the Aleutians were very active during the summer 2008 and several eruptions affected or threatened the Canadian airspace. VAAC Montreal issued several volcanic ash advisory messages and charts on the probable evolution of the ash plumes. Dispersion models were used to provide estimates of plumes motion and intensities, based on incomplete source term information. A fair amount of satellite data on the plumes, including SO_2 concentrations, became available during and after the eruptions. The satellite images were compared qualitatively with the dispersion model outputs. A few examples are shown and discussed briefly as part of this study. Also total air column SO_2 concentrations are used for quantitative assessments of the model performance and of the capabilities for the estimation of the emission characteristics through inverse modeling. The focus is on the early phases of the eruption episodes, which lasted several weeks in total.

5.6 The Okmok Eruption of July 2008

5.6.1 Initial Operational Modeling

Okmok's eruptive episode started with an explosive event occurring suddenly 12 July 19:43 UTC, as reported by the Alaska Volcano Observatory (AVO). An ash column rose rapidly to 15 km, well above the tropopause, which is estimated to have been around 11.8 km over the volcano at that time. The initial explosive event lasted several hours; peak seismicity was reached at about 22:00 UTC, 12 July, then declined gradually afterwards. The eruption continued for over five weeks at lower intensities. Early AURA/OMI imagery showed the volcanic plume moving slowly southeastward. Large amounts of SO_2 were injected into the upper atmosphere.

The first operational simulations of the dispersion model MLDP0 were executed on 14 July, with a release scenario based on the initial reported plume height, and using the emission rate derived with the best-fit equation of *Sparks et al.* [1997] to estimate the total amount of ash released in the atmosphere. A continuous constant rate of emission with a duration of

six hours was assumed; this appeared reasonable, in the absence of any other information. Meteorological fields were provided by the CMC GEM Regional NWP system. These simulations indicated that the ash cloud would likely affect Canadian airspace. During the next ten days, VAAC Montreal continued to track the cloud over Canada and US, in close coordination with VAAC Anchorage and VAAC Washington, using satellite data as well as updated analyzed and forecast meteorological fields for the dispersion modeling. Visual comparisons between the resulting modeled ash plume and the SO_2 concentration fields reconstructed from the AURA/OMI instrument show a fairly good correlation. Figure 5.1 is an example of guidance provided in real time to aviation meteorologists, and shows a model estimation of the "fine ash" concentration at high levels, five days after the start of the eruption, on 18 July 00:00 UTC. 10% of the estimated total ash release is considered as fine ash for which gravitational settling is neglected. Figure 5.2 shows the total column concentration of SO_2, constructed from the AURA/OMI scans on 17 July. The time match of the two images is not exact since the model plume represents a one-hour average for the period ending 18 July, 00:00 UTC, and the satellite field is a juxtaposition of the scans from successive orbits. However, the scans over the plume sectors were done just before 18 July, 00:00 UTC, so the time correspondence is adequate. The main morphologic features of the plume are well reproduced by the model, even the hook shape over the Pacific. According to the model, this results from a folding of the plume: the leading edge of the plume initially moved southwestward, then curved cyclonically eastward catching up with the trailing edge.

5.6.2 Modeling SO_2 Transport

5.6.2.1 Estimation of the Emission

The measurements of total column SO_2 concentration, resulting from the passage of the Okmok plume above the Multi-Function Differential Optical Absorption Spectroscopy (MF-DOAS) instrument at Washington State University (WSU, Pullman, WA), provided time series over three days, giving an opportunity for quantitative estimates. Of course these observations give no information on the vertical distribution of the SO_2. In order to estimate the vertical distribution of the observed SO_2, an exploratory dispersion simulation was done. The emission was uniformly distributed over a column 15 km high, since at this stage, one cannot make any hypothesis as to which part of the eruption column affected

the WSU site. The same amount and duration as the initial runs are used. Also, because the plume was traveling near the edge of the domain of the earlier model simulations, which were based on Regional NWP data, in order to avoid possible boundary effects, a hemispheric grid was used, with meteorological data from the CMC GEM Global NWP system, at a horizontal resolution of approximately 33 km.

Concentrations were calculated for several one-km-thick layers, above the location of the MFDOAS instrument in WSU, and can be compared with the measurements in Figure 5.3. According to the model, the bulk of the observed total concentrations appears to be caused by SO_2 streams traveling in the lower stratosphere; the tropopause was estimated to be between 10 km and 12 km above ground during the period. The measurements from MFDOAS-WSU are available during daytime, 18-20 July. On 18 July, the modeling indicates material from Okmok at levels between 10 km and 14 km and on 19 July, only in the 12 km to 14 km layer. The observations show two peaks on 19 July; the model seems to reproduce only the later one. The model does not show anything on 20 July, however, it indicates the presence of material on 17 July, where there is no data.

This information was then used as a basis for MLDP0 inverse simulations to better characterize the SO_2 discharges from Okmok. It was assumed that the column concentrations over WSU resulted from evenly distributed SO_2 in the layer 12-15 km above ground. Inverse runs were done for observation sampling periods around the three peaks: 18 July 15:00-17:00 UTC (Obs. 1), 19 July 14:00-16:00 UTC (Obs. 2), and 19 July 19:00-20:00 UTC (Obs. 3). Figures 5.4a, 5.4b and 5.4c show the SRS values, for a period of a few hours after the beginning of the eruption for one-km-thick layers, starting from 12 km. Essentially, the MFDOAS-WSU location shows sensitivity in the layers 14-15 km and 15-16 km. Interestingly, at the time of Obs. 3, the MFDOAS-WSU location is more sensitive to Okmok at the beginning of the eruption, while at the time of the earlier Obs. 1, the location was seeing air which originated from Okmok several hours later; this correlates with the folding process described earlier. The layer of maximum sensitivity is between 14 km and 15 km, for Obs. 1, and between 15 km and 16 km for Obs. 3. There is also some sensitivity at these levels for Obs. 2, but it is an order of magnitude lower. This is consistent with the results of the exploratory forward simulation. However, there appears to be an inconsistency between the forward and inverse simulations for 18 July. The forward simulation, which is based on a 6-hour long emission, clearly shows material reaching over the MFDOAS-WSU site

on 18 July, during the observation period, while the inverse simulation does not show any significant sensitivity until 10 hours after the start of the eruption. This is likely because, for practical reasons, the configurations of the forward and inverse versions of MLDP0 are not exactly the same. Figure 5.5 shows SRS for the one-hour period before the observation, and there is indeed quite a bit of sensitivity in the first 6 hours. This illustrates that the smaller scale features resolved by the measurements must be interpreted with care when compared with larger scale model results.

An elaborate reconstruction of the emission profile as done by *Eckhardt et al.* [2008] is beyond the scope of the present study. However, a crude estimation is attempted. In Table 5.1, the peak concentration measured in the three periods considered is compared to the maximum SRS obtained for that period. The total column concentrations were converted to an average concentration per unit volume in the 3-km-thick layer. The simple arithmetic comparison yields a release of the order of 10^{11} g or 100 kilotons, not taking into account the first peak observed on 19 July, which is not properly captured in the model. This crude estimation is quite consistent with the value of 110 kilotons obtained by Simon Carn (personal communication, 2009). An initial value of 101.329 kilotons, obtained from the AURA/OMI data, was reported in Figure 5.6.

5.6.2.2 Validation in Forward Mode

A forward simulation was performed with an emission of 100 kilotons, at a constant rate during 16 hours from the start of the eruption. This revised duration is based on Figure 5.4, which indicates that the observed peak on 18 July was sensitive to the volcano between 10 to 16 hours after the start of the eruption, as well as on Figure 5.6, which seems to indicate that significant SO_2 emissions had ceased only a few hours before the satellite scan. The discharge was, somewhat arbitrarily, distributed between 12 km and 16 km as follows: 10% in the layer 12-13 km, 20% between 13-14 km, 40% in the layer 14-15 km, and 30% 15-16 km, using the fact that the measuring site was sensitive to those levels only. The resulting total column concentrations at the MFDOAS-WSU location can be compared with the observations in Figure 5.7. The simulated concentrations are quite in line with the measurements. As expected, the early peak of 19 July is not reproduced. There is less material showing up on 17 July, and during the early hours of 18 July, than in the simulation with the uniform column emission (Figure 5.3).

Figure 5.8 shows an early morning visible image from GOES West valid 18 July 12:45 UTC, over the Northwestern USA and Southern Canadian Prairies. Due to the low sun angle, the aerosol plume associated with the SO_2 cloud is easily detectable. The elongated and thin structures in the plume are quite remarkable and indicative that it was not subject to much mixing, even after more than five days of traveling time. Figure 5.9 shows the plume formed by the model particles at 13:00 UTC on 18 July, just 15 minutes later than the GOES image. The thin stream-like structure is also evident there. The general position of the main plume is in fairly good agreement with the visible plume. The model shows a double structure as in the satellite image, but with more separation. In the model, the northern portion results from a folding of the plume. While there is some evidence of such a process on the AURA/OMI imagery (Figure 5.2), it is not clear that the double band structure on the visible GOES image (Figure 5.8) is the result of that process; it would appear more likely that it is related to a fine scale feature in the southern branch, which is not (and not expected to be) well resolved by the model. It could also be conjectured that the sharp peaks in the observed time series result from denser streams passing overhead as the whole plume meanders eastward. As it was mentioned in section 5.6.2.1, these small scale features could have induced larger scale responses in the inverse modeling.

5.7 The Kasatochi Eruption of August 2008

5.7.1 Initial Operational Modeling

The Kasatochi volcano started to erupt on 7 August, around 20:00 UTC, with an explosion that produced an ash and gas plume reaching as high as 14 km. Two other explosions separated by a few hours followed on 8 August 01:50 UTC and 8 August 04:35 UTC. According to the AVO, the eruption lasted nearly 20 hours, with more or less continuous intense gas and ash discharges.

The plume was rapidly caught in a strong cyclonic circulation associated with a well-formed weather system that moved slowly southeastward over the Gulf of Alaska and Western Pacific as it was weakening. As a result, the plume was subjected to extensive stretching and deformation, but remained very easily detectable on satellite imagery. The persistent volcanic ash clouds caused considerable disruption to airline operations during several days and were closely monitored by the Anchorage, Washington and Montreal

VAACs.

To support Montreal VAAC operations, MLDP0 was executed using a source term based on the best-fit equation of *Sparks et al.* [1997], and an initial plume height of 14 km, with the duration estimated by AVO. The driving meteorological fields were provided by the GEM Regional NWP system. The simulations were quite useful in describing the evolution of the plume and in assessing its arrival over Canadian airspace (Figs. 5.10 and 5.11). As for the Okmok event, several runs were performed on a daily basis during nearly two weeks, utilizing updated analyzed and forecast meteorological data.

5.7.2 Estimating Volcanic Ash Dispersion

Figure 5.10 shows images derived from the Advanced Very High Resolution Radiometer (AVHRR) sensors on NOAA-16 and NOAA-17 satellites, which can be compared with MLDP0 total column ash concentrations estimates for nearly the same times. The AVHRR imagery is showing brightness temperature differences $(T_4 - T_5)$. The negative differences, emphasized on the images, indicate the likely presence of volcanic ash, as described by *Prata* [1989b, a]. This technique, also known as the split-window technique, or reverse-absorption technique, takes advantage of the opposite absorption characteristics of water vapor or water/ice clouds and volcanic ash clouds in the infrared channel 4 (10.3–11.3 μm) and channel 5 (11.5–12.5 μm). The satellite images in Figure 5.10 and Figure 5.11 were produced by John Bailey (AVO). Both the model and the imagery indicate that the plume became rapidly wound-up in the cyclonic flow, drifting southeastwards with the low-pressure system. The texture of the plume is patchier on the satellite images. According to the imagery (top left hand side image Figure 5.10), the volcano is still releasing significant amounts of ash 9 August 17:09 UTC, i.e. more than 19 hours after the start of eruption, supporting the 20-hour long emission scenario.

In Figure 5.11, the areas of ash estimated by the model are significantly larger than what appears to be detected with the $(T_4 - T_5)$ technique. In fact, the shape of the model ash plume is much more similar to that of the SO_2 plume, also seen in Figure 5.11. MLDP0 accurately simulates the arrival of material from the eruption on the West Coast. With the information available for this study, the specific reasons for the differences cannot be established. However, the general limitations and uncertainty factors of the split-window technique [*Tupper et al.*, 2004], and of the model simulations [*Servranckx and*

Chen, 2004], are known. Certainly the presence of ash in the plume on the coast should not be discounted.

5.7.3 Modeling SO_2 Transport

The AURA/OMI data show that large quantities of SO_2 dispersed eastward over North America in fairly complex patterns (e.g. Figure 5.12). The initial MLDP0 simulations had also shown complex dispersion patterns which compare well with the satellite imagery.

The total SO_2 mass estimations derived from the AURA/OMI data are much larger than those for Okmok, and reach over one thousand kilotons. Because of the good agreement obtained between emission estimates derived from inverse modeling in the case of Okmok, and those derived from AURA/OMI, a forward simulation for SO_2 dispersion was done using a release quantity of 1.3 megaton based on AURA/OMI data (see total mass estimation reported on top of Figure 5.12). The release was distributed mostly in the high levels, 50% between 10 km and 14 km, at a constant rate for 20 hours. For the same reasons as those discussed for the Okmok simulations, the meteorological fields used to drive MLDP0 were provided by the GEM Global NWP system (33 km horizontal resolution).

Total column mass concentrations were calculated and converted to Dobson units (DU). The model results for 12 August 21:00 UTC, five days after the eruption began, are shown in Figure 5.13. The patterns are very similar to AURA/OMI SO_2 composite observations (Figure 5.12). The maximum value shown by the model is 192, compared to 166 for AURA/OMI, and the locations are very close to each other as well. In general, however, the model shows concentrations a few DU higher than observed.

Multiple Brewer Spectrophotometer [*Fioletov et al.*, 1998] instruments at Environment Canada (EC) in Toronto, Canada, detected significant SO_2 total column concentrations during the daytime hours, 12-13 August and again on 16 August; values are below background 14-15 August. These data, presented in Figure 5.14. On 12 August, the measurements appear to be higher than what could be expected from a quick look at the maps reconstructed from the AURA/OMI orbits. The difference between the AURA/OMI and the ground-based estimates is interesting: it could be due, among other things, to the fact that the map is a reconstruction from discrete orbital scans taken at different times during

the day. These orbits do not overlap exactly in time and space, thus perhaps missing some features when the plume is changing rapidly.

The Brewer spectrophotometer measurements can be compared with time series extracted from the modeled plume over the same location in Figure 5.14. The model values are lower than the measured ones. The model does not pick up the peak of 12 August; however, the model map does show values of the order of those measured from the surface just a bit to the northeast of the observation site. The model also indicates SO_2 passing over the site 13 August, which is detected by the daytime observations, but at a higher level than the modeled one. The model also shows SO_2 traveling over Toronto, on 16 August, nearly 10 days after the start of the eruption, which is confirmed by the observations.

5.8 Conclusion

The large plumes generated by the eruptions of the summer 2008 at Okmok and Kasatochi, together with the abundance of high quality satellite imagery provided an exceptional opportunity to illustrate the usefulness of the model in assessing the motion and dispersion of volcanic plumes over medium and large scales.

Ground based observations of column SO_2 concentrations combined with those derived from AURA/OMI allowed for quantitative comparison of model results. These comparisons show that the model can produce realistic estimates of air concentrations at long range in forward mode and realistic estimates of emissions in inverse mode. The SO_2 dispersion patterns observed on the satellite imagery and the model results show that dilution in the upper troposphere and the stratosphere is mostly the result of deformation, shearing and stretching caused by the winds.

Table 5.1: *Maximum Source-Receptor Sensitivity (SRS) Coefficients for the WSU Measurements.*

The maximum value of the SRS coefficient is used together with the maximum observed total column concentration, during the sampling period used for the inverse simulation.

Sampling Period for SRS calculation UTC	Maximum SRS at Okmok (no units)	Layer of Maximum SRS (km)	Time of Maximum in Hours from Eruption start	Peak Observed Concentration (DU)	Estimated Total Emission (g)
18 Jul 15-17	5.4E-16	15-16km	13	8.7	1.6E+11
18 Jul 14-15	6.7E-16	14-15km	5	8.7	1.3E+11
19 Jul 13-14	2.6E-17	14-15km	0	7.4	2.8E+12
19 Jul 19-20	6.4E-16	15-16km	6	5.8	9.1E+10

5.9 Acknowledgments

We wish to thank Simon Carn (Michigan Technological University) and Fred Prata (Norwegian Institute for Air Research) for SO_2 data derived from AURA/OMI; Dave Schneider and John Bailey (Alaska Volcano Observatory) for processed satellite imagery of SO_2 and $(T_4 - T_5)$ images; George Mount and Elena Spinei (Washington State University) for total column SO_2 measurements and Vitali Fioletov and David Tarasick (Environment Canada) for the SO_2 observations derived from the Brewer spectrophotometers.

5.10 Figures

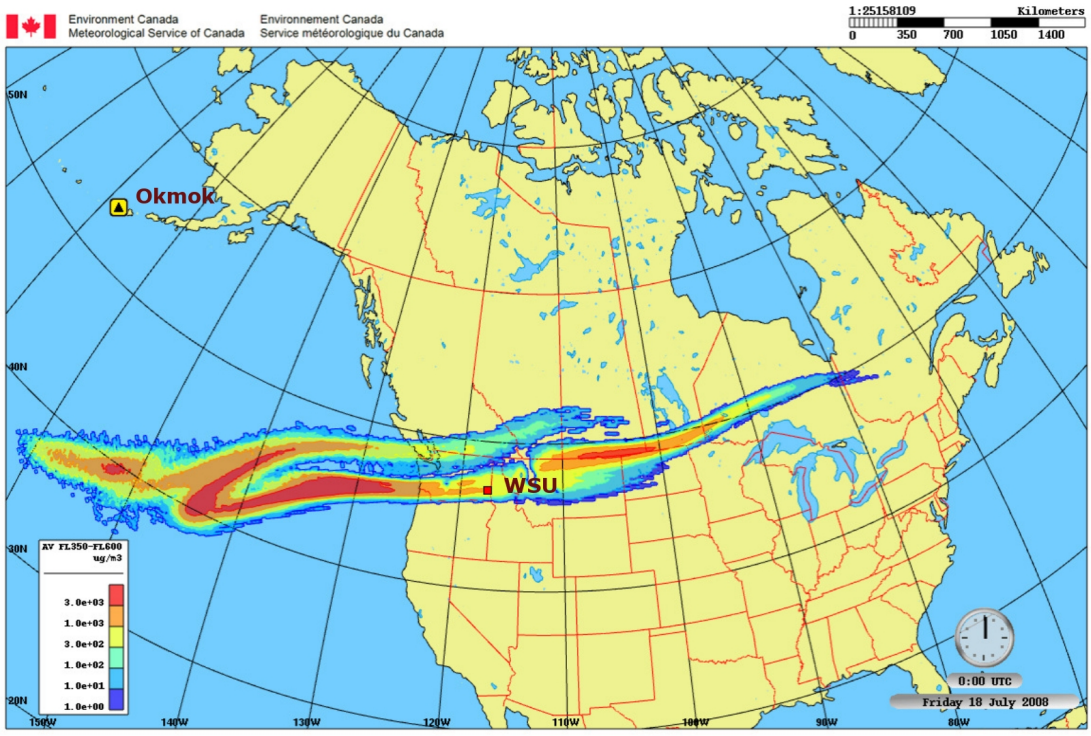

Figure 5.1: An example of real time product: MLDP0 estimation of the "fine ash" (see text) concentration.
Concentrations are in μg m^{-3}, within the layer FL350–FL600 (the layer between aviation flight levels 35-thousand feet and 60-thousand feet above sea level), valid 18 July 00:00UTC. The red square indicates the location of the Washington State University (WSU) MFDOAS spectrometer.

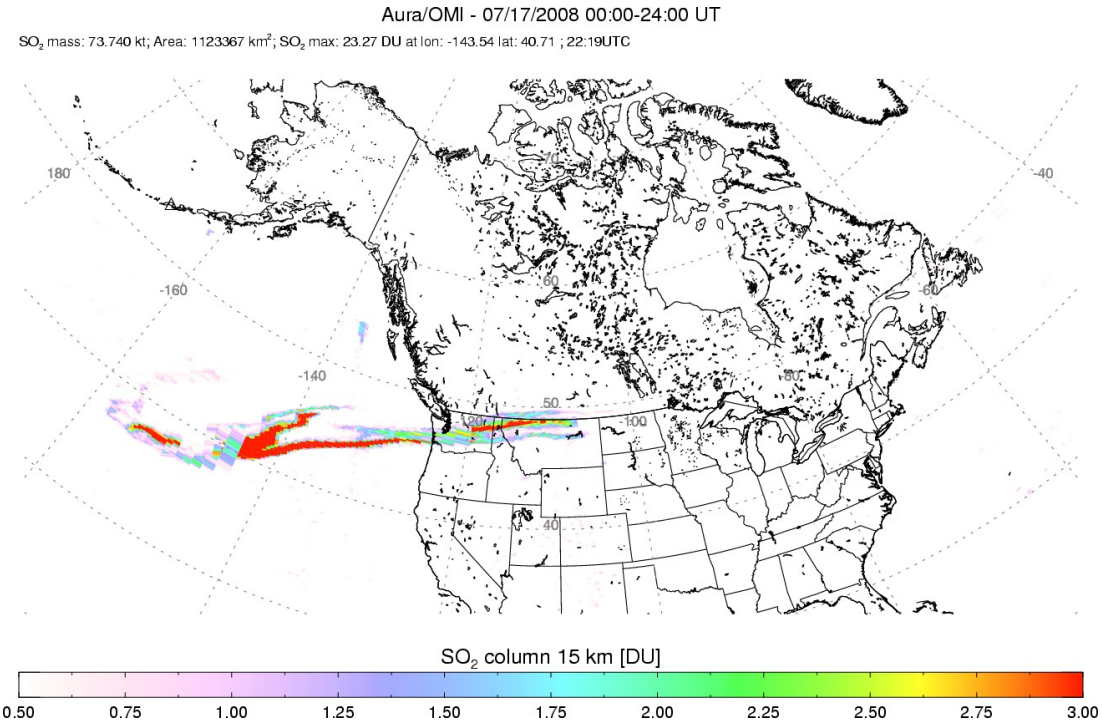

Figure 5.2: Total column SO_2 concentration derived from AURA/OMI scans, for July 17 2008.

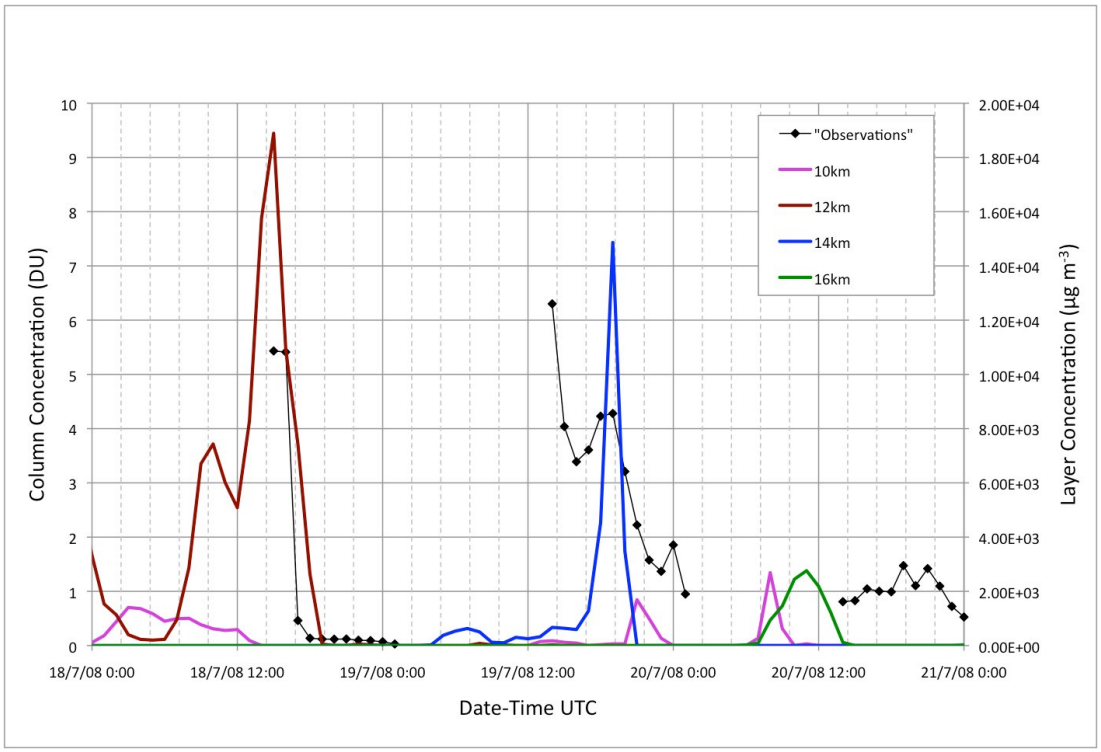

Figure 5.3: Time series of total column SO_2 concentration (DU) observations at the Washington State University Pullman.
Left-hand side axis, and model average layer concentrations (μg m^{-3}), right-hand side axis, resulting from a forward simulation, using a uniformly distributed emission in the vertical from the surface to 15 km. The observations were averaged over one hour, to correspond to the model averaging period. Comparison of timings and relative intensities can be made in order to estimate at which level the observed SO_2, should be found.

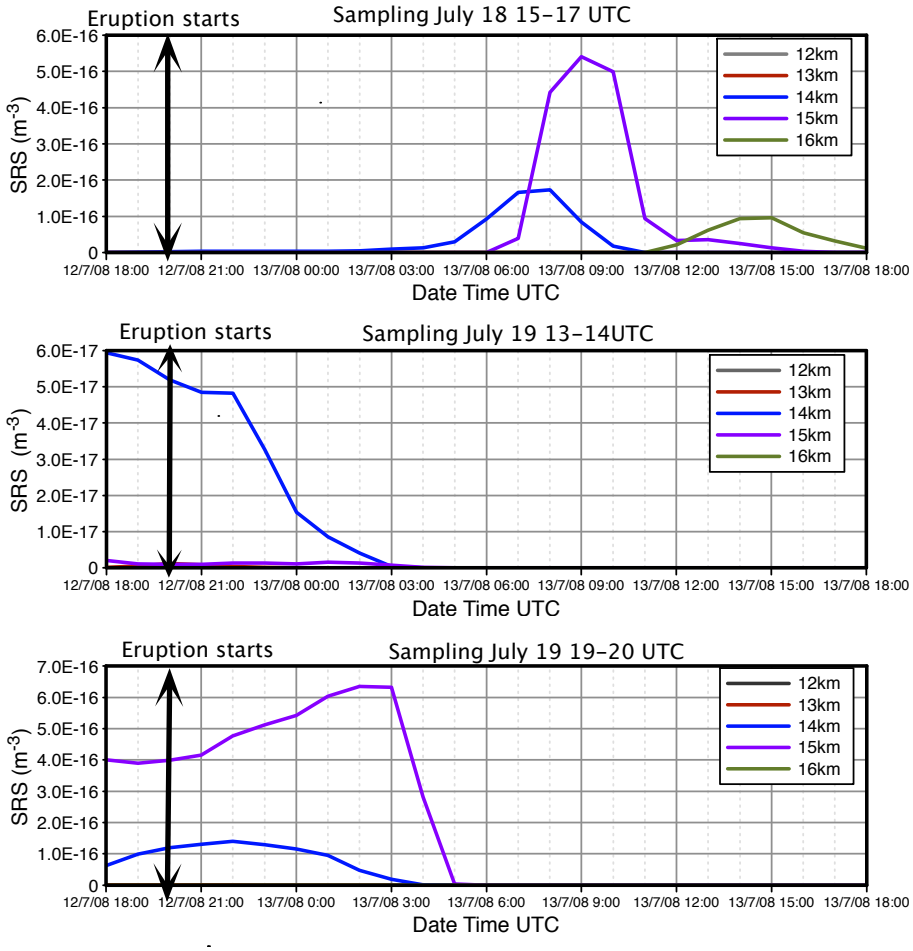

Figure 5.4: Source-Receptor-Sensitivity (SRS) coefficient of the 15 km column above the Washington State University Pullman Campus.
SRS to different levels above the Okmok Volcano. The SRS is a measure of the amount of air coming from the volcano location, during a given period of time, the sampling period. Values are shown for three sampling periods at WSU, when SO_2 measurements are significant, as a function of origin time at Okmok.

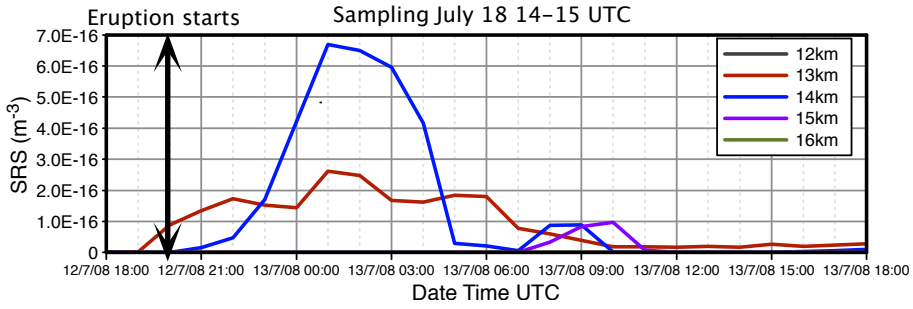

Figure 5.5: Same as in Figure 5.4, but for a sampling period just after the first observed SO_2 peak.

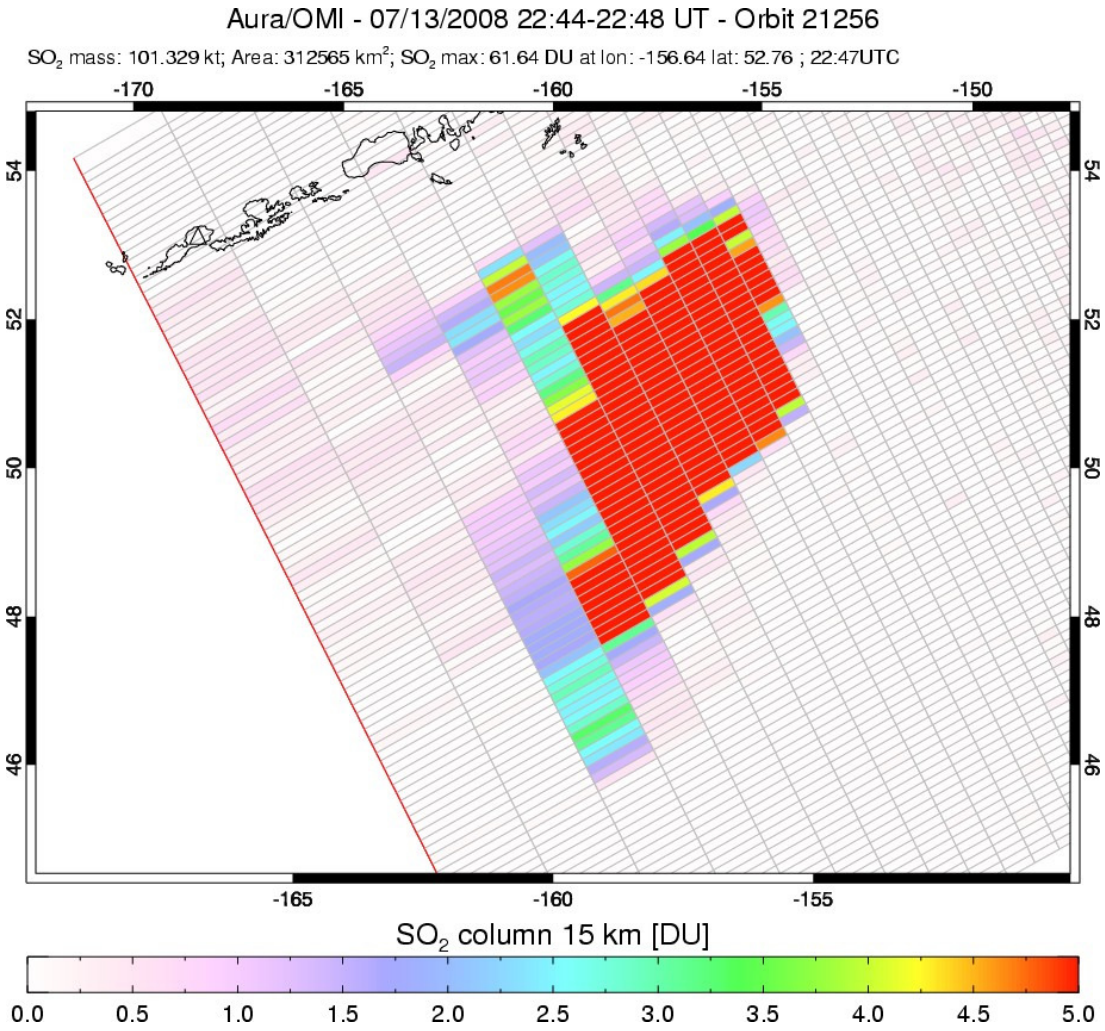

Figure 5.6: AURA/OMI total SO_2 content (indicated above the map) of the Okmok plume a few hours after the eruption.
The shown value of 101.329 kilotons (later revised to 110 kilotons, Simon Carn 2009, personal communication) compares well with the estimation resulting from inverse modeling (see text).

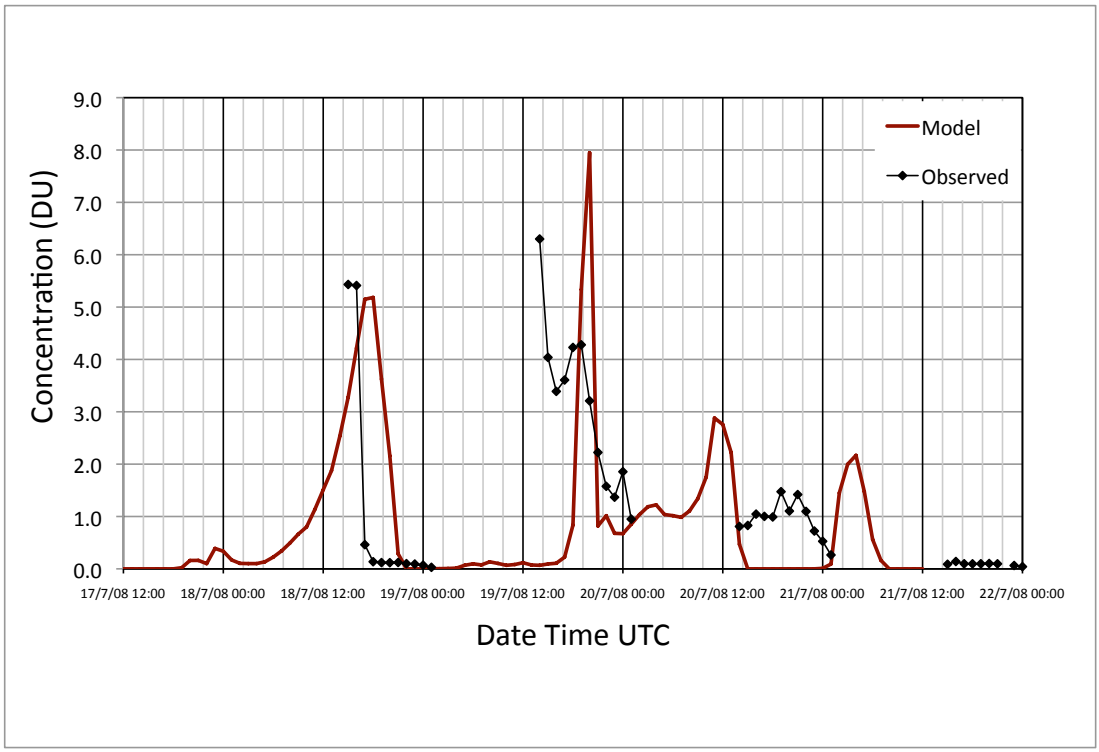

Figure 5.7: Time series of MLDP0 SO_2 column concentration estimates (DU) resulting from a forward simulation using a 100-kiloton emission, compared with WSU measurements.

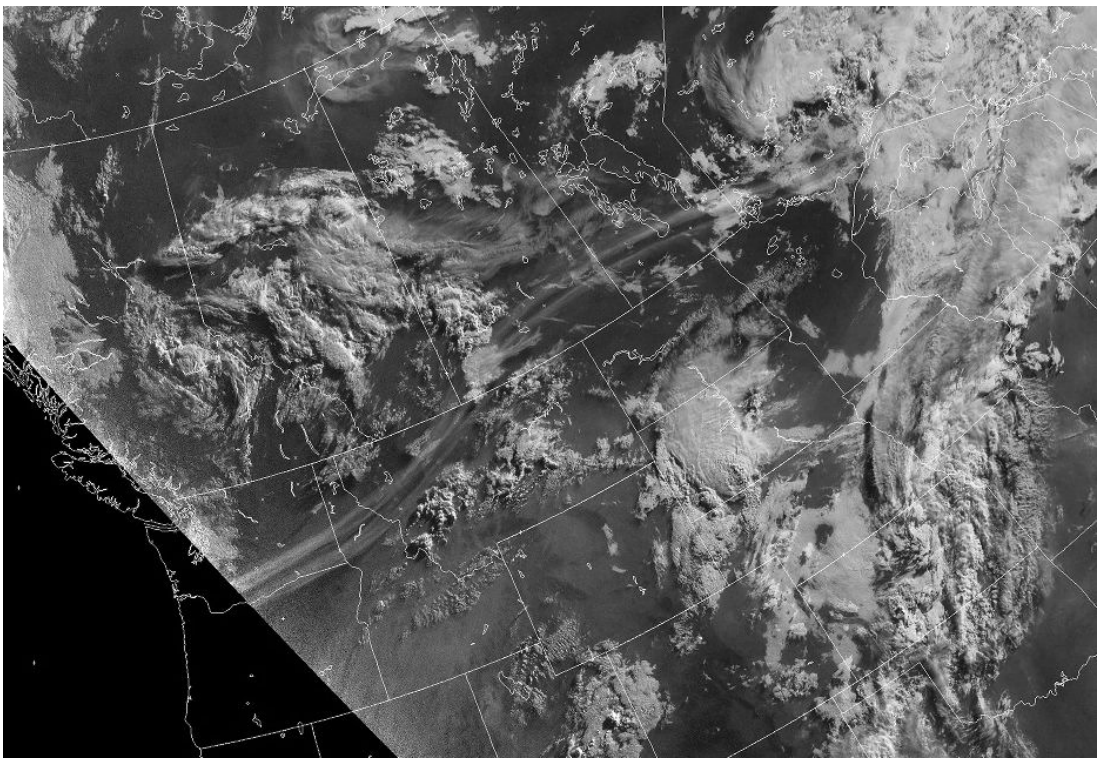

Figure 5.8: GOES-West image in the visible, valid 18 July 12:45 UTC, showing the aerosol plume associated with the SO_2 plume.

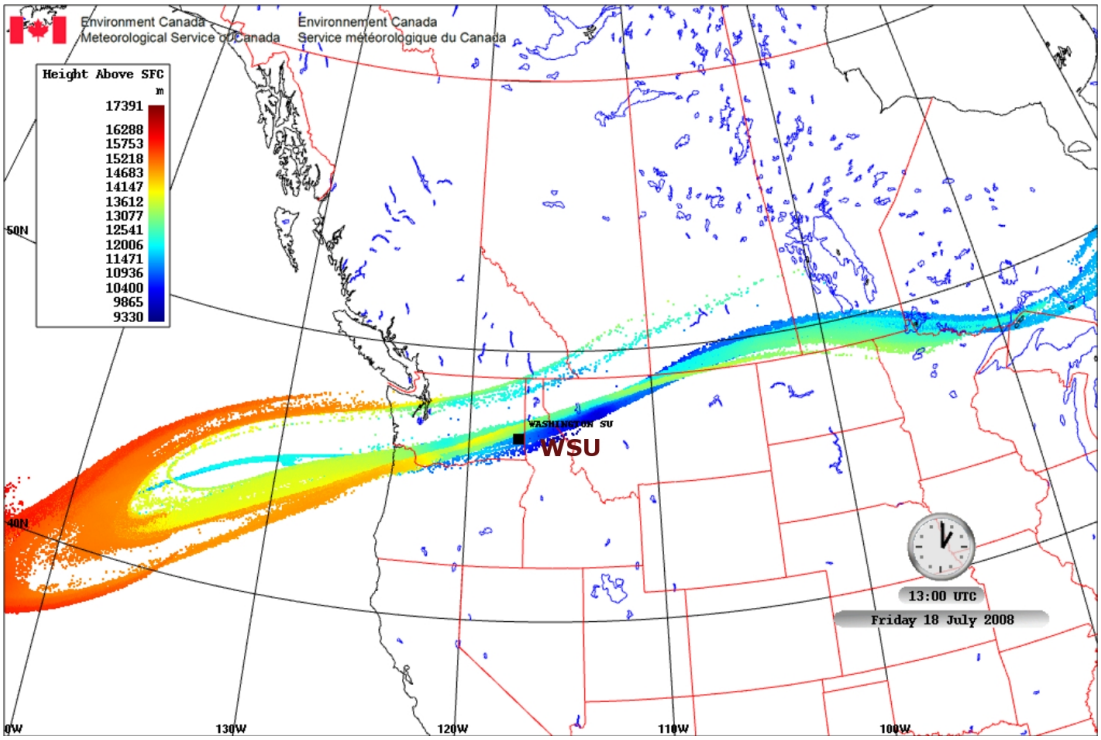

Figure 5.9: Position of MLDP0 particles, 18 July 13:00 UTC.
Height above ground in meters is indicated by the color scale. The black square indicates the location of the Washington State University (WSU) MFDOAS spectrometer.

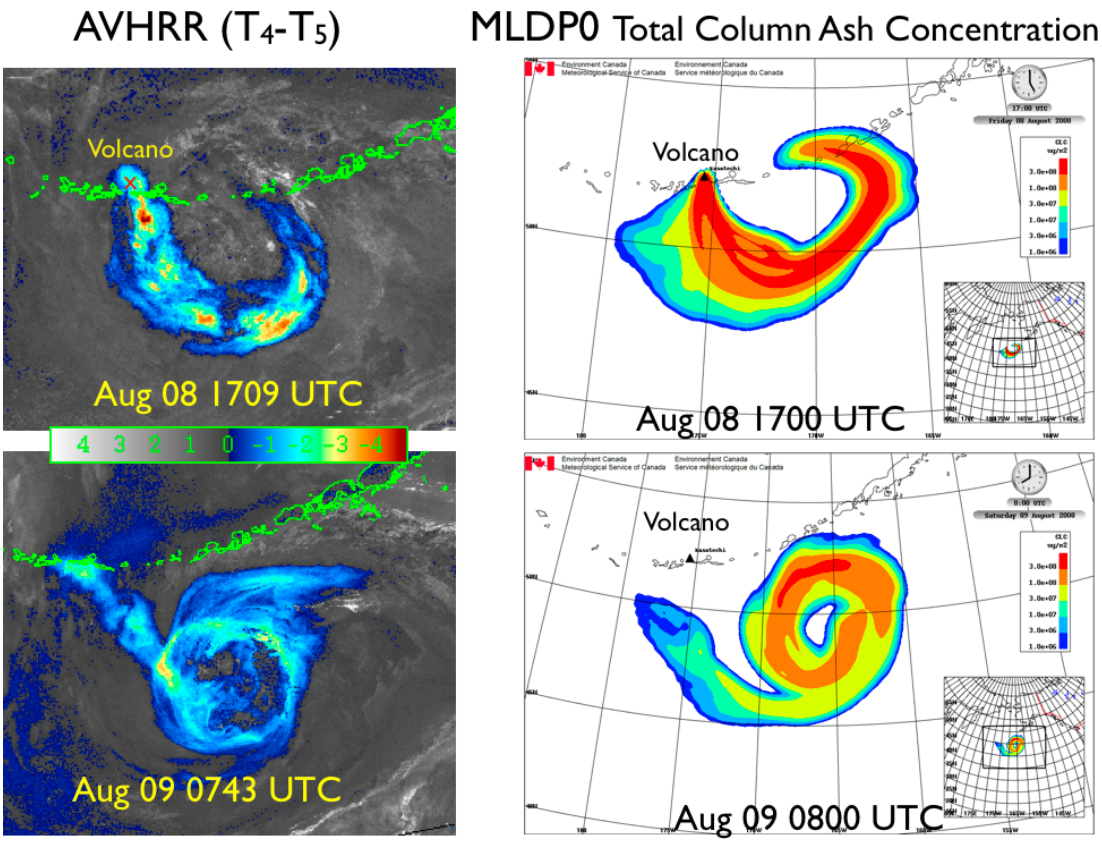

Figure 5.10: Comparison of Advanced Very High Resolution Radiometer (AVHRR) imagery (NOAA-16 and NOAA-17) showing brightness temperature differences ($T_4 - T_5$) with MLDP0 total column ash concentration, (μg m^{-2}).
The plumes are resulting from the Kasatochi eruption. The red X on the top left panel indicates the approximate position of the volcano.

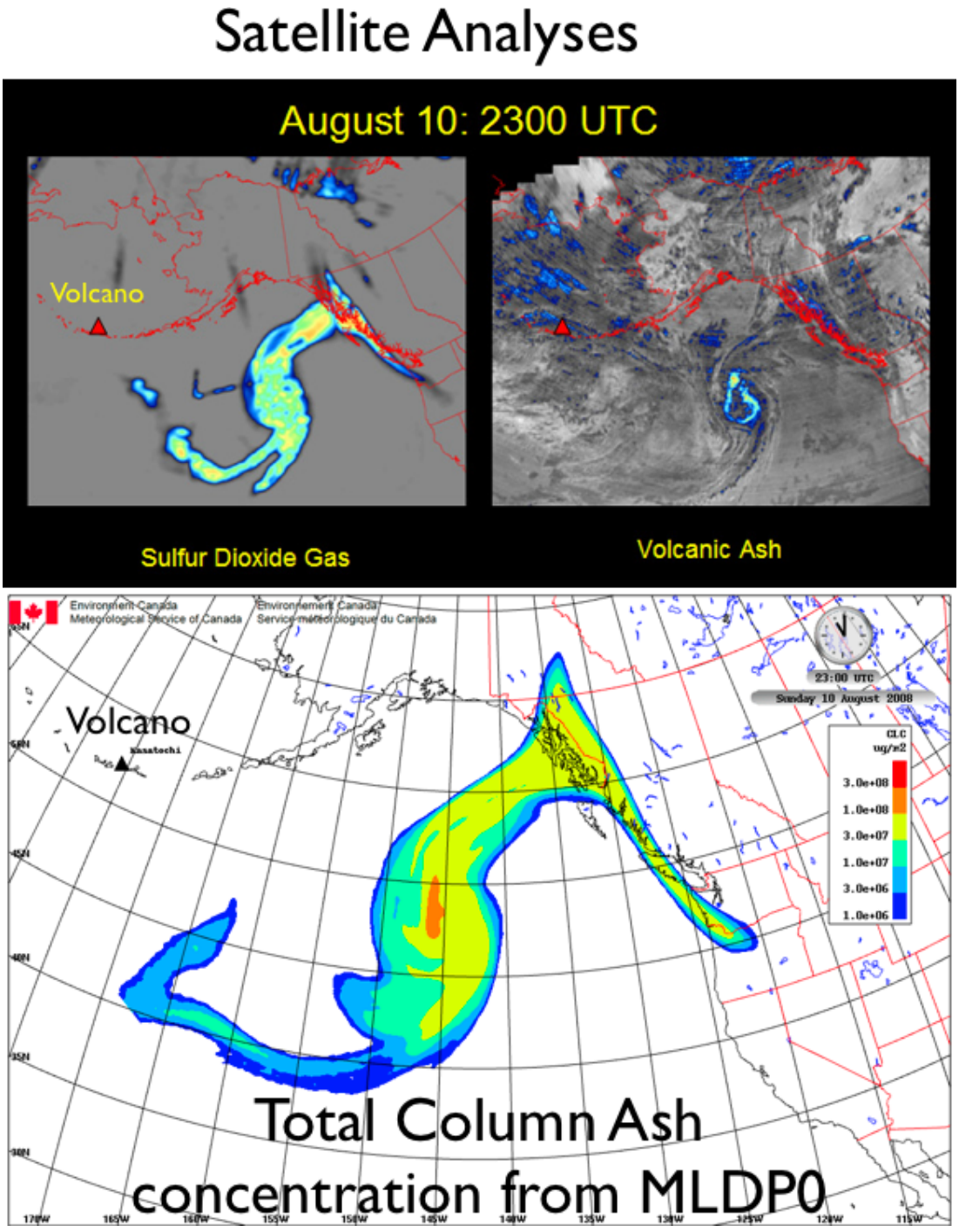

Figure 5.11: Comparison of AURA/OMI SO_2 gas and AVHRR $(T_4 - T_5)$ imagery with MLDP0 total column ash concentration (μg m^{-2}) on 10 August 23:00 UTC, for the Kasatochi eruption.

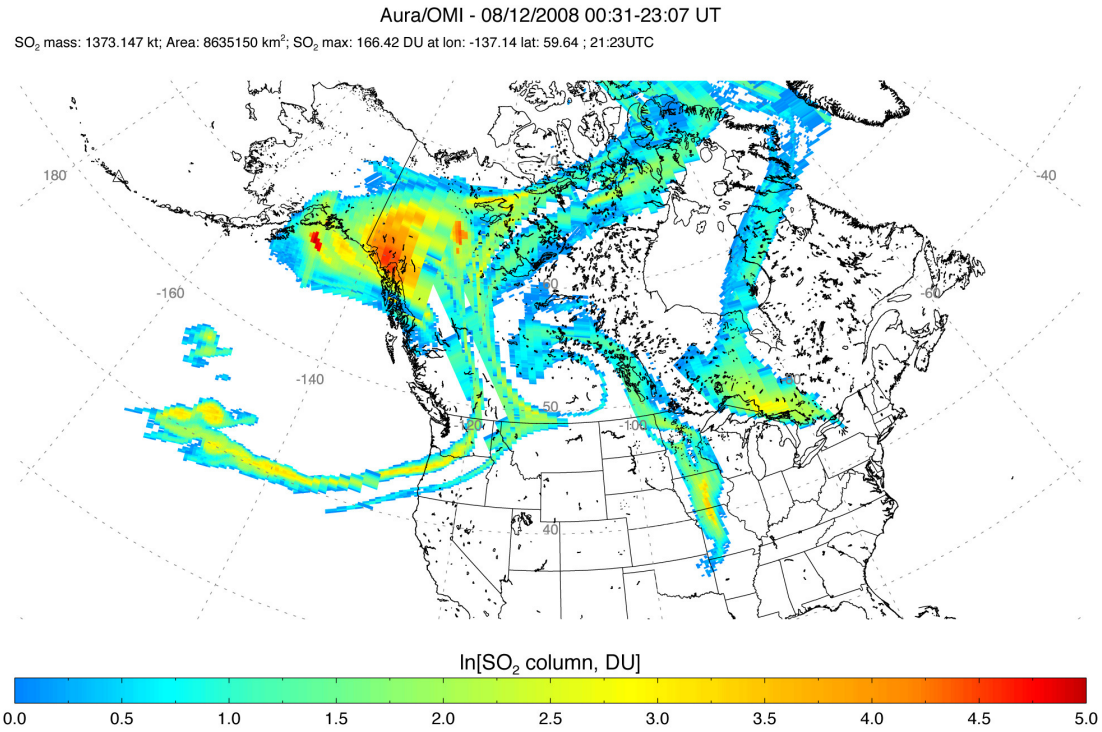

Figure 5.12: Kasatochi SO_2 plume reconstructed from AURA/OMI scans, for 12 August 2008.
Total column concentration (DU) are shown.

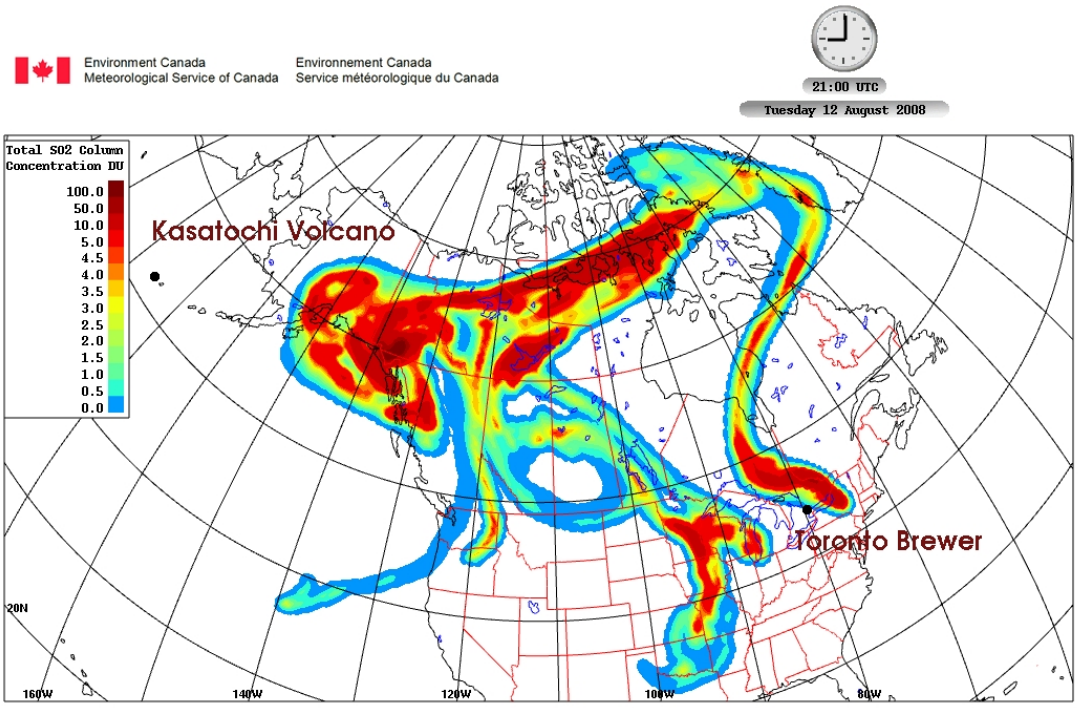

Figure 5.13: Total SO_2 column concentration (DU) resulting from a MLDP0 forward simulation.
Total emission of 1.3 megaton over 20 hours, starting 7 August 20:00 UTC ,from Kasatochi. The image is valid 12 August 21:00 UTC, and can be compared with Figure 12. The Toronto location of Environment Canada's Brewer spectrophotometers is indicated on the map.

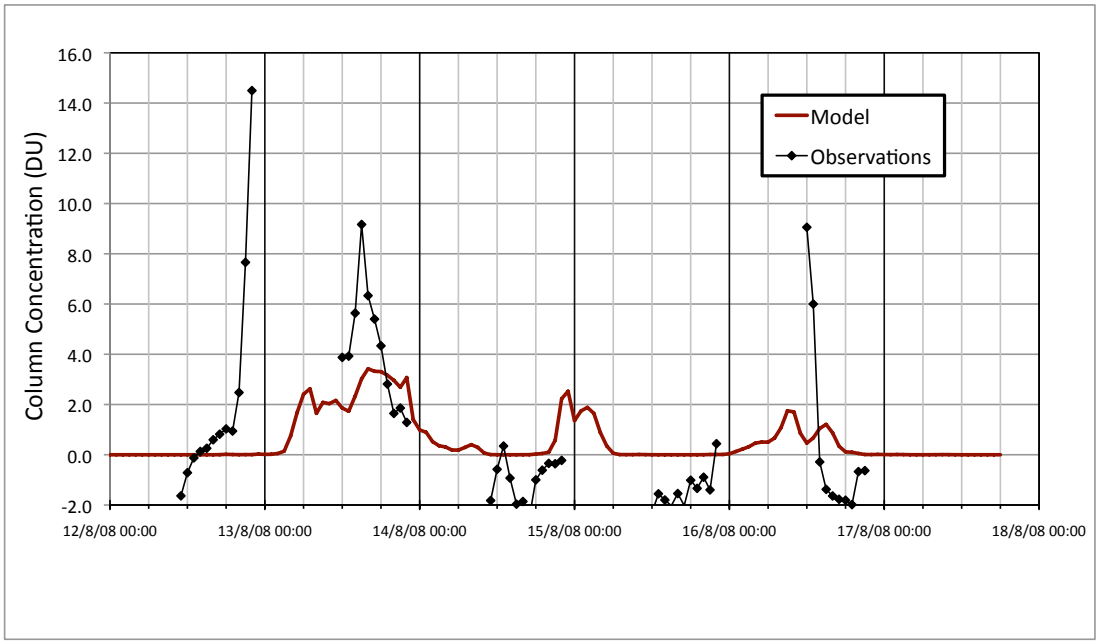

Figure 5.14: Time series of MLDP0 SO_2 column concentration estimates (DU) in Toronto compared with the Environment Canada's Brewer spectrophotometer measurements. The observations were averaged over one hour to correspond with the model estimations.

CHAPTER 6

"A modeling assessment of the origin of Beryllium-7 and Ozone in the Canadian Rocky Mountains" (published in J. Geophysical Research)

6.1 Preamble

This chapter presents a study assessing the origin of ^{7}Be and O_3 observed at one station, Harlech in the Alberta foothills, using inverse dispersion modelling. The investigation focuses on an intensive observation period of nearly four months from mid-March to the end of June 2004, during which daily average concentration of ^{7}Be was measured. The simulations were carried backward for an extended period of time, 14 days. In order to have an adequate sampling of all possible source regions 864000 particles, released continuously over the sampling period (24H), were used in each simulation. A total of 102 simulations were executed.

The perspective of the study is unique in the sense that it is the influence of large potential source areas on a single surface station which is investigated. Special metrics were developed for this purpose: the layer residence time fraction, the weighted layer residence time fraction, the layer exit rate and the layer exit time. The study illustrated very well how the ^{7}Be enriched air can travel close to the tropopause, moving across several times before descending to the surface (Figure 6.6).

The correlations between the observed O_3 and ^7Be concentrations, and their connection with exchanges between the stratosphere (ST) and the free troposphere (FT), strongly support the hypothesis that ozone observed in the Rocky Mountain foothills is of stratospheric origin.

6.2 Publication details

6.2.1 Journal

JOURNAL OF GEOPHYSICAL RESEARCH: ATMOSPHERES, VOL. 118, 10,12–10,138, doi:10.1002/jgrd.50761, 2013

6.2.2 Authors

R. D'Amours, R. Mintz, C. Mooney, and B.J. Wiens.

6.3 Introduction

There is general agreement that higher terrain, especially mountainous summits, are more frequently influenced by stratospheric intrusions. This is mainly due to elevation, but also in part to lee cyclogenesis generated by large mountain ranges [*Stohl et al.*, 2000; *Buzzi et al.*, 1984]. However, an STT can also happen far upstream from a site [*Stohl et al.*, 2003], with its effects measured at the surface many hours or sometimes days after the occurrence of the STT. These events can be referred to as"indirect STTs" because they enrich the upper troposphere with stratospheric constituents, but other processes, such as a subsident flow over the lee side of mountain ranges, are required to transport these constituents to the surface. Again, high elevation sites are more likely to measure the impact of indirect STTs simply because they are closer to the mid- or upper troposphere. Due to the province of Alberta's geographical location in the lee of the Canadian Rocky Mountains, there has been ongoing controversy in the Alberta air quality community regarding how much STT influences the province's surface ozone concentrations. In the absence of STT monitoring/modeling studies specific to Alberta, any conclusions drawn so far have been based on indirect inference from surface data [*Peake and Fong*, 1990]. This study was undertaken to

help address this issue, and to learn more about the nature of the STTs which affect Alberta.

Many studies make use of beryllium-7 (^{7}Be) measurements to aid in identifying an STT signature. ^{7}Be is a radionuclide with a half-life of 53.3 days, and is formed from spallation of nitrogen and oxygen nuclei by energetic particles associated with cosmic radiation entering the atmosphere [*Benioff*, 1956; *Lal et al.*, 1958; *Lal and Peters*, 1967; *Usoskin and Kovaltsov*, 2008]. The vertical concentration profile of ^{7}Be, which varies exponentially with altitude, depends mostly on its production rate which in turn depends on the depth of penetration of the cosmic particles having suitable energy. The largest ^{7}Be production rates and concentrations are typically found at altitudes above 20 km [*Lal and Peters*, 1967]. The availability of the cosmic ray particles for ^{7}Be production also varies greatly with geomagnetic latitude, with numbers increasing significantly towards the poles because of the redirection of initially isotropic incoming cosmic radiation by the earth's magnetic field [*Brost et al.*, 1991; *Kritz et al.*, 1991]. Once formed, ^{7}Be atoms almost immediately attach to aerosol particles, and their fate becomes dependent on the future of these aerosols. In particular, ^{7}Be depletion in the troposphere is caused by processes such as precipitation washout and vertical and horizontal transport [*Feely et al.*, 1989]. The advantages and disadvantages of ^{7}Be as a stratospheric tracer are well documented [*Lal et al.*, 1958; *Lal and Peters*, 1967; *Feely et al.*, 1989; *Brost et al.*, 1991; *Kritz et al.*, 1991; *Jordan et al.*, 2003; *Zanis et al.*, 2003b]. The primary advantages are that a significant portion of ^{7}Be is produced in the stratosphere, and its relatively short half-life (53.3 days) restricts its formation and transport to synoptic and slightly longer timescales. Also, ^{7}Be is not created in significant amounts by processes other than spallation, which simplifies source attribution. An important restriction is that ^{7}Be production occurs in the upper troposphere as well as the stratosphere; nearly $1/3$ of the total production in the mid-latitudes occurs below the tropopause [*Lal et al.*, 1958]. Another disadvantage is that ^{7}Be is subject to tropospheric removal processes, which complicates the assessment of surface concentrations. Many studies (e.g. [*Dibb et al.*, 1994; *Jordan et al.*, 2003; *Zanis et al.*, 2003a] utilize the ratio ^{10}Be/^{7}Be to at least partially overcome this. Beryllium-10 (^{10}Be) is formed in the same manner as ^{7}Be, and in the same regions of the atmosphere, but has a very long half-life (1.5×10^6 years [*Zheng et al.*, 2011]) and the ^{10}Be/^{7}Be ratio can be used as a stratospheric tracer not affected by tropospheric deposition processes [*Zheng et al.*, 2011]. Also the different half-lives of the two ratio components can be used to roughly estimate the relative

age of an air parcel, with air residing in the stratosphere for long periods having higher ratios [*Jordan et al.*, 2003].

The typical surface manifestations of a stratospheric intrusion event are well established: low RH, elevated O_3 concentrations, elevated ^{7}Be concentrations [*Elbern et al.*, 1997; *Stohl et al.*, 2000; *Cristofanelli et al.*, 2003] and high ratios of ^{10}Be/^{7}Be [*Dibb et al.*, 1994; *Jordan et al.*, 2003; *Zanis et al.*, 2003a]. Because of dilution and mixing with tropospheric air, STT events are not always associated with clearly elevated O_3 and low RH conditions [*Cristofanelli et al.*, 2003]. Pairing ^{7}Be and the ratio ^{10}Be/^{7}Be with O_3 and RH observations tends to give the best indication of potential stratospheric intrusion events. However, ^{10}Be data was not collected in this study, so similar to several other studies (e.g. [*Stohl et al.*, 2000; *Cristofanelli et al.*, 2003], the combination of ^{7}Be with O_3 and RH was used to identify potential STT events.

Modern long range transport models are also effective tools for the investigation of STT. Modeling approaches include the use of mean wind trajectories [*Bachmeier et al.*, 1994; *Stohl et al.*, 2000; *Colette et al.*, 2005], Lagrangian stochastic models [*Stohl et al.*, 2000; *Cristofanelli et al.*, 2003; *Cui et al.*, 2009] and Eulerian dispersion models [*Cristofanelli et al.*, 2003]. For example, Lagrangian models have been used to establish climatologies of STT events by initially distributing a large number of particles throughout the lower stratosphere and then running the model forward in time for long periods in order to describe STT temporally and spatially [*James et al.*, 2003; *Stohl et al.*, 2003]. Atmospheric transport models can also be executed in inverse mode (i.e., initialized at receptors) to not only determine probabilistically the source region of a tracer later observed at a receptor location, but also to make estimates of the tracer source strength [*Flesch et al.*, 1995; *Pudykiewicz*, 1998; *Seibert and Frank*, 2004].

This study investigates the extent to which STT impacts the foothills of the Canadian Rocky Mountains. During the spring of 2004, the monitoring of ^{7}Be was increased from weekly to daily at Harlech in the Alberta foothills. These data, together with hourly ozone (O_3) and RH measurements, are presented and analyzed. A Lagrangian particle dispersion model is used to investigate the origin of the observed ^{7}Be. The modeling study identifies potential

source regions by using a metric, the layer residence time fraction $\overline{F_t^l}$, based on the time an air parcel spends above certain pre-defined vertical atmospheric levels, including the tropopause. Model results are compared to the surface-based observations to evaluate if STT can be associated with periods of elevated ^{7}Be and O_3 surface concentrations, and of depressed RH.

6.4 Monitoring Site and Methodology

The Harlech monitoring site is located at 52.569°N, 116.003°W, near the edge of the foothills region east of the Rocky Mountain range, at an elevation near 1600 m (Figure 6.1). The vegetation in the area is largely coniferous forest. Harlech is located near the hamlet of Nordegg (population $\sim$ 200), approximately 80 km west of Rocky Mountain House (population 6,874, Statistics Canada, 2007), and several hundred kilometers away from Alberta's major cities. There is a major highway (the David Thompson Highway) located 8 km south of Harlech. The elevations of the mountains peaks in the vicinity are slightly over 2000 m, but can reach over 3000 m in the nearby Rocky Mountains. The area is used predominantly for camping, hiking and outdoor recreation.

Harlech ^{7}Be observations were taken from July 2003 to June 2004. Due to practical constraints, daily samples (24-hour average) were only taken from March–June 2004; all other samples were weekly averages. Based on conclusions drawn by *Gerasopoulos et al.* [2001] and *Cristofanelli et al.* [2006], the March to June period was chosen for daily sampling, on the assumption that chances of detecting STT-related events were good. Despite the fact that the ratio ^{10}Be/^{7}Be is considered a more effective stratospheric tracer than ^{7}Be alone [*Zanis et al.*, 2003a; *Zheng et al.*, 2011], it was not possible to make measurements of ^{10}Be, again for practical reasons.

Particulate matter was sampled with a high volume sampler using 3M F605 HEPA-rated (0.3 μm) filters. The sample filters were sent for analysis to SRC Analytical Lab in Saskatoon, Saskatchewan, Canada. Gamma spectroscopy was used to analyze the collected aerosol on the filters for ^{7}Be, corrected for decay to the midpoint of the sample collection period. Since the daily ^{7}Be measurement start and end times were based on local time

and varied slightly from day to day, a simple weighted average was applied to derive a ^{7}Be time series where each data point represented a 24-hour average starting and ending at 00:00 UTC.

Ozone was sampled continuously at five-minute intervals throughout the entire period July 2003 to June 2004. Continuous O_3 measurements were made with a UV-absorption analyzer (TECO 49C). The O_3 analyzer was calibrated monthly, and span and zeros conducted daily. Data presented in the sections below has been transformed into hourly and daily averages from the five-minute data. RH observations along with other routine meteorological data were acquired on an hourly basis during the sampling period. RH was monitored because it is the variable of choice to represent atmospheric moisture content in STT studies, rather than specific humidity [*Stohl et al.*, 2000; *Cristofanelli et al.*, 2003]. This is primarily due to significantly higher variability of specific humidity compared to RH in the troposphere, with lower values in winter and in the upper atmosphere and higher values close to the surface and in warmer months [*Stohl et al.*, 2000]. The meteorological station equipment was co-located with the O_3 and ^{7}Be instruments, and was calibrated monthly.

6.5 Overview of ^{7}Be and O_3 Data

Monthly average ^{7}Be and O_3 concentrations measured at Harlech are shown in Figure 6.2. The highest ^{7}Be average is found in September (4.59 mBq m^{-3}); however, 75% of the data was missing for this month. Of the 32 weeks of the weekly ^{7}Be monitoring (July 2003 –March 2004), a total of 8 weeks were missing from the months of August, September, October and November 2003. The daily ^{7}Be data (March– June 2004) was 93% complete. Despite the fact that only one year of data is available, the annual cycle described by *Gerasopoulos et al.* [2001] and *Cristofanelli et al.* [2006] appears to be present and is seen in Figure 6.2, which shows a ^{7}Be maximum in late-summer.

A statistical summary of O_3 and ^{7}Be concentrations measured at Harlech is presented in Table 6.1. Although ozone climatology varies from one alpine region to another, and

distinct differences can be observed at sites separated by relatively short distances [*Stohl et al.*, 2000], studies conducted in the province of Alberta and in the Canadian Rocky Mountains by *Angle and Sandhu* [1986] and *Peake and Fong* [1990] can be compared to the Harlech data. The average O_3 of 41 ppb and the median of 42 ppb in Harlech are close to the 43 ppb average and 41 ppb median of the nearly normally distributed data measured at the remote mountain site reported by *Peake and Fong* [1990]. The monthly averages in Harlech (Figure 6.2) show O_3 to have a late winter – early spring maximum (February – April) and a secondary summer maximum (July – August), but overall a relatively flat annual profile. This monthly profile is somewhat different from central European mountain sites which typically have a late spring maximum and winter minimum [*Logan*, 1985], but it does resemble the Alberta mountain site investigated by *Angle and Sandhu* [1986]. The highest monthly O_3 average at Harlech is found in February with an average of 46.5 ppb. The diurnal variation of hourly O_3 concentrations at Harlech over the July 2003 – June 2004 period is shown in Figure 6.3. The diurnal trend resembles the Alberta remote sites studied by *Angle and Sandhu* [1986] and *Peake and Fong* [1990], in which the trend is relatively flat. *Peake and Fong* [1990] compared the remote Canadian Rocky Mountain site at Fortress Mountain to two sites affected by a major urban center in the province of Alberta. The Fortress Mountain site had a small diurnal range (2.9 ppb), whereas the other two urban-affected sites had larger diurnal ranges of 11.6 ppb and 16.5 ppb, which suggests these sites were impacted by local photochemical production of O_3 and the associated diurnal NOx titration cycle. The $\sim$5 ppb diurnal range measured at Harlech is closer to the value determined for the remote mountain site investigated by *Peake and Fong* [1990], and thus is consistent with the assertion that Harlech is a relatively remote, pristine site, with no major anthropogenic sources that would lead to significant ozone production in the region.

It is interesting to note that studies of the seasonality of STTs in the mid-latitudes have shown discrepancies. Some studies have found spring and summer to have the highest likelihood of STTs [*Jordan et al.*, 2003; *Lefohn et al.*, 2011], while others have discussed sites where STTs were at a minimum in the summer [*Stohl et al.*, 2000]. Based on the monthly average plots shown in Figure 6.2 for ^{7}Be and O_3 measured at Harlech, it is reasonable to investigate the spring for STTs.

Figure 6.4 shows time series of the daily average of ^{7}Be and O_3 concentrations and of RH, for the time period between March - June 2004. The correlations between the three time series are shown in Table 6.2. In Figure 6.4, the larger peaks in ^{7}Be and O_3 are associated with localized minimums in RH, suggesting that those events are linked to subsiding (i.e. drying) air masses. This hypothesis is supported by the negative correlation of ^{7}Be and O_3 with RH (see Table 6.2). The auto-correlation within the ^{7}Be time series was assessed by correlating it to a lagged version of itself. With a one day lag, the correlation was greater than 0.8, while a two day lag resulted in a correlation below 0.5. A possible explanation for this phenomenon is that the effects of stratospheric intrusions often persist over several days, so that the auto-correlation over one or two day lag can be relatively strong.

In addition, singular spectrum analysis (SSA), which is a tool used to identify quasi-periodic features in noisy time series [*Vautard and Ghil*, 1989; *Ghil et al.*, 2002], was applied to the de-trended and normalised time series (using Analyseries, a time series analysis tool [*Paillard et al.*, 1996]). Figure 6.5 shows the ^{7}Be and O_3 filterered time series. The correspondence between the two time series is very apparent and does support the idea that the same dynamic features contribute to increase both ^{7}Be and O_3 concentrations in Harlech.

Four events stand out in Figure 6.4 and 6.5, and are numbered 1 to 4 in Figure 6.4. These events, discussed in some detail in section 6.7.2, are characterized by the occurrence of one ^{7}Be daily observation greater than the 90^{th} percentile. For all these events, O_3 is greater than 43 ppb (the O_3 average in spring 2004) and RH is less than 40% (the 20^{th} percentile for RH in spring 2004). These values are similar to the subjective criteria for identifying STT events found in the literature[*Stohl et al.*, 2000; *Cristofanelli et al.*, 2003], which are based on elevated ^{7}Be and O_3, and depressed RH in relation to the region's seasonal averages / maximums.

6.6 Dispersion Modeling

6.6.1 Application of the Canadian Meteorological Centre Lagrangian Dispersion Model

Lagrangian stochastic particle dispersion models (LSMs) simulate atmospheric dispersion by calculating the trajectories of a very large number of particles representing fluid elements. The effects of unresolved turbulent wind components are modeled through a

stochastic Langevin equation (for velocity increments) or a random displacement equation (for displacement increments). For this study, the Canadian Meteorological Centre (CMC) Lagrangian particle dispersion model, MLDP0 (modèle Lagrangien de dispersion de particules d'ordre zéro) was executed in inverse mode. MLDP0 uses the random displacement equation (RDE) to model turbulent mixing. Models using the RDE are often referred as "zeroth" order models. A discussion of the RDE can be found, for example, in *van Dop et al.* [1985], *Boughton et al.* [1987] or *Wilson and Sawford* [1996]. Tracer depletion due to radioactive decay is modeled according to the usual exponential decay. Wet scavenging is modeled utilizing of a wet scavenging coefficient which is dependent on the cloud fraction at the location of the fluid particles; the wet scavenging rate is proportional to the tracer concentration, which leads to an exponential decay [*Pudykiewicz*, 1989]. Dry deposition occurs when a fluid element reaches the ground and is modelled in terms of a reflection probability as in *Wilson et al.* [1989]. This is to account for the fact that while fluid elements are reflected upward after reaching the ground, only a fraction of the associated beryllium aerosols is reflected back with the fluid elements, depending on the absorption characteristics of the surface. The reflection probability is a function of the deposition velocity normally used to characterize the flux of airborne substances from the atmosphere to the surface. Gravitational settling is modeled in terms of a terminal velocity for the particulates [*Sparks et al.*, 1997; *Durant and Rose*, 2009]. For ^{7}Be however, it was considered negligible. More details as well as validation studies on MLDP0 can be found in (R. D'Amours and A. Malo, A Zeroth Order Lagrangian Dispersion Model MLDP0, Internal Report, Canadian Meteorological Centre, 2004) and in *D'Amours et al.* [2010]. Simulations were done for each 24-hour sample between March 2 – June 26, 2004. In each simulation, 864000 particles were released continuously during the sampling period (24 hours) from the observation site, and tracked 14 days backward in time.

The driving meteorological fields were provided by the CMC GEM (Global Environmental Multi-scale) Numerical Weather Prediction (NWP) system [*Côté et al.*, 1998a, b]. The horizontal resolution of the meteorological fields was approximately 100 km, with 58 η-levels in the vertical. MLDP0 was run with a global configuration, using a representative selection of 25 of these vertical η-levels, from $\eta = 1$ to $\eta = .027$ (i.e., surface to $\sim$22 km ASL).

6.6.2 Potential Source Layers for ^{7}Be

Several potential ^{7}Be source layers were considered in this study. A stratospheric layer was delineated by diagnosing the tropopause height using the isentropic coordinate form of Ertel's potential vorticity [*Holton*, 1992]. In the literature, potential vorticity thresholds used to estimate tropopause height range between 1 – 3.5 potential vorticity units (PVU, 1 PVU $= 1 \times 10^{-6}\,\mathrm{m^2\,K\,kg^{-1}\,s^{-1}}$) [*Bachmeier et al.*, 1994; *Holton et al.*, 1995; *Stohl et al.*, 2000; *Colette et al.*, 2005]. This study uses 2 PVU as the threshold, because observations indicate this metric provides a good estimate of the tropopause height in the mid-latitudes [*Holton et al.*, 1995]. Other layers were also considered: above 10 km (> 10 km), above 8 km (> 8 km), above 4 km (> 4 km), above 2 km (> 2 km) and less than ($\leqslant 2$) km. The layers are terrain following, all elevations above ground level (AGL), and are not mutually exclusive. While the > 2 km layer was selected to account for any transport from above the Planetary Boundary Layer (PBL), the > 4 km layer was chosen to investigate transport from the mid-troposphere. The $\leqslant 2$ km layer was considered to evaluate the effects of air masses circulating mainly in the PBL.

6.6.3 The Layer Residence Time Fraction

6.6.3.1 The Layer Residence Time

The influence of the different layers on the samples taken at Harlech was estimated by means of a layer residence time fraction $\overline{F_t^l}$. The $\overline{F_t^l}$ was determined by calculating the ratio of the total time particles spent in the layer of interest to the total duration of the particle trajectories over the course of the 14-day inverse simulation.

The residence time, τ_p, for particle p above a certain vertical level z_l is defined as follows:

$$\tau_p(> z_l) = \int_{t_s}^{t_s - T_p} f(z_p, t)dt \tag{6.1}$$

where T_p, is the particle's trajectory duration, t_s the sampling time, and:

$$f(z,t) = \begin{cases} 1 & z(t) \geq z_l \\ 0 & z(t) < z_l \,. \end{cases} \tag{6.2}$$

Finally an average ratio for the total number, N, of particles used in the simulation is calculated as follows:

$$\overline{F_t^l} = \frac{1}{N} \sum_{p=1}^{N} \frac{\tau_p(> z_l)}{T_p} \,. \tag{6.3}$$

The concept of residence time is illustrated in Figure 6.6, which shows the vertical position of three particles as a function of time along their 14-day trajectory. These particles were chosen because they follow fairly different vertical trajectories and illustrate that particles can move in and out of the stratosphere several times during 14 days in different ways. Particle 80k moves in and out of the stratosphere during the early part of its trajectory then permanently moves below the tropopause after 01 April, on its descent towards Harlech. Particle 120k starts above the tropopause on the first day of its 14-day trajectory then quickly crosses into in the upper troposphere (above 5 km) where it remains for nearly a week. On the other hand, particle 213k travels in the lower part of the stratosphere for more than five days, then moves very near the tropopause level for about three days, finally descending into the troposphere on 02 April. The $\tau_p(z_l >$2 PVU) value for particle 120k would be less than one day, while it would be nearly six days for particle 213k.

It is easily seen from Figure 6.6 how an estimation of the time at which particles exit a layer of interest can be obtained. The "exit time" for a particle is defined as the time at which the particle crosses a layer boundary for the last time before traveling to the Harlech sampler. The number of particles exiting a layer, using that definition, is calculated for each 6-hour period of the inverse simulation. The layer exit rate is defined as the ratio of the number of particles exiting a layer to the total number of particles used in the simulation.

6.6.3.2 Weighted Residence Time

The particles are emitted from the receptor at sample time t_s with an initial weight $m_p(t_s)$ which represents the relative importance of the particle in the sample. For example, if the sample is represented by N particles of equal weight, $m_p(t_s)$ could be chosen as $1/N$. This weight is reduced as a particle moves backward (from t_s) on its trajectory because of radioactive decay, wet scavenging and dry deposition. Hence at a time $t < t_s$, a particle's weight $m_p(t)$ is lower than it was at t_s. Since individual trajectories may differ significantly, the effect of the last two processes will also differ for different trajectories, ultimately resulting in a change in the relative contribution of each particle to the sample. A mass weighted residence time is calculated for each particle as follows:

$$\tau_p^w(> z_l) = \int_{t_s}^{t_s - T_p} \frac{m_p(t)}{m_p(t_s)} f(z,t) dt \,. \tag{6.4}$$

A ratio of the individual particle's mass weighted residence time to the total trajectory duration is then obtained with:

$$W_p^l = \frac{\tau_p w(> z_l)}{T_p} \,, \tag{6.5}$$

and an average ratio for the total number, N, of particles used in the simulation is calculated similarly to equation (6.3):

$$\overline{W_t^l} = \frac{1}{N} \sum_{p=1}^{N} W_p^l \,. \tag{6.6}$$

$\overline{W_t^l}$ defines the weighed layer residence time fraction.

Assuming that all the ^{7}Be measured in the sample originated from the layer above z_l, the average weighted residence time given by equation (6.3) could be used to estimate the

^{7}Be concentration in that potential source layer. Inverse Lagrangian stochastic dispersion modeling is often used in a similar fashion to estimate the source characteristics of an atmospheric tracer observed at one or more receptor points [*Flesch et al.*, 1995; *Wotawa et al.*, 2003]. However the main purpose for calculating $\overline{F_t^l}$ and $\overline{W_t^l}$ in this study is to assess the relative importance of the layers as potential sources for ^{7}Be measured at Harlech, and to look for connections between surface observations at Harlech and potential stratospheric/upper tropospheric input to those observations. The only hypothesis made is that the impact of the potential source layers on the nature of the air particles reaching the sampler can be related to the time spent in those layers.

6.7 Analysis of the Modeling Results

6.7.1 Comparison of ^{7}Be and O_3 Concentrations to the Layer Residence Time Fraction

Figure 6.7 shows the time series of $\overline{W_t^l}$ derived from the MLDP0 results for various layers, with the corresponding observed ^{7}Be concentration time series. The $\overline{W_t^l}$ values for the > 10 km layer are relatively small during the study period, indicating that there was little air originating from the > 10 km layer (for any time during the 14 days prior to the observation) which was ultimately sampled at Harlech. On the other hand, the $\overline{W_t^l}$ values for the > 8 km layer and for the stratosphere as defined by the > 2 PVU level, although not very large, are often appreciable, especially in March and April, and correlate with episodes of elevated ^{7}Be concentrations. The greatest contribution from the > 8 km and > 2 PVU layers occurs for the 24-hr sample ending 8 April, 00 UTC, the second highest ^{7}Be concentrations measured during the study period. For the three other elevated ^{7}Be and O_3 events, the > 8 km and > 2 PVU layers $\overline{W_t^l}$ values show local maxima but to a lesser extent than those values determined for event 1 (3-11 April).

Table 6.3 shows the Pearson linear correlation coefficient, ρ, between the $\overline{W_t^l}$ time series shown in Figure 6.7 and ^{7}Be and O_3 concentrations. Table 6.3 also shows ρ for the $\overline{F_t^l}$ time series (where depletion processes are not considered) and ^{7}Be and O_3 daily concentrations. There is little correlation between ^{7}Be concentrations and $\overline{W_t^l}$ for the layer below 2 km. In contrast, the correlation between ^{7}Be and $\overline{F_t^l}$ is strongly negative, meaning that

when air, which has been traveling near the surface for a significant portion of the preceding 14-days, reaches the sampler, there is an important drop in the ^{7}Be concentrations. However modeling removal mechanisms essentially decouples ^{7}Be concentrations from the $\leqslant 2$ km layer. This is a good indication that the ^{7}Be content of that air is typically very low. In the bottom panel of Figure 6.7, the $\overline{W_t^l}$ values for the > 2 km and the > 4 km layers generally track the ^{7}Be observations quite well throughout the monitoring period, and show the highest correlations, even when there does not seem to be much contribution from the upper layers associated with them. Table 6.3 also shows that ρ values are similar and fairly high for the $\overline{W_t^l}$ from the layers > 4 km and > 2 km; correlations for $\overline{F_t^l}$ are also significant, but lower than those for $\overline{W_t^l}$, indicating that there is information gained by modeling the removal mechanisms. For the > 10 km, > 8 km and > 2 PVU layers the correlations between ^{7}Be and $\overline{W_t^l}$, and between ^{7}Be and $\overline{F_t^l}$ are still important, but relatively less so than for the lower layers. These smaller correlations indicate that, on average and over a 14 day period, input from the > 10 km, > 8 km and > 2 PVU layers is not the most important contributor to ^{7}Be measured at Harlech, rather they suggest transport from within the mid-troposphere has the most significant effect on ^{7}Be at Harlech.

Due to the complexity of O_3 chemistry, there was no attempt in this study to model O_3 production or removal processes which may have helped clarify the relative contribution from the different layers. Nevertheless, correlations were calculated between the $\overline{F_t^l}$ and O_3 concentrations and show a pattern similar to correlations between $\overline{F_t^l}$ and ^{7}Be: negative for the layer $\leqslant 2$ km, and positive, for the layers above. It would appear that input from the mid- to upper troposphere and lower stratosphere has a significant effect on surface O_3 concentrations. In addition, the correlations indicate that, at Harlech, when air from above 2 km (normally from above the boundary layer) is transported to the surface, ^{7}Be and O_3 concentrations generally increase, whether or not stratospheric influx is detectable in the previous 14 days. When air originates mostly from the boundary layer, concentrations decrease. These findings support the idea that O_3 observed in the Alberta Foothills is often, if not mostly, the result of transport to the surface from above the boundary layer and that input from the stratosphere and upper and mid-troposphere has significant impact.

6.7.2 A closer Look at the Four Potential STT Events

Figure 6.8 shows the exit rates from the > 2 PVU and > 8 km layers, for one specific sampling day for each of the four events identified in Figures 6.4 and 6.7. The time series go back 14 days, at 6–hour intervals, for the 24–hour sampling period ending at the date/time indicated on the label.

Figure 6.4 shows a clear rise in ^{7}Be and O_3, and a significant drop in RH during the 3-11 April period (event 1). This period also corresponds to the largest $\overline{W_t^l}$ from the > 8 km and > 2 PVU layers (Figure 6.7). The top left panel of Figure 6.8 shows that the stratospheric air parcels sampled during the 24-hour period ending 8 April 00UTC, actually exited the stratosphere (> 2 PVU layer) almost entirely between 30 March and 4 April. The strongest efflux occurred on 1 April. This indicates that a significant amount of time passed between the injection of stratospheric air in the troposphere and the time where elevated O_3 and ^{7}Be concentrations were measured at Harlech. It is also interesting to note that the peaks in the stratospheric exit rates are preceded by peaks nearly equally spaced in time in the > 8 km exit rates, indicating that air parcels were exiting the > 8 km layer several hours before crossing the tropopause. Therefore it was likely that the tropopause was below 8 km (quite low) in the vicinity of the particle stratospheric exits, which is consistent with a deep upper trough, a common region for STT occurrences.

Figure 6.9 depicts the particle positions at 2 April, 00UTC, as they descend towards lower levels, en route to Harlech. This still image is associated with the simulation ending 08 April, 00UTC, and shows only the particles that were above the 2 PVU level at some time during the simulation, i.e. "stratospheric" particles. Figure 6.10 shows the time integrated plume formed by those "stratospheric" particles as they move to the Harlech sampler. Clearly, the stratospheric efflux is related to two distinct and well separated events. The two largest peaks seen in the particle exit rates are produced by two descending streams which can be related to the two deep low surface pressure systems seen in Figure 6.11, also valid at 2004 2 April, 00UTC. These two systems are associated with two well developed cyclonic upper level systems depicted by the potential vorticity at the 6000 m level shown on the same chart. Figure 6.12 shows a cross-section through the well developed

upper trough south of the Aleutians. There is a strong subsiding stream on the west side of the trough, with large downward vertical motions in what has all the appearances of a well-developed tropopause fold, where the 2 PVU surface lowers below 4000 m under a higher, second tropopause near 11000 m. This is where the model particles were descending, eventually making their way into the troposphere.

The top right-hand and lower left-hand panels in Figure 6.8 show the fraction of exiting particles and their exit times for simulations associated with events 2 and 3. In these cases, the contribution from the > 8 km layer as well as that from the stratosphere (> 2 PVU), are much less than for event 1, but still clearly detected by the modeling. A possible explanation is that ^{7}Be concentrations in the source areas for these events are higher. Another possible explanation is that important STT events occurred before the 14 day backward trajectory period. However a deeper investigation was beyond the scope of this study. In both cases the transfers occurred over a fairly long period, more than a week, many days before sampling. The lower right-hand panel in Figure 6.8 (event 4) indicates a relatively important input from the > 8 km layer, which also occurred over several days, long before sampling but there is a sharp burst from the > 2 PVU layer on June 17.

The exit rate plots in Figures 6.8 highlight the need to distinguish between the actual stratospheric intrusion events which transport stratospheric particles into the troposphere and the observation of this stratospheric air at a surface site. In all cases of significantly elevated ^{7}Be in this study period, the STT events occurred several days before their impact was observed at the Harlech station (i.e, no "direct" stratospheric events were detected at Harlech during the course of this study). This finding is consistent with comments made by *Davies and Schuepbach* [1994] and *Stohl et al.* [2000] on indirect STT events which are only seen at the surface after the passage of several days. In addition, *Cui et al.* [2009] ran forward Lagrangian simulations for longer than 10 days, and found a higher frequency of occurrence of STT events that took more than 4 days to reach the surface versus STT events that took less than 4 days to reach the surface. The MLDP0 simulations suggest that, for this data set, several STT events act to enrich the upper– and mid–troposphere with higher concentrations of ^{7}Be and O_3, and that it is this enriched air which is seen at the surface several days later and several thousand kilometers away from the original

STT events. Direct stratospheric intrusion events (i.e., where a tropopause fold actually makes contact with the ground) occurring near a site and whose impact is seen immediately at the surface, are actually relatively rare [*Stohl et al.*, 2003]. None were observed near Harlech during the study period. The investigation of the individual events (results presented in Table 6.3 and discussed in section 6.7.1), provides significant evidence that long range transport from the mid- and upper troposphere show the greatest contribution to the elevated ^{7}Be and O_3 concentrations.

6.8 Summary and Conclusions

^{7}Be was monitored weekly at Harlech, Alberta, from July 2003 to June 2004, and daily during the spring of 2004. These data, together with hourly O_3 and RH measurements, were presented and analyzed, with a focus on the spring of 2004. The Lagrangian particle dispersion model MLDP0, run in inverse mode, was used to assess the influence of air parcels originating from different layers in the atmosphere on the concentrations observed during that period. The analysis was mainly done by evaluating the relative contribution of the different atmospheric layers, using a metric developed for this purpose, the layer residence time fraction $\overline{F_t^l}$ and the weighted layer residence time fraction $\overline{W_t^l}$. Other metrics used include the rate at which the parcel finally exits the layer before reaching the observation site (the exit rate) and the time when these occur, the exit time.

MLDP0 model results show that at Harlech, above average observations of ^{7}Be and O_3, and below average observations of RH, are significantly correlated with the arrival at the surface of air originating from the mid- and upper troposphere. Generally there is a small contribution from particles originating from either the > 8 km or > 2 PVU layers, or both. The 3-11 April period, the longest period of elevated ^{7}Be and O_3 observations and the lowest RH recorded in the study, is the period where the model shows the strongest contribution from > 8 km and > 2 PVU layers. These can be related to two well identified stratospheric intrusions occurring over the northern Pacific, more than 5 days before associated observations. Three other events were also identified. In these cases, the elevated ^{7}Be cannot be clearly attributed to STT occurring in the 14–day period prior to observations, but it can be attributed to the impact of mid-tropospheric air subsiding into the site.

The modeling also shows that periods of below average ^{7}Be and O_3 occurred when the station was mainly influenced by air masses circulating in the boundary layer. Correlations between $\overline{W_t^l}$, $\overline{F_t^l}$, and the ^{7}Be and O_3 concentrations support the view that episodes of elevated ^{7}Be and O_3, and depressed RH, observed in the Alberta Foothills are typically the result of long range transport from the mid- or upper troposphere, or from STTs, that have occurred several days and thousands of kilometers away from the observation site.

In the future, a longer term field study which includes measurements of ^{10}Be as well as ^{7}Be at several sites would help clarify the nature and age of stratospheric and upper tropospheric input to the surface observations of in Alberta. Further modeling is needed to better understand the impact of trans-Pacific transport of anthropogenic O_3 on the Alberta O_3 budget.

6.9 Acknowledgments

The authors would like to thank Dan McLennan for his help preparing Figure 6.1. Comments and suggestions from two anonymous reviewers improved the paper significantly.

6.10 Tables

Table 6.1: *Statistical summary of hourly average O_3 concentrations for July 2003–June 2004, weekly ^{7}Be concentrations, July 2003–March 2004 and daily ^{7}Be concentrations, March – June 2004.*

	Hourly O_3 (ppb)	^{7}Be Weekly(mBq m^{-3})	^{7}Be Daily (mBq m^{-3})
Number of samples	7630	32	104
Average	41	2.76	3.39
Median	42	2.37	3.04
Range	80	4.54	7.23
Standard Deviation	9	1.39	1.93
Maximum	88	5.46	7.61

6.11 Figures

Table 6.2: *Pearson linear correlation coefficient ρ_P for daily mean ^7Be and O_3 concentrations, daily mean RH.*

Observation pair	ρ_P
^{7}Be – O_3	0.59
^{7}Be – RH	-0.51
O_3 – RH	-0.80

Table 6.3: *Pearson linear correlation coefficient ρ between the weighted layer residence time fraction, $\overline{W_t^l}$ and daily ^7Be, unweighted layer residence time fraction $\overline{F_t^l}$ (radioactive decay and other removal processes are not considered) and daily ^7Be and O_3 concentrations, for March – June 2004.*

	$\overline{W_t^l}$	$\overline{F_t^l}$	
Layer	^{7}Be	^{7}Be	O_3
$\leqslant$ 2 km	-0.15	-0.64	-0.52
$>$ 2 km	0.72	0.64	0.53
$>$ 4 km	0.71	0.63	0.60
$>$ 8 km	0.56	0.53	0.47
$>$ 10 km	0.36	0.34	0.32
$>$ 2 PVU	0.42	0.38	0.42

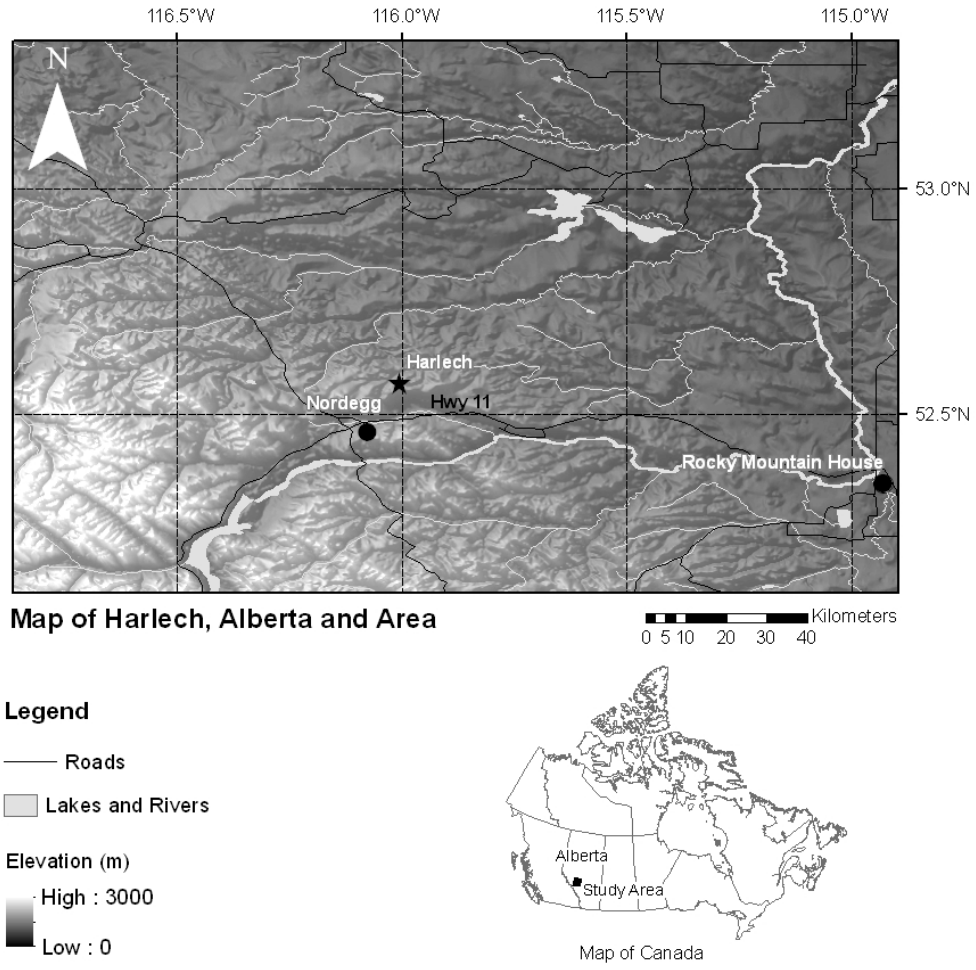

Figure 6.1: Map of the study area and location of the Harlech monitoring station.

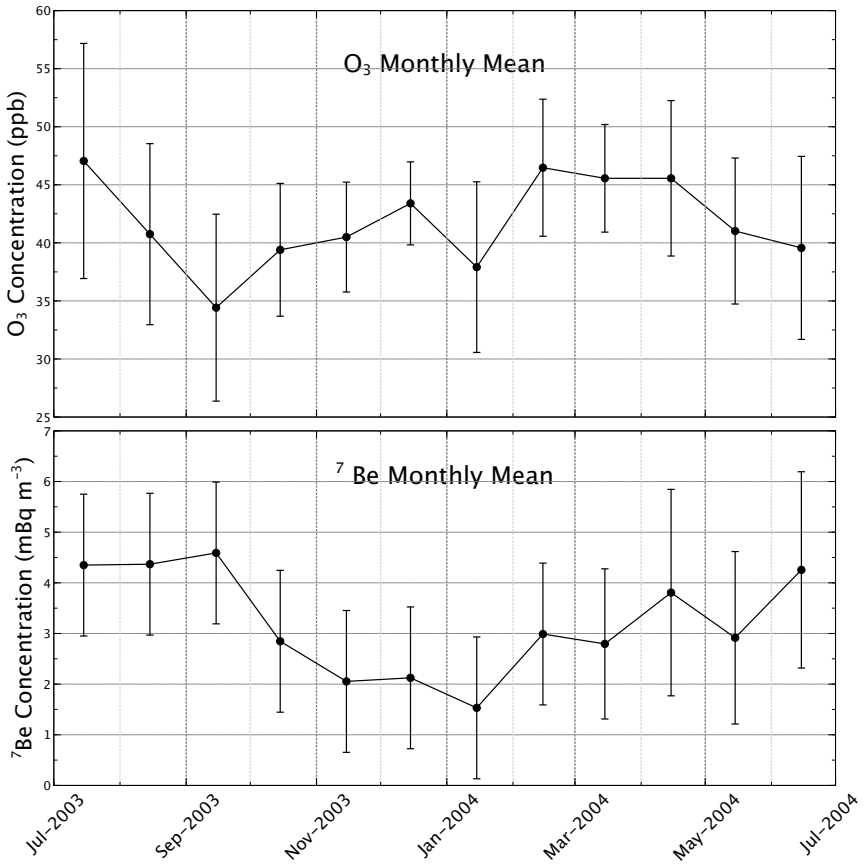

Figure 6.2: Monthly averages of ^{7}Be and O_3 concentrations measured at Harlech for July 2003 – June 2004.
The O_3 error bars show the standard deviation of the daily means for each month. The ^{7}Be error bars use the standard deviation of the all weekly averages (1.39 mBq m^{-3}) from June 2003 to February 2004, and the standard deviation of the daily means of each month for March, April, May and June 2004.

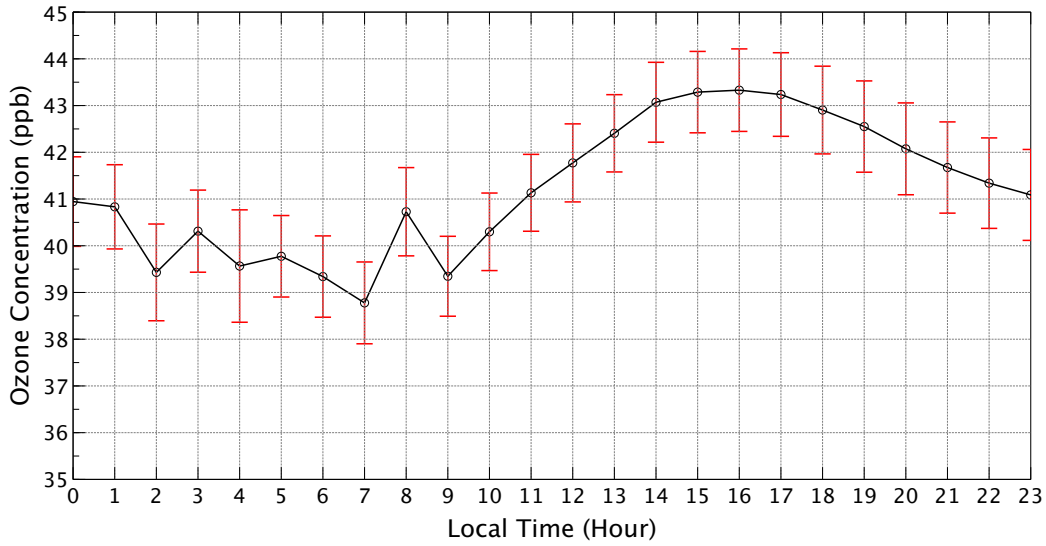

Figure 6.3: Mean diurnal variation of O_3 concentrations measured at Harlech for July 2003 – June 2004.
The error bars represent the 95% confidence interval for each hourly mean.

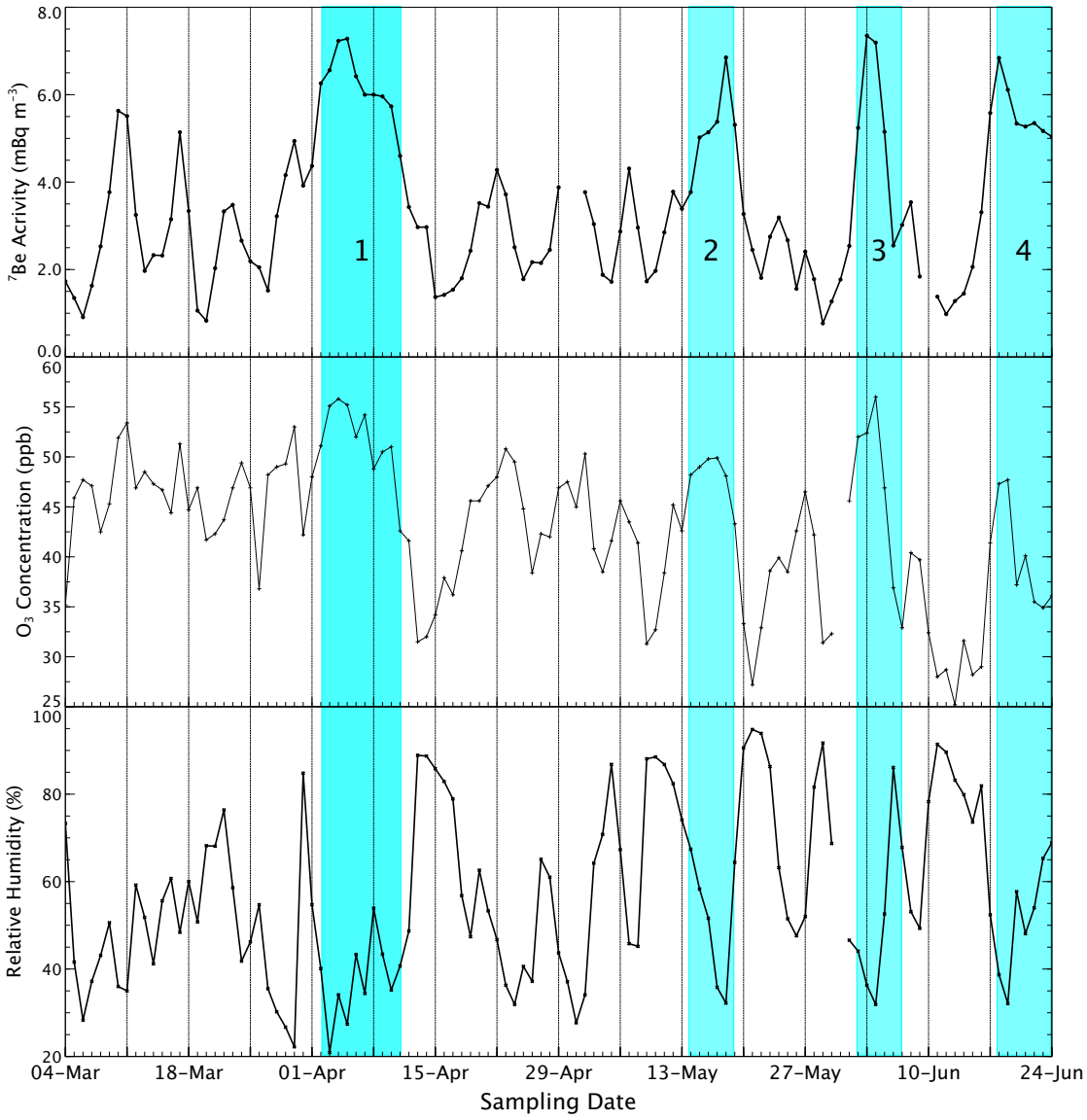

Figure 6.4: Daily averages of ^{7}Be, O_3 and RH at Harlech.
The cyan colored areas, numbered 1 to 4, correspond to investigated events.

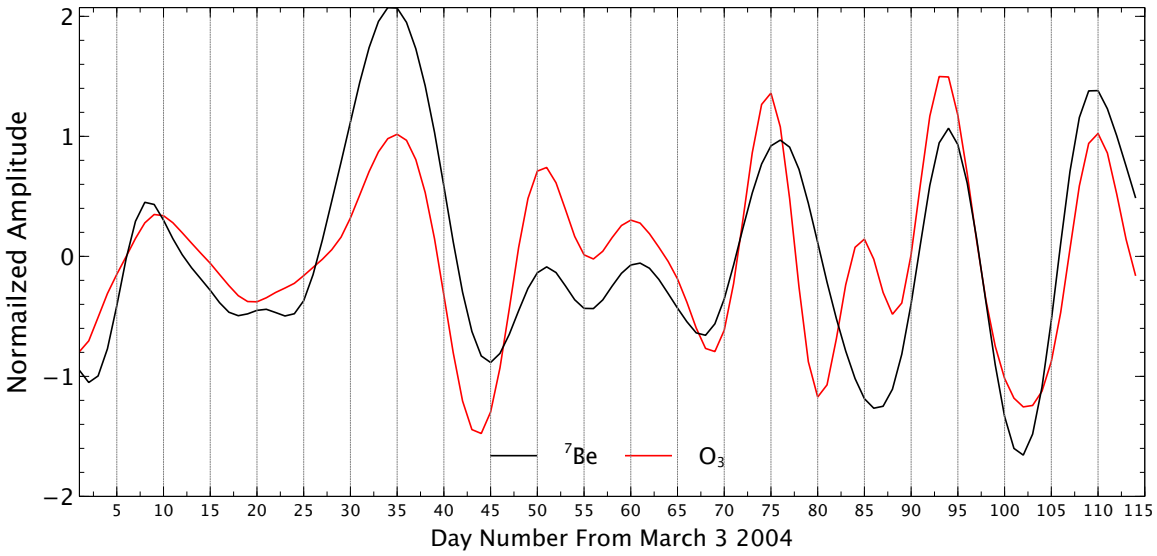

Figure 6.5: SSA filtered daily averages of ^{7}Be and O_3 at Harlech.

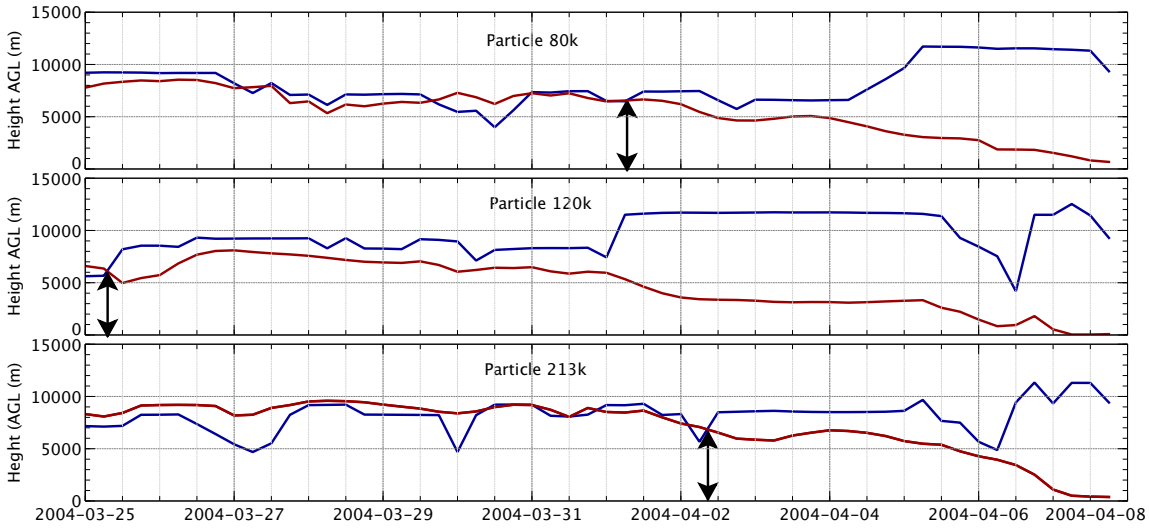

Figure 6.6: Vertical trajectories of selected particles, as a function of time, as they move towards the Harlech sampler.
Sampling ends at 8 April 00UTC. The dark red line represents the particle position, the dark blue line the tropopause height (2 PVU level), at the particle position. The vertical arrows indicate the time when the particle exits the stratosphere for the last time. This defines the "exit time" used in the study.

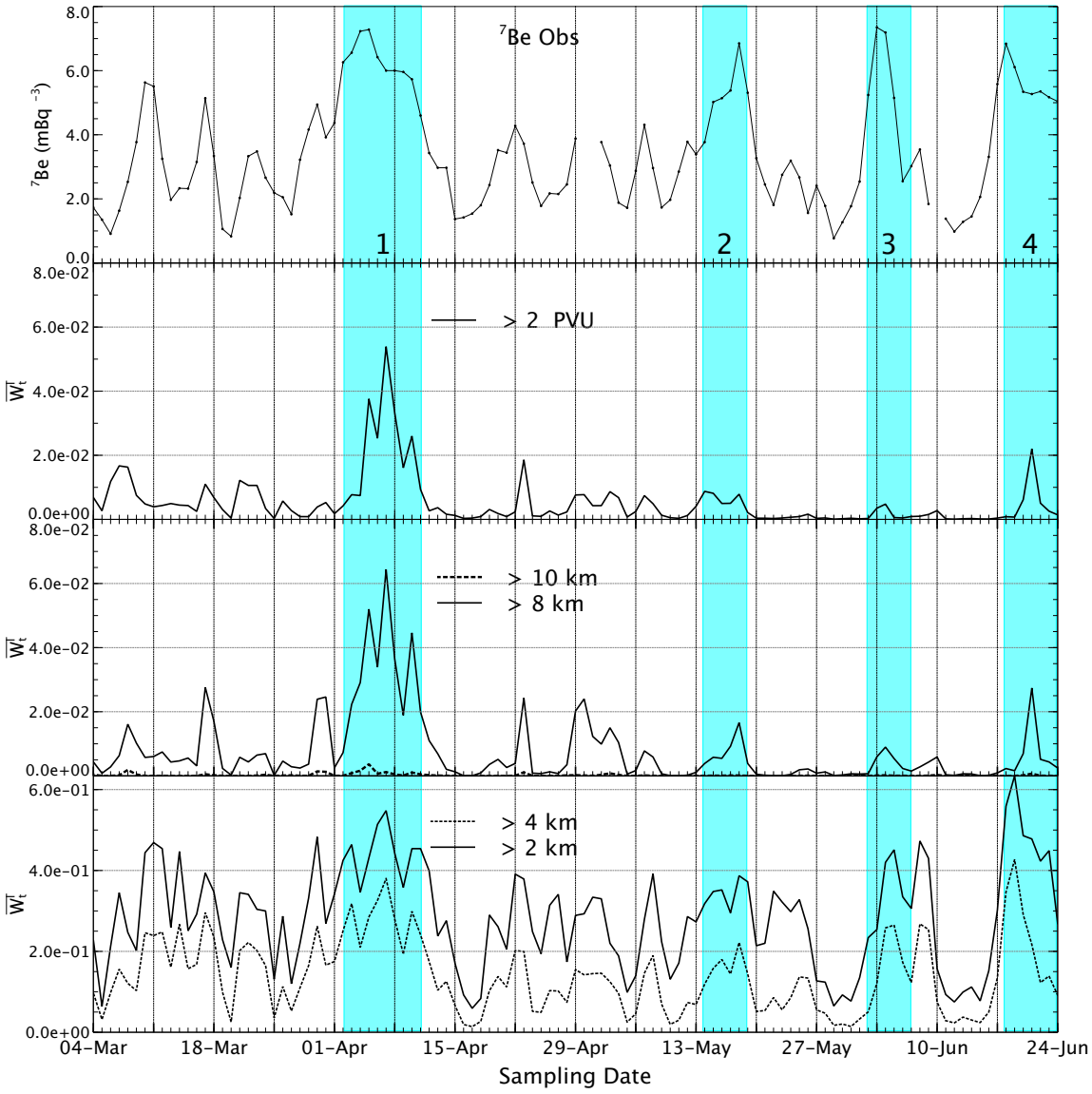

Figure 6.7: Observations of ^{7}Be daily average concentrations (top panel) compared to the weighted layer residence time fraction, $\overline{W_t^l}$, for various layers during the period March to June 2004.

Note the scale differences in the $\overline{W_t^l}$ values on the different panels. The cyan colored areas, numbered 1 to 4, correspond to investigated events.

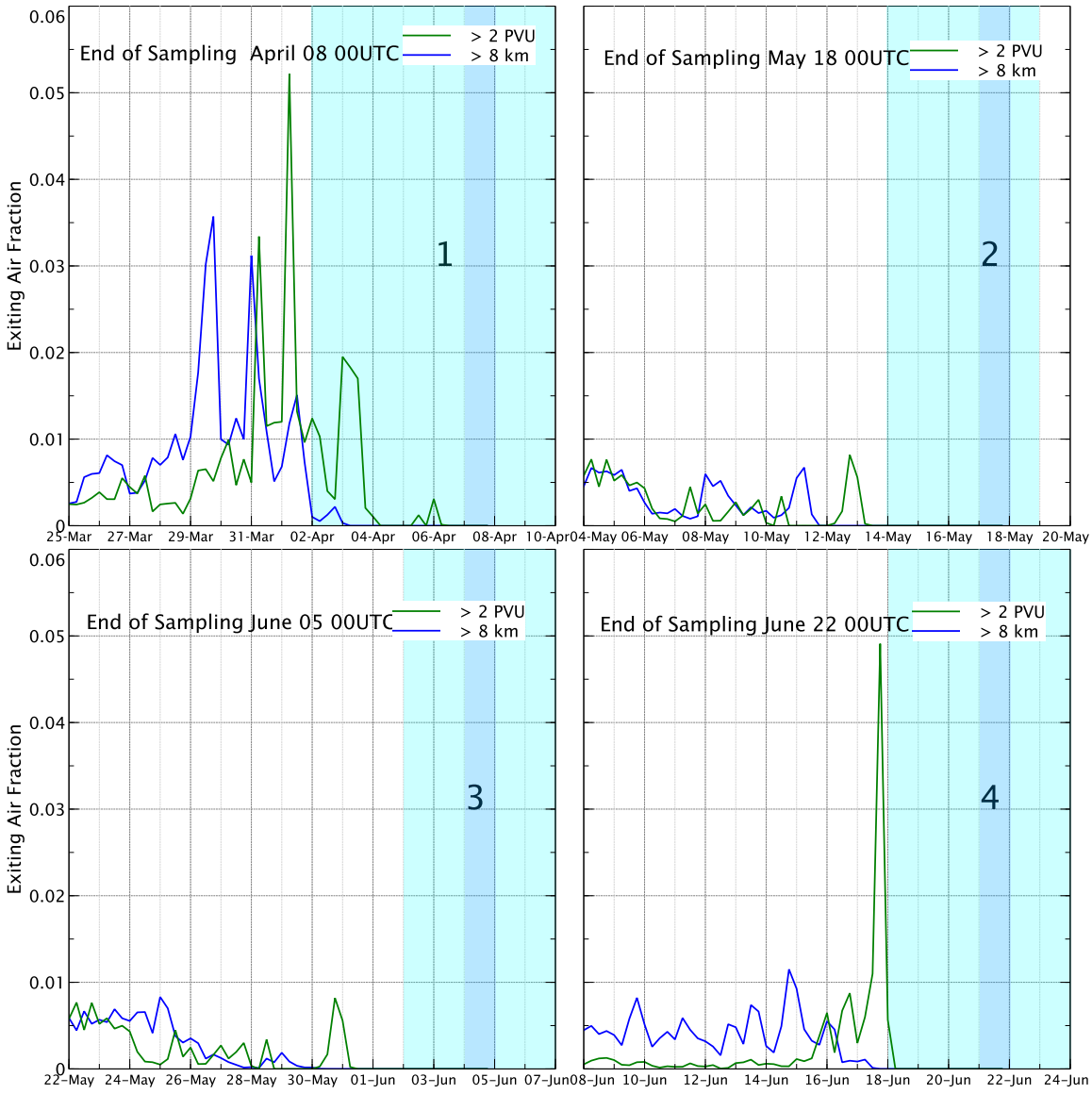

Figure 6.8: Layer exit rates for specific sampling days during the four investigated events. The layer exit rate is defined as the ratio of the number of particles exiting a layer for the last time, during a 6-hour period, to the total number of particles used in the simulation (864000).The areas colored in cyan indicate the total duration of the associated event (see Figure 6.7), while the blue colored areas show the duration of the sampling period for the specific day.

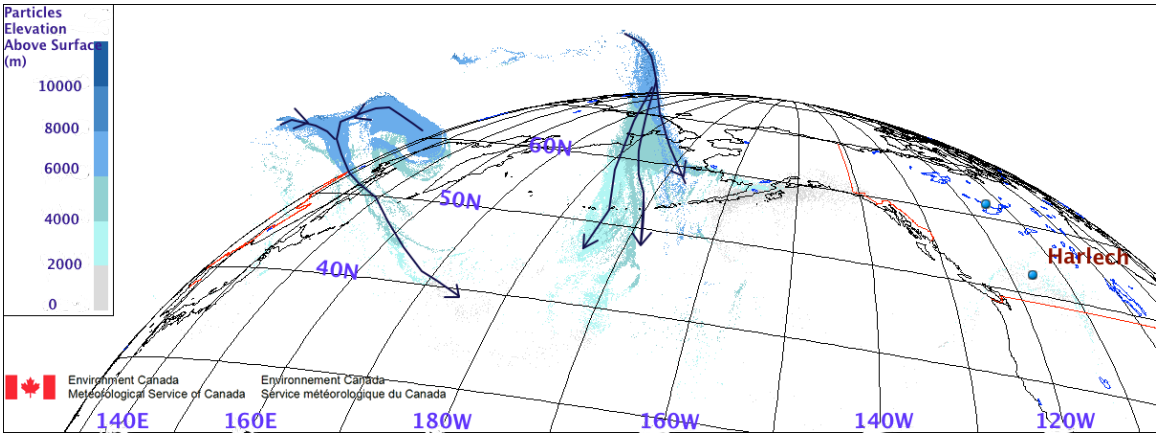

Figure 6.9: Position of the stratospheric particles (i.e. particles that have been above the 2 PVU level at least once), sampled at Harlech during a 24-hour period ending 8 April 00 UTC.
The arrows indicate the instantaneous motion direction of the particles, 2 April 00 UTC, as they move towards Harlech.

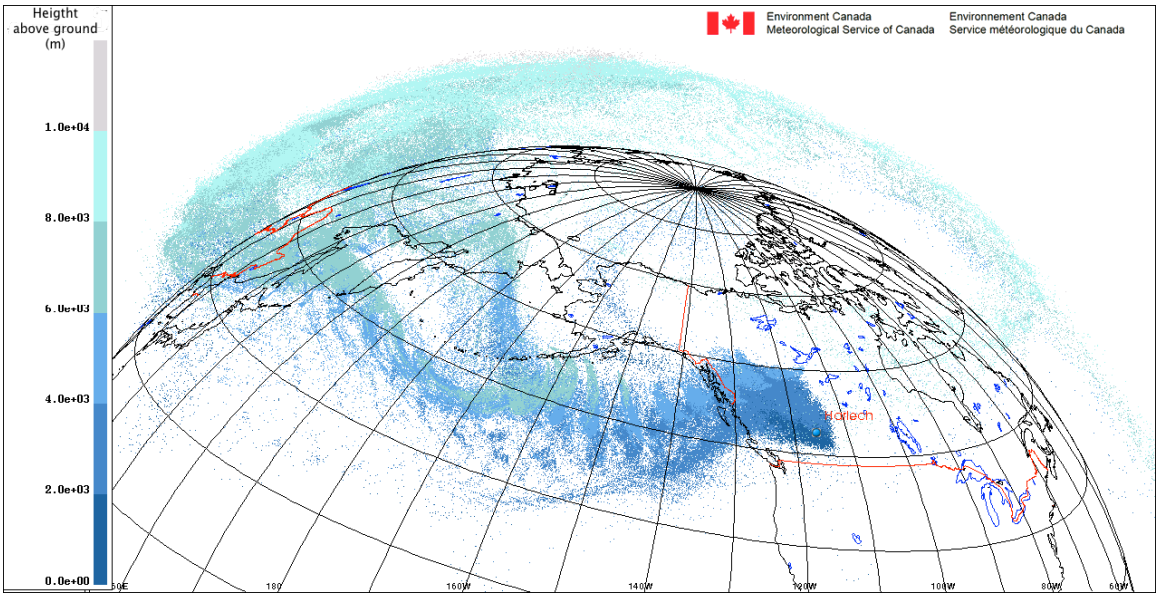

Figure 6.10: Time-integrated plume of the stratospheric particles (i.e., particles that have been above the 2 PVU level at least once), sampled at Harlech during the 24-hour period ending 8 April 00 UTC.
Particles were sampled from a reduced set of all the particles used in the simulation and are shown every 6 hours during their 14 day trajectory towards Harlech.

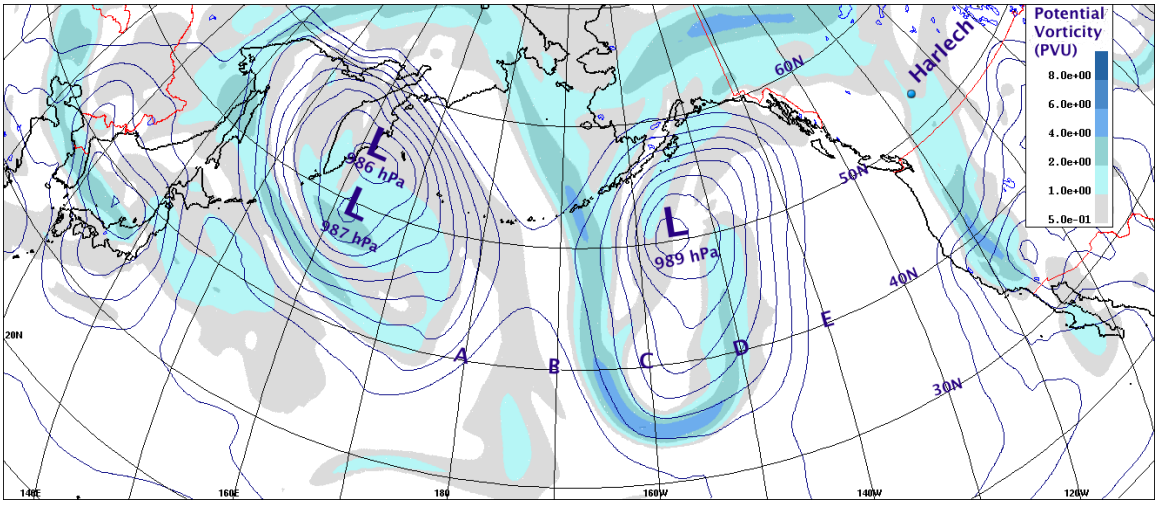

Figure 6.11: Potential vorticity (PV) 6000 m above the surface (color shading) and mean sea level pressure (continouous lines) valid April 02 2004, 00UTC.
The depth of the Pacific low pressure centers is shown in hPa, and their approximate position is indicated by a "L". A cross-section of the 3-D PV field along latitude 40°N, from points labelled A to E is shown in Figure 6.12.

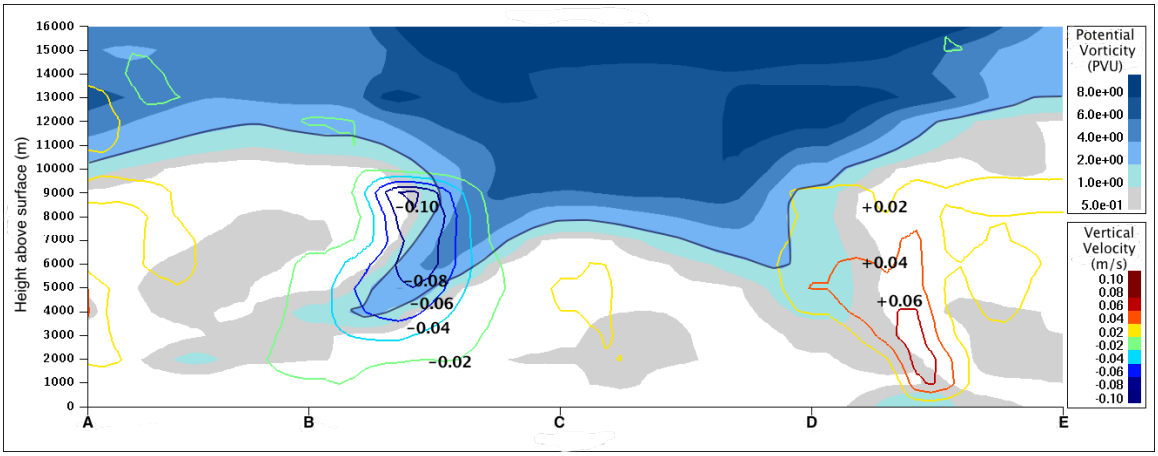

Figure 6.12: Cross-section of the potential vorticity in PVU, and of the vertical motion in m s^{-1}, shown by contour lines, along latitude 40°N valid 2 April 2004 00UTC.
The positions labeled A to E on the horizontal axis correspond to those in Figure 6.11. The continuous dark line delineates the tropopause according to the 2 PVU threshold.

CHAPTER 7

Exchanges between the Free Troposphere and the Boundary Layer

7.1 Introduction

The first section of this chapter presents a simple diagnostic model to estimate the vertical profiles of the turbulent wind velocity variances and of the turbulent kinetic energy (TKE). The model calculates the different terms of the turbulent velocity variance budget, with an emphasis on buoyancy and shear production terms. The model is applied to, and the results are compared with, observations from the Wangara field experiment and with micro-meteorological observations taken at the European Tracer Experiment (ETEX) release site.

The goal is eventually to apply this model to 3–D gridded "analyzed"[1] meteorological fields in a preprocessing step, in order to calculate 3–D fields of turbulent wind variances and turbulent kinetic energy. These fields are not usually available in meteorological analyses. However, here the model is only used to study the concept of an entrainment zone (EZ) and its implications on the turbulent wind variance and the vertical profile of TKE.

The second section discusses different strategies for modelling the transition between the

[1] 3–D gridded data meteorological fields derived from various meteorological observations which are unevenly distributed in space and time. These fields are then provided as initial conditions to the numerical weather prediction (NWP) models.

BL and the FT. It is shown that a realistic parametrization of σ_w^2 seems sufficient to estimate the trajectory of particles entering/exiting the PBL, only using the LSE's of equations (3.2) and (3.3) without any special treatment of the interface. This is the strategy now adopted in CMC long range dispersion models (section **4e** of the paper presented in section 4 of chapter 3).

7.2 A diagnostic model for turbulent fluxes in the PBL

7.2.1 Equations of motion in standard rotating coordinates

Newton's second law of motion, expressed in rotating coordinates, can be written as *Holton* [1992] equation (2.8) slightly modified):

$$\frac{D\mathbf{V}}{Dt} + f\mathbf{k} \times \mathbf{V} = -\frac{1}{\rho}\nabla p - \mathbf{g} + \mathbf{F}\,. \tag{7.1}$$

Here $\frac{D\mathbf{V}}{Dt}$ is the acceleration following the motion of the air parcel, $f\mathbf{k} \times \mathbf{V}$, the Coriolis effect, ∇p represents the pressure gradient force, $\mathbf{g}$, the gravitational acceleration, and $\mathbf{F}$, all other "body forces" that could be active.

7.2.2 Reynold's averaging

Equation (7.1) applies to the instantaneous properties of the atmospheric fluid. In the following sections, equations will generally be written in terms of mean properties and deviations from these means, using Reynolds averaging (e.g. *Wyngaard* [2010]). The instantaneous value of a given variable x is written as $\overline{x} + x'$ where $\overline{x}$ is the mean and x' the deviation from the mean; by definition $\overline{x'} = 0$, hence $\overline{x + x'} = \overline{x}$.

7.2.3 Mean momentum conservation

Neglecting viscous stresses, applying Reynolds averaging and assuming horizontal homogeneity, the mean horizontal components of equation (7.1) can be written as (e.g. *Wyngaard* [2010] p.207)

$$\frac{\partial \overline{u}}{\partial t} + \frac{\partial \overline{u'w'}}{\partial z} = f(\overline{v} - v_g)\,, \tag{7.2}$$

$$\frac{\partial \overline{v}}{\partial t} + \frac{\partial \overline{v'w'}}{\partial z} = f(u_g - \overline{u})\,, \tag{7.3}$$

where the mean pressure gradient forces are now expressed in terms of the geostrophic wind (u_g, v_g). Strictly speaking, the assumption of horizontal homogeneity would imply that the pressure force terms vanish. For now, we simply assume that the horizontal gradients of the turbulent fluxes are negligible in comparison with the vertical gradients. Furthermore, it is assumed that horizontal gradients of $\overline{u}$ and $\overline{v}$ are small enough to neglect mean horizontal momentum advection, and that transport of mean horizontal momentum by the mean vertical motion is negligible.

If profiles of $\overline{u}$ and $\overline{v}$ were available, equations (7.2) and (7.3) could be integrated with respect to z giving an estimation the fluxes $\overline{u'w'}$ and $\overline{v'w'}$:

$$\overline{u'w'}(z) = \int_{z_0}^{z} \Big[-\frac{\partial \overline{u}(\zeta)}{\partial t} + f(\overline{v}(\zeta) - v_g) \Big] d\zeta \,, \tag{7.4}$$

$$\overline{v'w'}(z) = \int_{z_0}^{z} \Big[-\frac{\partial \overline{v}(\zeta)}{\partial t} + f(u_g - \overline{u}(\zeta)\,) \Big] d\zeta \,, \tag{7.5}$$

with $\overline{u'w'}^2(z_0) + \overline{v'w'}^2(z_0) = u_*^4$, defining the friction velocity u_*, as in *Wilson* [2013].

7.2.4 Conservation of heat

The heat conservation equation is expressed in terms of the potential temperature θ, similarly to equation (3.5.3f) in *Stull* [1988]: [2]

$$\frac{d\overline{\theta}}{dt} = -\frac{1}{\overline{\rho} C_p} \left[L_\Upsilon \Upsilon + \frac{\partial \overline{Q^*}}{\partial x_j} \right] - \frac{\partial \overline{u_j' \theta'}}{\partial x_j}, \tag{7.6}$$

where, L_Υ is the latent heat of evaporation[3], Υ, the evaporation rate, $\overline{Q^*}$, the net radiation flux, $\overline{\rho}$, the mean air density, and C_p, the specific heat capacity of the air at constant pressure. Assuming horizontal homogeneity for the turbulent fluxes, and neglecting heating/cooling effects due to condensation/evaporation as well as radiation flux divergence, equation (7.6) reduces to:

$$-\frac{\partial \overline{w'\theta'}}{\partial z} = \frac{\partial \overline{\theta}}{\partial t} \,. \tag{7.7}$$

That equation could also be integrated with respect to z:

$$\overline{w'\theta'} - \overline{w'\theta'}(z_0) = -\int_{z_0}^{z} \frac{\partial \overline{\theta(\zeta)}}{\partial t} d\zeta \,, \tag{7.8}$$

[2] Einstein's summation convention is used

[3] for simplicity the difference between (gas – solid) or (gas – liquid) transition is not explicitly written

with $\overline{w'\theta'}(z_0) = Q_0/(\overline{\rho}C_p)$, where Q_0 is the sensible heat flux density at the surface (with the convention that a positive flux is upward).

7.2.5 Diagnostic model for the velocity variance

7.2.5.1 Budget equations for turbulent velocity variances and mean TKE

Under the assumptions expressed previously, the budget equations for the turbulent velocity variances are written similarly to equations (4.3.1h, i and j) in *Stull* [1988]:,

$$\frac{\partial \sigma_u^2}{\partial t} = -2\overline{u'w'}\frac{\partial \overline{u}}{\partial z} + \overline{\frac{2p'}{\rho_0}\frac{\partial u'}{\partial x}} - \frac{\partial \overline{w'u'^2}}{\partial z} - \epsilon_{uu}\,, \tag{7.9}$$

$$\frac{\partial \sigma_v^2}{\partial t} = -2\overline{v'w'}\frac{\partial \overline{v}}{\partial z} + \overline{\frac{2p'}{\rho_0}\frac{\partial v'}{\partial y}} - \frac{\partial \overline{w'v'^2}}{\partial z} - \epsilon_{vv}\,, \tag{7.10}$$

$$\frac{\partial \sigma_w^2}{\partial t} = \frac{2g}{\theta_0}\overline{w'\theta'} + \overline{\frac{2p'}{\rho_0}\frac{\partial w'}{\partial z}} - \frac{\partial \overline{w'w'^2}}{\partial z} - \frac{2}{\rho_0}\frac{\partial \overline{w'p'}}{\partial z} - \epsilon_{ww}\,. \tag{7.11}$$

σ_u^2, σ_v^2, σ_w^2 are the perturbation variances of the three wind components, and ϵ_{uu}, ϵ_{vv}, ϵ_{ww}, their respective viscous dissipation rates. Since equations (7.9), (7.10) and (7.11) were derived using the Boussinesq approximation, they are rewritten in terms of ρ_0 and θ_0, the density and potential temperature of a motionless adiabatic base (or reference) state. Setting $\tilde{\rho}$ and $\tilde{\theta}$ as the average deviations from the base state, then:

$$\overline{\rho} = \rho_0 + \tilde{\rho}\,, \tag{7.12}$$

$$\overline{\theta} = \theta_0 + \tilde{\theta}\,. \tag{7.13}$$

The Boussinesq approximation requires that $\tilde{\theta} \ll \theta_0$, and that $\tilde{\rho} \ll \rho_0$.

Summing equations (7.9), (7.10) and (7.11) and dividing by 2 yields the TKE budget:

$$\frac{\partial E}{\partial t} = -\overline{u'w'}\frac{\partial \overline{u}}{\partial z} - \overline{v'w'}\frac{\partial \overline{v}}{\partial z} + \frac{g}{\theta_0}\overline{w'\theta'} - \frac{\partial(\overline{w'E'})}{\partial z} - \frac{1}{\rho_0}\frac{\partial \overline{w'p'}}{\partial z} - \epsilon\,, \tag{7.14}$$

$$\tag{7.15}$$

where the mean TKE, E, is defined as:

$$E = \frac{1}{2}(\sigma_u^2 + \sigma_v^2 + \sigma_w^2)\,. \tag{7.16}$$

E' the instantaneous TKE is written as:

$$E' = \frac{1}{2}(u'^2 + v'^2 + w'^2)\,, \tag{7.17}$$

and the vertical flux of TKE $\overline{w'E'}$, as:

$$\overline{w'E'} = \frac{1}{2}\overline{w'(u'^2 + v'^2 +' w'^2)}\,. \tag{7.18}$$

A local convergence of $\overline{w'E'}$ indicates a local increase in turbulence. Because of the incompressibility approximation,

$$\overline{\frac{2p'}{\rho_0}\left(\frac{\partial w'}{\partial z} + \frac{\partial u'}{\partial x} + \frac{\partial v'}{\partial y}\right)} = 0\,, \tag{7.19}$$

and this sum does not appear in the mean TKE budget. However equation (7.19) shows how the pressure perturbations redistribute turbulence amongst the three components.

The budget equations (7.9) to (7.14) constitute the basis for the diagnostic model.

7.2.5.2 Turbulence production

In budget equations (7.9), (7.10), horizontal turbulence results from vertical shearing of the horizontal wind, the first term on the right-hand side of each of the equations. Vertical turbulence is produced or damped by buoyancy, which appears as the first term on the right-hand side of equation (7.11). As discussed above, a possible model for shear production would be:

$$S_u = -\,2\overline{u'w'}\frac{\partial \overline{u}}{\partial z}\,, \tag{7.20}$$

$$S_v = -\,2\overline{v'w'}\frac{\partial \overline{v}}{\partial z}\,, \tag{7.21}$$

and for the buoyancy:

$$B = \quad \frac{2g}{\theta_0}\,\overline{w'\theta'}\,. \tag{7.22}$$

The variance budget equations are rewritten as:

$$\frac{\partial(\sigma_u^2 + \sigma_v^2)}{\partial t} = (S_u + S_v) \quad + \overline{\frac{2p'}{\rho_0}\left(\frac{\partial u'}{\partial x} + \frac{\partial v'}{\partial y}\right)} - \frac{\partial \overline{w'(u'^2 + v'^2)}}{\partial z} \quad -(\epsilon_{uu} + \epsilon_{vv})\,, \tag{7.23}$$

$$\frac{\partial \sigma_w^2}{\partial t} = B \quad + \overline{\frac{2p'}{\rho_0}\frac{\partial w'}{\partial z}} - \frac{\partial \overline{w'w'^2}}{\partial z} - \frac{2}{\rho_0}\frac{\partial \overline{w'p'}}{\partial z} \quad -\epsilon_{ww}\,, \tag{7.24}$$

$$\textbf{Rate} = \textbf{Production} \quad + \textbf{Redistribution} + \textbf{Vertical Transport} \quad - \textbf{Dissipation}$$

and for the TKE:

$$\frac{\partial E}{\partial t} = -\frac{1}{2}(S_u + S_v + B) - \frac{\partial \overline{w'E'}}{\partial z} - \frac{1}{\rho_0}\frac{\partial \overline{w'p'}}{\partial z} - \epsilon\,. \tag{7.25}$$

7.2.5.3 Redistribution

It can easily be seen that vertical shear only acts to produce horizontal turbulence and that buoyancy only acts on the vertical component. It is only through pressure redistribution that shear generated horizontal turbulence can be transformed into vertical turbulence, similarly for buoyancy to affect horizontal turbulence.

Following *Wilson* [2012] and many earlier authors, the pressure redistribution term, also known as return to isotropy, is modelled as:

$$R_{ww} = \overline{\frac{2p'}{\rho_0}\frac{\partial w'}{\partial z}} = c_R \frac{2/3E - \sigma_w^2}{\tau_w}\,, \tag{7.26}$$

$$R_{uu} + R_{vv} = -R_{ww}\,, \tag{7.27}$$

and vertical transport of TKE and of pressure perturbation are modelled in terms of a diffusion coefficient and vertical gradients of the mean quantities:

$$-\frac{\partial \overline{w'u'^2}}{\partial z} = \frac{\partial}{\partial z}\left[K\frac{\partial \sigma_u^2}{\partial z}\right], \tag{7.28}$$

$$-\frac{\partial \overline{w'v'^2}}{\partial z} = \frac{\partial}{\partial z}\left[K\frac{\partial \sigma_v^2}{\partial z}\right], \tag{7.29}$$

$$-\frac{\partial \overline{w'w'^2}}{\partial z} - \frac{2}{\rho_0}\frac{\partial \overline{w'p'}}{\partial z} = \frac{\partial}{\partial z}\left[K\frac{\partial \sigma_w^2}{\partial z}\right], \tag{7.30}$$

$$-\frac{\partial (\overline{w'E'})}{\partial z} - \frac{1}{\rho_0}\frac{\partial \overline{w'p'}}{\partial z} = \frac{\partial}{\partial z}\left[K\frac{\partial E}{\partial z}\right]. \tag{7.31}$$

The diffusion coefficient K is parameterized as a function of the vertical velocity variance and a time scale τ_w such that $K = c_K \sigma_w^2 \tau_w$ where c_K is an empirical constant. The TKE dissipation rate ϵ is modelled in term of the timescale τ_w:

$$\epsilon = c_\epsilon \frac{E}{\tau_w}\,, \tag{7.32}$$

$$\epsilon_{ww} = c_\epsilon \frac{\sigma_w^2}{\tau_w}. \tag{7.33}$$

The time scale τ_w is also modelled as in *Wilson* [2012]:

$$\frac{1}{\tau_w} = \frac{\phi_m}{k_V z}\frac{\sigma_w^2}{u_*} + N + \frac{1}{\tau_\infty}\,, \tag{7.34}$$

where ϕ_m is a stability function. k_V is the von Karman constant, and N is a buoyancy frequency

$$N = \begin{cases} 0 & \partial\overline{\theta}/\partial z \le 0\,, \\ \left(\frac{g}{\theta_0}\frac{\partial \overline{\theta}}{\partial z}\right)^{1/2} & \partial\overline{\theta}/\partial z > 0\,. \end{cases} \tag{7.35}$$

The time scale limit τ_∞ is set at 600 seconds, and the surface layer stability correction function ϕ_m was specified as [*Högström*, 1988],

$$\phi_m(z/L) = \begin{cases} (1 - 19.3z/L)^{-1/4} & L < 0\,, \\ 1 + 4.8z/L & L \geq 0\,, \end{cases} \tag{7.36}$$

where L is the Obukhov length

$$L = \frac{-\theta_0 u_*^3}{k_V g Q_0}\,. \tag{7.37}$$

7.2.5.4 Quasi-steadiness

The quasi-steadiness hypothesis would imply that:

$$\frac{\partial E}{\partial t} = (S_u + S_v + B) + \frac{\partial}{\partial z}\left[c_K \sigma_w^2 \tau_w \frac{\partial E}{\partial z}\right] - c_\epsilon \frac{E}{\tau_w} \qquad = 0\,, \tag{7.38}$$

$$\frac{\partial \sigma_w^2}{\partial t} = 2B + \frac{\partial}{\partial z}\left[c_K \sigma_w^2 \tau_w \frac{\partial \sigma_w^2}{\partial z}\right] + c_R \frac{(2/3E - \sigma_w^2)}{\sigma_w} - c_\epsilon \frac{\sigma_w^2}{\tau_w} \qquad = 0\,. \tag{7.39}$$

Our hypothesis is that vertical profiles of σ_w^2 and E satisfying the above equations do exist and can be found by integrating equations (7.38) and (7.39) with respect to time, maintaining constant the buoyancy B and shear S terms, until a steady state for σ_w^2 and E is found.

From equations (7.7) and (7.8) one expects the potential temperature $\theta(z)$ to be changing in time, otherwise the buoyancy production term B has to be constant in the vertical. This would seem to contradict the quasi-steadiness hypothesis. It will be seen further down that this is not the case.

7.2.5.5 Numerical solution

The time integration of equations (7.38) and (7.39) is performed in two steps. In a first intermediate step, production, redistribution and dissipation are handled with a simple forward time step:

$$E(t + \Delta t)^\star = E(t) + \left[(S_u + S_v + B) - c_\epsilon \frac{E}{\tau_w}\right]\Delta t\,, \tag{7.40}$$

$$\sigma_w^2(t + \Delta t)^\star = \sigma_w^2(t) + \left[2B + c_R \frac{(2/3E - \sigma_w^2)}{\sigma_w} - c_\epsilon \frac{\sigma_w^2}{\tau_w}\right]\Delta t\,. \tag{7.41}$$

Then a semi-implicit Crank-Nicholson scheme is applied to the diffusive terms, using the intermediate values $E^\star$ and $\sigma_w^{2\star}$. Details on the implementation of the scheme are given in Appendix B.

7.2.6 Application to day 33 of the Wangara experiment

Observed data for day 33 of the Wangara experiment [*Clarke*, 1970] has often been used to test boundary layer models (e.g. *Yamada and Mellor* [1975]; *André et al.* [1978]; *Sun and Ogura* [1980]; *Wilson* [2012]).

Figure 7.1 shows wind and temperature profiles observed for hour 15 EST, on day 33. The wind profiles are not very regular and show vertical gradients which are changing sign a few times in the 2 km layer. Winds are generally increasing in intensity from hour 14 to hour 15, up to about 1200 m. Using these winds and the given geostrophic wind to evaluate the shear production terms (equations (7.20), (7.21)), it was found that the integral equations (7.4) and (7.5) do not provide useful estimates of the vertical momentum fluxes, and occasionally result in negative shear production. Likely some of the hypotheses behind those are not holding up. It was therefore decided to use the gradient approximation for shear production, again as in *Wilson* [2012]. The shear production terms become:

$$S_u + S_v \quad = \quad \sigma_w^2 \tau_w \left[\left(\frac{\partial u}{\partial z} \right)^2 + \left(\frac{\partial v}{\partial z} \right)^2 \right], \tag{7.42}$$

where the constant c_K is set to one. Constants c_R and c_ϵ are respectively set to 0.122 and 0.233, again after *Wilson* [2012].

On the other hand, the potential temperature in Figure 7.1 is quite constant up to the inversion level, which could be seen as the top of the boundary layer (BL). The temperature profile was also relatively uniform 3 hours before, indicating that the BL is been warmed at a nearly uniform rate during that time. This implies that turbulent mixing is occurring quite rapidly and that the BL is nearly in thermal equilibrium during the 3-hour period, supporting the quasi-steadiness hypothesis for θ.

Figure 7.2 shows the shear production and potential temperature flux obtained by applying the model directly to the observed profiles. There is a large shear production very close to the surface and significant production in the upper part of the BL. There is also important production above the θ inversion level. The vertical flux of temperature decreases almost linearly, to become negative just below the inversion level. It becomes slightly positive again in the stable layer, at about the same level as shear production is again significant. This coincidence would result in turbulence generation above what seems the top of the BL, based on the θ profile. It seems that the fairly large vertical variations in the production terms result from rather small fluctuations, localized in space and time, in the observed profiles. According to *Clarke et al.* [1971], measurements for the 2 km radiosonde flights were taken in about 7 minutes.

Figure 7.3 shows results from the application of the diagnostic model to filtered profiles, using equations 7.42 for shear production, and 7.22 for buoyancy production. The filtering results from the application a least square seventh order polynomial fit to the observations. The TKE is smaller than σ_w^2 up to about 600 m, most of the turbulent velocity variance being in the vertical component below that level. Above 600 m, shear production becomes larger than buoyancy production, and the TKE increases because of a significant increase in the horizontal velocity variance. Despite filtering, the vertical wind shear seen in Figure 7.1 remains significant. The layer where buoyancy is negative could delineate the entrainment zone as in the Deardorff model (Fig. 7.4). The sharp cut-off in the diffusion and shear terms near the top of the BL, in the middle panel, results from σ_w^2 not being allowed to fall below a low threshold value (and certainly not < 0) while the buoyancy term remains more or less constant at a negative value with increasing z.

Figure 7.5 shows results from the application of the diagnostic model to the modelled profiles of potential temperature and horizontal wind given by *Wilson* [2012] (Figures 2 and 3) for 15H00 EST. In this application buoyancy is also diagnosed using the gradient approximation, for coherence:

$$B = -\frac{2g}{\theta_0}\sigma_w^2 \tau_w \frac{\partial \overline{\theta}}{\partial z}\,. \tag{7.43}$$

It can be seen that most of the TKE results from vertical turbulence. This indicates that buoyancy is the dominant production term, and results from the small $\overline{\theta}$ gradients. As

soon as $\partial\overline{\theta}/\partial z$ becomes positive, buoyancy shuts off. The various budget terms indicate the presence of an entrainment zone topped by the sharp $\overline{\theta}$ inversion. Figure 7.6 shows that steadiness is achieved in about $1/2$ hour by the diagnostic model, and that variance and TKE from *Wilson* [2012] first-order closure model are reproduced, given the appropriate wind and temperature profiles as input.

Figure 7.7 shows the different TKE budget terms which can be compare roughly with the *Sun and Ogura* [1980] third-order closure model. Results from the diagnostic model appear just as plausible as those from the more complex model. The entrainment zone, defined by the region where buoyancy destroy turbulence is about 400 m, (Figure 7.5, is about the same thickness as the layer of high variability in the instantaneous specific humidity in Figure 2.3, which can also be seen as the entrainment zone.

7.2.7 Application to meteorological observation data for the European Tracer Experiment, ETEX

The European Tracer Experiment – ETEX– was a large scale controlled tracer dispersion experiment which took place in the fall of 1994 [*van Dop. H. et al.*, 1998]. A large number of surface tracer concentration observations were collected during several days following the release and were assembled in a database which constitutes one of the very few tools to test and validate long range dispersion models. The use of this data is discussed in sections **5c** and **5e** of the paper presented in chapter 3. Special meteorological observations were made at the tracer source location, before and while the tracer was being released [*Gryning et al.*, 1998]. The ETEX data can be retrieved from the following URL: http://rem.jrc.ec.europa.eu/etex/.

Detailed radiosoundings were taken at three hour intervals from Oct 23 12H UTC to Oct 24 03H UTC. A sonic anemometer, positioned 18 m above ground, was also active Oct 23 - 26 providing time series of 10-minute averaged momentum and temperature fluxes (effective 10 Hz sampling rate). Figure 7.8 shows vertical profiles of wind and potential temperature taken in the afternoon and evening of Oct 23. Data is available every 5 – 10 m intervals up 5 km or more. For this analysis the data were averaged into layers of about 40 m depth, and filtering was applied by fitting a least-square eleventh order polynomial. All

soundings show a very strong wind shear, especially near the surface. According to the θ profiles, at 12H UTC and 15H UTC, a shear driven CBL should exist. At 19H UTC and 23H UTC there is a fairly strong θ surface inversion in conjunction with a strong vertical wind shear. At 15H UTC, the observed vertical wind profile is peculiar in the sense that winds are decreasing with altitude producing a negative shear. According to *Gryning et al.* [1998], this could have been caused by very light and barely noticeable showers.

The full gradient version of the diagnostic model (where shear and buoyancy are modelled according to wind and temperature vertical gradients, equation (7.42) and (7.43), respectively) was applied to the four filtered profiles shown in Figure 7.8. For the 12H UTC and 15H UTC profiles, unstable conditions, the effect of shear is to produce fairly high horizontal velocity variances, Figures 7.9 and 7.10. In stable conditions, the 19H UTC and 23H UTC profiles, the model equilibrium state is minimum variance and TKE; the damping effect of buoyancy is simply to destroy all turbulence, despite the strong vertical shear. It is difficult to validate the results, the only reliable data being that of the sonic anemometer. A quick comparison with the modelling results with the sonic data can be made in Table 7.1. Modelled and observed values are comparable at 12H UTC. At 15H UTC, the modelled TKE is stronger than observed, but still within believable range.

Table 7.1: *Observed and modelled vertical velocity variance and TKE, on October 23 1994.*

ß Modelled values were abstracted from the profiles shown in Figures 7.9 and 7.10, at 20 m above ground. The model did not produce any results for SBL conditions. The observed values were obtained from the sonic anemometer records, and the values shown are averaged over one hour, centered on the hour. The sonic anemometer was positioned 18 m above ground.

Time	Sonic σ_w^2	Sonic E	Model σ_w^2	Model E
12H UTC	1.0	2.7	1.5	4.5
15H UTC	0.6	1.3	1.7	7.8
19H UTC	0.6	1.2	$\sim$	$\sim$
23H UTC	0.6	1.3	$\sim$	$\sim$

7.3 Modelling transport across the Entrainment Zone

In many dispersion models (e.g. FLEXPART: *Stohl et al.* [2005]) turbulence alone cannot move particles from the BL into the FT. When the displacement resulting from the application of a finite time-step Δt to equations (3.2) and (3.3) would cross the top of the BL, a total reflection is applied to the trajectory element, sending the particle downward by the same distance it would have moved above the BL top. One of the reasons for imposing this total reflection is that the size of the incremental trajectory element could be of order of the EZ thickness itself, resulting in numerical errors and possibly violating the *wmc*. *Wilson and Flesch* [1993] discuss the implications of reflective boundaries on the *wmc*. Such a total reflection condition had been implemented in CMC's models (this is the case for the simulations described in chapters 5 and 6). A particle can nevertheless be entrained in the BL, if the BL thickness increases enough to reach the particle's level, because of daytime heating for example. Likewise, a particle can be left suspended in the FT, when the BL thins out at night time.

As discussed in section **3b** of the paper section 4, the time step in a first order Lagrangian model must be much smaller than $T_L = 2\sigma_w^2/C_0\epsilon$. Typically the constraint is less stringent near the top of the BL than near the ground surface. The diagnostic model results, and available observation data, indicate that the vertical velocity variance σ_w^2 decreases rather smoothly near the top of the BL, and that even a parameterized profile can yield plausible turbulence statistics in that region without an explicit modelling of the EZ. For those reasons the reflection condition was removed for the BL top, in the updated version of CMC's long-range Lagrangian dispersion model presented in the paper of section 4.

Figure 7.11 shows FT – BL exchanges during 3-hour periods, for 2 different BL top algorithms. The simulations are for ETEX first release, and both are using a first-order LSM for the complete duration of the simulation. Values are expressed in terms of the tracer mass fraction (i.e. relative to the total tracer mass inside the model domain) because the tracer mass is not constant during the course of the simulation. It increases continuously during the release period, the first 12 hours, and near the end of the simulation, some of the tracer is transported outside of the model domain. The two algorithms produce slightly

different results, especially in the first 12 hours of the simulations where the solid "lid" of the reflection approach has clearly the effect of keeping more tracer in the BL. In the last part of the simulation, starting around Oct 26 06H, the tracer mass fraction inside the BL (bottom panel in Fig. 7.11) is consistently slightly higher with the non-reflection algorithm. A possible explanation would be that the non-reflection approach allows for more diffusion between the two layers. There are some indications for this in the 3-hour exchanges shown in the two upper panels. Later on it is easily seen that it is the diurnal cycle driving the BL depth which determines the exchange rate between the FT and the BL. However no firm conclusions can be drawn from this analysis since the FT – BL transfers are based on the boundray layer height provided the GEM model. Discrepancies between TKE profiles and the boundary layer height provided by GEM have often be noticed.

Figure 7.12 allows to compare profiles of the vertical velocity variance obtained using an empirical parameterization with those resulting from the diagnostic model simulation. The parameterization used is that of equation (15), in the paper of section 4. There are no claims at this stage that the diagnostic model can produce better turbulence statistics than the empirical parameterization. However the profiles of σ_w^2 look reasonable enough to think that the associated budget terms, shown in the central panels of Figures 7.3, 7.5, 7.9 and 7.10, give a credible picture of an entrainment zone where buoyancy gradually dampens turbulence. The EZ so depicted extends over a layer that constitutes a sizable fraction of the BL. This is coherent with the observed specific humidity profiles shown in Figures 2.2 and 2.3. It is also of interest to not that the profiles of σ_w^2 decrease relatively smoothly wiith height within the EZ. Another perhaps minor advantage of the model, is that a prior estimation of the CBL depth is not required.

7.4 Figures

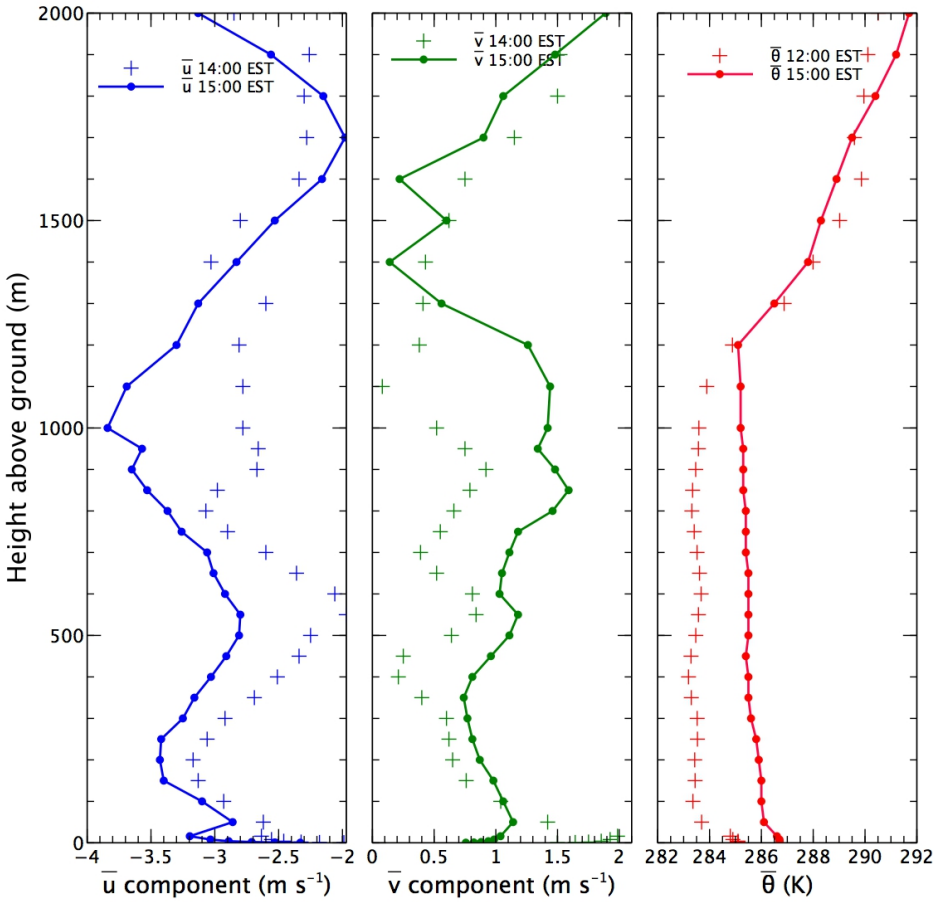

Figure 7.1: Observed vertical profiles from radio soundings for 14H00 EST and 15H00 EST on day 33 of the Wangara Experiment [*Clarke et al.*, 1971].
Observations taken one hour earlier are also shown for the $\overline{u}$ and $\overline{v}$ wind components. The radiosonde winds were completed with observations in the surface layer. These were taken at slightly different locations and show some discrepancies. Potential temperatures ($\overline{\theta}$) are available only at 3 hour intervals, so the profile for 12H00 EST is shown. $\overline{\theta}$ values in the surface layer were interpolated linearly between the surface and the lowest radiosonde level.

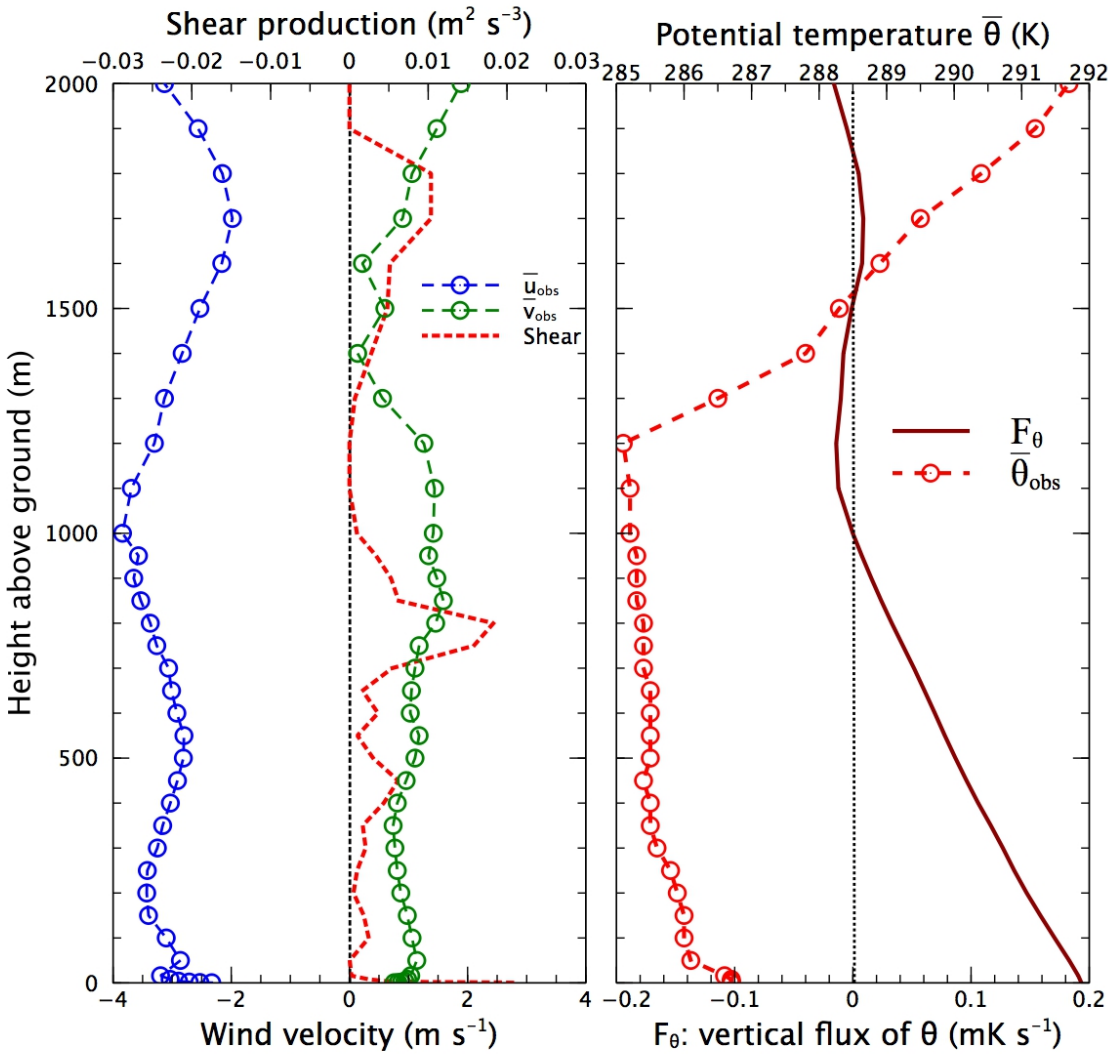

Figure 7.2: Shear production and potential temperature flux based on raw observations, for 15H00 EST on day 33.
For comparison, profiles of the wind components and of $\overline{\theta}$ values are also shown.

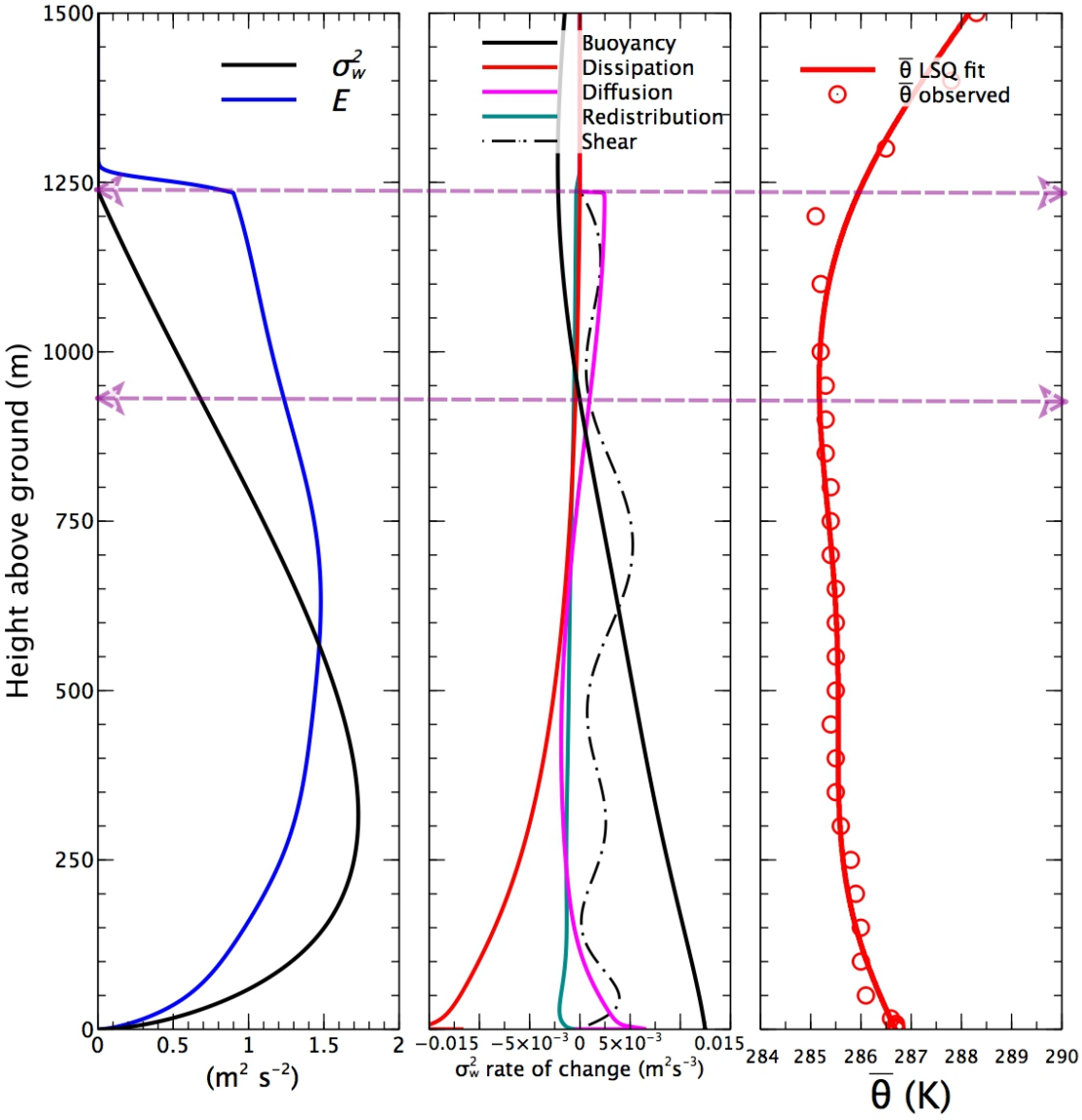

Figure 7.3: Diagnostic model results based on filtered observations for 15H00 EST. Leftmost panel: vertical profiles of turbulent kinetic energy E, σ_w^2. Central panel: budget terms for σ_w^2. Shear production, active only in the E budget, is also shown. Right hand panel: observed and filtered $\overline{\theta}$ profiles. The horizontal purple lines delineate the possible entrainment zone as in the Deardorff model, shown in Figure 7.4.

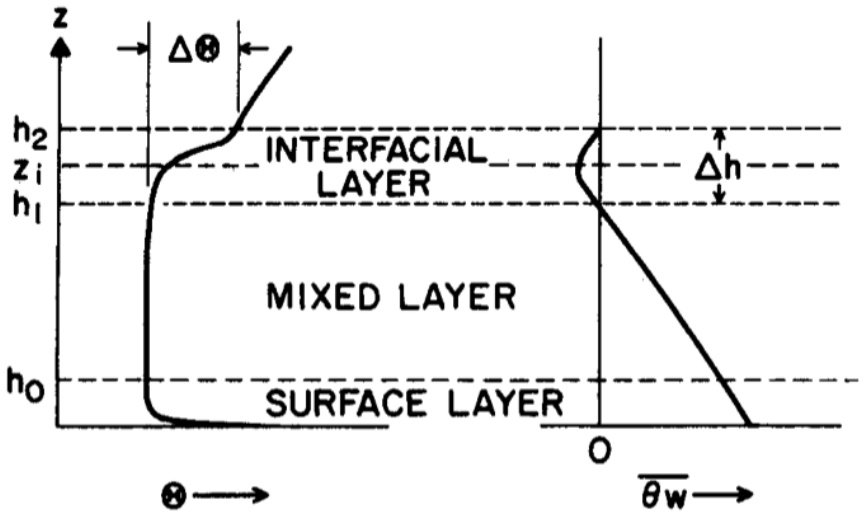

FIG. 1. A three-layer model of the averaged structure of the convective PBL (after Deardorff, 1979).

Figure 7.4: Entrainment zone model proposed by Deardorff [*Wyngaard*, 1985]

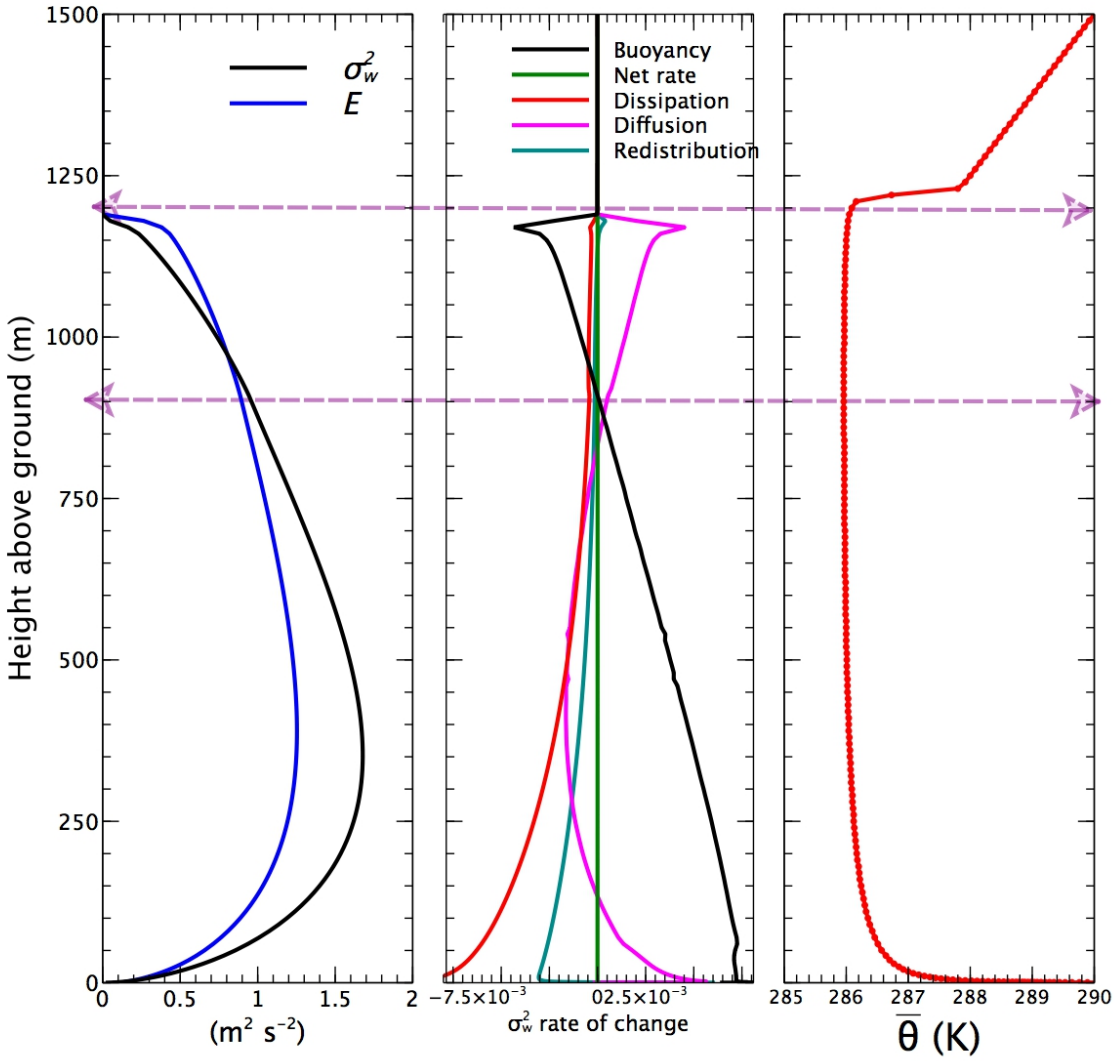

Figure 7.5: Diagnosed vertical profiles of the turbulent kinetic energy E, and vertical velocity variance σ_w^2.
Imposing the vertical profiles of $\overline{u}, \overline{v}$ (leftmost panel) and of $\overline{\theta}$ (shown on the rightmost panel) from *Wilson* [2012], for 15H00 EST. The middle panel shows the budget terms for σ_w^2. The dashed purple lines define the entrainment zone.

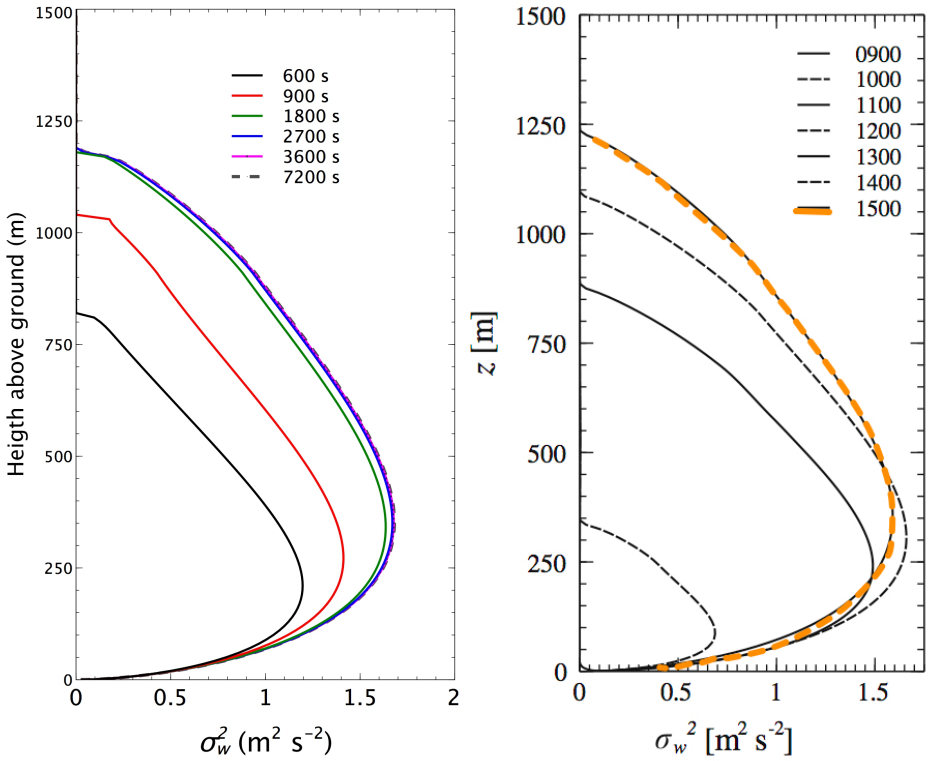

Figure 7.6: Left hand panel:vertical profiles of σ_w^2 for 15H00 EST, after different integration times.
A steady state is achieved after 1800 s. Right hand panel: vertical profiles obtained by *Wilson* [2012]. The profile for hour 15H00 EST is enhanced in orange. Given the the same profiles, the diagnostic model reproduces essentially the same σ_w^2.

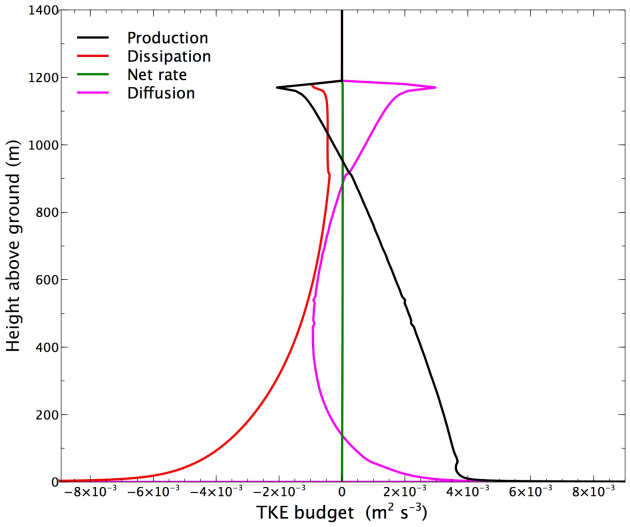

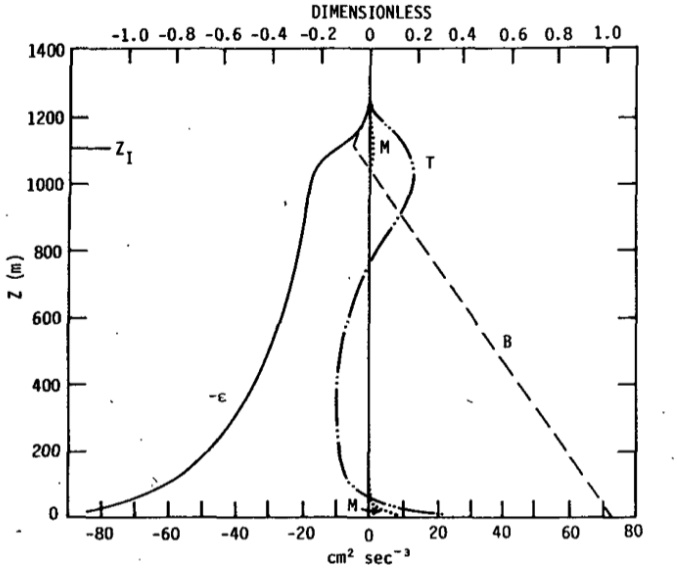

FIG. 13. Eddy kinetic energy budget at 1400 EST; *B*, buoyant production; *M*, mechanical (shear) production; $-\epsilon$, dissipation; *T*, turbulent transport. The variables are made dimensionless by w_*^3/Z_I (=71.8 cm² s⁻³).

Figure 7.7: Vertical distribution of the turbulent kinetic energy, E, budget terms. In the upper panel, for a simulation using profiles $\overline{u}, \overline{v}$ and $\overline{\theta}$ profiles for 15H00 EST from *Wilson* [2012]. These can be roughly compared with results for 14H00 EST obtained by *Sun and Ogura* [1980] with a level 3 turbulence closure model, in the lower panel.

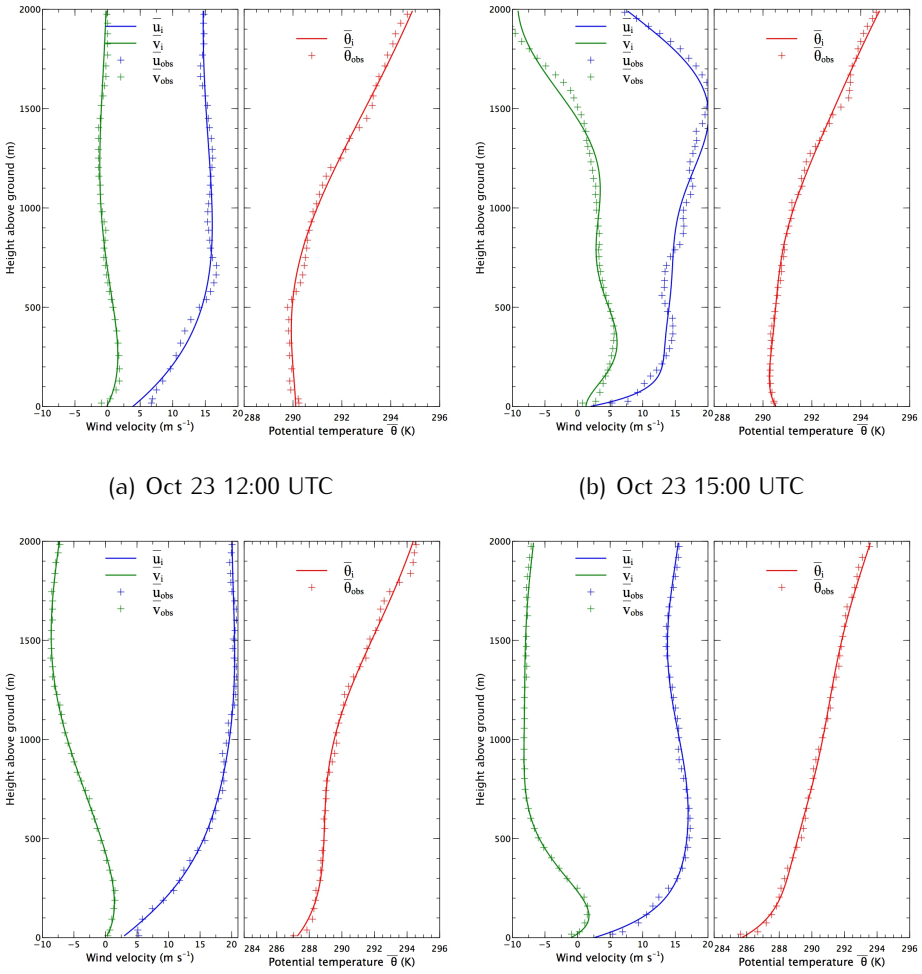

(a) Oct 23 12:00 UTC

(b) Oct 23 15:00 UTC

(c) Oct 23 19:00 UTC

(d) Oct 23 23:00 UTC

Figure 7.8: Wind and potential temperature profiles observed at the beginning of the first ETEX.
The vertical resolution is about 5 – 10 m, but the data have here been aggregated into $\sim$ 40 m layers. Aggregated observations are indicated by a + symbol. An eleventh order polynomial least-square fit is shown as a continuous line.

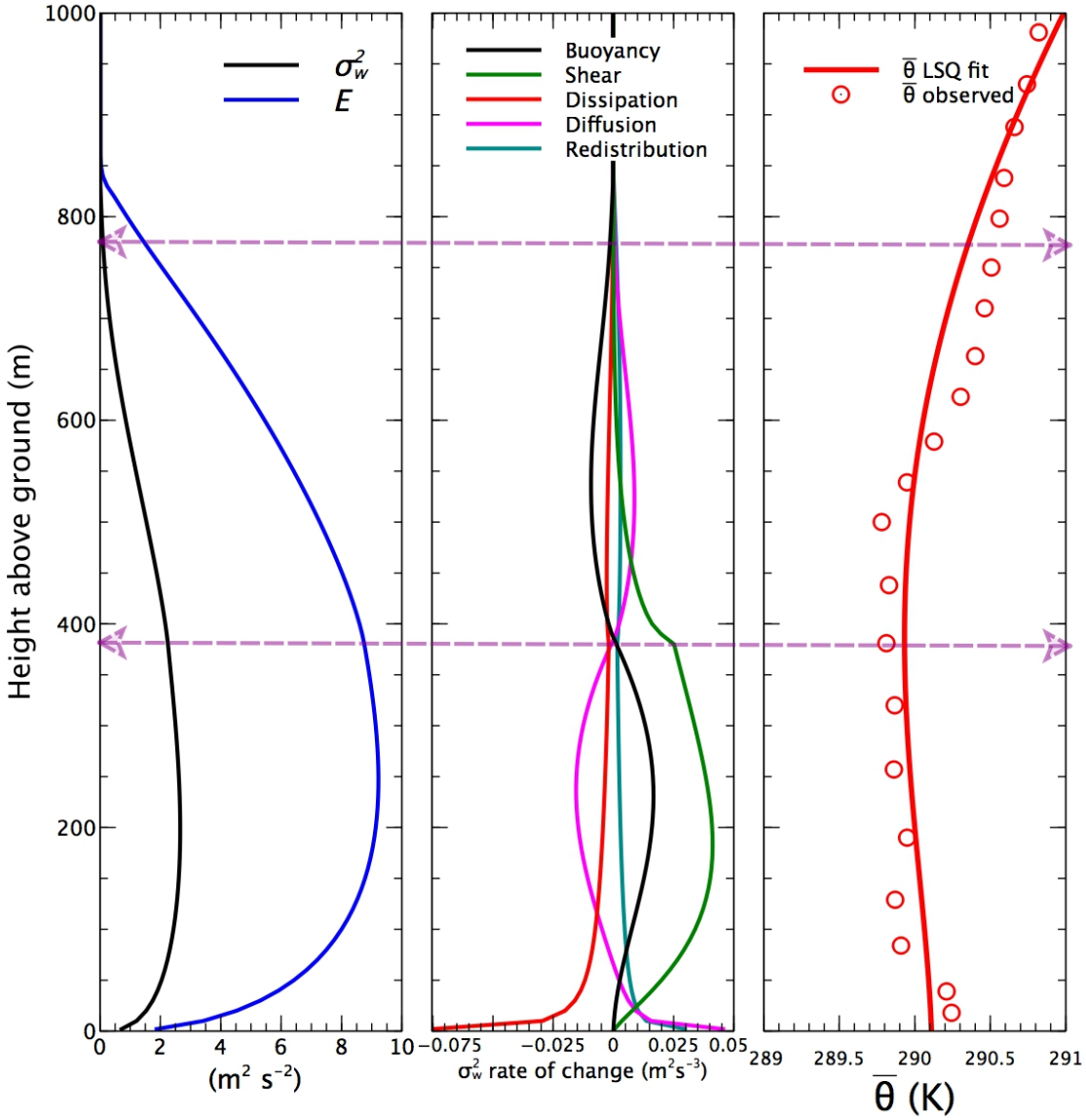

Figure 7.9: Model results based on filtered ETEX observations for Oct 23 12:00 UTC. The filtered data result from an eleventh order polynomial least-square fit. Left hand side panel: vertical profiles of turbulent kinetic energy E, σ_w^2. Central panel: budget terms for σ_w^2; the "Shear" component is for the TKE budget. Right hand side panel: observed and filtered θ profiles

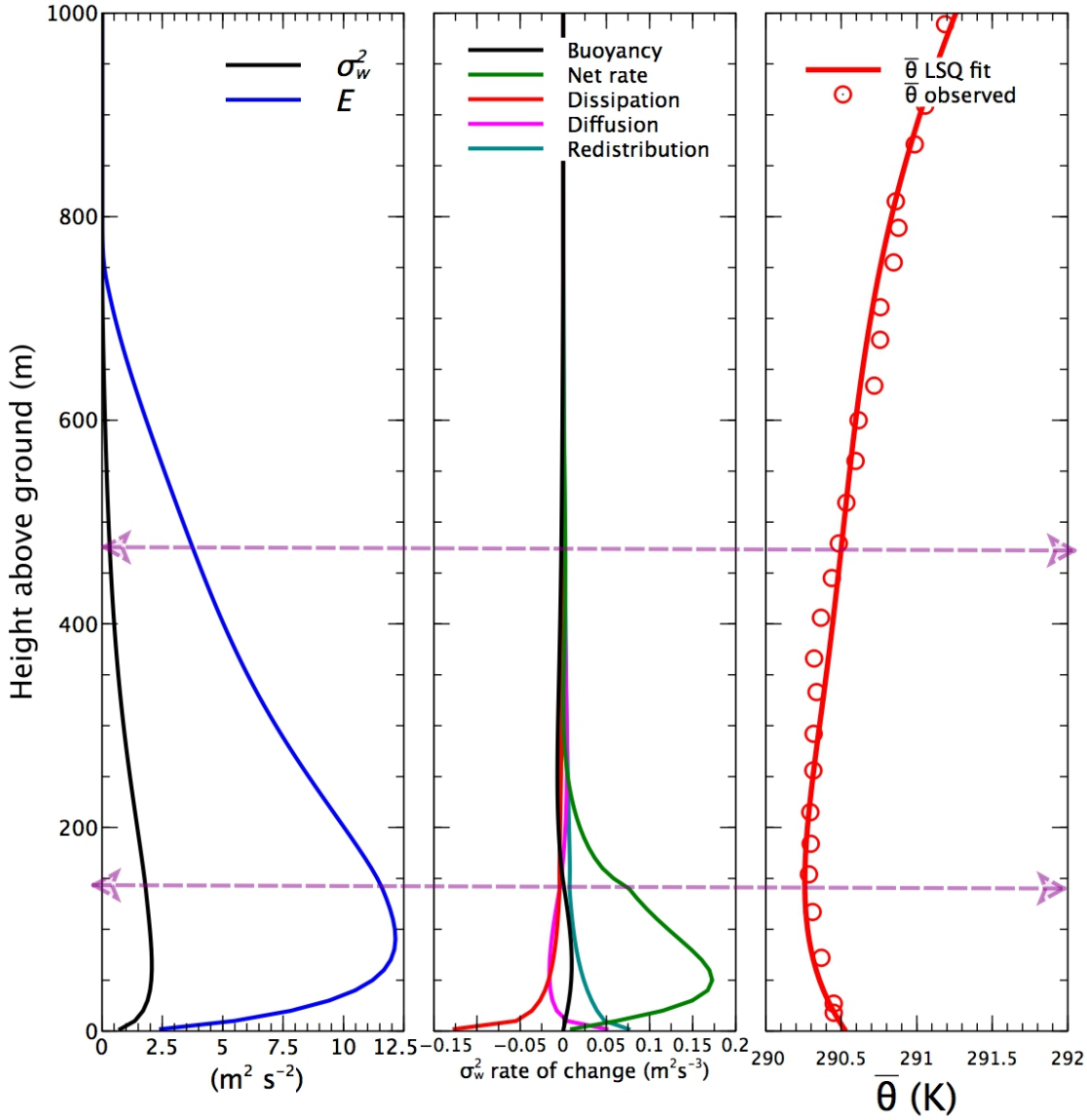

Figure 7.10: Model results based on filtered ETEX observations for Oct 23 15:00 UTC. The filtered data results from an eleventh order polynomial least-square fit. Left hand side panel: vertical profiles of turbulent kinetic energy E, σ_w^2. Central panel: budget terms for σ_w^2; the "Shear" component is for the TKE budget. Right hand side panel: observed and filtered θ profiles

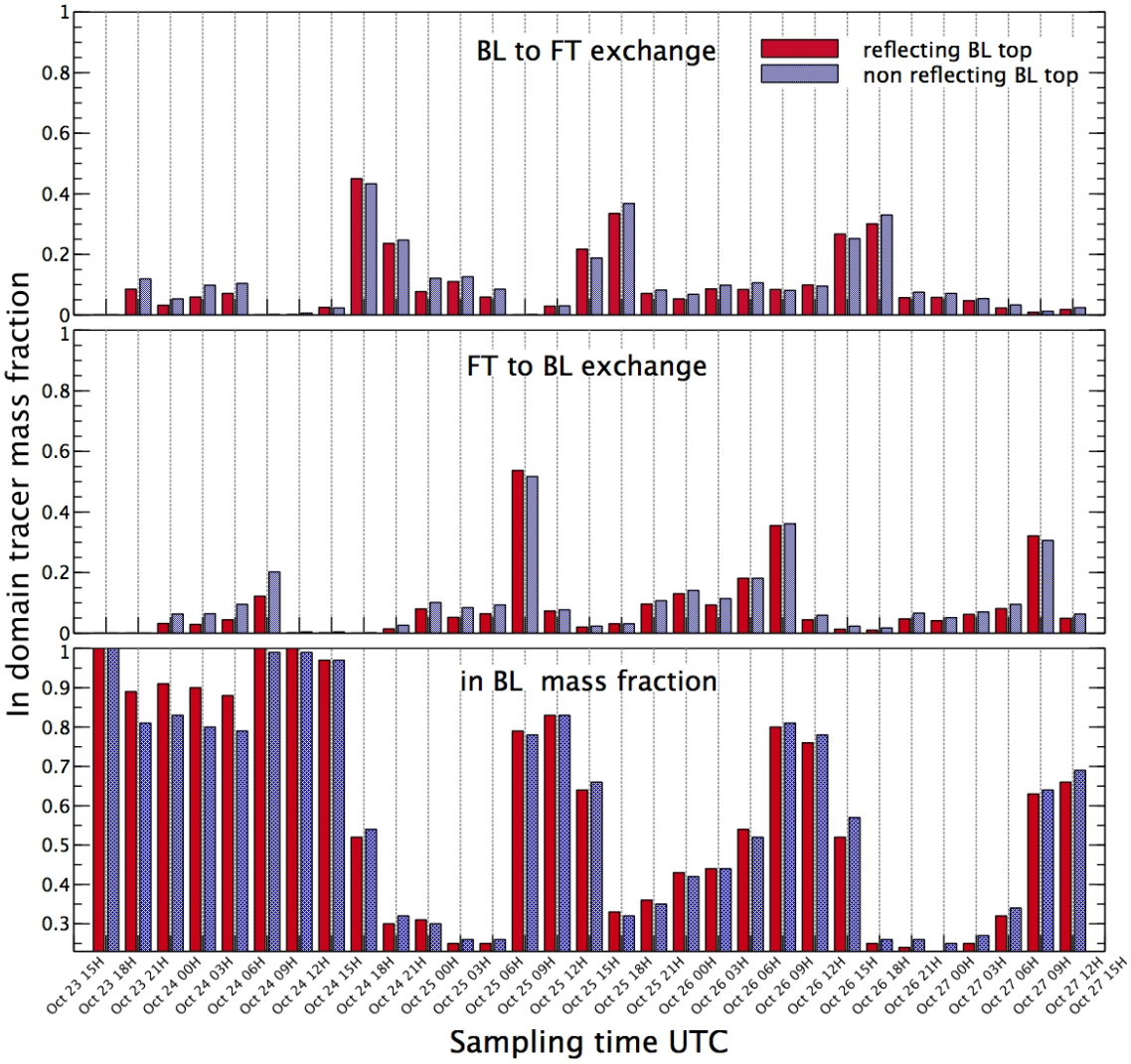

Figure 7.11: FT – BL exchanges for 3-hour periods, for 2 different BL top algorithms. The simulations are for ETEX first release using full first-order LSM. The top panel shows exchanges from the BL to the FT, the middle panel exchanges from the FT to the BL, and the bottom panel, the fraction of the tracer mass inside the BL. The mass fraction is relative to the total tracer mass in the model domain (see text).

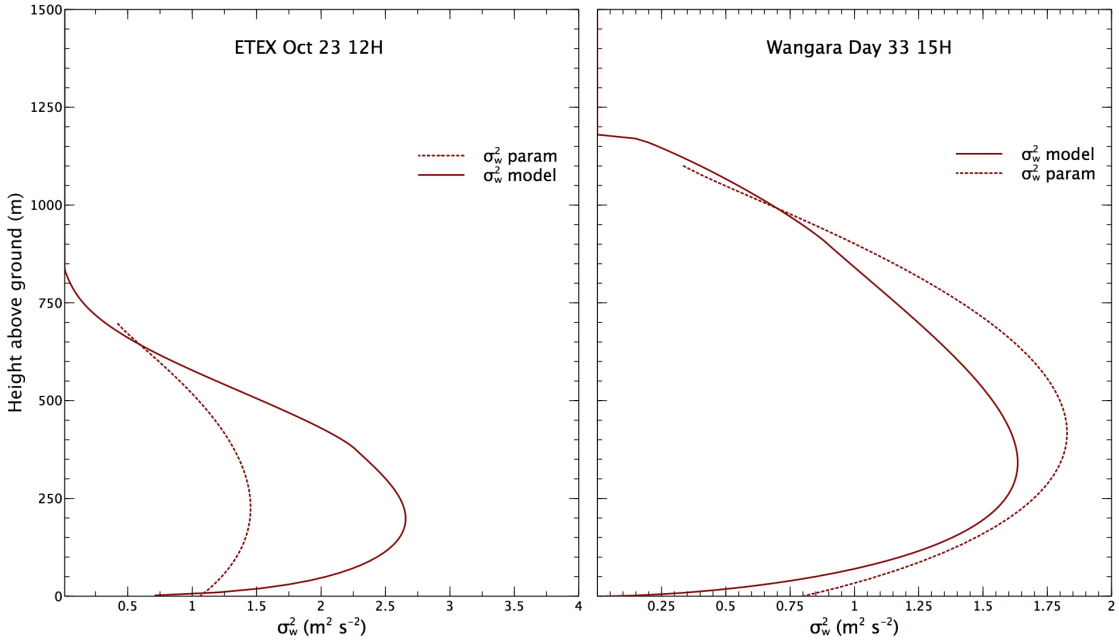

Figure 7.12: Vertical velocity variance σ_w^2 profiles resulting from an empirical parameterization and from a diagnostic model simulation for two cases.
The parameterization used is that of equation (15), in the paper of section 4.

CHAPTER 8

Conclusions

The thesis presents investigations of transport and dispersion within the different layers of the atmosphere, and of the exchanges between those layers. The investigations are based on simulations using Lagangian dispersion models for real cases, where observations are available. All of the cases presented here were published in one or another of three different papers.

The theoretical basis of the Lagrangian models is reviewed in depth in Chapter 3 asserting the validity of the approach. In particular the relationship between the Langevin equation and the Fokker-Planck equation is illustrated by comparing the evolving cloud of particles, in phase-space, resulting from the trajectories of a large number of fluid elements, with the evolving probability density distribution of these elements in this phase-space. The characteristics of the models used for this thesis are discussed in detail in the paper presented in Chapter 4. This paper establishes the accuracy and credibility of the modelling with extensive validation of real case simulations where observations are available. Some of the results are also used to support the main conclusions of the thesis.

The paper presented in Chapter 5 shows clearly that in the stratosphere, the air circulates in well maintained streams with little vertical mixing. The sulfate aerosol plumes resulting

from the volcanic eruptions in the Alaskan Peninsula during the summer of 2008 could be followed for many days after their injection into the stratosphere (e.g. Figures 5.8 and 5.9, and Figures 5.12 and 5.13).

On the other hand the paper presented in Chapter 6 investigates the processes by which stratospheric air could be transported to the surface. This was done by investigating the possible source regions of ^{7}Be observed near the surface, at Harlech in the Albeta foothills. For that purpose special metrics were developed, the Layer Mean Residence Time, and the Weighted Layer Mean Residence Time, in order to assess the relative contribution of air originating from different layers of the atmosphere in the total air volume sampled at the station. Other metrics were also developed, the Layer Exit Rate and the Layer Exit Time. The calculation of these metrics is only possible in the context of Lagrangian modelling, by considering all the individual particle trajectories. It is seen that transfers between the lower stratosphere and the upper troposphere do occur regularly, but are generally confined to regions fairly close to the tropopause (e.g. Figure 6.6). Nevertheless it is also seen that strong and deep subsidence in tropopause folds associated with well developed cyclonic systems, occur frequently enough to feed regular streams of stratospheric air into the mid and low troposphere (e.g. Figure 6.8) which can be entrained in the boundary layer at later times.

The mechanisms governing exchange between the free troposphere and the boundary layer are examined in detail in Chapter 7. A simple diagnostic model to calculate the turbulent kinetic energy and the turbulent velocity variances was developed and is used to investigate the entrainment zone at the interface between the PBL and the FT. Application to day 33 of Wangara experiment shows that the model produces plausible profiles of the vertical velocity variance σ_w^2, and that the vertical distribution of buoyancy production/destruction of this variance, implies to an entrainment zone (EZ), just as credible as that resulting from more complex models (e.g. Figure 7.7). This EZ compares well with the EZ deduced from specific humidity observations in the Oklahoma Boundary Layer Experiment (Figure 2.3). The application of the diagnostic model to wind and temperature profiles observed during the ETEX-1 release period produced turbulent velocity variances in the middle of the BL that seemed rather high. These are the result of very strong vertical wind shears within a

fairly unstable boundary layer. From the available observations it is not possible to conclude whether those variances are indeed excessive. In the low levels the model results compare reasonably well with sonic anemometer observations (Table 7.1). An examination of the buoyancy production term indicates a fairly thick EZ, in which σ_w^2 also decreases smoothly.

This smooth attenuation with height of the diagnosed σ_w^2 profile, within the EZ, gives further support to the removal (in Lagarangian models) of the total reflection condition at the top of the BL discussed in Chapter 4, section 4.6.6. A comparison of BL-FT exchanges with and without the reflection does not show a very important effect except for a small enhancement in the exchange rate when total reflection is removed (Figure 7.11). Further studies are needed to assess the full impacts of this change. For example, comparison with other BL-FT transmission aglorithms would be very interesting. Nevertheless, modelling results for ETEX using the no-reflection algorithm, shown in section 4.7.3, are rather good.

Bibliography

André, J. C., G. De Moor, P. Lacarrère, and R. du Vachat, Modeling the 24-hour evolution of the mean and turbulent structures of the planetary boundary layer, *Journal of the Atmospheric Sciences*, *35*(10), 1861–1883, doi:10.1175/1520-0469(1978)035$⟨$1861:MTHEOT$⟩$2.0.CO;2, 1978.

Angle, R. P., and H. S. Sandhu, Rural ozone concentrations in Alberta, Canada, *Atmospheric Environment (1967)*, *20*(6), 1221–1228, doi:10.1016/0004-6981(86)90157-5, 1986.

Bachmeier, A. S., M. C. Shipham, E. V. Browell, W. B. Grant, and J. M. Klassa, Stratospheric/tropospheric exchange affecting the northern wetlands regions of Canada during summer 1990, *J. Geophys. Res.*, *99*(D1), 1793–1804, doi:10.1029/93JD02179, 1994.

Barad, M. (Ed.), *Project Prairie Grass, A Field Program In Diffusion.*, *Geophysical Research Paper*, vol. 1, 299 pp., Air Force Cambridge Research Center, 1958.

Becker, A., et al., Global backtracking of anthropogenic radionuclides by means of a receptor oriented ensemble dispersion modelling system in support of Nuclear-Test-Ban Treaty verification, *Atmospheric Environment*, *41*(21), 4520 – 4534, doi:10.1016/j.atmosenv.2006.12.048, 2007.

Bélair, S., J. Mailhot, J. W. Strapp, and J. I. MacPherson, An examination of local versus nonlocal aspects of a TKE-based boundary layer scheme in clear convective conditions, *Journal of Applied Meteorology*, *38*(10), 1499–1518, doi:10.1175/1520-0450(1999)038$⟨$1499:AEOLVN$⟩$2.0.CO;2, 1999.

Benioff, P. A., Cosmic-ray production rate and mean removal time of beryllium-7 from the atmosphere, *Physical Review*, *104*(4), 1122–1130, 1956.

Boughton, B. A., J. M. Delaurentis, and W. E. Dunn, A stochastic model of particle dispersion in the atmosphere, *Boundary-Layer Meteorology*, *40*(1), 147–163, doi:10.1007/BF00140073, 1987.

Brost, R. A., J. Feichter, and M. Heimann, Three-Dimensional Simulation of ^{7}Be in a Global Climate Model, *J. Geophys. Res.*, *96*(D12), 22,423–22,445, doi:10.1029/91JD02283, 1991.

Businger, J. A., J. C. Wyngaard, Y. Izumi, and E. F. Bradley, Flux-profile relationships in the atmospheric surface layer, *Journal of the Atmospheric Sciences*, *28*(2), 181–189, doi:10.1175/1520-0469(1971)028⟨0181:FPRITA⟩2.0.CO;2, 1971.

Buzzi, A., G. Giovanelli, T. Nanni, and M. Tagliazucca, Study of high ozone concentrations in the troposphere associated with lee cyclogenesis during ALPEX, *Beitr. Phys. Atmos*, *57*, 1984.

Canadian Meteorological Centre (CMC), The Experimental High Resolution Deterministic Prediction System, *Tech. rep.*, Canadian Meteorological Centre, 2011.

Canadian Meteorological Centre (CMC), Improvements to the Global Deterministic Prediction System (from version 2.2.2 to3.0.0), and related changes to the regional deterministic prediction system (from version 3.0.0 to 3.1.0), *Tech. rep.*, Canadian Meteorological Centre, 2013a.

Canadian Meteorological Centre (CMC), Improvements to the Regional Deterministic Prediction system (RDPS), *Tech. rep.*, Canadian Meteorological Centre, 2013b.

CHINO, M., H. NAKAYAMA, H. NAGAI, H. TERADA, G. KATATA, and H. YAMAZAWA, Preliminary estimation of release amounts of ^{131}I and ^{137}Cs accidentally discharged from the Fukushima Daiichi nuclear power plant into the atmosphere, *Journal of Nuclear Science and Technology*, *48*(7), 1129–1134, 2011.

Clarke, R. H., Observational studies in the atmospheric boundary layer, *Quarterly Journal of the Royal Meteorological Society*, *96*(407), 91–114, doi:10.1002/qj.49709640709, 1970.

Clarke, R. H., R. Brook, D. Reid, and A. Troup, The Wangara Experiment: Boundary Layer Data, *Technical Paper 19*, CSIRO, Australia, 1971.

Colette, A., Gérard Ancellet, and F. Borchi, Impact of vertical transport processes on the tropospheric ozone layering above Europe. part I: Study of air mass origin using multivariate analysis, clustering and trajectories, *Atmospheric Environment*, *39*(29), 5409 – 5422, doi:10.1016/j.atmosenv.2005.06.014, 2005.

Colette, A., L. Menut, M. Haeffelin, and Y. Morille, Impact of the transport of aerosols from the free troposphere towards the boundary layer on the air quality in the Paris area, *Atmospheric Environment*, *42*(2), 390 – 402, doi:10.1016/j.atmosenv.2007.09.044, 2008.

Colonna, N. M., E. Ferrero, and U. Rizza, Nonlocal boundary layer: The pure buoyancy-driven and the buoyancy-shear-driven cases, *J. Geophys. Res.*, *114*, doi:10.1029/2008JD010682, 2009.

Côté, J., J.-G. Desmarais, S. Gravel, A. Méthot, A. Patoine, M. Roch, and A. Staniforth, The Operational CMC–MRB Global Environmental Multiscale (GEM) model. Part II: Results, *Monthly Weather Review*, *126*(6), 1397–1418, doi:10.1175/1520-0493(1998)126$⟨$1397:TOCMGE$⟩$2.0.CO;2, 1998a.

Côté, J., S. Gravel, A. Méthot, A. Patoine, M. Roch, and A. Staniforth, The Operational CMC–MRB Global Environmental Multiscale (GEM) model. Part I: Design considerations and formulation, *Monthly Weather Review*, *126*(6), 1373–1395, doi:10.1175/1520-0493(1998)126$⟨$1373:TOCMGE$⟩$2.0.CO;2, 1998b.

Cristofanelli, P., P. Bonasoni, L. Tositti, U. Bonafe, F. Calzolari, F. Evangelisti, S. Sandrini, and A. Stohl, A 6-year analysis of stratospheric intrusions and their influence on ozone at Mt. Cimone (2165 m above sea level), *J. Geophys. Res.*, *111*(D3), doi:10.1029/2005JD006553, 2006.

Cristofanelli, P., et al., Stratosphere-to-troposphere transport: A model and method evaluation, *J. Geophys. Res.*, *108*(D12), doi:10.1029/2002JD002600, 2003.

Crum, T. D., and R. B. Stull, Field measurements of the amount of surface layer air versus height in the entrainment zone, *Journal of the Atmospheric Sciences*, *44*(19), 2743–2753, doi:10.1175/1520-0469(1987)044⟨2743:FMOTAO⟩2.0.CO;2, 1987.

Cui, J., M. Sprenger, J. Staehelin, A. Siegrist, M. Kunz, S. Henne, and M. Steinbacher, Impact of stratospheric intrusions and intercontinental transport on ozone at Jungfraujoch in

2005: comparison and validation of two Lagrangian approaches, *Atmos. Chem. Phys.*, *9*(10), 3371–3383, 2009.

D'Amours, R., Modeling the ETEX plume dispersion with the Canadian emergency response model, *Atmospheric Environment*, *32*(24), 4335 – 4341, doi:10.1016/S1352-2310(98)00182-4, 1998.

D'Amours, R., A. Malo, R. Servranckx, D. Bensimon, S. Trudel, and J.-P. Gauthier-Bilodeau, Application of the atmospheric Lagrangian particle dispersion model MLDP0 to the 2008 eruptions of Okmok and Kasatochi volcanoes, *Journal of Geophysical Research: Atmospheres*, *115*(D2), doi:10.1029/2009JD013602, 2010.

D'Amours, R., R. Mintz, C. Mooney, and B. J. Wiens, A modeling assessment of the origin of Beryllium-7 and Ozone in the Canadian Rocky Mountains, *Journal of Geophysical Research: Atmospheres*, *118*(17), 10,125–10,138, doi:10.1002/jgrd.50761, 2013.

D'Amours, R., A. Malo, T. Flesch, J. Wilson, J.-P. Gauthier, and R. Servranckx, The Canadian Meteorological Centre's Atmospheric Transport and Dispersion Modelling Suite, *Atmosphere-Ocean*, *53*(2), 176–199, doi:10.1080/07055900.2014.1000260, 2015.

Davies, T. D., and E. Schuepbach, Episodes of high ozone concentrations at the earth's surface resulting from transport down from the upper troposphere/lower stratosphere: a review and case studies, *Atmospheric Environment*, *28*(1), 53–68, doi:10.1016/1352-2310(94)90022-1, 1994.

Davis, P., F. Johnston, W. Workman, and S. Chouhan, The G2 dispersion study, confidential - revised in 2011, 2005.

de Haan, P., On the use of density kernels for concentration estimations within particle and puff dispersion models, *Atmospheric Environment*, *33*(13), 2007 – 2021, doi:10.1016/S1352-2310(98)00424-5, 1999.

Delage, Y., A parameterization of the stable atmospheric boundary layer, *Boundary-Layer Meteorology*, *43*(4), 365–381, doi:10.1007/BF00121713, 1988.

Delage, Y., Parameterising sub-grid scale vertical transport in atmospheric models under statically stable conditions, *Boundary-Layer Meteorology*, *82*(1), 23–48, doi:10.1023/A:1000132524077, 1997.

Dibb, J. E., L. D. Meeker, R. C. Finkel, J. R. Southon, M. W. Caffee, and L. A. Barrie, Estimation of stratospheric input to the Arctic troposphere: ^{7}Be and ^{10}Be in aerosols at Alert, Canada, *J. Geophys. Res.*, *99*(D6), 12,855–12,864, doi:10.1029/94JD00742, 1994.

Draxler, R., et al., World Meteorological Organization's model simulations of the radionuclide dispersion and deposition from the Fukushima Daiichi nuclear power plant accident, *Journal of Environmental Radioactivity*, *139*(0), 172–184, doi:10.1016/j.jenvrad.2013.09.014, 2015.

Draxler, R. R., and G. D. Rolph, Evaluation of the Transfer Coefficient Matrix (TCM) approach to model the atmospheric radionuclide air concentrations from Fukushima, *Journal of Geophysical Research: Atmospheres*, *117*(D5), n/a–n/a, doi:10.1029/2011JD017205, 2012.

Durant, A. J., and W. I. Rose, Sedimentological constraints on hydrometeor-enhanced particle deposition: 1992 eruptions of Crater Peak, Alaska, *Journal of Volcanology and Geothermal Research*, *186*(1-2), 40 – 59, doi:10.1016/j.jvolgeores.2009.02.004, 2009.

Durbin, P. A., A random flight model of inhomogeneous turbulent dispersion, *Physics of Fluids*, *23*(11), 2151–2153, doi:10.1063/1.862908, 1980.

Dyer, A. J., and E. F. Bradley, An alternative analysis of flux-gradient relationships at the 1976 ITCE, *Boundary-Layer Meteorology*, *22*(1), 3–19, doi:10.1007/BF00128053, 1982.

Eckhardt, S., A. J. Prata, P. Seibert, K. Stebel, and A. Stohl, Estimation of the vertical profile of sulfur dioxide injection into the atmosphere by a volcanic eruption using satellite column measurements and inverse transport modeling, *Atmospheric Chemistry and Physics*, *8*(14), 3881–3897, 2008.

Elbern, H., J. Kowol, R. Sladkovic, and A. Ebel, Deep stratospheric intrusions: a statistical assessment with model guided analyses, *Atmospheric Environment*, *31*(19), 3207–3226, 1997.

Feely, H. W., R. J. Larsen, and C. G. Sanderson, Factors that cause seasonal variations in beryllium-7 concentrations in surface air, *Journal of Environmental Radioactivity*, *9*(3), 223–249, 1989.

Feng, J., A 3-mode parameterization of below-cloud scavenging of aerosols for use in atmospheric dispersion models, *Atmospheric Environment*, *41*(32), 6808 – 6822, doi:10.1016/j.atmosenv.2007.04.046, 2007.

Fioletov, V. E., E. Griffioen, J. B. Kerr, D. I. Wardle, and O. Uchino, Influence of volcanic sulfur dioxide on spectral UV irradiance as measured by Brewer spectrophotometers, *Geophys. Res. Lett.*, *25*(10), 1665–1668, doi:10.1029/98GL51305, 1998.

Flesch, T., R. D'Amours, C. Mooney, and J. Wilson, Mldp: A long-range lagrangian stochatic dispersion model, *Tech. rep.*, University of Alberta and Canadian Meteorological Centre, 2004.

Flesch, T. K., J. D. Wilson, and E. Yee, Backward-time Lagrangian stochastic dispersion models and their application to estimate gaseous emissions, *Journal of Applied Meteorology*, *34*(6), 1320–1332, doi:10.1175/1520-0450(1995)034$\langle$1320:BTLSDM$\rangle$2.0.CO;2, 1995.

Gerasopoulos, E., P. Zanis, C. Papastefanou, C. S. Zerefos, A. Ioannidou, and H. Wernli, A complex case study of down to the surface intrusions of persistent stratospheric air over the Eastern Mediterranean, *Atmospheric Environment*, *40*(22), 4113 – 4125, doi:10.1016/j.atmosenv.2006.03.022, 2006.

Gerasopoulos, E., et al., A climatology of ^{7}Be at four high-altitude stations at the Alps and the Northern Apennines, *Atmospheric Environment*, *35*(36), 6347–6360, doi:10.1175/1520-0450(1995)034$\langle$1320:BTLSDM$\rangle$2.0.CO;2, 2001.

Ghil, M., et al., Advanced spectral methods for climatic time series, *Rev. Geophys.*, *40*, 2002.

Girardi, F., G. Graziani, D. van Velzen, S. Galmarini, S. Mosca, R. Bianconi, R. Bellasio, W. Klug, and G. Fraser, *The European Tracer Experiment*, EUR 18143 EN, Office for Official Publications of the European Communities, 1998.

Gloster, J., et al., Airborne spread of foot-and-mouth disease –model intercomparison, *The Veterinary Journal*, *183*(3), 278–286, 2010.

Graziani, G., W. Klug, and S. Mosca, *Real-time Long-range Dispersion Model Evaluation of the ETEX First Release*, EUR 17754 EN, Office for Official Publications of the European Communities, 1998.

Gryning, S.-E., E. Batchvarova, D. Schneiter, P. Bessemoulin, and H. Berger, Meteorological conditions at the release site during the two tracer experiments, *Atmospheric Environment*, *32*(24), 4123–4137, doi:http://dx.doi.org/10.1016/S1352-2310(98)00191-5, 1998.

Gupta, S., R. T. McNider, M. Trainer, R. J. Zamora, K. Knupp, and M. P. Singh, Nocturnal wind structure and plume growth rates due to inertial oscillations, *Journal of Applied Meteorology*, *36*(8), 1050–1063, doi:10.1175/1520-0450(1997)036⟨1050:NWSAPG⟩2.0.CO;2, 1997.

Hanna, S. R., Lagrangian and Eulerian time-scale relations in the daytime boundary layer, *Journal of Applied Meteorology*, *20*(3), 242–249, doi:10.1175/1520-0450(1981)020⟨0242:LAETSR⟩2.0.CO;2, 1981.

Hanna, S. R., Spectra of concentration fluctuations: The two time scales of a meandering plume, *Atmospheric Environment (1967)*, *20*(6), 1131–1137, doi:10.1016/0004-6981(86)90145-9, 1986.

Haugen, D. A., J. C. Kaimal, and E. F. Bradley, An experimental study of Reynolds stress and heat flux in the atmospheric surface layer, *Quarterly Journal of the Royal Meteorological Society*, *97*(412), 168–180, doi:10.1002/qj.49709741204, 1971.

Hazi, Y., M. S. A. Heikkinen, and B. S. Cohen, Size distribution of acidic sulfate ions in fine ambient particulate matter and assessment of source region effect, *Atmospheric Environment*, *37*(38), 5403–5413, doi:10.1016/j.atmosenv.2003.08.034, 2003.

Health Canada, *Federal Nuclear Emergency Plan Part 1: Master Plan*, 5th edition ed., Government of Canada, 2014.

Högström, U., Non-dimensional wind and temperature profiles in the atmospheric surface layer: A re-evaluation, *Boundary-Layer Meteorology*, *42*(1-2), 55–78, doi:10.1007/BF00119875, 1988.

Holton, J. R., *An Introduction to Dynamic Meteorology*, *International Geophysics Series*, vol. 48, third ed., Academic Press, 1250 Sixth Avenue, San Diego, California, 1992.

Holton, J. R., P. H. Haynes, M. E. McIntyre, A. R. Douglass, R. B. Rood, and L. Pfister, Stratosphere-troposphere exchange, *Rev. Geophys.*, *33*(4), 403–439, doi:10.1029/95RG02097, 1995.

ICAO, *Handbook of the International Airways Volcano Watch (IAVW) - Operational Procedures and Contact List,*, International Civil Aviation Organization, Montreal, Canada, second edition ed., 2004.

James, P., A. Stohl, C. Forster, S. Eckhardt, P. Seibert, and A. Frank, A 15-year climatology of stratosphere-troposphere exchange with a Lagrangian particle dispersion model 2. Mean climate and seasonal variability, *J. Geophys. Res.*, *108*(D12), doi:10.1029/2002JD002639, 2003.

Joly, A., et al., Characterisation of particulate exposure during fireworks displays, *Atmospheric Environment*, *44*(34), 4325–4329, doi:10.1016/j.atmosenv.2009.12.010, 2010.

Jordan, C. E., J. E. Dibb, and R. C. Finkel, ^{10}Be/^{7}Be tracer of atmospheric transport and stratosphere-troposphere exchange, *J. Geophys. Res.*, *108*, doi:10.1029/2002JD002395, 2003.

Katata, G., M. Ota, H. Terada, M. Chino, and H. Nagai, Atmospheric discharge and dispersion of radionuclides during the Fukushima Dai-ichi Nuclear Power Plant accident. Part I: Source term estimation and local-scale atmospheric dispersion in early phase of the accident, *Journal of Environmental Radioactivity*, *109*(0), 103 – 113, doi:10.1016/j.jenvrad.2012.02.006, 2012.

Krasnoff, E., and R. L. Peskin, The Langevin model for turbulent diffusion, *Geophysical & Astrophysical Fluid Dynamics*, *2*(1), 123–146, doi:10.1080/03091927108236054, 1971.

Kritz, M. A., S. W. Rosner, E. F. Danielsen, and H. B. Selkirk, Air mass origins and troposphere-to-stratosphere exchange associated with mid-latitude cyclogenesis and tropopause folding inferred from ^{7}Be measurements, *J. Geophys. Res.*, *96*(D9), 17,405–17,414, doi:10.1029/91JD01358, 1991.

Lal, D., and B. Peters, Cosmic ray produced radioactivity on the earth, in *Handbuch der Physik*, edited by K. Sittle, 46/2, pp. 551–612, Springler, Berlin, 1967.

Lal, D., P. K. Malhotra, and B. Peters, On the production of radioisotopes in the atmosphere by cosmic radiation and their application to meteorology, *Journal of Atmospheric and Terrestrial Physics*, *12*(4), 306–328, 1958.

Langevin, P., Sur la théorie du mouvement brownien, in *Comptes rendus hebdomadaires de l'Académie des sciences*, vol. 146, edited by M. les secrétaires perpétuels, pp. 530–533, Gauthier-Villars, Paris, 1908.

Lefohn, A. S., H. Wernli, D. Shadwick, S. Limbach, S. J. Oltmans, and M. Shapiro, The importance of stratospheric–tropospheric transport in affecting surface ozone concentrations in the western and northern tier of the United States, *Atmospheric Environment*, *45*(28), 4845–4857, 2011.

Legg, B. J., M. R. Raupach, and P. A. Coppin, Experiments on scalar dispersion within a model plant canopy, part III: An elevated line source, *Boundary-Layer Meteorology*, *35*(3), 277–302, doi:10.1007/BF00123645, 1986.

Leon, J. D., D. A. Jaffe, J. Kaspar, A. Knecht, M. L. Miller, R. G. H. Robertson, and A. G. Schubert, Arrival time and magnitude of airborne fission products from the Fukushima, Japan, reactor incident as measured in Seattle, WA, USA, *Journal of Environmental Radioactivity*, *102*(11), 1032–1038, 2011.

Logan, J. A., Tropospheric ozone: Seasonal behavior, trends, and anthropogenic influence, *J. Geophys. Res.*, *90*(D6), 10,463–10,482, doi:10.1029/JD090iD06p10463, 1985.

Mailhot, J., and R. Benoit, A finite-element model of the atmospheric boundary layer suitable for use with numerical weather prediction models, *Journal of the Atmospheric Sciences*, *39*(10), 2249–2266, 1982.

Mailhot, J., S. Bélair, R. Benoit, B. Bilodeau, Y. Delage, L. Filion, L. Garand, C. Girard, and A. Tremblay, Scientific description of the RPN Physics Library, *CMC NWP Models Documentation*, Canadian Meteorological Centre, Dorval, QC, Canada, 1998.

Maryon, R. H., Determining cross-wind variance for low frequency wind meander, *Atmospheric Environment*, *32*(2), 115 – 121, doi:10.1016/S1352-2310(97)00325-7, 1998.

Mastin, L., et al., A multidisciplinary effort to assign realistic source parameters to models of volcanic ash-cloud transport and dispersion during eruptions, *Journal of Volcanology and Geothermal Research*, *186*(1-2), 10 – 21, doi:10.1016/j.jvolgeores.2009.01.008, 2009.

Mercier, J.-F., B. Tracy, R. d'Amours, F. Chagnon, I. Hoffman, E. Korpach, S. Johnson, and R. Ungar, Increased environmental gamma-ray dose rate during precipitation: a strong

correlation with contributing air mass, *Journal of Environmental Radioactivity*, *100*(7), 527 – 533, doi:10.1016/j.jenvrad.2009.03.002, 2009.

Moeng, C.-H., and P. P. Sullivan, A comparison of shear- and buoyancy-driven planetary boundary layer flows, *Journal of the Atmospheric Sciences*, *51*(7), 999–1022, 1994.

Mosca, S., R. Bianconi, R. Bellasio, G. Graziani, and W. Klug, *ATMES-II: Evaluation of Long-range Dispersion Models Using 1st ETEX Release Data. models description : draft report prepared for ETEX Symposium on Long-range Atmospheric Transport, Model Verification and Emergency Response, Vienna, 13-16 May 1997*, Office for Official Publications of the European Communities, 1998a.

Mosca, S., G. Graziani, W. Klug, R. Bellasio, and R. Bianconi, A statistical methodology for the evaluation of long-range dispersion models: an application to the ETEX exercise, *Atmospheric Environment*, *32*(24), 4307–4324, doi:http://dx.doi.org/10.1016/S1352-2310(98)00179-4, 1998b.

Nieuwstadt, F. T. M., The turbulent structure of the stable, nocturnal boundary layer, *Journal of the Atmospheric Sciences*, *41*(14), 2202–2216, doi:10.1175/1520-0469(1984)041⟨2202:TTSOTS⟩2.0.CO;2, 1984.

Nodop, K., R. Connolly, and F. Girardi, The field campaigns of the European Tracer Experiment (ETEX): overview and results, *Atmospheric Environment*, *32*(24), 4095–4108, doi:http://dx.doi.org/10.1016/S1352-2310(98)00190-3, 1998.

O'Brien, J. J., A Note on the Vertical Structure of the Eddy Exchange Coefficient in the Planetary Boundary Layer, *Journal of the Atmospheric Sciences*, *27*(8), 1213–1215, doi:10.1175/1520-0469(1970)027$⟨$1213:ANOTVS$⟩$2.0.CO;2, 1970.

Paillard, D., L. Labeyrie, and P. Yiou, Macintosh program performs time-series analysis, *Eos, Transactions American Geophysical Union*, *77*(39), 379–379, 1996.

Paquin, M., and R. D'Amours, An example of real-time emergency response: The SO_3 release in valleyfield, quebec, in *Proceedings of the Twenty-Eighth Arctic and Marine Oilspill Program (AMOP) Technical Seminar [including sessions for the Twenty-Second Technical Seminar on Chemical Spills (TSOCS)] ;*, vol. 2, edited by Environment Canada, pp. 735–743, 2005.

Peake, E., and B. D. Fong, Ozone concentrations at a remote mountain site and at two regional locations in southwestern Alberta, *Atmospheric Environment. Part A. General Topics*, *24*(3), 475–480, doi:10.1016/0960-1686(90)90004-7, 1990.

Prata, A. J., Observations of volcanic ash clouds in the 10-12 μm window using AVHRR/2 data, *International Journal of Remote Sensing*, *10*(4), 751–761, doi:10.1080/01431168908903916, 1989a.

Prata, A. J., Infrared radiative transfer calculations for volcanic ash clouds, *Geophys. Res. Lett.*, *16*(11), 1293–1296, doi:10.1029/GL016i011p01293, 1989b.

Pudykiewicz, J., Numerical simulation of the transport of radioactive cloud from the Chernobyl nuclear accident, *Tellus B*, *40B*(4), 241–259, 1988.

Pudykiewicz, J., Simulation of the Chernobyl dispersion with a 3-D hemispheric tracer model, *Tellus B*, *41B*(4), 391–412, doi:10.1111/j.1600-0889.1989.tb00317.x, 1989.

Pudykiewicz, J. A., Application of adjoint tracer transport equations for evaluating source parameters, *Atmospheric Environment*, *32*(17), 3039 – 3050, doi:10.1016/S1352-2310(97)00480-9, 1998.

Rodean, H. C., *Stochastic Lagrangian Models of Turbulent Diffusion*, no. 48 in Meteorological Monographs, American Meteorological Society, 45 Beacon Street, Boston, Massachusetts 02108, doi:10.1175/0065-9401-26.48.1, 1996.

Sawford, B. L., Lagrangian statistical simulation of concentration mean and fluctuation fields, *Journal of Applied Meteorology*, *24*(11), 1152–1166, doi:10.1175/1520-0450(1985)024⟨1152:LSSOCM⟩2.0.CO;2, 1985.

Seibert, P., and A. Frank, Source-receptor matrix calculation with a Lagrangian particle dispersion model in backward mode, *Atmos. Chem. Phys.*, *4*(1), 51–63, doi:10.1016/0960-1686(90)90004-7, 2004.

Servranckx, R., and P. Chen, Modeling volcanic ash transport and dispersion: Expectation and reality, in *Proceedings of the Second International Conference on Volcanic Ash and Aviation Safety*, edited by S. Williamson, pp. 3.1–3.5, U.S. Department of Commerce - NOAA, 2004.

Simpson, J. J., J. S. Berg, G. L. Hufford, C. Bauer, D. Pieri, and R. Servranckx, The February 2001 Eruption of Mount Cleveland, Alaska: Case Study of an Aviation Hazard, *Weather and Forecasting*, *17*(4), 691–704, doi:10.1175/1520-0434(2002)017⟨0691:TFEOMC⟩2.0.CO;2, 2002.

Sinclair, L. E., et al., Aerial measurement of radioxenon concentration off the west coast of Vancouver Island following the Fukushima reactor accident, *Journal of Environmental Radioactivity*, *102*(11), 1018–1023, doi:10.1016/j.jenvrad.2011.06.008, 2011.

Smith, F. B., The role of wind shear in horizontal diffusion of ambient particles, *Quarterly Journal of the Royal Meteorological Society*, *91*(389), 318–329, doi:10.1002/qj.49709138906, 1965.

Sokolnikoff, I. S., and R. M. Redheffer, *Mathematics of physics and modern engineering*, McGraw-Hill, 1966.

Sparks, R., M. Bursik, S. Carey, J. Gilbert, L. Glaze, H. Sigurdsson, and A. Woods, *Volcanic Plumes*, John Wiley & Sons, Baffin Lane, Chichester, West Sussex PO19 1UD, England, 1997.

Stocki, T., et al., Measurement and modelling of radioxenon plumes in the Ottawa Valley, *Journal of Environmental Radioactivity*, *99*(11), 1775 – 1788, doi:10.1016/j.jenvrad.2008.07.009, 2008.

Stohl, A., and D. J. Thomson, A Density Correction for Lagrangian Particle Dispersion Models, *Boundary-Layer Meteorology*, *90*, 155–167, 10.1023/A:1001741110696, 1999.

Stohl, A., H. Wernli, P. James, M. Bourqui, C. Forster, M. A. Liniger, P. Seibert, and M. Sprenger, A new perspective of stratosphere–troposphere exchange, *Bulletin of the American Meteorological Society*, *84*(11), 1565–1573, doi:10.1175/BAMS-84-11-1565, 2003.

Stohl, A., C. Forster, A. Frank, P. Seibert, and G. Wotawa, Technical note: The Lagrangian particle dispersion model FLEXPART version 6.2, *Atmospheric Chemistry and Physics*, *5*(9), 2461–2474, doi:10.5194/acp-5-2461-2005, 2005.

Stohl, A., P. Seibert, G. Wotawa, D. Arnold, J. F. Burkhart, S. Eckhardt, C. Tapia, A. Vargas, and T. J. Yasunari, Xenon-133 and caesium-137 releases into the atmosphere from the Fukushima Dai-ichi nuclear power plant: determination of the source term, atmospheric

dispersion, and deposition, *Atmospheric Chemistry and Physics*, *12*(5), 2313–2343, doi:10.5194/acp-12-2313-2012, 2012.

Stohl, A., et al., The influence of stratospheric intrusions on alpine ozone concentrations, *Atmospheric Environment*, *34*(9), 1323–1354, doi:10.1016/S1352-2310(99)00320-9, 2000.

Stull, R. B., *An Introduction to Boundary Layer Meteorology*, Atmospheric Sciences Library, Kluwer Academic Publishers, 1988.

Stull, R. B., and E. W. Eloranta, Boundary layer experiment - 1983, *Bulletin of the American Meteorological Society*, *65*(5), 450–456, 1984.

Sun, W.-Y., and Y. Ogura, Modeling the evolution of the convective planetary boundary layer, *Journal of the Atmospheric Sciences*, *37*(7), 1558–1572, doi:10.1175/1520-0469(1980)037⟨1558:MTEOTC⟩2.0.CO;2, 1980.

Taylor, G. I., Diffusion by continuous movements, *Proceedings of the London Mathematical Society*, *s2-20*(1), 196–212, 1922.

TEPCO, The Great East Japan Earthquake and Current Status of Nuclear Power Stations, *Tech. rep.*, Tokyo Electric Power Company, 2012.

Terada, H., G. Katata, M. Chino, and H. Nagai, Atmospheric discharge and dispersion of radionuclides during the Fukushima Dai-ichi Nuclear Power Plant accident. Part II: verification of the source term and analysis of regional-scale atmospheric dispersion, *Journal of Environmental Radioactivity*, *112*(0), 141 – 154, doi:10.1016/j.jenvrad.2012.05.023, 2012.

Thompson, R., Numeric calculation of turbulent diffusion, *Quarterly Journal of the Royal Meteorological Society*, *97*(411), 93–98, doi:10.1002/qj.49709741109, 1971.

Thomson, D. J., Random walk modelling of diffusion in inhomogeneous turbulence, *Quarterly Journal of the Royal Meteorological Society*, *110*(466), 1107–1120, doi:10.1002/qj.49711046620, 1984.

Thomson, D. J., Criteria for the selection of stochastic models of particle trajectories in turbulent flows, *Journal of Fluid Mechanics*, *180*, 529–556, doi:10.1017/S0022112087001940, 1987.

Thomson, D. J., and J. D. Wilson, *History of Lagrangian Stochastic Models for Turbulent Dispersion*, pp. 19–36, American Geophysical Union, Washington, D. C., doi:10.1029/2012GM001238, 2012.

Tupper, A., S. Carn, J. Davey, Y. Kamada, R. Potts, F. Prata, and M. Tokuno, An evaluation of volcanic cloud detection techniques during recent significant eruptions in the western 'Ring of Fire', *Remote Sensing of Environment*, *91*(1), 27 – 46, doi:10.1016/j.rse.2004.02.004, 2004.

USGS, The Eruption of Redoubt volcano, Alaska, December 14, 1989-August 31, 1990, *CIRCULAR 1061*, U.S. Geological Survey, Denver, CO 80225, 1990.

Usoskin, I. G., and G. A. Kovaltsov, Production of cosmogenic ^{7}Be isotope in the atmosphere: Full 3-D modeling, *J. Geophys. Res.*, *113*(D12), doi:/10.1029/2007JD009725, 2008.

van Dop, H., F. T. M. Nieuwstadt, and J. C. R. Hunt, Random walk models for particle displacements in inhomogeneous unsteady turbulent flows., *Physics of Fluids (00319171)*, *28*(6), 1985.

van Dop. H., et al., ETEX: A European Tracer Experiment; observations, dispersion modelling and emergency response, *Atmospheric Environment*, *32*(24), 4089 – 4094, doi:10.1016/S1352-2310(98)00248-9, 1998.

Van Kampen, N. G., *Stochastic Processes in Physics and Chemistry*, North Holland Personal Library, Elsevier, 2008.

Vautard, R., and M. Ghil, Singular spectrum analysis in nonlinear dynamics, with applications to paleoclimatic time series, *Physica D: Nonlinear Phenomena*, *35*(3), 395 – 424, doi:10.1016/0167-2789(89)90077-8, 1989.

Warner, S., N. Platt, and J. F. Heagy, Application of user-oriented measure of effectiveness to transport and dispersion model predictions of the european tracer experiment, *Atmospheric Environment*, *38*(39), 6789–6801, doi:10.1016/j.atmosenv.2004.09.024, 2004.

Webley, P., B. Stunder, and K. Dean, Preliminary sensitivity study of eruption source parameters for operational volcanic ash cloud transport and dispersion models – A case study of the August 1992 eruption of the Crater Peak vent, Mount Spurr, Alaska, *Journal of Volcanology and Geothermal Research*, *186*(1-2), 108 – 119, doi:10.1016/j.jvolgeores.2009.02.012, 2009.

Weil, J. C., A diagnosis of the asymmetry in top-down and bottom-up diffusion using a lagrangian stochastic model, *Journal of the Atmospheric Sciences*, *47*(4), 501–515, doi:10.1175/1520-0469(1990)047$⟨$0501:ADOTAI$⟩$2.0.CO;2, 1990.

Wilson, J., An alternative eddy-viscosity model for the horizontally uniform atmospheric boundary layer, *Boundary-Layer Meteorology*, *145*(1), 165–184, 2012.

Wilson, J., and E. Yee, A critical examination of the random displacement model of turbulent dispersion, *Boundary-Layer Meteorology*, *125*(3), 399–416, doi:10.1007/s10546-007-9201-x, 2007.

Wilson, J., F. Ferrandino, and G. Thurtell, A relationship between deposition velocity and trajectory reflection probability for use in stochastic Lagrangian dispersion models, *Agricultural and Forest Meteorology*, *47*(2-4), 139 – 154, doi:10.1016/0168-1923(89)90092-0, biometeorology, 1989.

Wilson, J. D., Trajectory models for heavy particles in atmospheric turbulence: Comparison with observations, *Journal of Applied Meteorology*, *39*(11), 1894–1912, doi:10.1175/1520-0450(2000)039⟨1894:TMFHPI⟩2.0.CO;, 2000.

Wilson, J. D., Turbulent Schmidt Numbers Above a Wheat Crop, *Boundary-Layer Meteorology*, *148*(2), 255–268, doi:10.1007/s10546-013-9819-9, 2013.

Wilson, J. D., and T. K. Flesch, Flow Boundaries in Random-Flight Dispersion Models: Enforcing the Well-Mixed Condition, *Journal of Applied Meteorology*, *32*(11), 1695–1707, doi:10.1175/1520-0450(1993)032{⟨1695:FBIRFD⟩}2.0.CO;2, 1993.

Wilson, J. D., and T. K. Flesch, An idealized mean wind profile for the atmospheric boundary layer, *Boundary-Layer Meteorology*, *110*(2), 281–299, doi:10.1023/A:1026044025803, 2004.

Wilson, J. D., and B. L. Sawford, Review of Lagrangian stochastic models for trajectories in the turbulent atmosphere, *Boundary-Layer Meteorology*, *78*(1), 191–210, doi:10.1007/BF00122492, 1996.

Wilson, J. D., G. W. Thurtell, and G. E. Kidd, Numerical simulation of particle trajectories in inhomogeneous turbulence, III: Comparison of predictions with experimental data for the atmospheric surface layer, *Boundary-Layer Meteorology*, *21*(4), 443–463, doi:10.1007/BF02033593, 1981a.

Wilson, J. D., G. W. Thurtell, and G. E. Kidd, Numerical simulation of particle trajectories in inhomogeneous turbulence, I: Systems with constant turbulent velocity scale, *Boundary-Layer Meteorology*, *21*(3), 295–313, 1981b.

Wilson, J. D., B. J. Legg, and D. J. Thomson, Calculation of particle trajectories in the presence of a gradient in turbulent-velocity variance, *Boundary-Layer Meteorology*, *27*(2), 163–169, doi:10.1007/BF00239612, 1983.

Wilson, J. D., T. K. Flesch, and G. E. Swaters, Dispersion in sheared Gaussian homogeneous turbulence, *Boundary-Layer Meteorology*, *62*(1), 281–290, doi:10.1007/BF00705559, 1993.

Wilson, J. D., T. K. Flesch, and R. d'Amours, Surface delays for gases dispersing in the atmosphere, *Journal of Applied Meteorology*, *40*(8), 1422–1430, doi:10.1175/1520-0450(2001)040⟨1422:SDFGDI⟩2.0.CO;2, 2001.

Witham, C. S., M. C. Hort, R. Potts, R. Servranckx, P. Husson, and F. Bonnardot, Comparison of VAAC atmospheric dispersion models using the 1 november 2004 Grimsvötn eruption, *Meteorological Applications*, *14*(1), 27–38, doi:10.1002/met.3, 2007.

WMO, *Manual on the Global Data-Processing and Forecasting System, Global Aspects*, World Meteorological Organization, Geneva, Switzerland, 2007.

WMO, *Manual on the Global Data-Processing and Forecasting System, Volume 1, Global Aspects*, World Meteorological Organization, 7 bis, avenue de la Paix, Geneva, Switzerland, 2010, updated 2012.

Wotawa, G., et al., Atmospheric transport modelling in support of CTBT verification–overview and basic concepts, *Atmospheric Environment*, *37*(18), 2529 – 2537, doi:10.1016/S1352-2310(03)00154-7, 2003.

Wyngaard, J. C., Structure of the planetary boundary layer and implications for its modeling, *Journal of Climate and Applied Meteorology*, *24*(11), 1131–1142, 1985.

Wyngaard, J. C., *Turbulence in the Atmosphere*, Cambridge University Press, 2010.

Yamada, T., and G. Mellor, A simulation of the wangara atmospheric boundary layer data, *Journal of the Atmospheric Sciences*, *32*(12), 2309–2329, 1975.

Yee, E., F.-S. Lien, A. Keats, and R. D'Amours, Bayesian inversion of concentration data: Source reconstruction in the adjoint representation of atmospheric diffusion, *Journal of Wind Engineering and Industrial Aerodynamics*, *96*(10–11), 1805–1816, doi:10.1016/j.jweia.2008.02.024, 2008.

Zanis, P., et al., An estimate of the impact of stratosphere-to-troposphere transport [STT) on the lower free tropospheric ozone over the Alps using ^{10}Be and ^{7}Be measurements, *J. Geophys. Res.*, *108*(D12), 2003a.

Zanis, P., et al., Forecast, observation and modelling of a deep stratospheric intrusion event over Europe, *Atmos. Chem. Phys. Discuss.*, *3*(1), 1109–1138, 2003b.

Zheng, X., C. Shen, G. Wan, K. Liu, J. Tang, and X. Xu, ^{10}Be/^{7}Be implies the contribution of stratosphere-troposphere transport to the winter-spring surface O_3 variation observed on the Tibetan Plateau, *Chinese Science Bulletin*, *56*(1), 84–88, 2011.

APPENDIX A

Thomsons's simplest solution

Assuming that the velocity fluctuations are uncorrelated, equation (3.17) becomes:

$$V_{i,j} = \overline{u_i u_j} = \begin{cases} 0 & i \neq j \\ \sigma_u^2 & i = 1\,, \\ \sigma_v^2 & i = 2\,, \\ \sigma_w^2 & i = 3\,. \end{cases} \tag{A.1}$$

Looking at the along x components of equation (3.18), term by term:

$$\frac{1}{2}\frac{\partial V_{i,l}}{\partial x_l} + \frac{\partial U_i}{\partial t} + U_l \frac{\partial U_i}{\partial x_l} \rightarrow \frac{1}{2}\frac{\partial \sigma_u^2}{\partial x} + \frac{\partial U}{\partial t} + U\frac{\partial U}{\partial x}\,,$$

$$\left[\frac{1}{2}(\boldsymbol{V}^{-1})_{l,j}\left(\frac{\partial V_{i,l}}{\partial t} + U_m \frac{\partial V_{il}}{\partial x_m}\right) + \frac{\partial U_i}{\partial x_j}\right](u_j - U_j) \rightarrow \left[\frac{1}{2\sigma_u^2}\left(\frac{\partial \sigma_u^2}{\partial t} + U_m \frac{\partial \sigma_u^2}{\partial x_m}\right) + \frac{\partial U}{\partial x}\right]u\,,$$

$$\frac{1}{2}(\boldsymbol{V}^{-1})_{l,j}\frac{\partial V_{i,l}}{\partial x_k}(u_j - U_j)(u_k - U_k) \rightarrow \frac{1}{2\sigma_u^2}\left(\frac{\partial \sigma_u^2}{\partial x}u^2 + \frac{\partial \sigma_u^2}{\partial y}uv + \frac{\partial \sigma_u^2}{\partial z}uw\right).$$

Then assuming quasi-steadiness and horizontal quasi-homogeneity, we get:

$$\begin{aligned}
\frac{1}{2}\frac{\partial\sigma_u^2}{\partial x}+\frac{\partial U}{\partial t}+U\frac{\partial U}{\partial x} &\rightarrow 0\,,\\
\left[\frac{1}{2\sigma_u^2}\left(\frac{\partial\sigma_u^2}{\partial t}+U_m\frac{\partial\sigma_u^2}{\partial x_m}\right)+\frac{\partial U}{\partial x}\right]u &\rightarrow \frac{1}{2\sigma_u^2}Wu\frac{\partial\sigma_u^2}{\partial z}\,,\\
\frac{1}{2\sigma_u^2}\left(\frac{\partial\sigma_u^2}{\partial x}u^2+\frac{\partial\sigma_u^2}{\partial y}uv+\frac{\partial\sigma_u^2}{\partial z}uw\right) &\rightarrow \frac{1}{2\sigma_u^2}\frac{\partial\sigma_u^2}{\partial z}uw\,.
\end{aligned}$$

Collecting, we get:

$$\begin{aligned}
\frac{\phi_x}{g_a} &= \frac{1}{2\sigma_u^2}Wu\frac{\partial\sigma_u^2}{\partial z}+\frac{1}{2\sigma_u^2}\frac{\partial\sigma_u^2}{\partial z}uw\,,\\
\frac{\phi_x}{g_a} &= \frac{1}{2\sigma_u^2}\frac{\partial\sigma_u^2}{\partial z}(W+w)u\,.
\end{aligned}\tag{A.2}$$

The y terms are treated the same way:

$$\frac{\phi_y}{g_a}=\frac{1}{2\sigma_u^2}\frac{\partial\sigma_u^2}{\partial z}(W+w)v\,.\tag{A.3}$$

Now looking at the z terms, i.e. $i\rightarrow 3$, and because $V_{il}=0$ for $l\neq 3$, the terms on the first line of (3.18) become:

$$\frac{1}{2}\frac{\partial V_{il}}{\partial x_l}+\frac{\partial U_i}{\partial t}+U_l\frac{\partial U_i}{\partial x_l}\rightarrow\frac{1}{2}\frac{\partial\sigma_w^2}{\partial z}+\frac{\partial W}{\partial t}+W\frac{\partial W}{\partial z}\,.\tag{A.4}$$

Since $i=3$ and $l=3$, j can only be 3. However m can still vary from 1 to 3, and the terms on the second line of (3.18) become:

$$\left[\frac{1}{2}V_{lj}^{-1}\left(\frac{\partial V_{il}}{\partial t}+U_m\frac{\partial V_{il}}{\partial x_m}\right)+\frac{\partial U_i}{\partial x_j}\right](u_j-U_j)\rightarrow\left[\frac{1}{2\sigma_w^2}\left(\frac{\partial\sigma_w^2}{\partial t}+U_m\frac{\partial\sigma_w^2}{\partial x_m}\right)+\frac{\partial W}{\partial z}\right]w\,.\tag{A.5}$$

Those on the third line become:

$$\frac{1}{2}V_{lj}^{-1}\frac{\partial V_{il}}{\partial x_k}(u_j-U_j)(u_k-U_k)\rightarrow\frac{1}{2\sigma_w^2}\left(\frac{\partial\sigma_w^2}{\partial x}uw+\frac{\partial\sigma_w^2}{\partial y}vw+\frac{\partial\sigma_w^2}{\partial z}ww\right).\tag{A.6}$$

Again, under quasi-steadiness and horizontal quasi-homogeneity hypotheses, terms in $\partial/\partial t$, $\partial/\partial x$ and $\partial/\partial y$ vanish, we then get:

$$\frac{1}{2}\frac{\partial\sigma_w^2}{\partial z}+\frac{\partial W}{\partial t}+W\frac{\partial W}{\partial z}\rightarrow\frac{1}{2}\frac{\partial\sigma_w^2}{\partial z}+W\frac{\partial W}{\partial z}\,,\tag{A.7}$$

$$\left[\frac{1}{2\sigma_w^2}\left(\frac{\partial\sigma_w^2}{\partial t}+U_m\frac{\partial\sigma_w^2}{\partial x_m}\right)+\frac{\partial W}{\partial z}\right]w\rightarrow\frac{1}{2\sigma_w^2}\left(W\frac{\partial\sigma_w^2}{\partial z}+\frac{\partial W}{\partial z}\right)w\,,\tag{A.8}$$

$$\frac{1}{2\sigma_w^2}\left(\frac{\partial\sigma_w^2}{\partial x}uw+\frac{\partial\sigma_w^2}{\partial y}vw+\frac{\partial\sigma_w^2}{\partial z}ww\right)\rightarrow\frac{1}{2\sigma_w^2}\frac{\partial\sigma_w^2}{\partial z}ww\,.\tag{A.9}$$

Collecting:

$$\frac{\phi_z}{g_a} = \frac{1}{2}\frac{\partial \sigma_w^2}{\partial z} + W\frac{\partial W}{\partial z} + \frac{1}{2\sigma_w^2}\left(W\frac{\partial \sigma_w^2}{\partial z} + \frac{\partial W}{\partial z}\right)w + \frac{1}{2\sigma_w^2}\frac{\partial \sigma_w^2}{\partial z}ww\,, \tag{A.10}$$

$$= \frac{1}{2\sigma_w^2}\frac{\partial \sigma_w^2}{\partial z}(W+w)w + \frac{\partial W}{\partial z}(W+w) + \frac{1}{2}\frac{\partial \sigma_w^2}{\partial z}\,. \tag{A.11}$$

This differs slightly from the equations used by *D'Amours et al.* [2015] and *Flesch et al.* [2004]; we have an extra term: $\partial W/\partial z(W+w)w$. However as discussed by *Flesch et al.* [1995], since we are assuming quasi-stationary conditions, we should also assume incompressibility. Therefore, because we are also assuming horizontal homogeneity, $\partial W/\partial z$ must also vanish, which implies that $W = 0$. Then equations (A.2), (A.3) and (A.11) become

$$\frac{\phi_x}{g_a} = \frac{1}{2\sigma_u^2}\frac{\partial \sigma_u^2}{\partial z}wu\,, \tag{A.12}$$

$$\frac{\phi_y}{g_a} = \frac{1}{2\sigma_u^2}\frac{\partial \sigma_u^2}{\partial z}wv\,, \tag{A.13}$$

$$\frac{\phi_z}{g_a} = \frac{1}{2}\frac{\partial \sigma_w^2}{\partial z}\left(1 + \frac{w^2}{\sigma_w^2}\right). \tag{A.14}$$

APPENDIX B

A Crank-Nicholson scheme for TKE and σ_w^2

Because of the numerical instability associated with the diffusion term, it is handled separately with Crank-Nicholson scheme. We recall the model equations :

$$\frac{\partial E}{\partial t} = (S_u + S_v + B) + \frac{\partial}{\partial z}\left[c_K \sigma_w^2 \tau_w \frac{\partial E}{\partial z}\right] - c_\epsilon \frac{E}{\tau_w}\,, \tag{B.1}$$

$$\frac{\partial \sigma_w^2}{\partial t} = 2B + \frac{\partial}{\partial z}\left[c_K \sigma_w^2 \tau_w \frac{\partial \sigma_w^2}{\partial z}\right] + c_R \frac{(2/3E - \sigma_w^2)}{\sigma_w} - c_\epsilon \frac{\sigma_w^2}{\tau_w}\,. \tag{B.2}$$

In a first intermediate step, production, redistribution and dissipation are handled with a simple forward time step:

$$E(t+\Delta t)^\star = E(t) + \left[(S_u + S_v + B) - c_\epsilon \frac{E}{\tau_w}\right]\Delta t\,, \tag{B.3}$$

$$\sigma_w^2(t+\Delta t)^\star = \sigma_w^2(t) + \left[2B + c_R \frac{(2/3E - \sigma_w^2)}{\sigma_w} - c_\epsilon \frac{\sigma_w^2}{\tau_w}\right]\Delta t\,, \tag{B.4}$$

then

$$E(t+\Delta t) = E(t+\Delta t)^\star + \mathbb{D}[E(t+\Delta t)^\star]\Delta t\,, \tag{B.5}$$

$$\sigma_w^2(t+\Delta t) = \sigma_w^2(t+\Delta t)^\star + \mathbb{D}[\sigma_w^2(t+\Delta t)^\star]\Delta t\,, \tag{B.6}$$

where $\mathbb{D}[\,]$ is a diffusion operator based on the Crank-Nicholson scheme to estimate

$$\frac{\partial}{\partial z}\left[c_K \sigma_w^2 \tau_w \frac{\partial E}{\partial z}\right] \text{ and } \frac{\partial}{\partial z}\left[c_K \sigma_w^2 \tau_w \frac{\partial \sigma_w^2}{\partial z}\right].$$

B.1 Variance of the turbulent vertical velocity σ_w^2

First we look at σ_w^2. We use n for time indexing, and k as index for the vertical levels. It is not assumed that levels are distributed evenly in the vertical. For simplicty $\sigma_w^2(z,t)$ is written as S_k^n at the corresponding level k and time index n, and the vertical diffusion coefficient $c_K\sigma_w^2\tau_w$ is written, similarly, as K_k^n.

We start by discretizing the vertical derivatives. The first derivative at level k and time index n is written as:

$$K\frac{\partial\sigma_w^2}{\partial z} \approx K_k^n\frac{S_k^n - S_{k-1}^n}{\Delta z_k}\,, \tag{B.7}$$

where $\Delta z_k = z_k - z_{k-1}$. At the next level,

$$K\frac{\partial\sigma_w^2}{\partial z} \approx K_{k+1}^n\frac{S_{k+1}^n - S_k^n}{\Delta z_{k+1}}\,. \tag{B.8}$$

The discretized second derivative at level k and time index n can be written as:

$$\begin{aligned}\frac{\partial}{\partial z}\left[K\frac{\partial\sigma_w^2}{\partial z}\right]_k^n &\approx \frac{K_{k+1}^n\frac{S_{k+1}^n-S_k^n}{\Delta z_{k+1}} - K_k^n\frac{S_k^n-S_{k-1}^n}{\Delta z_k}}{1/2(\Delta z_{k+1}+\Delta z_k)}\,,\\ &\approx \frac{1}{1/2}\left[K_{k+1}^n\frac{S_{k+1}^n - S_k^n}{\Delta z_{k+1}(\Delta z_{k+1}+\Delta z_k)} - K_k^n\frac{S_k^n - S_{k-1}^n}{\Delta z_k(\Delta z_{k+1}+\Delta z_k)}\right].\end{aligned} \tag{B.9}$$

Similarly at time index $n+1$, the second derivative is written as:

$$\frac{\partial}{\partial z}\left[K\frac{\partial\sigma_w^2}{\partial z}\right]_k^{n+1} \approx \frac{1}{1/2}\left[K_{k+1}^{n+1}\frac{S_{k+1}^{n+1} - S_k^{n+1}}{\Delta z_{k+1}(\Delta z_{k+1}+\Delta z_k)} - K_k^n\frac{S_k^{n+1} - S_{k-1}^{n+1}}{\Delta z_k(\Delta z_{k+1}+\Delta z_k)}\right]. \tag{B.10}$$

The increment of S_k^n (which represents σ_w^2) to S_k^{n+1} after a time step Δt, due to diffusion, is estimated by taking the average of (B.9) and (B.10):

$$\begin{aligned}(S_k^{n+1} - S_k^n) = \Delta t\Bigg\{&\left[K_{k+1}^{n+1}\frac{S_{k+1}^{n+1} - S_k^{n+1}}{\Delta z_{k+1}(\Delta z_{k+1}+\Delta z_k)} - K_k^n\frac{S_k^{n+1} - S_{k-1}^{n+1}}{\Delta z_k(\Delta z_{k+1}+\Delta z_k)}\right]\\ &+\left[K_{k+1}^n\frac{S_{k+1}^n - S_k^n}{\Delta z_{k+1}(\Delta z_{k+1}+\Delta z_k)} - K_k^n\frac{S_k^n - S_{k-1}^n}{\Delta z_k(\Delta z_{k+1}+\Delta z_k)}\right]\Bigg\}.\end{aligned} \tag{B.11}$$

To simplify more, we write $\Delta t/(\Delta z_{k+1}+\Delta z_k)$ as α_k, and $\frac{1}{\Delta z_k}$ as β_k. After rearranging we get:

$$\begin{aligned}(S_k^{n+1} - S_k^n) = {}&\alpha_k\beta_{k+1}K_{k+1}^{n+1}(S_{k+1}^{n+1} - S_k^{n+1}) - \alpha_k\beta_k K_k^n(S_k^{n+1} - S_{k-1}^{n+1})\\ &+\alpha_k\beta_{k+1}K_{k+1}^n(S_{k+1}^n - S_k^n) - \alpha_k\beta_k K_k^n(S_k^n - S_{k-1}^n)\,,\end{aligned} \tag{B.12}$$

$$(S_k^{n+1} - S_k^n) = \alpha_k\beta_{k+1}K_{k+1}^{n+1}S_{k+1}^{n+1} - \alpha_k\beta_{k+1}K_{k+1}^{n+1}S_k^{n+1} - \alpha_k\beta_k K_k^n S_k^{n+1} + \alpha_k\beta_k K_k^n S_{k-1}^{n+1} + \alpha_k\beta_{k+1}K_{k+1}^n S_{k+1}^n - \alpha_k\beta_{k+1}K_{k+1}^n S_k^n - \alpha_k\beta_k K_k^n S_k^n + \alpha_k\beta_k K_k^n S_{k-1}^n \,,$$

$$-S_k^{n+1} + \alpha_k\beta_{k+1}K_{k+1}^{n+1}S_{k+1}^{n+1} - \alpha_k\beta_{k+1}K_{k+1}^{n+1}S_k^{n+1} - \alpha_k\beta_k K_k^n S_k^{n+1} + \alpha_k\beta_k K_k^n S_{k-1}^{n+1} = -S_k^n - \alpha_k\beta_{k+1}K_{k+1}^n S_{k+1}^n + \alpha_k\beta_{k+1}K_{k+1}^n S_k^n + \alpha_k\beta_k K_k^n S_k^n - \alpha_k\beta_k K_k^n S_{k-1}^n \,,$$

$$+\alpha_k\beta_{k+1}K_{k+1}^{n+1}S_{k+1}^{n+1} - \alpha_k\beta_{k+1}K_{k+1}^{n+1}S_k^{n+1} - S_k^{n+1} - \alpha_k\beta_k K_k^n S_k^{n+1} + \alpha_k\beta_k K_k^n S_{k-1}^{n+1} = -\alpha_k\beta_{k+1}K_{k+1}^n S_{k+1}^n + \alpha_k\beta_{k+1}K_{k+1}^n S_k^n + \alpha_k\beta_k K_k^n S_k^n - S_k^n - \alpha_k\beta_k K_k^n S_{k-1}^n \,,$$

$$+\alpha_k\beta_{k+1}K_{k+1}^{n+1}S_{k+1}^{n+1} - (\alpha_k\beta_{k+1}K_{k+1}^{n+1}S_k^{n+1} + S_k^{n+1} + \alpha_k\beta_k K_k^n S_k^{n+1}) + \alpha_k\beta_k K_k^n S_{k-1}^{n+1} = -\alpha_k\beta_{k+1}K_{k+1}^n S_{k+1}^n + (\alpha_k\beta_{k+1}K_{k+1}^n S_k^n + \alpha_k\beta_k K_k^n S_k^n - S_k^n) - \alpha_k\beta_k K_k^n S_{k-1}^n \,,$$

$$\alpha_k\beta_{k+1}K_{k+1}^{n+1}S_{k+1}^{n+1} - (\alpha_k\beta_{k+1}K_{k+1}^{n+1} + \alpha_k\beta_k K_k^n + 1)S_k^{n+1} + \alpha_k\beta_k K_k^n S_{k-1}^{n+1} = -\alpha_k\beta_{k+1}K_{k+1}^n S_{k+1}^n + (\alpha_k\beta_{k+1}K_{k+1}^n + \alpha_k\beta_k K_k^n - 1)S_k^n - \alpha_k\beta_k K_k^n S_{k-1}^n \,.$$

After expansion and some rearrangements, we get:

$$-\alpha_k\beta_{k+1}K_{k+1}^{n+1}S_{k+1}^{n+1} + (1 + \alpha_k\beta_{k+1}K_{k+1}^{n+1} + \alpha_k\beta_k K_k^n)S_k^{n+1} - \alpha_k\beta_k K_k^n S_{k-1}^{n+1} = \alpha_k\beta_{k+1}K_{k+1}^n S_{k+1}^n + (1 - \alpha_k\beta_{k+1}K_{k+1}^n - \alpha_k\beta_k K_k^n)S_k^n + \alpha_k\beta_k K_k^n S_{k-1}^n \,.$$

This set of equations defines a tri-diagonal system where S_{k-1}^{n+1}, S_k^{n+1} and S_{k+1}^{n+1} are the unknown variables. K_k^n is the diffusion coefficient for level k, and time index n and is equal to $\lambda(k)\sqrt{S_k^n}$. Therefore K_k^n varies with time. Here, we assume that K_k^n remains constant during time interval Δt.

$$-\alpha_k\beta_k K_k^n\, S_{k-1}^{n+1} + (1 + \alpha_k\beta_{k+1}K_{k+1}^n + \alpha_k\beta_k K_k^n)\, S_k^{n+1} - \alpha_k\beta_{k+1}K_{k+1}^n\, S_{k+1}^{n+1} = \alpha_k\beta_k K_k^n\, S_{k-1}^n + (1 - \alpha_k\beta_{k+1}K_{k+1}^n - \alpha_k\beta_k K_k^n)\, S_k^n + \alpha_k\beta_{k+1}K_{k+1}^n\, S_{k+1}^n \,. \tag{B.13}$$

For further simplification of the notation we write;

$a_k = -\alpha_k\beta_k K_k^n$,

$b_k = (1 + \alpha_k\beta_{k+1}K_{k+1}^n + \alpha_k\beta_k K_k^n)$,

$c_k = -\alpha_k\beta_{k+1}K_{k+1}^n$,

$d_k = (1 - \alpha_k\beta_{k+1}K_{k+1}^n - \alpha_k\beta_k K_k^n)$,

$$a_k\, S_{k-1}^{n+1} + b_k\, S_k^{n+1} + c_k\, S_{k+1}^{n+1} = -a_k\, S_{k-1}^n + d_k\, S_k^n - c_k\, S_{k+1}^n \,. \tag{B.14}$$

In matrix form, where index L stands for the last level:

$$\begin{pmatrix} a_1 & b_1 & c_1 & 0 & \cdots & \cdots & 0 \\ 0 & a_2 & b_2 & c_2 & \cdots & \cdots & 0 \\ \ddots & \ddots & \ddots & \ddots & \ddots & \ddots & \ddots \\ 0 & \cdots & a_k & b_k & c_k & \cdots & 0 \\ \ddots & \ddots & \ddots & \ddots & \ddots & \ddots & \ddots \\ 0 & \cdots & \cdots & 0 & a_L & b_L & c_L \end{pmatrix} \begin{pmatrix} S_1^{n+1} \\ S_2^{n_1} \\ \ddots \\ S_k^{n+1} \\ \ddots \\ S_{Lev}^{n+1} \end{pmatrix} =$$

$$\begin{pmatrix} -a_1 & d_1 & -c_1 & 0 & \cdots & \cdots & 0 \\ 0 & -a_2 & d_2 & -c_2 & \cdots & \cdots & 0 \\ 0 & \ddots & \ddots & \ddots & \ddots & \ddots & 0 \\ 0 & \cdots & -a_k & d_k & -c_k & \cdots & 0 \\ 0 & \ddots & \ddots & \ddots & \ddots & \ddots & 0 \\ 0 & \cdots & \cdots & 0 & -a_L & d_L & -c_L \end{pmatrix} \begin{pmatrix} S_1^n \\ S_2^n \\ \ddots \\ S_k^n \\ \ddots \\ S_L^n \end{pmatrix}. \tag{B.15}$$

The known terms are first caluclated as the vector R_k:

$$\begin{pmatrix} R_1 \\ R_2 \\ \ddots \\ R_k \\ \ddots \\ R_L \end{pmatrix} = \begin{pmatrix} -a_1 & d_1 & -c_1 & 0 & \cdots & \cdots & 0 \\ 0 & -a_2 & d_2 & -c_2 & \cdots & \cdots & 0 \\ 0 & \ddots & \ddots & \ddots & \ddots & \ddots & 0 \\ 0 & \cdots & -a_k & d_k & -c_k & \cdots & 0 \\ 0 & \ddots & \ddots & \ddots & \ddots & \ddots & 0 \\ 0 & \cdots & \cdots & 0 & -a_L & d_L & -c_L \end{pmatrix} \begin{pmatrix} S_1^n \\ S_2^n \\ \ddots \\ S_k^n \\ \ddots \\ S_L^n \end{pmatrix}. \tag{B.16}$$

Then the tridiagonal system is solved for S_k^{n+1}:

$$\begin{pmatrix} a_1 & b_1 & c_1 & 0 & \cdots & \cdots & 0 \\ 0 & a_2 & b_2 & c_2 & \cdots & \cdots & 0 \\ \ddots & \ddots & \ddots & \ddots & \ddots & \ddots & \ddots \\ 0 & \cdots & a_k & b_k & c_k & \cdots & 0 \\ \ddots & \ddots & \ddots & \ddots & \ddots & \ddots & \ddots \\ 0 & \cdots & \cdots & 0 & a_L & b_L & c_L \end{pmatrix} \begin{pmatrix} S_1^{n+1} \\ S_2^{n_1} \\ \ddots \\ S_k^{n+1} \\ \ddots \\ S_L^{n+1} \end{pmatrix} = \begin{pmatrix} R_1 \\ R_2 \\ \ddots \\ R_k \\ \ddots \\ R_L \end{pmatrix}. \tag{B.17}$$

We recall that S_k^n represents $\sigma_w^2(t+\Delta t)^\star$ after incrementation due to production, redistribution and dissipation.

B.2 Variance of the TKE

The TKE represented by E is handled the same way by replacing S_k^n by E_k^n in the system (B.16), then solving the system (B.17) will give E_k^{n+1}.